Geological setting and evolution of the Omitiomire Cu deposit in the Southern Zone accretionary prism of the Damara Belt, Namibia

by

Shawn Kitt

Dissertation presented for the degree of Doctor of Philosophy
in the Faculty of Science at the University of Stellenbosch

Promoters:

Professor Alexander Kisters
Professor Ian Buick

December 2017

Declaration

By submitting this dissertation electronically, I declare that the entirety of the work contained herein is my own, original work, that I am the sole author thereof (save to the extent explicitly otherwise stated), that reproduction and publication thereof by Stellenbosch University will not infringe any third party rights and that I have not previously in its entirety or in part submitted it for obtaining any qualification.

This dissertation includes two original papers published in peer-reviewed journals and one unpublished publication. The development and writing of the papers (published and unpublished) were the principal responsibility of myself and, for each of the cases where this is not the case, a declaration is included in the dissertation indicating the nature and extent of the contributions of co-authors.

Shawn Kitt

Date: December 2017

"I may not have gone where I intended to go,

but I think I have ended up where I needed to be."

Douglas Adams

Abstract

Shear Zone hosted Cu mineralisation in the Deep Level Southern Zone accretionary prism of the Damara Belt is associated with deformation and fluid flow related to the exhumation of the Mesoproterozoic Ekuja basement gneiss dome during the Pan-African convergence of the Congo and Kalahari Cratons. In terms of tectonic setting, metamorphic grade and age structure, the mineralisation has no real equivalent in Namibia and seems to defy current classification schemes of Cu deposits. This study aims to describe the geometry and controls of mineralisation and the sources of fluids and metals in Omitiomire Cu deposit, and constrain the internal dynamics and processes that led to the imbrication of 100 km^2 slivers of basement gneisses with the overlying prism metasediments.

The Omitiomire Cu deposit (137 Mt at 0.54% Cu) is hosted by a low-angle, late-Damaran (ca. 520 Ma) shear zone system, referred to as the Omitiomire Shear Zone (OSZ), that developed around an older (ca. 1100–1060 Ma), late Mesoproterozoic intrusive breccia between a suite of mafic rocks (originally lava flows) and later tonalitic gneisses. The chalcocite-dominated mineralisation is associated with biotite-epidote assemblages that formed through the progressive hydration of the original mafic rocks to amphibole-biotite gneiss and biotite-epidote schist during deformation and fluid infiltration along the OSZ. Stable isotope (O, H and S) data indicate upper-greenschist-to middle amphibolite-facies conditions, a low fluid-rock ratio and a local redistribution of sulfur during fluid flow and mineralisation. This points to the remobilisation by epigenetic fluid flow of an older Cu mineralisation event.

The geometry of the mineralisation is controlled by the spatial coincidence of the OSZ and the inherent heterogeneity of the original intrusive amphibolite–tonalite breccia. The gently undulating, shallowly-east dipping orebody is composed of several mineralised lenses that are

contained in the regional S2 fabric. High-grade ore shoots are parallel to a prominent N-S trending L2 stretching lineation and are correlated with the cumulative number and thickness of several thin quartz-biotite-epidote-chalcocite shear zones at the contacts of interleaved schists and felsic gneisses.

The kinematics and the association of the Cu mineralisation with retrograde assemblages in the OSZ link the mineralisation with the exhumation of the Ekuja Dome. The timing of exhumation is constrained to between 526.4 ± 3.5 and 521.9 ± 3.6 Ma by $^{40}Ar/^{39}Ar$ dating of biotite from the OSZ. Peak metamorphic assemblages in amphibolite gneisses from the Ekuja dome record PT conditions of 8.5-9.15 kbar and 635-655 °C, which equates burial to ca. 35 km. In contrast, PT estimates and U-Pb xenotime age determinations in the overlying prism metasediments show that peak metamorphic conditions of 7-9.25 kbar and 640-675 °C were only reached at ca. 515 Ma. This suggest that exhumation of the Ekuja dome started some ~10 Ma before maximum burial and peak metamorphism was reached in the overlying prism sediments and reflects the complexities of subduction-exhumation processes in accretionary complexes.

The results of this study highlight the striking similarities with basement dome hosted deposits in the Lufilian Arc of Zambia and suggest the existence of a contiguous convergent margin along the leading edge of the Congo Craton that was active to at least ca. 515 Ma.

Opsomming

Cu-mineralisasie in `n skuifskeer sone in die Deep Level Southern Zone (DLSZ) van die aanwas prisma van die Damara gordel word geassosieer met deformasie en vloeistof vloei wat verband hou met die herblootstelling van die Mesoprotersoïese Ekuja vloergneis koepel tydens die Pan-Afrika botsing tussen die Kongo en Kalahari kratone. Die mineralisasie het geen werklike ekwivalent in Namibië in terme van tektoniese omgewing, metamorfe graad en ouderdom, en pas ook nie werklik in die huidige klassifikasieskemas van Cu afsettings nie. Die doel van hierdie studie is om die geometry en beheer van die mineralisasie en die bronne van vloeistowwe en metale in Omitiomire Cu afsetting te beskryf, en om die interne dinamika en prosesse te ontsyfer wat daartoe gelei het dat 100 km^2 plate van vloergesteentes met die oorliggende prisma afsettings geimbrikeer word.

Die Omitiomire Cu afsetting (137 Mt by 0.54% Cu) kom voor in `n lae-hoek, laat-Damaran (ongeveer 520 Ma) skuifskeer sone, bekend as die Omitiomire Shear Zone (OSZ), wat ontwikkel is rondom `n ouer (ongeveer 1100-1060 Ma), laat Mesoprotersoïese intrusiewe breksie tussen `n reeks mafiese gesteentes (oorspronklike lavavloei) en later tonalitiese intrusiewe gesteentes. Die chalcosiet gedomineerde mineralisasie word geassosieer met biotite en epidoot samestellings wat gevorm het deur die progressiewe hidrasie van die oorspronklike mafiese gesteentes na amfibool-biotiet gneis en biotite-epidoot skis gesteentes tydens deformasie en infiltrasie van vloeistof langs die OSZ. Stabiele isotoop (O, H en S) data dui hoë-graadse metamorfe toestande aan, `n lae vloeistof-tot-rots verhouding en `n plaaslike migrasie van swael tydens mineralisasie. Dit dui op die hermobiliseering deur epigenetiese vloeisof vloei vanaf `n ouer singenetiese Cu mineralisasie.

Die geometry van die mineralisasie word beheer deur die ruimetelik toeval van die OSZ en die inherente heterogeniteit van die oorspronklike intrusiewe amfiboliet-tonaliet breksie. Die sag golwende, oos hellende ertsliggaam bestaan uit verskeie gemineralisserde lense wat in die plaaslike S2-maaksel voorkom. Hoë graadse ertsstroke is parallel aan `n prominente noord-suid neigende L2 strekkings lineasie en word gekorrelleer met die kumulatiewe aantal en dikte van verskeie dun kwarts-biotiet-epidote-chalcocite-skuifskeer sones langs die kontak tussen mafiese biotite skis gesteentes en tonalitiese gneis.

Die kinematika en die assosiasie van die Cu mineralisasie met retrogressiewe samestellings in die OSZ verbind die mineralisasie met die herblootstelling van die Ekuja koepel. Die tydsberekening van herblootstelling is beperk tussen 526.4 ± 3.5 en 521.9 ± 3.6 Ma met $^{40}Ar/^{39}Ar$ dateering van biotiet vanaf die OSZ. Piek metamorfiese samestellings in amfiboliet gneis van die Ekuja koepel dui aan op druk en temperatuur (PT) toestande van 8.5-9.15 kbar en 635-655 °C, wat aandui dat die Ekuja vloergsteentes begrawe was tot ongeveer 35 km. In teenstelling hiermee toon PT beramings en U-Pb xenotime dateering aan dat die oorliggende prisma metasedimente piek druk en temperatuur toestande van 7-9.25 kbar en 640-675 °C bereik het eers teen 515 Ma. Dit wys dat die herblootselling van die Ekuja koepel begin het ongeveer ~ 10 Ma voordat piek metamorfiese toestande bereik is in die oorliggende prisma metasedimente en weerspieël die kompleksiteite van subduksie-herblootstelling prosesse in aanwas komplekse.

Die resultate van hierdie studie beklemtoon die opvallende ooreenkoms met Cu afsettings in vloergesteente koepels in die Lufilian Arc van Zambia en stel voor dat daar 'n aaneenlopende konvergente plaatgrens aan die voorpunt van die Kongo kraton is wat aktief was tot ten minste 515 Ma.

Acknowledgements

First and foremost, I express my utmost gratitude to Alex Kisters for this incredible opportunity. Thank you Alex, for your unequalled vision and direction, your encouragement, enthusiasm and patience, and all the enlightening discussions, in the field, in your office and most importantly (and refreshingly), over a pilsner (or two) at Triggerfish. It's been 20 years and I (still) owe you a lot of beer!

I thank my co-supervisor, Ian Buick and co-authors, Karl Hartmann, Ken Maiden, Torsten Vennemann, Jan Kramers and Nick Steven for the time you invested in this project and the many discussions and emails during the preparation of the manuscripts.

To Nick, who left far too soon. Your giant geological footprints will be hard to fill. You were a mentor and friend and I will never forget you. Thanks for sharing.

I thank the reviewers Gregor Borg, Michael Meyer and Bjorn Von der Heyden for their constructive feedback that greatly improved the quality of this dissertation.

International Base Metals Limited (IBML) and its wholly-owned Namibian subsidiary, Craton Mining and Exploration (Pty) Ltd. are thanked for financially support. Simon Brodie is acknowledged for access to a faultless drill hole database. Ziggy Hartmann, Marina Bezuidenhoudt and the administrative staff at Craton are thanked for logistical support. Benson Bhunu, Sakkie Likuwa and the field crew at Borealis and Omitiomire camps are thanked for their kind assistance.

I thank Frik Badenhorst for the good company in the field and many discussions in the evening around the camp fire. Your support over the last 20 years is much appreciated.

To Loxie, George and Fiazel. Thanks for the administrative assistance at Stellenbosch. Loxie, enjoy your retirement and know that you will be missed.

The staff at the XRF, ICP-MS and SEM analytical facilities in Stellenbosch are thanked for their assistance. In particular, Madelaine Frazenburg, who spend many hours on the SEM with me.

Leapfrog Africa and ARANZ Geo Pty. Ltd. are acknowledged for their generous assistance with the 3D modelling and providing an academic licence for the Leapfrog Geo software package.

I am grateful to Ute Schreiber from the Geological Survey of Namibia for generously sharing regional GIS mapping data and also her coffee.

To all the friends I made in Stellenbosch over the last four years. You made this an unforgettable and welcoming experience! Thank you! Dankie! Merci! Obrigado! Grazie! Gracias! Dank je! Tack! Danke! Enkosi!

To my family and friends all over the world. I got a whole lot of love for you guys.

“While the rest of the species is descended from apes, redheads are descended from cats.” To Maddie, my partner, bestie and editor-in-chief. You are one of a kind and I’m your barista and scullion, forever! - Terms and conditions apply.

Dedicated to my amazing mother, for all the sacrifices you made,
and your unconditional love.

Table of Contents

List of figures

Chapter 1: Introduction

Chapter 2: Controls of fluid flow and Cu mineralisation

Chapter 3: Geometry of the orebody and sources of fluids and metals

Chapter 4: Structural, geochronological and P-T constraints on subduction-accretion processes in the DLSZ of the Damara Belt in Namibia

Chapter 5: Conclusion

List of tables

Chapter 4: Structural, geochronological and P-T constraints on subduction-accretion processes in the DLSZ of the Damara Belt in Namibia

Chapter 1

Introduction

1.1. Preface

This thesis is a compilation of three manuscripts, two published, one submitted, that focus on the Omitiomire Cu deposit in the Damara Belt of Namibia. As a whole, these publications encompass detailed studies on a number of aspects that aim to characterise the controls of fluid flow and Cu mineralisation (Kitt et al., 2016), the geometry and sources of fluids and metals (Kitt et al., 2017), and the tectonic setting and timing of regional events associated with the mineralisation (Kitt et al., in review). By integrating the deposit-scale data with regional-scale data, this study provides novel and valuable insights into the overall geodynamic evolution of the deposit within the broader context of the Damara Belt, but as well as similarly old belts in southern Africa.

1.2. Background

Central and southern Africa hosts a variety of world-class Cu deposits, including the world`s largest (>200 Mt contained Cu) and highest-grade (0.5% to 6% Cu) sediment-hosted Cu province that stretches for more than 2000 km from the Central African Copperbelt in the Democratic Republic of Congo (DRC) and Zambia, to possibly the Kalahari Copperbelt of Botswana and Namibia (Borg and Maiden, 1989; Cailteux et al., 2005; Selley et al., 2005; Sillitoe et al., 2010; Hitzman et al., 2012).

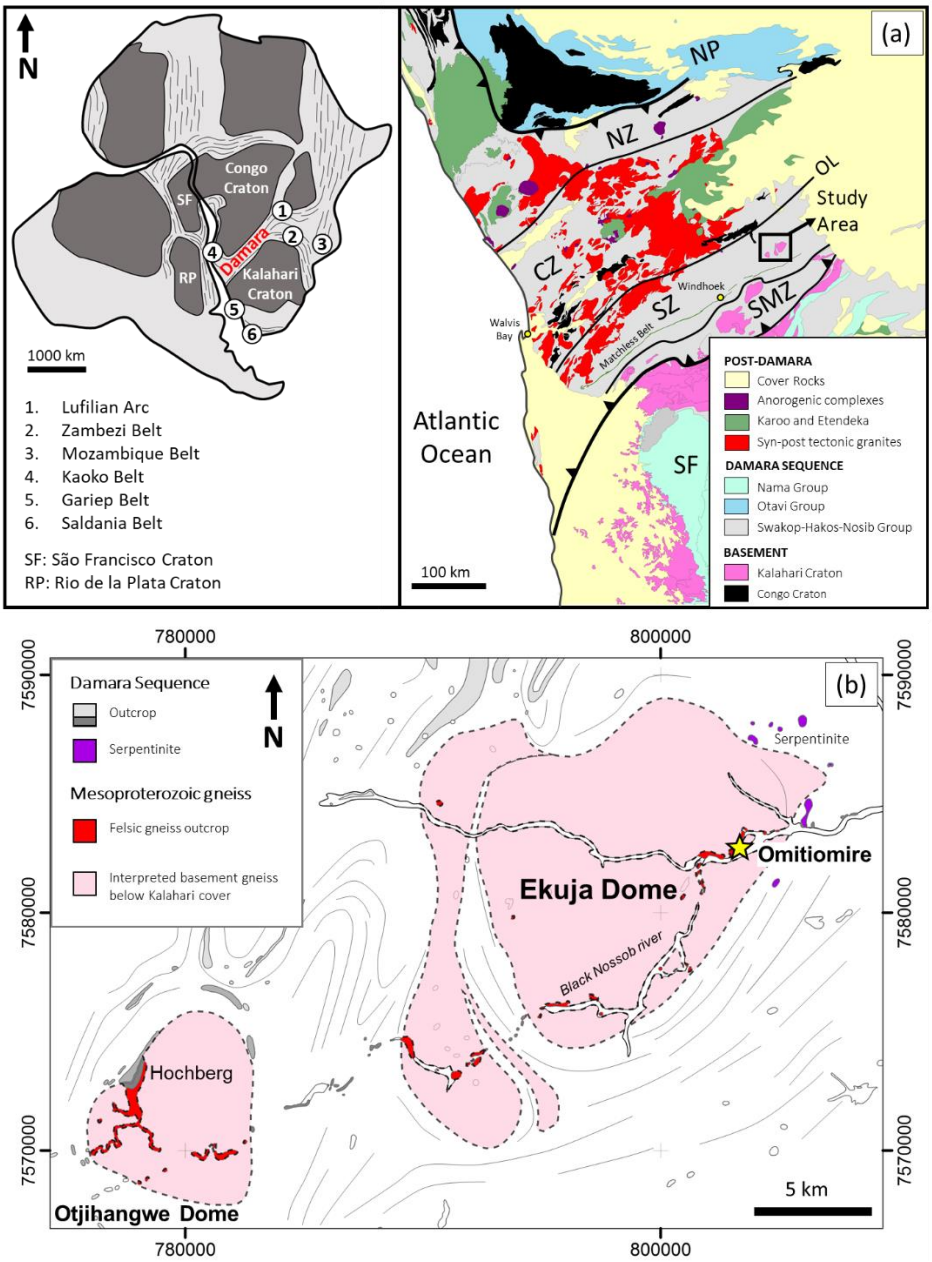

Fig 1. (a) Simplified geological map of the NE trending Damara Belt of Namibia with tectonostratigraphic zones, NP: Northern Platform; NZ: Northern Zone; CZ: Central Zone; OL: Okahandja Lineament; SZ: Southern Zone; SMZ: Southern Margin Zone; SF: Southern Front (modified from Miller, 2008). (b) Simplified geological and structural form line map showing the Ekuja Dome and adjoining gneiss complexes in the Deep Level Southern Zone (modified from Kasch, 1986). Surface exposure is poor with most of area covered by up to 10 m thick cover. Regional mapping relied on interpretations from satellite imagery and observations from isolated outcrops along the Black Nossob river and at Hochberg hill. The inset is a schematic map showing the location of Pan-African orogenic belts in southern Africa around the Congo and Kalahari cratons during the late assembly of Gondwana (modified from Gray et al., 2006).

In Namibia, Cu mineralisation occurs in a wide range of different deposit styles, including the famous hydrothermal, carbonate-hosted mineralisation of the Tsumeb Mine in northern Namibia, the VMS-type deposits of the Matchless Amphibolite Belt and the deposits of the Kalahari Copperbelt (Lombaard et al., 1986; Innes and Chaplin, 1986; Klemd, 1987; Borg and Maiden, 1989; Maiden and Borg, 2011). The Kalahari Copperbelt is a belt of intermittent Cu mineralisation in Mesoproterozoic greenschist-facies metasedimentary rocks that extends for more than 800 km along the northern margin of the Kalahari Craton, from central Namibia into northern Botswana (Borg and Maiden, 1989; Maiden and Borg, 2011; Lehmann et al., 2016). The largely stratiform mineralisation is epigenetic and show a structural and lithological control that are related to tectonism and fluid flow during the Pan-African Damaran orogeny (Maiden and Borg, 2011). Although regional studies have recognised a connection between the Damara, Lufilian and Zambezi orogenic belts (Unrug, 1983; Kampunzu and Cailteux, 1999; Porada and Berhorst, 2000; Rainaud, 2005), direct correlations between the Kalahari Copperbelt and the Zambian Copperbelt are complicated by the extensive sand cover in northern Namibia and Botswana.

1.3. The Omitiomire Cu deposit

The Omitiomire Cu deposit, situated some 120 km NE of Windhoek (Fig. 1a), is hosted by Mesoproterozoic gneisses of the Ekuja Dome and enveloped by amphibolite-facies metasediments of the Kuiseb Formation of the Southern Zone of the Damara Belt (Fig. 1b; Steven et al., 2000; Maiden et al., 2013). The mineralisation is distinct from that of the Kalahari Copperbelt to the immediate south and in terms of its tectonic setting, metamorphic grade and age structure, the Omitiomire Cu mineralisation has no real equivalent in Namibia and seems to defy current classification schemes of Cu deposits.

The Cu mineralisation was first reported in the mid-1970s following the discovery of rather inconspicuous malachite occurrences associated with sporadic outcrops of metabasite. Following a regional soil geochemical survey by General Mining and Finance Corporation (GenMin), several Cu-in-soil geochemical anomalies were targeted through exploration drilling between 1976 and 1978 (Steven et al., 2000; Hartmann, 2016). Disappointing Cu assay results and failure to understand the geology due to the relatively wide spacing of drill holes, resulted in no further work on the project for more than a decade. In 1989, after a sharp increase in global Cu prices, renewed interest in the project resulted in sampling and drilling campaigns by Nossib River Mining and Anglo American Corporation. Although some holes intercepted chalcocite mineralisation over a thickness of more than 100 m, the Cu grades were regarded as too low for economic extraction at the time. In 1998, Strait Resources conducted a small drilling campaign and a metallurgical study, but again, further interest in the project diminished due to a slump in Cu prices. The first detailed description of the geology of the Omitiomire deposit was published by Steven et al. (2000). A global commodity boom between 2004 and 2008 resulted in Cheetah Minerals Exploration obtaining the exclusive prospecting rights (EPL 3589) for the project. Following a joint venture partnership between Cheetah and International Base Metals of Australia (IMBL), and the establishment of its Namibian subsidiary Craton Mining and Exploration (Pty) Ltd, drilling resumed at Omitiomire in late 2007. In late 2008, Craton acquired full ownership of EPL3589 and embarked on an intensive exploration program consisting of soil sampling, geophysics, extensive drilling campaigns and metallurgical test work followed by a full pre-feasibility study (Hartmann, 2016). Following a JORC compliant resource estimation in 2012 that showed a resource of 136 Mt @ 0.53% Cu and a Definitive Feasibility Study (DFS) for a mixed near-surface oxide and sulphide mining and processing operation, Craton proceeded with the application for a mining licence (Hartmann, 2016).

In June 2013, Craton realised that a detailed study of the structure and controls of Cu mineralisation in the deposit was still lacking and approached Stellenbosch University for a research proposal.

1.4. Research rationale and thesis structure

The limited understanding of the deposit is largely related to a lack of outcrop due to the extensive Cenozoic (Kalahari) sand, silt and calcrete that cover most of the eastern parts of Namibia. Previous interpretations of the deposit geology were solely based on a few boreholes, petrography, limited structural studies and geochronology (Steven et al., 2000; Maiden et al., 2013). The unusual setting in the Southern Zone of the Damara Belt and evidently multiphase mineralisation required a new, state-of-the-art approach highlighting the geometry of the mineralisation and host rock structure, controls of mineralisation, potential source of fluids and metals, relative timing and broader tectonic setting. In October 2013, after Craton provided funding for the project, fieldwork for this dissertation began, using a multi-scale and multi-disciplinary approach, described as follows.

1) As a first step, 15 km of diamond drill core from the deposit was re-logged on site over a period of 3 months. The results were integrated into an existing drill hole database consisting of ~100 km of exploration drilling data and imported, along with structural data from down-the-hole photography of 60 RC holes, into the latest Leapfrog Geo modelling software. A 3D geological and mineralisation model of the deposit was constructed. The 3D model was compared with structural and lithological data generated from detailed mapping of a small bulk sample pit over the deposit and sporadic outcrops along the ephemeral Black Nossob River. The results allowed for a

detailed description of the geometry of the deposit and the controls of fluid flow and mineralisation and are summarised in the first paper presented in Chapter 2.

2) In order to better constrain fluid and metal sources and controls of mineralisation on a deposit scale, the geochemistry of samples was integrated with petrography, stable isotopes and interpreted in conjunction with structural geology of the deposit. This is summarised in the second paper presented in Chapter 3.
3) Following the characterisation of the deposit, Chapter 4 focuses on the broader tectonic setting and geodynamic evolution. For this purpose, P-T estimates and U-Pb xenotime and $^{40}Ar/^{39}Ar$ mineral age data of basement and cover rocks were integrated with detailed petrography and previous structural work on the kinematics. The results allows for the construction of a partial P-T-t path that describes the complexity of burial and exhumation in this part of the SZ accretionary prism and is presented as a third paper.

These three papers represent a progression from deposit-scale structure and processes to regional scale processes and correlations. I have refrained from presenting the regional and local geology, as well as the analytical techniques here, because both are presented and discussed in detail in the relevant papers.

1.5. References

Borg, G., and Maiden, K.J., 1989. The Middle Proterozoic Kalahari Copperbelt of Namibia and Botswana: Geological Association of Canada Special Paper 36, 525–540.

Cailteux J.L.H., Kampunzu A.B., Lerouge C., Kaputo A.K., Milesi J.P., 2005. Genesis of sediment hosted stratiform copper–cobalt deposits, central African Copperbelt. J Afr Earth Sci 42, 134–158.

Gray, D.R., Foster, D.A., Goscombe, B., Passchier, C.W. and Trouw, R.A.J., 2006. $^{40}Ar/^{39}Ar$ thermochronology of the Pan-African Damara Orogen, Namibia, with implications for tectonothermal and geodynamic evolution. Precambrian Research **150**, 49-72.

Hartmann, K. (2016) Omitiomire Project History. Unpublished report, November 2016, 4p.

Hitzman, M.W., Broughton D., Selley D., Woodhead J., Wood D., Bull S., 2012. The Central African Copperbelt: diverse stratigraphic, structural, and temporal settings in the world`s largest sedimentary copper district. In: Hedenquist JW, Harris M, Camus F (eds) Geology and genesis of major copper deposits and districts of the world: a tribute to Richard H. Sillitoe, Society of Economic Geologist Special Publication16, 487–514.

Innes, J., Chaplin, R.C., 1986. Ore bodies of the Kombat Mine, South West Africa/Namibia. In: Anhaeusser, C.R., Maske, S. (Eds.), Mineral Deposits of Southern Africa II. Soc. S. Afr. Spec. Publ, Geol, 1789–1805.

Kampunzu, A.B., Cailteux, J., 1999. Tectonic evolution of the Lufilian Arc during Neoproterozoic Pan-African orogenesis. Gondwana Research 2, 401–421.

Kasch K.W., 1986. Tectonic subdivision, lithostratigraphy and structural geology of the Upper Black Nossob river area. Comm Geol Soc Namibia 2, 117–129.

Kitt, S., Kisters, A., Steven, N., Maiden, K., Hartmann, K., 2016. Shear-zone hosted copper mineralisation of the Omitiomire deposit — Structural controls of fluid flow and mineralisation during subduction accretion in the Pan-African Damara Belt of Namibia. Ore Geol Rev. 75, 1-15.

Kitt, S., Kisters, A., Vennemann, T., Steven, N., 2017. Orebody geometry, fluid and metal sources of the Omitiomire Cu deposit in the Ekuja Dome of the Damara Belt in Namibia. Mineralium Deposita (in press).

Kitt, S., Kisters, A., Buick, I., Kramers, J., (in review). Structural, geochronological and P-T constraints on subduction-accretion processes in a Pan-African accretionary wedge – the Deep Level Southern Zone of the Damara Belt in Namibia, Precambrian Research (in review).

Klemd, R., 1987. The matchless copper deposit, South West Africa/Namibia a deformed and metamorphosed massive sulfide deposit. Economic Geology 82, 587–599.

Lehmann J., Master S., Rankin W., Milani L., Kinnaird J.A., Naydenov K.V., Saalmann K.A., Kumar M., 2015. Regional aeromagnetic and stratigraphic correlations of the Kalahari Copperbelt in Namibia and Botswana. Ore Geology Reviews 71, 169–190.

Lombaard, A.F., Günzel, A., Innes, J., Krüger, T.L., 1986. The Tsumeb Lead–Copper–Zinc–Silver Deposit, South West Africa/Namibia. In: Anhaeusser, C.R., Maske, S. (Eds.), Mineral Deposits of Southern Africa II. Soc. S. Afr. Spec. Publ, Geol, pp. 1761–1787.

Maiden, K.J. and Borg, G., 2011. The Kalahari Copperbelt in central Namibia: controls on copper mineralization. SEG Newsletter 87, 14–19.

Maiden, K.J., Hartmann, K., Steven, N.M., Armstrong, R.A., 2013. The Omitiomire deposit, Namibia: Late Tectonic copper emplacement in a Neoproterozoic (Pan-African) imbricate shear system. Extended Abstract, SGA Meeting, 12–15 Aug 2013. Sweden, Uppsala.

Miller, R. McG., 2008. The Geology of Namibia. Volume 2: Neoproterozoic to Lower Palaeozoic. Geological Survey of Namibia, Windhoek, Namibia.

Porada, H., 1989. Pan-African Rifting and Orogenesis in Southern to Equatorial Africa and Eastern Brazil. Precambrian Research 44, 103-136.

Porada, H., Berhorst, V., 2000. Towards a new understanding of the Neoproterozoic–Early Palaeozoic Lufilian and northern Zambezi belts in Zambia and the Democratic Republic of Congo. J. Afr. Earth Sci. 30, 727–771.

Rainaud, C., Master, S., Armstrong, R.A., Robb, L.J., 2005. Geochronology and nature of the Palaeoproterozoic basement in the central African Copperbelt (Zambia and Democratic Republic of Congo), with regional implications. J. Afr. Earth Sci. 42, 1–31.

Selley, D., Broughton, D., Scott, R., Hitzman, M., Bull, S., Large, R., McGoldrick, P., Croaker, M., Pollington, N., and Barra, F., 2005. A new look at the geology of the Zambian Copperbelt: Economic Geology 100th Anniversary Volume, 965–1000.

Sillitoe R.H., Perelló J., García A., 2010. Sulfide-bearing veinlets throughout the stratiform mineralisation of the Central African Copperbelt: temporal and genetic implications. Economic Geology 105, 1361–1368.

Steven, N.M., Armstrong, R.A., Smalley, T.I., Moore, J.M., 2000. First geological description of a late Proterozoic (Kibaran) andesite-hosted chalcocite deposit at Omitiomire, Namibia. In: Cluer, J.K., Price, J.G., Struchsacker, E., Hardyman, R.F., Morris, C.L. (Eds.), Geology and Ore Deposits 2000: The Great Basin and Beyond. Geological Society of Nevada Symposium Proceedings, pp. 711–734.

Unrug, R., 1983. The Lufilian Arc: a microplate in the Pan-African collision zone of the Congo and Kalahari cratons. Precambrian Research. 21, 181–196.

Chapter 2

Controls of fluid flow and Cu mineralisation

This chapter presents the published research paper: "*Shear-zone hosted copper mineralisation of the Omitiomire deposit —Structural controls of fluid flow and mineralisation during subduction accretion in the Pan-African Damara Belt of Namibia"* by Shawn Kitt, Alex Kisters, Nick Steven, Ken Maiden and Karl Hartmann.

The manuscript was submitted to Ore Geology Reviews on the 28th of August 2015 and was accepted for publication on the 16th October 2015. The paper (1) documents the structural and lithological controls of Cu mineralisation, (2) illustrates the geometry and controls of mineralisation on a deposit scale, (3) integrates the mineralisation with the regional geological evolution of the Southern Zone accretionary prism and, (4) place the mineralisation within the broader regional context of similar deposits along strike in the Domes Region of the Lufilian Arc, Zambia. The following aspects of the research were done independently by Shawn Kitt with supervision by Alex Kisters: (i) regional and pit scale geological mapping and sampling (ii) logging of ~15,000m of diamond drill core (iii) compilation and processing of ~100,000m of exploration drill hole data (iv) 3D modelling in Leapfrog Geo software (v) interpretation of results (vi) preparation and submission of the manuscript. Alex Kisters also contributed with editorial work towards the final draft. Nick Steven, Ken Maiden and Karl Hartmann contributed with the preparation of the manuscript.

Ore Geology Reviews 75 (2016) 1–15

Contents lists available at ScienceDirect

Ore Geology Reviews

journal homepage: www.elsevier.com/locate/oregeorev

Shear-zone hosted copper mineralisation of the Omitiomire deposit — Structural controls of fluid flow and mineralisation during subduction accretion in the Pan-African Damara Belt of Namibia

Shawn Kitt [a,*], Alexander Kisters [a], Nick Steven [b,1], Ken Maiden [c], Karl Hartmann [d]

[a] Department of Earth Sciences, Stellenbosch University, South Africa
[b] Rockwater Consulting Namibia, PO Box 27344, Windhoek, Namibia
[c] International Base Metals Limited, 47 Neridah Street, Chatswood NSW 2057, Australia
[d] Craton Mining and Explorations, PO Box 81136, Olympia, Windhoek, Namibia

ARTICLE INFO

Article history:
Received 28 August 2015
Received in revised form 15 October 2015
Accepted 16 October 2015
Available online 2 December 2015

Keywords:
Copper mineralisation
Chalcocite
Shear zone hosted
Amphibolite
Retrograde biotite–epidote schists
Damara Belt
3D modelling
Exhumed basement dome

ABSTRACT

The Omitiomire copper deposit is a relatively recent discovery in the Pan-African Damara Belt of central Namibia. The deposit is situated in Mesoproterozoic gneisses and amphibolites of the Ekuja Dome overlain by amphibolite-grade metaturbidites of the Southern Zone accretionary prism that formed during northward subduction of the Kalahari Craton below the Congo Craton between ca. 580–520 Ma. Copper mineralisation is confined to an anastomosing system of shallowly-dipping, retrograde mylonitic shear zones within the Ekuja Dome. The shear zones are centred around a lithologically heterogeneous amphibolite-gneiss sequence. Mylonitisation and copper mineralisation are closely associated with the retrogression of particularly amphibolites and the partial or complete replacement of amphibolites by biotite–epidote and biotite–chlorite–epidote schists that host the chalcocite-dominated mineralisation.

Deformation and mineralisation in the heterogeneous shear-zone system can be shown to describe a progression. Initial strain localization is confined to lithological (amphibolite-gneiss) contacts and associated quartz veining and fluid flow are preferentially developed around the margins of competent amphibolite units. Fluid infiltration and the retrogression of amphibolites to biotite–epidote schists leads to strain localization into the marginal schists that envelop amphibolites. Further veining and fluid flow are localised into the central parts of amphibolite units leading to the pervasive retrogression to biotite–epidote schists that dominate the central parts of the shear-zone system. Earlier quartz-vein generations appear as isoclinally folded and dismembered ribbons or boudins in mineralised schists. The clearly syntectonic introduction of the copper mineralisation is underlined by the intergrowth of chalcocite with the retrograde assemblages and chalcocite forming part of the mylonitic shear-zone fabric.

3D modelling of drillhole data combined with limited surface exposure delineates a shallow east dipping, gently undulating ore body parallel to the regional gneissosity of the Ekuja Dome. The ore body comprises several mineralised lenses varying in thickness from 10 m to >100 m. Prominent ore shoots are gently doubly plunging to the N and S and parallel to the regionally developed L > S fabric in the gneisses. Kinematic indicators in the mineralised shear zone system point to a top-to-the S sense of shear, parallel to the regional L fabric and parallel to the southverging transport recorded in the structurally overlying prism metasediments.

The regional setting of the Omitiomire deposit, kinematics, and retrograde, but high-temperature overprint of original mineral assemblages in the mineralised shear zones indicate deformation and fluid flow during the expulsion of the basement gneisses during N-ward direction subduction of the Kalahari Craton below the Congo Craton. Lithological, geochronological, structural and P–T data suggest numerous similarities and, indeed, correlations between the Omitiomire-style copper mineralisation of the Damara Belt with the large copper deposits hosted by basement gneisses in the Domes Region of the Lufilian Arc in Zambia.

1. Introduction

Copper has traditionally been a most important commodity in Namibia with a wide range of different deposit styles (Miller, 1983; Anhaeusser and Maske, 1986; Schneider and Seeger, 1992). This includes the platform carbonate-hosted mineralisation of the Tsumeb

* Corresponding author at: Dept. of Earth Sciences, Stellenbosch University, Private Bag X1, Matieland 7602, Stellenbosch, South Africa.
E-mail address: shawnkitt@gmail.com (S. Kitt).
[1] Deceased.

http://dx.doi.org/10.1016/j.oregeorev.2015.10.035
0169-1368/

and Kombat Mines in northern Namibia, the VMS-type deposits of the Matchless Amphibolite Belt in the Damara Belt, and the Kalahari Copper Belt that stretches for >800 km from central Namibia into northern Botswana (Lombaard et al., 1986; Innes and Chaplin, 1986; Klemd, 1987; Borg and Maiden, 1989; Maiden and Borg, 2011). The Omitiomire copper deposit is situated some 120 km NE of Windhoek in the Pan-African (550–500 Ma) Damara Belt of central Namibia (Figs. 1 and 2). The mineralisation is hosted by kilometre-scale gneissic basement domes that are structurally overlain by high-grade metamorphic, multiply deformed metasediments of the Southern Zone accretionary prism of the Damara Belt (Kasch, 1986, 1987). Previous works have described a high-grade metamorphic (T > 600 °C, P ca. 7 kbar) chalcocite-dominated sulphide assemblage confined to a lithologically heterogeneous zone of interleaved amphibolites, biotite–epidote schists and felsic gneisses (Steven et al., 2000, 2001; Maiden, 2013). Existing U–Pb zircon ages from wall rocks underline the late-Mesoproterozoic, Namaqua age (ca. 1110–1060 Ma) of the basement gneisses, but U–Pb sphene ages from alteration-related assemblages suggest a Pan-African timing of the mineralisation at ca. 520 Ma (Steven et al., 2000; Maiden et al., 2013). Based on this, Steven et al. (2000) suggested a mineralisation model in which a Namaqua age copper mineralisation hosted by an original bimodal volcanic suite was overprinted and remobilised during Pan-African accretionary tectonics in the Southern Zone. These studies were based on early exploration efforts and samples taken from isolated boreholes that intersected the mineralisation. However, little is known about the geometry and controls of the mineralisation and since >99% of the area around Omitiomire is covered by Kalahari sands, exploration relies on extensive drilling and geophysics, highlighting the need for an integrated exploration approach through the compilation and interpretation of sub-surface geological data.

Since 2007, exploration drilling, geophysical exploration and the development of surface pits have greatly expanded the previous data base and we present results that utilise the new and vastly improved data set around the Omitiomire deposit. The Omitiomire deposit currently has a published mineral resource estimate of 137 Mt at 0.54% Cu at a cut-off grade of 0.25% Cu (International Base Metals Limited Quarterly Activities Report — End September 2014).

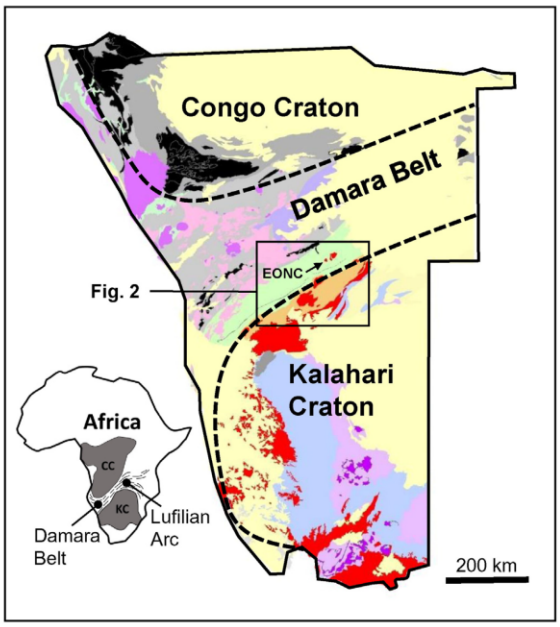

Fig. 1. Geological map of Namibia showing the location of the Ekuja-Otjihangwe Nappe Complex (EONC) in the Damara Belt relative to the Congo and Kalahari cratons (after Miller, 2008). The inset shows the location of the Pan-African Damara Belt and Lufilian Arc in Africa. CC = Congo Craton; KC = Kalahari Craton.

The aims of the paper are to (1) document the structural and lithological controls of the copper mineralisation, (2) illustrate the geometry and controls of the mineralisation on a deposit scale based on the 3D modelling of wall rocks, wall-rock structures and ore-grade zones, and (3) integrate the Omitiomire mineralisation with the regional geological evolution of this part of the Southern Zone accretionary prism. Finally, we attempt to place the Omitiomire mineralisation within the broader regional context of somewhat similar deposits along strike, in particular, the Domes Region of the Lufilian Arc close to the Zambian Copper Belt. This has potentially important implications for exploration in Mesoproterozoic basement rocks that link the lesser known copper deposits of the Kalahari Copperbelt with the very large deposits of the Central African Copperbelt in Zambia and the Democratic Republic of Congo (Selley et al., 2005; Hitzman et al., 2012).

2. Regional geological setting

The east-northeast trending Pan-African Damara Belt in central Namibia chronicles the high-angle convergence and closure of the Khomas Sea ocean basin between the Congo and Kalahari cratons in the latest Neoproterozoic and early Phanerozoic (Fig.1) (Coward, 1983; Miller, 1983). The Southern Zone (SZ) forms the deeply eroded accretionary wedge of the belt, underlain by the thick (>10 km) sequence of the mainly metaturbiditic Kuiseb Formation. Medium-P, low-T amphibolite-facies metamorphism and the south- to southeast-vergent folding and thrusting of the Kuiseb Formation record the offscraping, underplating and burial of originally trench sediments during north- or northwestward subduction of the Kalahari below the Congo Craton between ca. 580–520 Ma (Kukla, 1991; Miller, 2008; Meneghini et al., 2014). To the north, the SZ prism borders against the magmatic arc of the Central Zone along the subvertical Okahandja Lineament Zone, the backstop of the prism (Fig. 2) (Miller, 2008). In the south, the prism structurally overlies with shallow dips older rocks of the Southern Marginal Zone foreland that is part of the underthrusted Kalahari Craton (Porada, 1989; Miller, 1983, 2008).

The Omitiomire deposit is located in the Ekuja Dome, one of three gneiss domes that occur within the northeastern parts of the SZ accretionary prism (Figs. 2 and 3). This part of the SZ is also referred to as the Deep Level Southern Zone (Kasch, 1986, 1987; Miller, 2008), indicating the juxtaposition of structural and lithological domains that share similarities with both the SZ and the structurally underlying Southern Marginal Zone and a position close to the base of the accretionary prism. Rock exposure is poor and structural relationships are far from clear, but Kasch (1986) defined three lithologically and structurally distinct and overlying tectonostratigraphic units in the Deep Level Southern Zone around Omitiomire (Fig. 3). The lowermost unit is the Ekuja-Otjihangwe Nappe Complex (EONC) made up of sheet-like quartzo-feldspathic gneisses and tonalites interleaved with volumetrically minor paragneisses and amphibolites and intruded by pegmatites. This lower gneiss complex is exposed in three kilometre-scale, round- to oval dome-like structures that pierce through the overlying high-grade metasediments of the SZ (Fig. 3). Contacts with the overlying metasediments are highly sheared and structural in nature. The Ekuja Dome is the largest of these dome structures covering an area of ca. 400km^2. The Omitiomire deposit is hosted in the eastern parts of the dome (Fig. 3). For the most part, gneisses of the Ekuja Dome are banded or augen textured. Isoclinal, intrafolial folds testify to the transposition of fabrics and original intrusive contacts into the shallowly-dipping (<20–30°) gneissosity (S2) of the domes. The dome-like structure is defined by the roughly concentric and outward dipping pattern of the S2 gneissosity, parallel to the outline of the domes (Fig. 3). The S2 gneissosity contains a widespread rodding lineation (L2) with more or less unidirectional northerly trends and shallow

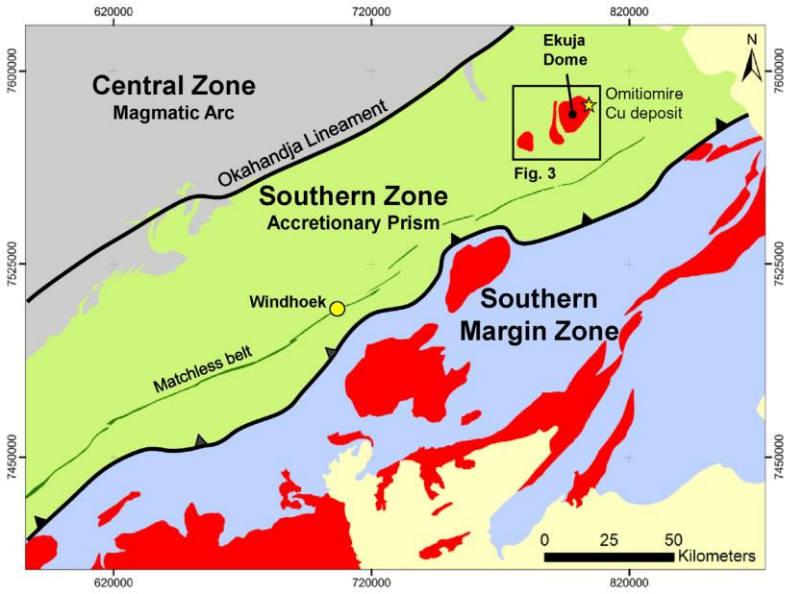

Fig. 2. Simplified map showing the location of the Ekuja Dome and the Omitiomire Cu deposit in the Southern Zone (SZ) of the Damara Belt. Also shown are the Central Zone (CZ), Southern Margin Zone (SMZ), Matchless amphibolite belt, Okahandja lineament and basement complexes (red). (For interpretation of the references to color in this figure legend, the reader is referred to the web version of this article.)

plunges to both the north and south (Fig. 3). In outcrop, the lineation is parallel to deci- to dekameter-scale open, upright folds that fold the S2 gneissosity. Kasch (1986) referred to the gneisses as a pre-Damara basement based on the close resemblance of the rocks with lithologies and structures in the Southern Marginal Zone. More recent U–Pb zircon ages of 1115 ± 13 Ma for amphibolites and 1084 ± 7 and 1063 ± 9 Ma for quartzo-feldpathic gneisses from the Ekuja Dome around Omitiomire confirm the late-Mesoproterozoic, pre-Damara age of the basement domes (Steven et al., 2000). The margins of the Ekuja Dome are lined by sporadically occurring large (>100 m strike extent) plugs of ultramafic serpentinites and talc carbonate schists (Fig. 3). The ultramafic rocks are not part of the regional stratigraphy and rather form tectonic slivers along the basement-cover contact.

The uppermost structural unit of the Deep Level Southern Zone is the Onyati Mountains Schist Belt (OMSB) (Kasch, 1986) that comprises the monotonous sequence of pelitic, semi-pelitic and psammitic schists and intercalated amphibolites of the Kuiseb Formation that underlies the largest parts of the SZ (Sawyer, 1981; Miller, 2008). Most of the rocks are garnet–biotite schists with variable amounts of staurolite and/or kyanite. Sillimanite seems restricted to the northwestern parts of the Deep Level Southern Zone (Kasch, 1987) (Fig. 3). Structurally, the schists have been affected by polyphase, but largely coaxial southverging, west- to westnorth-west trending, shallowly plunging folds and associated southvergent thrusts. Lineations show westerly trends, parallel to fold hinges. Transposition of earlier folds and associated axial planar foliations into the moderately- to steep north dipping foliation testifies to the high-strain nature of these composite fabrics during the offscraping and imbrication of the metasediments (Kukla et al., 1991; Miller, 2008; Meneghini et al., 2014).

A central tectonostratigraphic unit that separates the basement domes from the overlying Kuiseb Formation is referred to as the Onjona-Vrolikheid Fold Complex (OVFC) (Kasch, 1986) (Fig. 3). The fold complex comprises a sequence of mainly quartzitic rocks, meta-conglomerates, amphibolites and marble units infolded between the basement domes. Folds show northerly trends and, importantly, east–west-trending folds and fabrics of the structurally higher Kuiseb Formation of the OMSB can be seen to be progressively rotated into and refolded by N–S-trending folds in the underlying fold complex. Prominent stretching lineations show northerly plunges, similar to rodding fabrics in the basement domes. Hence, the central OVFC appears to represent a transitional zone, linking the structural domains of the basement domes with that of the overlying Kuiseb Formation in the upper parts of the SZ. Importantly, these regional fabric relationships illustrate that N–S trending constrictional strains and associated folding in the older basement gneisses refold the east–west-trending folds and thrusts related to the imbrication and burial of the younger cover rocks during regional-scale convergence (Kasch, 1986). This has important implications for later structural considerations as to the overall evolution of the area.

Metamorphic studies by Kasch (1987) in rocks of the SZ overlying the Ekuja Dome demonstrate a general increase in temperature and an associated decrease in pressure from south to north, across kyanite–sillimanite and staurolite isograds in metapelitic units (Fig. 3). Estimated peak metamorphic PT conditions reached 6 kb and 590 °C in the south and 4.5 kb and 630 °C in the north of the DLSZ. Notably, metamorphic reaction textures and garnet zoning profiles indicate a late-stage isothermal decompression path, suggesting rapid exhumation after the earlier burial of the rocks (Kasch, 1987). There are, to date, no metamorphic data for the structurally lower basement domes.

3. Geology of the Omitiomire copper deposit

The Omitiomire deposit is located on the eastern margin of the Ekuja Dome, enveloped by and contained within shallow (<20–25°) easterly dipping gneisses (Fig. 3). Outcrop is very sparse in the area and previous studies (Steven et al., 2000) were largely based on observations made on core from two diamond drillholes through the central parts of the Omitiomire ore body. These studies described the chalcocite-dominated copper mineralisation to be hosted by a lithologically heterogeneous, sheared sequence of amphibolite, biotite–epidote gneiss and schist that are enveloped by and contained within the gneiss sequence of the Ekuja Dome. In this study, we are able to expand on this work by combining observations from some 14,000 m of drill core and down-the-hole photography of an additional 60 drillholes with regional

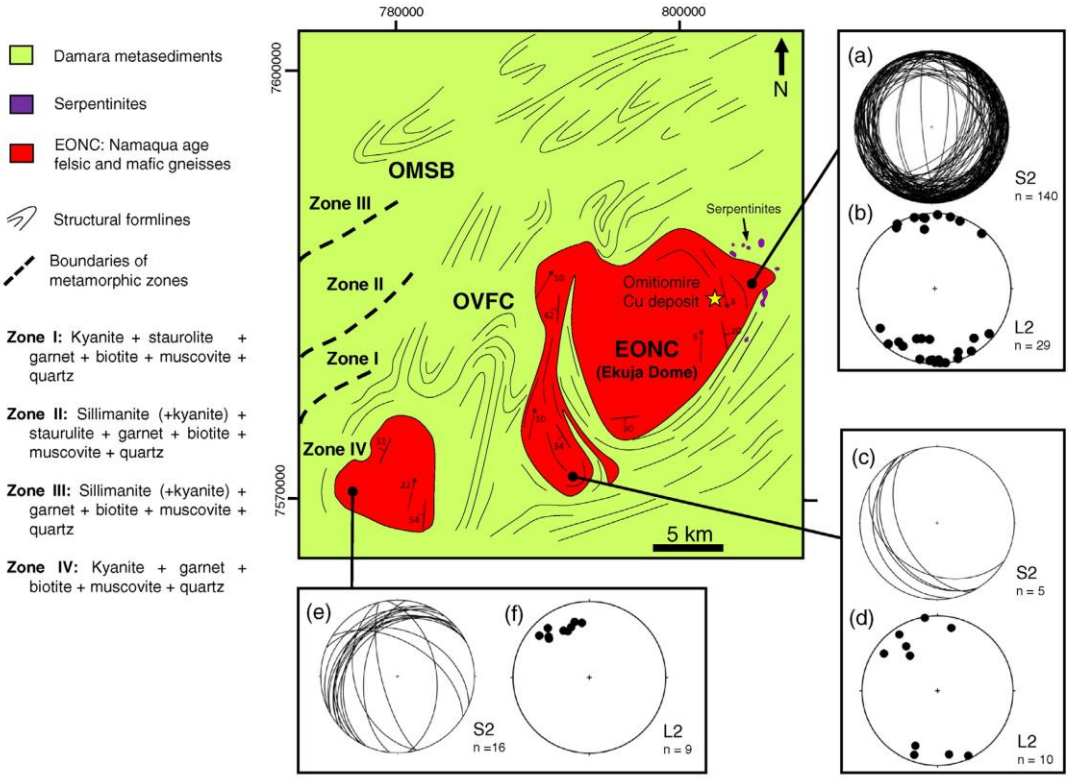

Fig. 3. Simplified geological and structural formline map of the Ekuja-Otjihangwe Nappe Complex (EONC) and surrounding areas. Modified from Kasch (1986, 1987) and the *2117D EKUJA Sheet* from the Geological Survey of Namibia 1:100,000 Map series. Note the change from dominantly NE trending formlines in the Onyati Mountain Schist Belt (OMSB), to a NNE trend in the Onjona-Vrolikheid Fold Complex (OVFC). (a–d) Stereonets of S2 fabric and L2 lineations from rare outcrops along the Black Nossib River in the Ekuja Dome and (e–f) the Otjihangwe Dome. The S2 fabric data demonstrate the gently undulating and shallow dipping dome-like shape of the Ekuja Dome. L2 lineations are consistently shallow N–S trending in the EONC. All stereonets are equal area, lower hemisphere.

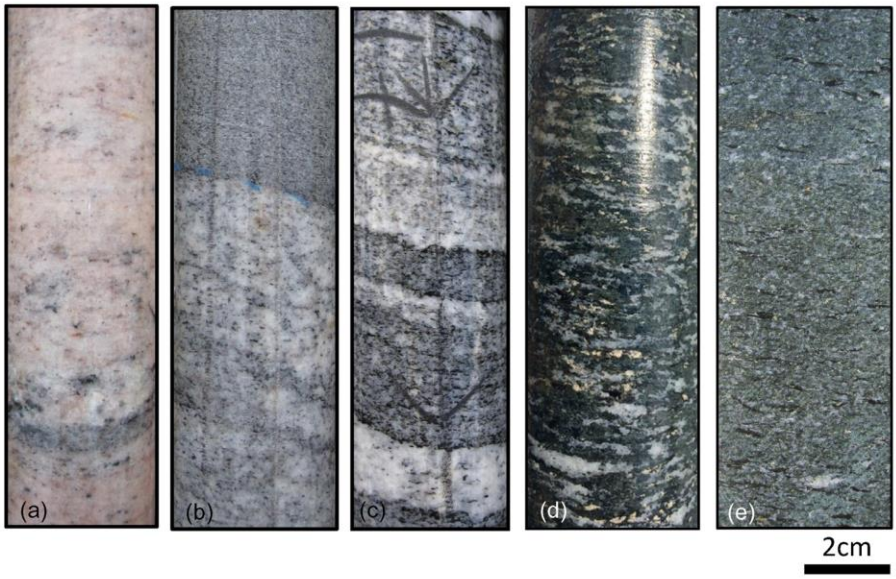

Fig. 4. Main types of wall rocks found at the Omitiomire deposit. (a) Pink tonalitic gneisses. (b) Light grey tonalitic gneisses with bands of finer dark grey biotite gneiss. (c) Banded gneisses. (d) Coarse grained augen textured mafic gneiss. Note the well-developed L2 lineation defined by stretched plagioclase. (e) Fine grained mafic gneiss.

and detailed mapping data from river sections and a recently established sampling pit. The 3D exposure in the open pit, in particular, provides excellent controls on the spatial relationship of lithotypes, deformation partitioning and mineralisation that can be integrated with the borehole data.

3.1. Wall rocks

Wall rocks of the Omitiomire mineralisation comprise two main rock suites including a dominant felsic suite made up of a variety of tonalitic gneisses and pegmatites and a volumetrically subordinate, but economically significant mafic suite of amphibolite, hornblende–biotite–gneiss and biotite–epidote schist (Fig. 4).

3.1.1. Felsic gneisses

Granitic and mainly tonalitic gneisses are by far the dominant rock types and constitute the hanging- and footwall rocks of the mineralisation. This felsic suite forms part of the basement gneisses of the Ekuja Dome. The gneisses are commonly medium-to-coarse grained and greyish-pinkish or white in colour (Figs 4a and b). The tonalites have a holocrystalline, medium grained (1–2 mm), granoblastic texture and are dominated by quartz (~40–45%), plagioclase (~45%) and minor biotite and microcline (~5–10%). Accessory minerals include epidote, muscovite, sphene, zircon, apatite and chlorite. Quartz and plagioclase are equigranular, occurring as subhedral aggregates, surrounded by minor interstitial fine-grained microcline, which may be responsible for the pinkish colouration in some of the gneisses (Steven et al., 2000). A gneissic fabric (S1/S2, see below) is defined by the preferred orientation of biotite and flattened quartz aggregates (Fig 4c). The finer grained grey gneisses are composed of quartz (~30%), plagioclase (~50%), biotite (~10%) and accessory epidote, muscovite, microcline, sphene, apatite, and zircon. Quartz and plagioclase make up a fine (<1 mm), equigranular and granoblastically arranged holocrystalline mass. Biotite occurs as elongated grains with a preferred orientation that form the strong gneissic fabric in the rock.

Multiple intrusive relationships between the mainly sheet-like tonalitic phases are common and indicate a complex and protracted emplacement history of the granitoids. Quartz-K-feldspar pegmatite sheets seem to have intruded throughout the deformation of the gneiss sequence and early, isoclinally folded and partly transposed pegmatites can be distinguished from sharply cross-cutting, post-tectonic pegmatites.

3.1.2. Amphibolites

The mafic suite consists of amphibolite, hornblende–biotite gneiss and schist and epidote–biotite schist. The biotite-dominated rocks show a close spatial relation with amphibolites, but are mainly confined and closely associated with the copper mineralisation, so that they will be described further below and together with the mineralisation zone.

In the wall rocks surrounding the mineralisation, amphibolites occur as deci- to dekametre large, mostly angular to lensoid blocks within and enveloped by the sheet-like tonalites (Fig. 5). Despite later strains, clear intrusive contacts between tonalitic gneisses and amphibolites indicate that the heterogeneous mafic–felsic association at Omitiomire originally represented an intrusive breccia. These field relationships correspond to the existing U–Pb zircon ages reported by Steven et al. (2000).

Amphibolites are black to dark green in colour (Figs 4d and e). They are dominated by amphibole (pargasitic hornblende) and plagioclase (oligoclase-andesine, $An_{25–35}$), variable amounts of quartz, biotite and accessory epidote, sphene, rutile and, in places, garnet. Greenish hornblende and plagioclase constitute more than 80 vol.% of the rock and based on the relative abundances of the rock-forming minerals, both leucocratic and more melanocratic varieties occur. Hornblende and plagioclase show granoblastic textures and typically form elongated aggregates that define a moderate S2 fabric together with the grain-shape preferred orientation of biotite. A well-developed L2 stretching lineation is present and defined by stretched aggregates of plagioclase and/or hornblende and/or biotite (Fig 4d). Two textural variants of amphibolite gneisses are present. Fine grained amphibolites have an equigranular texture, consisting of fine (~1 mm) subhedral hornblende, plagioclase and biotite (Fig. 4e). Coarser grained amphibolites are inequigranular and characterised by a banded and/or augen texture composed of aggregates of plagioclase and quartz that define mm-sized augen- or sheet-like aggregates (Fig. 4d). Garnet is rare, but where present, occurs as large (5 mm), sub to anhedral porphyroblasts in the S2 fabric. The commonly poikilitic garnet contains inclusions of plagioclase, quartz, amphibole and ilmenite and has an almandine composition with a significant pyrope-grossular content. Along its margins, garnet has been extensively resorbed by plagioclase that also forms strain shadows around larger porhyroblasts.

Fig. 5. Intrusive contact relationship between felsic and mafic gneisses, showing xenoliths of amphibolite floating in tonalite.

3.2. Structural geology

The rocks around Omitiomire show evidence of two deformation phases, D1 and D2, of which the second deformation phase is by far the most dominant, forming part of the regional structural pattern in the Ekuja Dome. An early gneissosity (S1) is defined by the grain-shape preferred orientation of quartz–feldspar aggregates and biotite. This gneissosity is only evident in the hinges of later (F2) metre-wide, high-amplitude isoclinal, near recumbent to shallowly dipping folds that refold the sheeted gneisses and the S1 gneissosity. F2 folds show shallow northerly plunges parallel to the very prominent regional stretching lineation (L2) (Fig. 6b). Tight- to isoclinal folding results in the progressive transposition of earlier intrusive contacts and the S1 fabrics into the regional S2 gneissosity that shows gently undulating, but overall shallow easterly dips at Omitiomire, axial planar to F2 folds (Fig. 6a and c). S2 wraps around isolated angular xenoliths of amphibolite that largely retain their angular shapes and original intrusive contacts with the gneisses. S2 and L2 are defined by amphibolite-facies assemblages such as the grain-shape preferred orientation of hornblende and/or plagioclase in amphibolites, or pervasively recrystallized feldspar and quartz–feldspar aggregates in gneisses.

3.3. Geology of the mineralisation zone

Copper mineralisation is hosted by strongly foliated and lineated hornblende–biotite gneisses and biotite–epidote schists that form an up to 100 m thick, semi-continuous, gently undulating unit of variably deformed mafic xenoliths, dismembered and brecciated by tonalites and confined to the S2 gneissosity. The formation of the biotite-rich lithologies corresponds to a gradual strain increase from wall rock

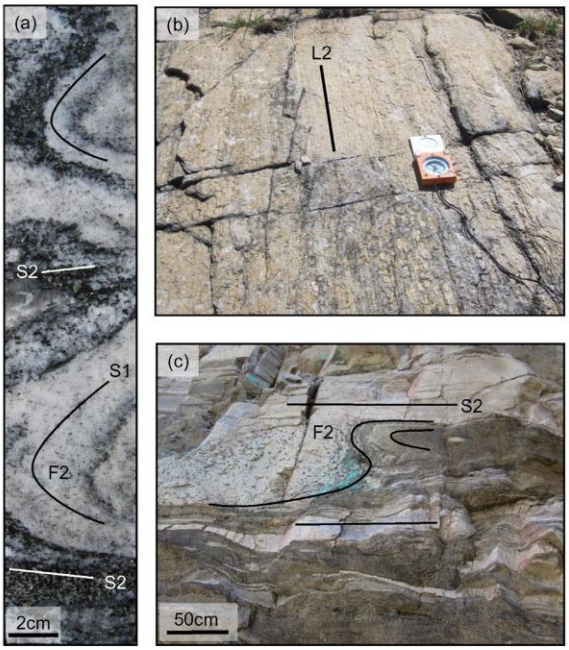

Fig. 6. Photographs of the main structural elements within the study area. (a) Drill core of wall rocks from the Omitiomire deposit showing an early S1 fabric that has been folded by tight to isoclinal F2 folds to form a dominant S2 transposition fabric. (b) Prominent shallow plunging regional L2 rodding lineation on a felsic gneiss pavement along the Black Nossob River. (c) Transposed mafic and felsic gneisses on the eastern wall of the Palm Pit showing an F2 fold refolding earlier intrusive contacts and S1 fabrics to form the dominant S2 fabric in the deposit.

gneisses and amphibolites into highly sheared and attenuated rocks of the mineralised zone over a distance of 5–10 m (Fig. 7). There is clear textural evidence that the biotite schists and gneisses represent variably hydrated equivalents of original amphibolites as a result of fluid infiltration. These relationships are well displayed in sections from the unmineralised hanging-wall gneisses into the upper parts of the mineralisation as they are exposed in the southern sampling pit, but also intersected in boreholes (Figs. 8 and 9). At lower fabric intensities and outside the main mineralisation, amphibolites are rimmed by 5–15 cm wide hornblende–biotite schists, where hornblende is partly replaced by biotite (Fig. 9b). Biotite defines the strong foliation in the hornblende–biotite schists that wraps around the xenoliths and original hornblende–plagioclase assemblages are preserved in the cores of xenoliths. High-strain mylonitic fabrics are initially confined to lithological contacts between the gneisses and amphibolite xenoliths. Mylonitic fabrics in gneisses are evident through a pervasive grain refinement and the presence of quartz ribbons that define the mylonitic foliation. The mylonites show overall shallow easterly dips, parallel to the enveloping S2 gneissosity and form an anastomosing pattern that wraps around the mafic xenoliths (Fig. 8). The shallow northerly plunging L2 lineation is also developed in the hydrated mylonitic zones, despite the predominance of biotite and epidote (Fig. 8d). The retrogression and mylonitization is closely associated with quartz veins (Fig. 9d).

In the central parts of the mineralised zone, biotite–epidote schist are dominant and amphibolites or amphibolite–biotite schists are only preserved as relics. With increasing biotite content, originally angular xenoliths become increasingly flattened in the mylonitic S2 foliation to progressively more lensoid geometries. Deformation and the strain softening associated with the increased biotite content in mafic rocks results in the formation of metre-thick ribbon-like stringers of biotite–epidote schists (Fig. 9c). The sheet-like biotite–epidote schists are isoclinally folded into high amplitude folds with boudinaged limbs and dismembered, rootless fold hinges and are transposed together with tonalite sheets and intrusive pegmatites into the high-strain S2 gneissosity (Fig. 6). Shear sense indicators are common in the biotite–epidote schists of the mineralised zone, but also tonalitic gneisses and mainly include S–C′ fabrics and mantled porphyroclasts. They generally show a top-to-the-south sense of movement along the shallowly-dipping high strain S2b mylonitic fabric, parallel to the strong mineral stretching lineation (L2) (Fig. 10).

Petrographically, biotite and epidote can be seen to progressively replace the original hornblende–plagioclase assemblages of amphibolites outside and along the margins of the mineralisation zone (Fig. 11). The epidote–biotite schist contains up to >60–80% biotite, ~15% epidote, ~15% plagioclase, ~5% sphene, ~5% quartz and minor amounts of chlorite,

Fig. 7. Photograph of drill core from Omitiomire to illustrate the heterogeneity of strain in the deposit. In this example, high strains are confined to a 6 m wide zone (between arrows) of transposed biotite–epidote schists. Note the F2 folds and quartz veins associated with the high strain zone.

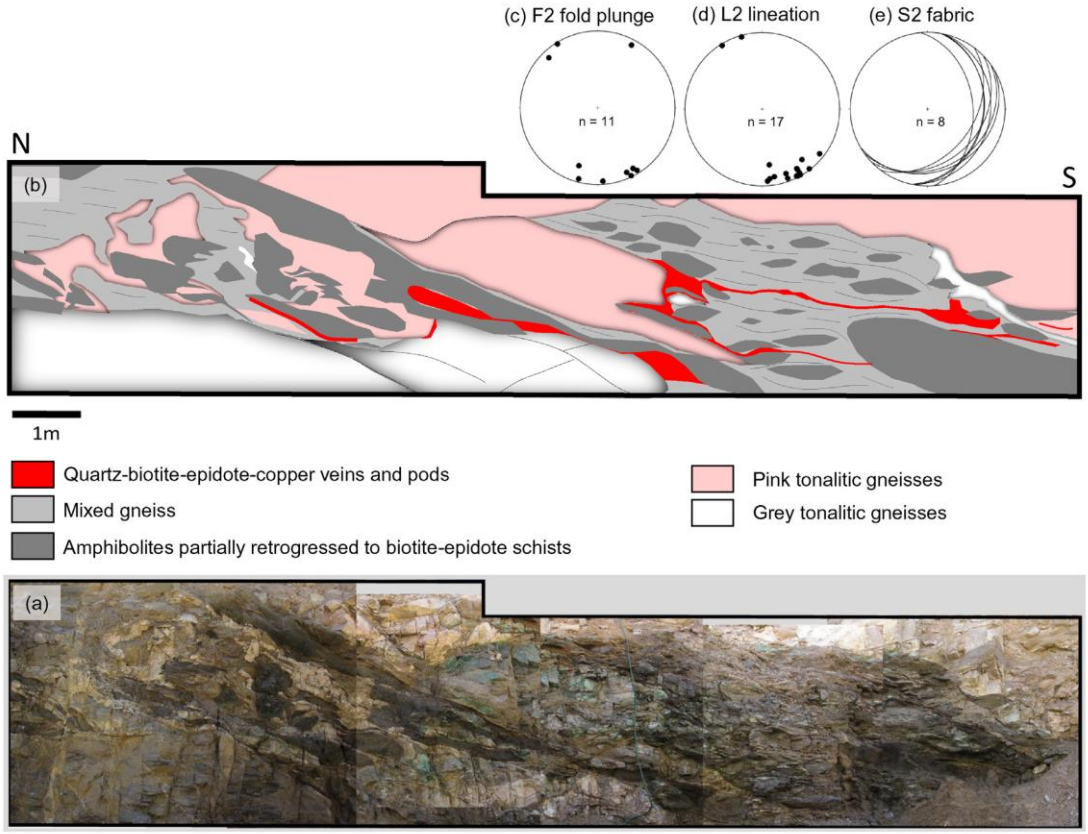

Fig. 8. (a) Stitched photograph and (b) sketch of a mapped panel on the eastern side of the Palm pit. It illustrates the typical brecciated and transposed nature of the gneisses and the location of high grade mineralisation (details in Fig 9). (c) Stereonet showing the northerly plunge of fold axis of F2 folds measured in the pit. (d) Stereonet showing the shallow N–S plunge of lineations and (e) shallow easterly dips of the dominant S2 fabric. Stereonets are equal area, lower hemisphere.

apatite and rutile. Biotite occurs as large (~2–5 mm wide) foliation-parallel aggregates that define the wavy, anastomosing foliation (S2), typically wrapping around relic and only partially replaced grains of hornblende and/or plagioclase or epidote (Figs. 11c and d). In places, biotite may form massive, several cm-wide sheet-like aggregates that result in a compositional banding and a much stronger fabric compared to the relic hornblende–biotite schists or amphibolites. Biotite is texturally intergrown with hornblende, usually enveloping the latter. Olive green to yellowish Cr-rich epidote forms large porphyroblasts that are aligned in the S2 fabric and epidote can be seen to overgrow the biotite foliation but also being enveloped by biotite (Fig. 11d). Larger epidote may reach up to 1 cm in diameter and is commonly anhedral and strongly poikilitic, with inclusions of hornblende, plagioclase, quartz, sphene and some opaques, including chalcocite, rutile and ilmenite. Smaller (<5 mm) epidote is subhedral and elongated in the S2 fabric. Sphene occurs as flattened wedge shaped to highly stretched eyes in the S2 fabric and is closely associated with the mineralisation.

3.4. Cu mineralisation

Copper mineralisation is associated with the biotite–epidote–quartz mineral assemblages that formed after original amphibolites. Copper ore minerals are, in decreasing order of abundance, chalcocite, digenite, bornite, covellite and chalcopyrite (Steven et al., 2000) with chalcocite accounting for more than 98% of sulphide minerals. Chalcocite is typically bluish grey in colour and varies in size from 1 to 2 mm for single subhedral grains to more than 10 mm for aggregates. Even larger aggregates of massive chalcocite are locally developed in strain shadow positions around competent clasts or low-strain areas in the biotite–epidote schists such as boudinaged quartz veins or dismembered fold hinges (Fig. 12). Chalcocite is replaced by digenite, commonly forming lamellar interstices and a characteristic exsolution texture. Digenite is partially replaced by covellite and bornite, the latter typically forming in the interstices of laminae (Steven et al., 2000). Oxides such as magnetite, ilmenite, rutile and rare pyrite are closely associated with the mineralisation and commonly occur as elongated interstitial masses in the fabric or as inclusions in sphene, hornblende and epidote.

The distribution of chalcocite along the mineralised zone is highly heterogeneous. Chalcocite typically occurs as (1) interstitial masses, associated with quartz, biotite and epidote assemblages in high strain shear zones along the contacts between mafic and felsic gneisses (Fig. 11), (2) texturally intergrown and disseminated parallel to the S2 fabric of retrograde biotite–epidote assemblages, (3) in strain shadows of large epidote porphyroblasts, (4) as foliation-parallel folded stringers in folded biotite–epidote schists (Fig 12a,b), and (5) small inclusions within epidote and sphene porphyroblasts in hornblende–biotite gneisses and biotite–epidote schists.

The highest copper grades (>5 wt.% Cu) are associated with quartz ±epidote–biotite veins, shears and pods in strain shadows, along the contacts between felsic and mafic gneisses (Figs 9 and 11). Although generally only a few centimetres wide, the biotite–epidote–chalcocite dominated shears and quartz veins commonly form part of a much

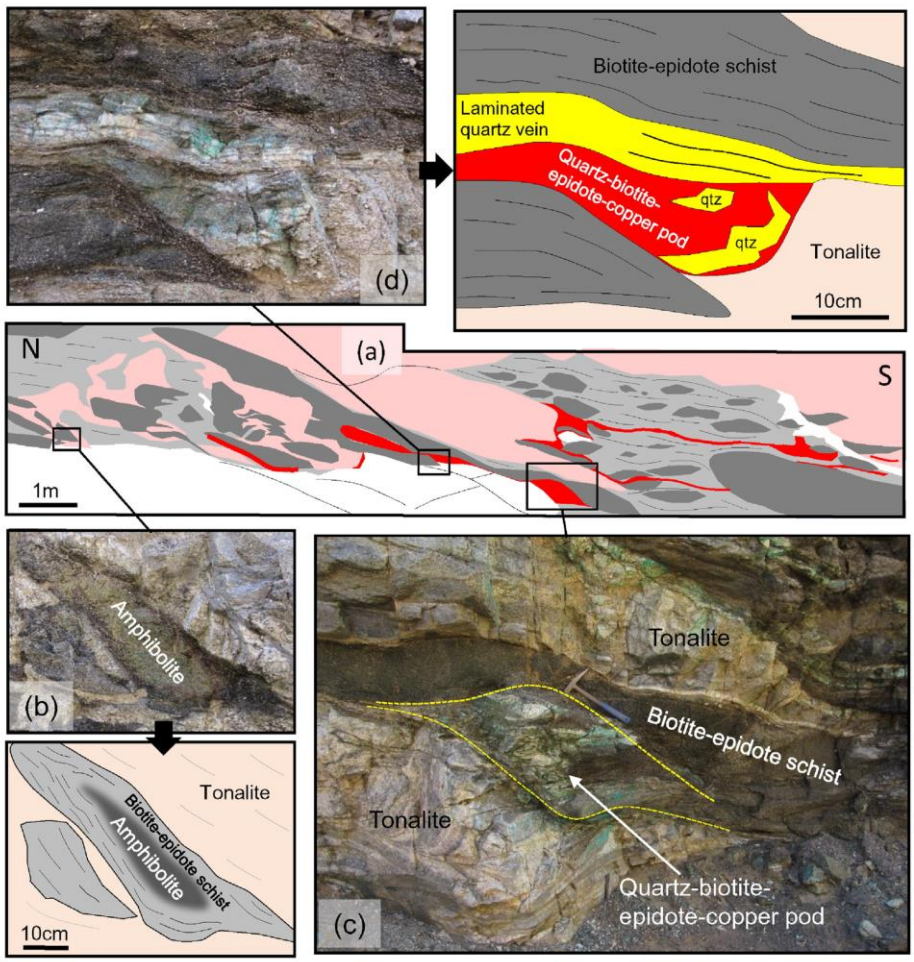

Fig. 9. Annotated sketches and close up photographs of the panel in Fig 8 on the eastern side of the Palm pit. See Fig. 8 for legend. (b) Relic amphibolite xenolith, retrogressed along the margins to biotite and epidote. (c) Large high copper grade (Cu = 6.5 wt.%) quartz–biotite–epidote and copper pod in a low-strain domain at the contact between biotite schists and tonalites. Note the transposed nature of the original amphibolite xenolith. Samples from the biotite schists returned between 0.4 wt.% and 0.8 wt.% copper. (d) Laminated mineralised quartz vein (Cu = 5 wt.%) with quartz–biotite–epidote and copper pod in the strain shadow between biotite schists and tonalites.

larger anastomosing network of shears that can be up to several metres wide. Quartz occurs as gently undulating veins that may pinch and swell along strike or as highly deformed stringers and blebs. In most cases, quartz veins have been transposed into the S2 mylonitic foliation where they occur as 1–10 cm wide, clear to slightly grey, laminated veins around the amphibolite-gneiss contacts, but also as highly deformed, boudinaged and/or folded veins or aggregates in biotite–epidote schist (Figs. 12c and d). Mineralised quartz–epidote–biotite shears are characterised by (1) a reduction in grain size, (2) an increase in biotite content, (3) a decrease in hornblende, (4) increase in epidote content and porphyroblast size, (4) occurrence of quartz and (5) increase in chalcocite content. Most of the chalcocite is confined to thin (<5 mm) biotite-epidote rich laminations in the vein that are parallel to the vein walls. Large, up to metre-wide pods of massive quartz, biotite, epidote and chalcocite occur in low-strain domains at the contact between felsic and mafic rocks (Fig. 9c). The mineralised pods appear to pinch and swell and are stretched in a north–south direction, parallel to the regional stretching lineation (L2).

4. 3D modelling

A deposit scale model of the ore body was constructed using Leapfrog Geo modelling software which uses an implicit modelling approach to create three-dimensional (3D) geological models from large datasets (Cowan et al., 2002; Cowan et al., 2003). The main aims of the modelling were to visualise the 3D geometry of the ore body relative to host lithologies and controlling structures, and describe the deposit-scale controls of mineralisation by comparing the 3D model with observations from pit mapping and drill core logging.

4.1. Data sets

The model area is ~4 km in the N–S direction, 2 km in the E–W direction and ~780 m in the Z direction. The surface elevation is ~1685 m above sea level. Most of the model is based on the extensive drillhole database, composed of numerical (collar, assay and survey) and non-numerical (lithology and structure) data from roughly 100,000 m of

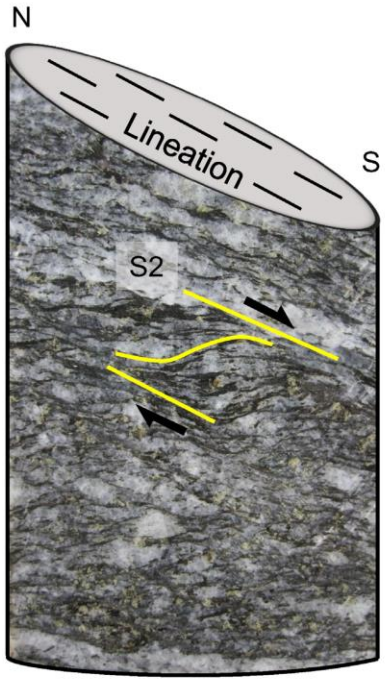

Fig. 10. Drill core from the Omitiomire deposit showing a typical S–C fabric with a top-to-the-south sense of movement.

exploration drillholes. This includes 70,000 m of rotary percussion or reverse circulation (RC) holes, roughly 10,000 m of Rotary Air Blast (RAB) holes and more than 15,000 m of diamond drill core (DD). The drill pattern consists of a series of subparallel E–W trending drill lines that differ in line and drillhole spacing from north to south (Fig. 13). In the northern part of the deposit, deep (up to 780 m) exploration holes were drilled on a relatively wide drill spacing of roughly 100 m between lines and 50 m–100 m between drillholes. The central and southern parts of the ore body are covered by exploration holes on a drill pattern of ~50 m between line and hole and shallow, grade-control style holes, ~25 m apart. For this project, ~14,000 m of the diamond drill core were re-logged. Although none of the core was orientated, structural orientation readings were available from an extensive down-the-hole photography database from 60 RC holes.

4.2. Modelling approach

All data were first verified and correlated to ensure compatibility between different datasets before they could be imported. Drillhole data were automatically validated by the Leapfrog Geo software when imported, allowing inconsistencies in the database such as duplicate, missing and incorrect samples to be quickly identified and corrected. Assays from drillhole data were modelled within the boundaries of the transposed biotite–epidote and amphibolite gneiss dominated host rock unit. Copper interpolants with cut-off grades of 0.25 wt.%, 0.5 wt.% and 1 wt.% were created and a structural trend that was generated from the downhole photography and surface mapping data was applied for a more realistic representation of the interpolants within the main S2 fabric of the host rock.

4.3. Modelling results

4.3.1. Geometry of the ore body

The 3D shape of the ore body shows a semi-continuous, sheet-like, very gently arcuate geometry that dips at a moderate angle of 20–30 degrees to the east, conformable with the regional S2 fabric and eastern boundary of the Ekuja Dome (Fig. 14). Both the down dip and strike extensions remain open, but the current dimensions show copper

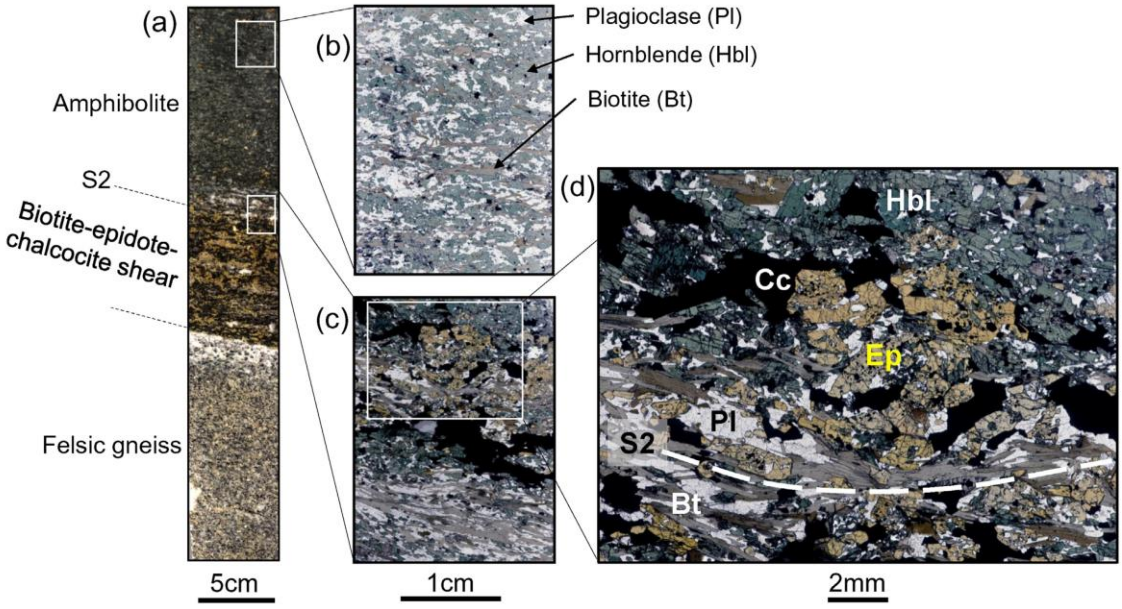

Fig. 11. (a) Drill core from the mineralised zone showing a typical biotite–epidote–chalcocite shear at the contact between a fine grained amphibolitic gneiss and a felsic gneiss. (b) Photomicrograph of fine grained amphibolitic gneiss composed of hornblende (Hbl), plagioclase (Pl) and biotite (Bt). (c–d) Photomicrograph of mineralised contact shear composed of biotite, hornblende, epidote (Ep), plagioclase and chalcocite (Cc). Biotite occurs as elongated sheets along the S2 fabric and typically wraps around large poikilitic epidote porphyroblasts. Note how smaller epidotes are aligned within the S2 fabric. Chalcocite is closely associated with epidote, occurring in the strain shadow of large porphyroblasts.

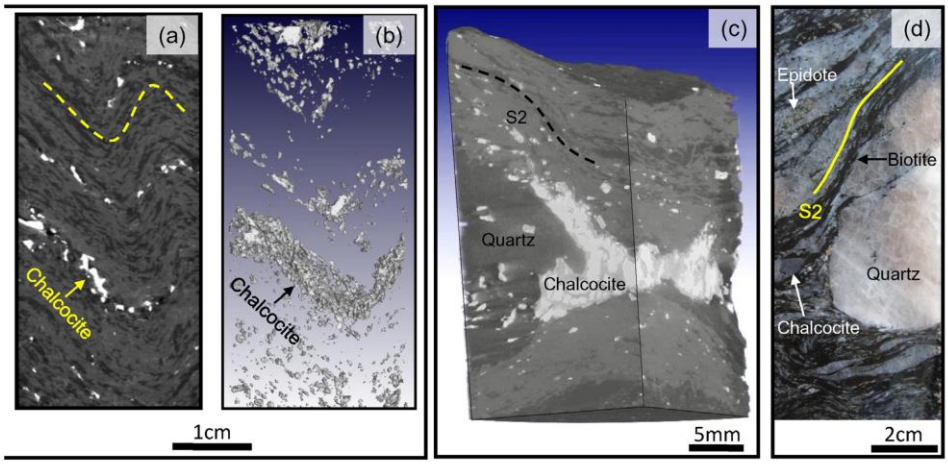

Fig. 12. High resolution X-ray computed tomography and photograph of drill core samples from the mineralised zone at Omitiomire. (a–b) Chalcocite grains folded (F2) with the S2 fabric in biotite–hornblende schists. (c) 3D image of chalcocite in the neck of a boudinaged quartz vein and enveloped by the S2 fabric. (d) boudinaged quartz veins enveloped by the S2 fabric, defined by biotite. Note the chalcocite in the boudin neck.

mineralisation confined to a between 10 and 100 m thick, 4 km long, and up to 750 m wide, north–south striking ore zone that gently undulates along the dominant S2 fabric.

Locally, the ore body (>0.25 wt.% Cu) shows distinct variations in thickness, shape and orientation. When viewed in a longitudinal N–S section the deposit is characterised by an upward convex lens shape that plunges at shallow angles (20°) to the north and south. Both the hangingwall and footwall boundaries of the deposit are gently undulating which may explain the local thickening and thinning of the ore body. Correlation of locally thickened lenses in the 3D model with core intersections indicates that thickened areas correspond to the occurrence of isoclinal folds in the mineralised shear zone where the mineralised biotite–epidote schists have been duplicated and transposed into the shear-zone fabric. In cross-section, and based on the available drillhole data, the deposit can be subdivided into a deeper north-eastern domain and shallower west and south-western domains. The north-eastern domain is characterised by a consistent, slightly undulating, moderate dip to the east, reaching a depth of up to 780 m below surface, that remains open ended. Here, the width of the ore body varies between 10 m and a maximum of 50 m. In the central, western and south western domains, the ore zone either pierces through the surface or is situated just below it, making this domain particularly attractive for exploration and mining. The central domain is characterised by a marked thickening of the ore body to up to 100 m. Toward the southwest, the ore body appears to be gently undulated around a shallow south plunging fold hinge to form an anticline-syncline fold pair. The gentle folding of the ore schist seems to be supported by structural data from downhole photography. In the hinges of the undulations the ore zone thickens and appears to split into several stacked lenses that then seem to merge into a thinner lens along the eastward-dipping, western limb of the syncline.

4.3.2. Ore grade distribution

The association between mafic dominated lithologies, high strain fabrics and copper mineralisation are well illustrated by overlaying the copper interpolants with lithological and structural data from drillholes (Fig. 15). High strain zones are almost exclusively associated with biotite–epidote dominated lithologies underlining that copper mineralisation corresponds with the spatial association between mafic lithologies, dominated by biotite–epidote schists, and zones of high strain (Fig. 15). Several unmineralised mafic lenses occur outside the mineralised zone but these mafics lack the intense transposition, quartz veining and mylonitisation that are characteristic of the biotite–epidote dominated schists in the ore zone. On a deposit scale, the up to a 100 m thick ore body is made up of several thin, east-dipping and shallow north and south plunging mineralised lenses ranging in thickness from less than a metre to up to several tens of metres. The highest copper grades (>1 wt.% Cu) are concentrated in shallow, L2 parallel, north–south trending shoots that occur in the upper parts of the ore body close to the contact with the overlying hanging wall felsic gneisses (Figs. 14 and 15). This concentration of higher copper grades against the hanging wall contact is evident throughout the ore body and are not the result of supergene enrichment, but rather due to the concentration of mineralised quartz veins and shears close to the contact. Individual shoots can be up to 20 m wide, and although they may pinch and swell, continue along strike for up to 2 km. Ore shoots coincide with shallow N–S trending hinge lines of gentle flexures in the undulating S2 fabric. These folds correspond to the more or less upright open- to tight L2 parallel corrugation type folds that can also be mapped regionally.

5. Discussion

5.1. Controls of fluid flow

The key observations at Omitiomire are that copper mineralisation is associated with (1) a gently dipping, protomylonitic and/or mylonitic high-strain zone contained within the regionally flat lying D2 (Pan-African, ca. 520 Ma) fabrics of the Ekuja Dome that is, (2) centred around a lithologically heterogeneous, originally intrusive, Namaqua age (ca. 1060–1080 Ma) breccia between older amphibolites and younger tonalites (Fig. 16a). The strain gradient from wall rocks around the Omitiomire mineralisation into the mineralised shear zone illustrates the progressive development of the shear zone and associated fluid flow and mineralisation. D2 high-strain fabrics outside the mineralised zone are commonly concentrated along lithological contacts and particularly along the margins of amphibolite xenoliths against tonalitic gneisses. Mylonitic high-strain zones wrap around amphibolites and form an overall anastomosing pattern of thin, cm-wide shear zones within the regionally flatlying S2 gneissosity (Fig. 16b). Importantly, quartz veining is spatially closely associated with these mylonites and localised along the margins of amphibolite blocks. Quartz veins originate along the mylonites and project preferentially into the more massive amphibolites. This reflects the competence contrast and

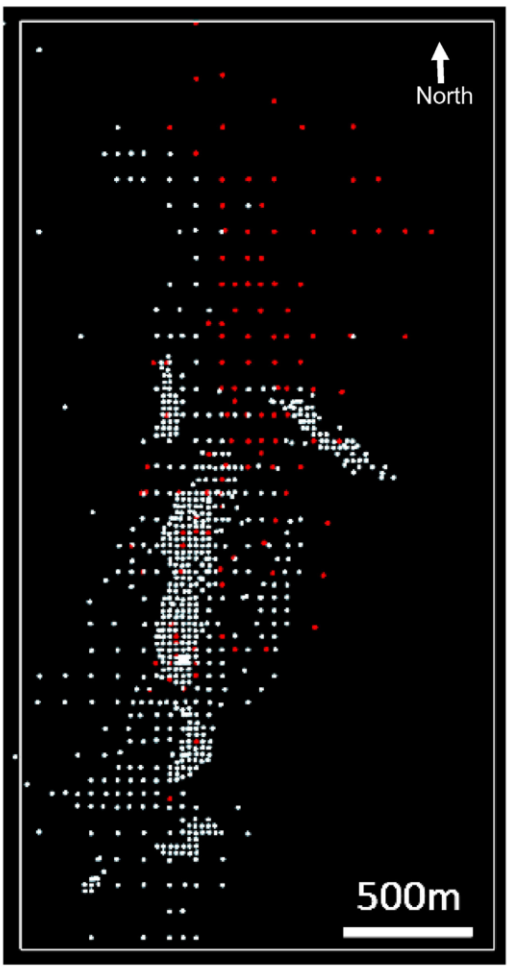

Fig. 13. Plan map of holes drilled in the Omitiomire deposit and used in the 3D model. The highest density of drillholes occurs in the southern and central part of the ore body and follows an E–W drill line pattern. Reverse circulation (RC) and percussion drillholes are in white; diamond drillholes in red.

resulting strain-rate gradients between ductilely deforming quartzo-feldspathic gneisses and the brittlely behaving hornblende-plagioclase dominated amphibolites. This is well illustrated in the literature (Handy and Brun, 2004; Passchier and Trouw, 2005). The mylonitisation and pervasive dynamic recrystallisation of feldspars in the tonalitic gneisses indicates temperatures >500 °C during deformation and associated veining (Passchier and Trouw, 2005). Fluid infiltration associated with the quartz veining leads to the hydration of initially the margins of amphibolites and the formation of biotite- and biotite–epidote assemblages. This is well documented in the small sampling pit, but also in drill core where pristine or only partly hydrated hornblende-plagioclase assemblages are preserved in the core of xenoliths and are partially or completely replaced by biotite and biotite–epidote assemblages along the margins of larger xenoliths (Fig. 9b). Biotite is interpreted to have formed during hydration and retrogression of the amphibolites through the general reaction:

hornblende + plagioclase + H_2O + K = biotite + epidote + quartz.

The pervasive fabric development in biotite–schists around amphibolites indicates that further deformation is localised and concentrated into the rheologically weaker biotite-dominated margins (Kronenberg et al., 1990; Wintsch et al., 1995). This is particularly the case once biotite is the dominant mineral in the hydrated assemblage, thus forming an interconnected weak layer structure able to lead to further strain localisation. As a result, the originally narrow shear zones along the margins of the amphibolite become wider and form an increasingly larger continuous and interconnected network of anastomosing shears that surround rigid phacoids or lithons of tonalite and relic amphibolite (Fig. 16c.). Earlier formed high-angle quartz veins are rotated and progressively transposed into the mylonitic fabric. This results in the commonly observed up to15 cm wide and metre-long, laminated and recrystallized quartz ribbons (Fig. 9d) that anastomose around outlines of former amphibolite xenoliths in the central parts of the Omitiomire shear zone. This rheological weakening from earlier hornblende-plagioclase to biotite-dominated assemblages marks an important rheological transition in the shear zone. It leads to further strain localisation, but also increases rheological contrasts in the shear zone that, in turn, promote brittle fracturing, veining and fluid infiltration, particularly along lithological contacts and in competent lithologies.

Further strain localisation into the marginal biotite schist zones results in the inward migration of quartz veining during progressive deformation, away from the original tonalite–amphibolite contacts into the interior of amphibolites. This positive feedback between the lithologically controlled strain localisation and fluid flow leads to the complete transformation of amphibolite to biotite schists that characterises the central parts of the Omitiomire shear zone system. Originally angular amphibolite xenoliths occur as highly drawn out and transposed biotite schists within the flat-lying, anastomosing mylonitic foliation, intercalated with tightly folded tonalitic gneisses (Fig. 16c). Importantly, the pervasive hydration of wall rocks is largely restricted to the mafic suite. Tonalitic gneisses bordering against the mineralisation, in contrast, have not been affected by this alteration and remain largely unaltered. This highlights the very focused fluid flow in the Omitiomire shear zone confined to brittle fracture networks in more competent amphibolites against a rheologically weaker matrix, initially made up of tonalitic gneisses and, subsequently, biotite–epidote schists.

5.2. Deposit-scale geometry, controls of mineralisation and timing

The gently east dipping, anastomosing Omitiomire shear zone is contained within the regional S2 foliation that wraps around the Ekuja Dome and L fabrics in the mineralisation are parallel to the regional L2 lineation (Fig. 14). Isoclinal F2 folds similar to those found in the regional S2 fabric are common in the Omitiomire shear zone and underline the high-strain nature of the mineralisation zone. F2 folds also refold and transpose the alteration related biotite–epidote schists and the chalcocite mineralisation (Figs 6 and 7.). Importantly, the very pronounced linear geometry and shallow north–south plunge of high-grade ore shoots of the Omitiomire mineralisation are parallel to the regional L2 stretching lineation (Fig. 3). Taken in conjunction, both the structural inventory and the geometry of the deposit suggest the evolution of the mineralised Omitiomire shear zone system as part of the regional, broadly D2 evolution of the Ekuja Dome within the SZ.

Previous works have suggested a largely late- to post-tectonic timing of the copper mineralisation (Steven et al., 2000; Maiden et al., 2013), but there are several textural lines of evidence that suggest the main phase of chalcocite mineralisation to be syn-tectonic and introduced during syn-deformational biotite–epidote alteration. This includes (1) the occurrence of lath-like chalcocite along biotite foliae, (2) the presence of chalcocite aggregates in strain shadow positions around epidote pophyroblasts, and (3) the folding of laths or trains of chalcocite within the main S2 foliation (Fig. 12). The highest copper grades are typically found in specific structural sites such as low-strain domains (Fig. 9). This also underlines the syn-tectonic timing of copper mineralisation associated with the main phase of fluid flow and biotite–epidote alteration in the Omitiomire shear zone. Replacement textures and relative age relationships in section indicate a sequence of (1) early hornblende, overprinted by (2) biotite followed by

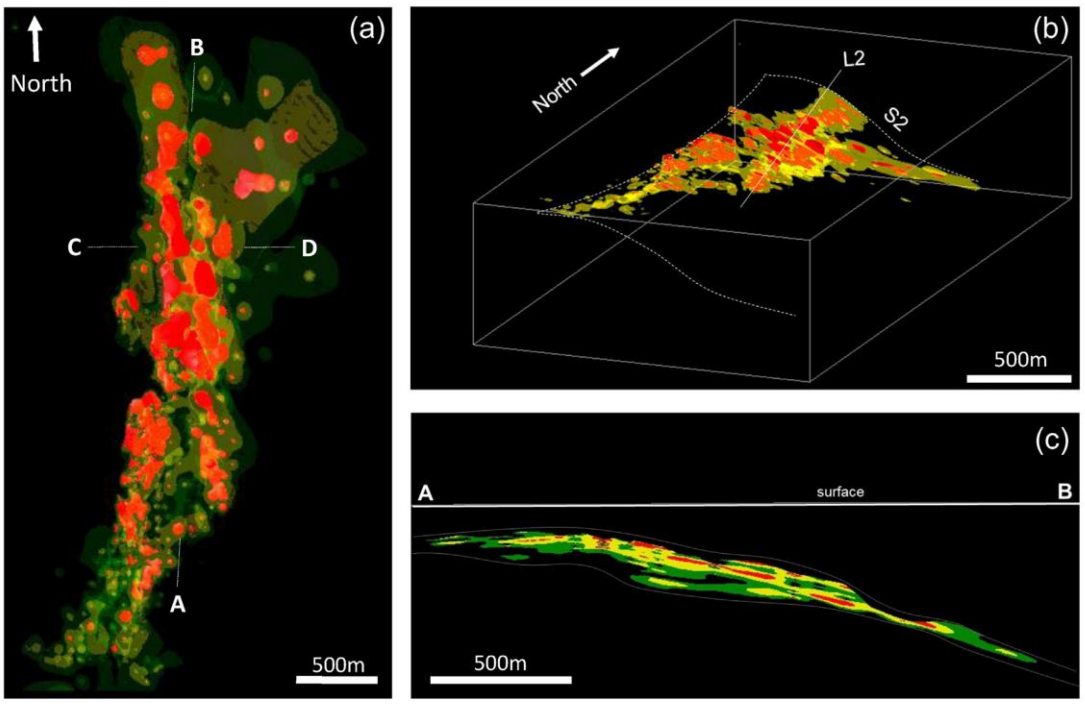

Fig. 14. Different views of the Omitiomire copper mineralisation model. The highest grade shell are in red and envelope copper assays >1%. Copper assays >0.5% are in yellow and >0.25% in green. (a) Plan map of copper grade shells showing the L2 parallel N–S trend of the long axis of the high grade shoot. The location of the longitudinal (Fig 14c) and cross-section (Fig 15) are indicated. (b) 3D view of copper grade shells >0.25% showing the shallow east dipping, arcuate sheet-like geometry of the ore body. (c) Longitudinal N–S section through the deposit showing an upward convex lens shape that plunges at shallow angles (20°) to the north and south. Note how the highest copper grades occur in the upper parts of the ore body (also refer to Fig 15).

(3) epidote and chalcocite. The seemingly post-tectonic overgrowth of chalcocite is mainly observed in polished section and reflects the late-stage, static recrystallization of chalcocite.

5.3. Regional tectonic setting

Sphene U–Pb ages of ca. 520–485 Ma in the mylonitic foliation of biotite–epidote schists confirm the Pan-African timing of deformation and mineralisation in the older, Namaqua age basement gneisses (Steven et al., 2000; Maiden et al., 2013) This timing correlates with the late stages of subduction of the Kalahari Craton below the Congo Craton (Meneghini et al., 2014). Kasch (1986) pointed out that the northerly trending D2 structures and flatlying fabrics in the Ekuja Dome post-date and refold the structures and fabrics of the structurally highest OMSB that constitutes much of the SZ accretionary prism. Importantly, the top-to-the-south kinematics established here for the Omitiomire shear zone and, by inference, D2 fabrics in the Ekuja Dome, correspond with the south vergence and top-to-the-south kinematics recorded in the OMSB complex. Hence, kinematics are identical, but timing relationships and strains seem different in structurally overlying units (Kasch, 1986).

Gneisses of the Ekuja Dome are located at the base of the SZ accretionary prism. The affinity of the Mesoproterozoic gneisses to rocks of the Southern Marginal Zone suggests that they form part of the underthrusted Kalahari Craton. Slivers of serpentinite are abundant in these basal parts of the SZ (Barnes, 1983). The slivers range from 10s to 100 s of metres in length and also occur along the outer perimeter of the Ekuja Dome against overlying metasediments (Kasch, 1986). Both the presence of basement gneisses and imbricated serpentinites along the base of the accretionary wedge point to a position of the Ekuja Dome within or close to the subduction channel of the subduction zone (Fig. 17). The subduction channel forms a tectonically complex, often mélange-like zone along the interface between the downgoing slab and the overriding plate. The structural complexity arises from the juxtaposition of subducted and tectonically underplated rocks with originally deeper parts of the subduction zone that are exhumed during return flow in the subduction channel (Agard, 2009; Angiboust, 2010). Serpentinites play a critical role in this process due to their buoyancy and rheologically weaker nature that is thought to lubricate the subduction channel (Guillot et al., 2000; Hermann et al., 2000; Agard et al., 2009; Angiboust and Agard, 2010). We suggest that the north-trending L–S fabrics in the Ekuja Dome record the down-dip parallel transport and flow on top of the northward subducting Kalahari plate in the subduction channel. The south-verging and east–west trending fold-and-thrust belt of the overlying OMSB, in contrast, records the offscraping of metasediments during the northward subduction of the Kalahari plate. In other words, the refolding of fabrics and structures from the upper OMSB into the lower Ekuja Dome may not necessarily be the result of two successive deformation phases. Different strains and overprinting relationships rather record deformation at different structural levels in the convergent Damara margin and document the strain gradient from the upper parts of the SZ, dominated by accretion, into the subduction channel that records the northward subduction.

Based on the above, we suggest that the structurally lowermost EONC, including the Ekuja Dome, represents imbricated slivers of the upper parts of the Kalahari Craton that were sliced off as nappes and accreted to the base of the SZ accretionary prism during the later stages of convergence along the Damaran subduction zone margin (Fig. 17). The isothermal decompression path recorded by Kasch (1987) for the lower parts of the intermediate OVFC may suggest that this part was

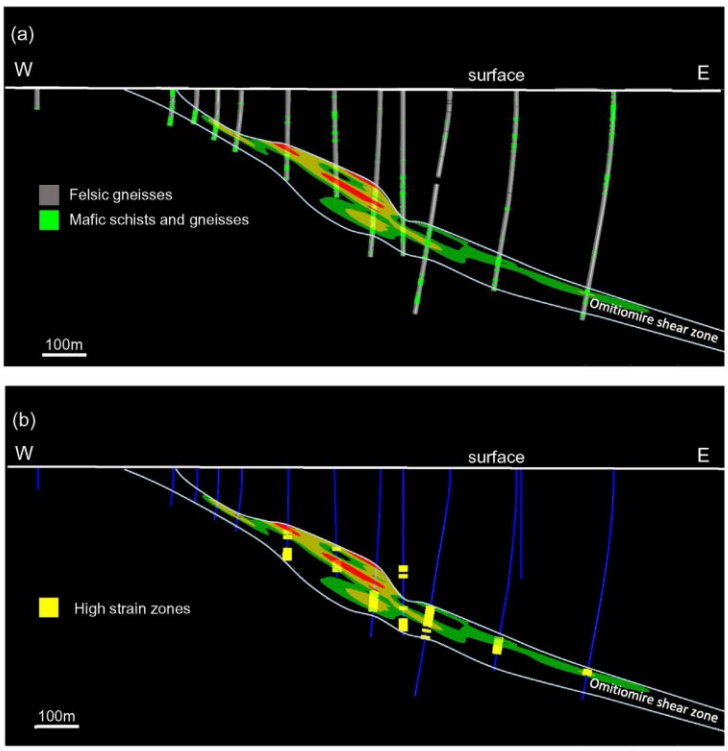

Fig. 15. East–west cross-sections through the deposit showing drillholes and displaying the relationships between (a) copper mineralisation and intercepts of mafic schists and gneisses and (b) high strain zones as logged in the drillholes. Note how copper mineralisation is associated with the spatial coincidence of mafics units and high strain zones. Mafic units outside the Omitiomire high strain shear zone are unmineralised. Location of cross-section is indicated by C–D in Fig 14a.

exhumed and structurally expelled along the subduction channel during ongoing subduction. This agrees with the top-to-the-south kinematics and prominent L–S fabrics in the basement gneisses and also with the late Pan-African timing of deformation indicated for the mineralisation at Omitiomire (Steven et al., 2000). Fluid flow and mineralisation are associated with this phase of southward stacking and evidently involved the channelling of hydrous fluids along the Omitiomire shear zone system.

5.4. Regional correlation

Most copper deposits in Southern Africa are related to Neoproterozoic to Paleozoic, Damara-Lufilian supracrustal sedimentary successions (Selley et al. 2005; Hitzman et al., 2012; Unrug, 1983; Kampunzu, 1999; Gray, 2008) that extend from the Kalahari Copperbelt of western Namibia and northern Botswana (Borg and Maiden, 1989; Maiden and Borg, 2011; Lehmann et al., 2015) to the Central African Copperbelt (Lufilian Arc) in Zambia and the Democratic Republic of Congo (Kampunzu and Cailteux, 1999; Cailteux, 2005). The Omitiomire deposit does not form part of the Kalahari Copperbelt, and although unmetamorphosed age correlatives of the Omitiomire gneisses could be the Kgwebe volcanic rocks (Schwartz et al., 1995; Kampunzu et al., 1998), it does not share any of the characteristics of the copper mineralisation. Direct correlations between the Damara Belt and the Lufilian Arc are complicated by extensive sand cover in northern Namibia and Botswana, but geophysics (Lehmann et al., 2015) and regional works by (Unrug, 1983; Kampunzu and Cailteux, 1999; Porada and Berhorst, 2000; Rainaud, 2005) suggest an along-strike correlation of tectonostratigraphic units, including basement terranes between Zambia and Namibia. Some of the largest copper deposits of the Domes Region in the Lufillian arc of northern Zambia, including Lumwana (Bernau et al., 2013), Kansanshi (Hitzman et al., 2012) and Sentinel/Kalumbila (Steven and Armstrong, 2003; Hitzman, 2012) are associated with Paleo- to Mesoproterozoic gneiss domes, overlain by high-grade metamorphic metasediments of the Katanga Supergroup that share numerous similarities with Omitiomire in the Damara Belt. Available geochronological, P–T and structural data in particular, emphasise the timing of mineralisation during late-Pan-African convergence during which basement gneisses were juxtaposed against the metasedimentary cover (Torrealday, 2000, Bernau et al., 2013). Constrictional-type strains and copper mineralisation confined to high-strain zones in the basement gneisses in the Domes Region are also remarkably similar to the Omitiomire deposit (Bernau et al., 2013). Given that the Southern Zone of the Damara Belt and the Domes Region of the Lufilian Arc form structurally contiguous terranes characterised by the Pan-African juxtaposition of Paleo- to Mesoproterozoic basement gneisses against Neoproterozoic metasedimentary cover during the convergence between the Kalahari and Congo Cratons, a correlation can be made between the Omitiomire deposit and the basement associated deposits of the Domes Region.

6. Conclusions

Copper mineralisation at Omitiomire formed during deformation and associated fluid infiltration along a shallowly-dipping, anastomosing shear-zone system contained in Mesoproterozic basement gneisses of the Ekuja Dome. Copper mineralisation is hosted by biotite- and biotite–epidote schists that form during the progressive hydration of particularly mafic lithologies (amphibolites). The deposit geometry and control of mineralisation is defined by the spatial coincidence of

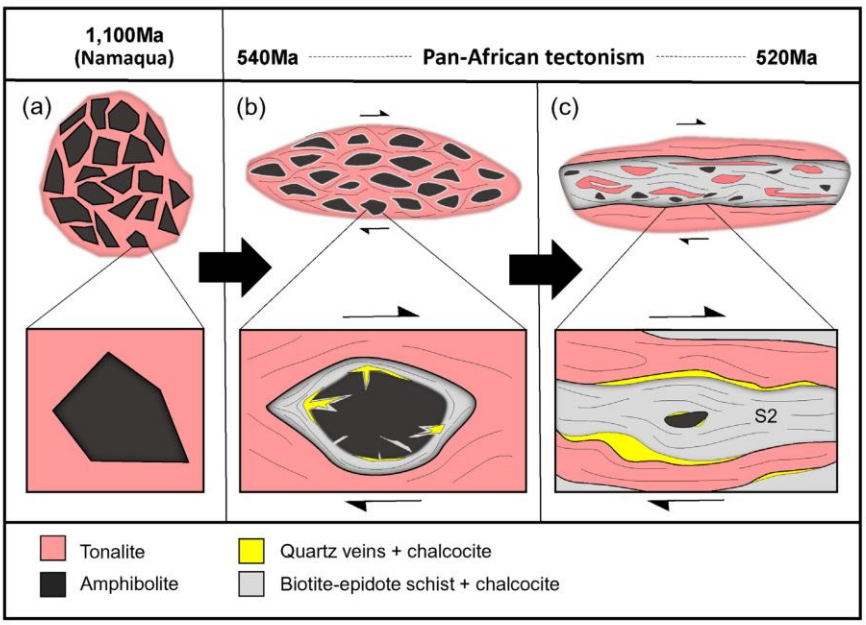

Fig. 16. Schematic model illustrating the main stages for the development of copper mineralisation at Omitiomire. (a) Angular blocks of amphibolite floating in tonalite suggest that the host rock was originally a Namaqua age intrusive breccia between older amphibolite and younger tonalite. (b) Pan-African deformation and associated fluid flow resulted in the hydration and the formation of biotite-epidote assemblages and quartz veining along the margins of amphibolites. Further deformation were localised into weaker biotite dominated margins resulting in the inward migration of quartz veining, further hydration and widening of the originally narrow shear zones along the margins of the amphibolites. (c) This positive feedback between lithologically controlled strain localisation and fluid flow eventually led to a complete transformation of amphibolite to biotite schists and resulted in an interconnected network of anastomosing shears focused in the biotite schists and surrounding the rigid lenses of tonalite and relic amphibolite. Copper mineralisation (chalcocite) occurs disseminated within the main S2 foliation in biotite schists, as quartz–biotite–epidote veins and shears along the contacts between mafic and felsic gneisses and as massive quartz–biotite and epidote pods in low strain domains.

an original intrusive amphibolite–tonalite breccia and associated inherent heterogeneity and a heterogeneous high strain zone. High-grade ore shoots occur parallel to the regional N–S trending L2 lineation and close to the contact with the hanging wall felsic gneisses. On an outcrop scale the highest copper grades are associated with quartz–epidote–biotite veins along the contact between biotite–epidote schists and felsic gneisses and also with low-strain domains. On a micro scale chalcocite, the dominant copper sulphide, is texturally intergrown and folded along the S2 fabric of retrograde biotite–epidote dominated assemblages and also occurs in the strain shadows of epidote porphyroblasts. This clearly illustrates the structural control of the mineralisation, and also that competency contrast on all scales played an important role. Regionally, we correlate the development of the Omitiomire deposit with the D2 exhumation of the Ekuja Dome during

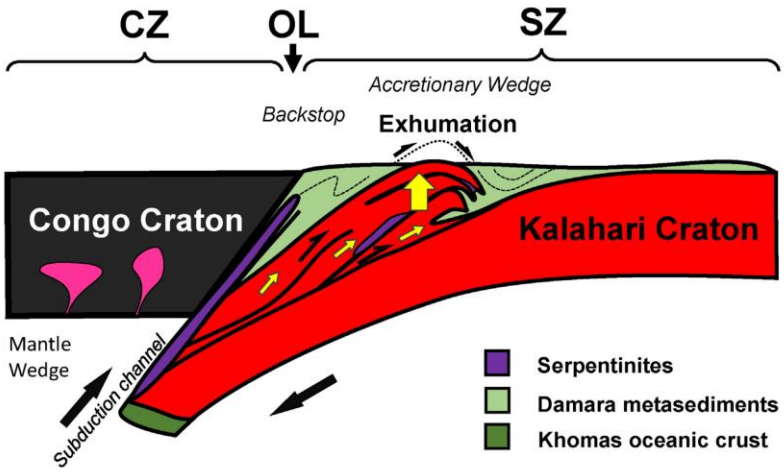

Fig. 17. Schematic model for the exhumation of the Ekuja Dome. During Pan-African convergence and subduction the upper parts of the Kalahari Craton were sliced off as nappes against the leading edge of the Congo Craton. Exhumation is aided by serpentinites that acted as lubricants for the nappes. During the last stages of convergence the nappes were stacked, expelled and exhumed, forming dome structures that pierced through the cover of the Kuiseb formation of the Southern Zone Accretionary Prism.

the late stages of subduction of the Kalahari below the Congo Craton. Exhumation occurred along the base of the SZ accretionary wedge, close to the subduction channel as is shown by the presence of imbricated serpentinites. The striking similarities between the Omitiomire deposit and basement associated Cu deposits of the Domes Region in the Lufilian Arc of Zambia, suggests a potentially much larger regional control on mineralisation with significant implications for the exploration potential of other Proterozoic basement domes hidden under cover.

Acknowledgements

We acknowledge International Base Metals Limited (IBML) and its wholly-owned Namibian subsidiary, Craton Mining and Exploration for financially sponsoring this project. For administrative and logistical support we thank Ziggy Hartmann, Marina Bezuidenhoudt, Desmond Schnugg and Holger Wittsack. We acknowledge Simon Brodie for providing a well maintained drillhole and GIS data set. Frik Badenhorst, Benson Bhunu, Sakkie Likuwa and the field crew at Borealis and Omitiomire camps are thanked for their assistance and discussions in the field. Karl Kasch and Ute Schreiber for interesting discussions and access to original maps. Loxie Conradie and George Olivier are thanked for administrative support at the University of Stellenbosch. SK thanks Desmond Subramani, Kim Moodley and Stephan Fuchsloch from Leapfrog Africa and ARANZ Geo Pty. Ltd. for their generous assistance with the 3D modelling and providing an academic licence for the Leapfrog Geo software package. NS would like to thank Richard Armstrong from the Australian National University for his geochronological support over the years. We acknowledge the constructive comments of Prof Gregor Borg and the excellent editorial handling of Prof Franco Pirajno. This paper is dedicated to Dr. Nick Steven, friend, colleague, mentor and outstanding geologist who sadly passed away recently.

References

Agard, P., Yamato, P., Jolivet, L., Burov, E., 2009. Exhumation of oceanic blueschists and eclogites in subduction zones: timing and mechanisms. Earth Sci. Rev. 92 (1–2), 53–79.
Angiboust, S., Agard, P., 2010. Initial water budget: the key to detaching large volumes of eclogitized oceanic crust along the subduction channel? Lithos 120, 453–474.
Anhaeusser, C.A., Maske, S., 1986. Mineral deposits of Southern Africa. Geol. Soc. S. Afri. II, 1725–1738.
Barnes, S.-J., 1983. Pan-African serpentinites in central South West Africa/Namibia and the classification of serpentinites. Spec. Publ. geol. Soc. S. Afr. 11, 147–155.
Bernau, R., Roberts, S., Richards, M., Nisbet, B., Boyce, A.J., Nowecki, J., 2013. The geology and geochemistry of the Lumwana Cu (±Co ± U) deposits, NW Zambia. Mineral. Deposita 48, 137–153.
Borg, G., Maiden, K.J., 1989. The middle Proterozoic Kalahari copper belt of Namibia and Botswana. In: Boyle, R.W., Brown, A.C., Jefferson, C.W., Jowett, E.C., Kirkham, R.V. (Eds.), sediment-hosted stratiform copper depositsGeol. Assoc. Can. Spec. Pap. 36, 525–540.
Cailteux, J.L.H., Kampunzu, A.B., Lerouge, C., Kaputo, A.K., Milesi, J.P., 2005. Genesis of sediment-hosted stratiform copper–cobalt deposits, central African Copperbelt. J. Afr. Earth Sci. 42, 134–158.
Cowan, E.J., Beatson, R.K., Fright, W.R., Mclennan, T.J., Mitchell, T.J., 2002. Rapid geological modelling. Applied Structural Geology for Mineral Exploration and Mining, International Symposium, pp. 23–25 , 23–25 September 2002. Kalgoorlie.
Cowan, E.J., Beatson, R.K., Ross, H.J., Fright, W.R., Mclennan, T.J., Evans, T.R., Carr, J.C., Lane, R.G., Bright, D.V., Gillman, A.J., Oshust, P.A., T., M., 2003. Practical implicit geological modelling. In: Dominy, S. (Ed.), Fifth International Mining Geology Conference Proceedings. AusIMM Publication Series No 8/2003, pp. 89–99.
Coward, M.P., 1983. The tectonic history of the Damaran belt. Spec. Publ. geol. Soc. S. Afr. 11, 409–421.
Guillot, S., Hattori, K., de Sigoyer, J., 2000. Mantle wedge serpentinization and exhumation of eclogites: Insights from eastern Ladakh, northwest Himilaya. Geology 28, 199–202.
Gray, D.R., Foster, D.A., Meert, J.G., Goscombe, B.D., Armstrong, R., Trouw, R.A.J., Passchier, C.W., 2008. A Damaran Perspective on the Assembly of Southwestern Gondwana. Geological Society of London Special Publication.
Handy, M.R., Brun, J.-P., 2004. Seismicity, structure, and strength of the lithosphere. Earth Planet. Sci. Lett. 223, 427–441.
Hermann, J., Müntener, O., Scambelluri, M., 2000. The importance of serpentinite mylonites for subduction and exhumation of oceanic crust. Tectonophysics 327, 225–238.
Hitzman, M.W., Broughton, D., Selley, D., Woodhead, J., Wood, D., Bull, S., 2012. Geology and genesis of major copper deposits and districts of the world — a tribute to Richard H sillitoe.Society of Economic Geologists Special Publication. In: Hedenquist, J.W., Harris, M., Camus, F. (Eds.), 2012 — The Central African Copperbelt: Diverse Stratigraphic, Structural, and Temporal Settings in the World's Largest Sedimentary Copper District. 16, pp. 487–514.
Innes, J., Chaplin, R.C., 1986. Ore bodies of the Kombat Mine, South West Africa/Namibia. In: Anhaeusser, C.R., Maske, S. (Eds.), Mineral Deposits of Southern AfricaGeol. Soc. S. Afr II, 1789–1805.
International Base Metals Limited Quarterly Activities Report – End September 2014 (http://www.interbasemetals.com/sites/default/files/IBML-Quarterly-to-Sept%202014.pdf)
Kampunzu, A.B., Akanyang, P., Mapeo, R.B.M., Modie, B.N., Wendorff, M., 1998. Geochemistry and tectonic significance of the Mesoproterozoic Kgwebe metavolcanic rocks in northwest Botswana: implications for the evolution of the Kibaran Namaqua-Natal belt. Geol. Mag. 135, 669–683.
Kampunzu, A.B., Cailteux, J., 1999. Tectonic evolution of the Lufilian Arc (central Africa copperbelt) during the Neoproterozoic Pan-African orogenesis. Gondwana Res. 2, 401–421.
Kasch, K.W., 1986. Tectonic subdivision, lithostratigraphy and structural geology of the Upper Black Nossob river area. Communications of the Geological Society of Namibia. vol. 2, pp. 117–129.
Kasch, K.W., 1987. Metamorphism of pelites in the Upper Black Nossob river area of the Damara Orogen. Communications of the Geological Society of Namibia. vol. 3, pp. 63–82.
Klemd, R., 1987. The matchless copper deposit, South West Africa/Namibia a deformed and metamorphosed massive sulfide deposit. Econ. Geol. 82, 587–599.
Kronenberg, A.K., Kirby, S.H., Pinkston, J., 1990. Basal slip and mechanical anisotropy of biotite. J. Geophys. Res. 95, 19257–19278.
Kukla, C., Kramm, U., Kukla, P.A., Okrusch, M., 1991. U–Pb monazite data relating to metamorphism and granite intrusion in the northwestern Khomas Trough, Damara Orogen, central Namibia. Communications of the Geological Survey of Namibia. 7, pp. 49–54.
Lehmann, J., Master, S., Rankin, W., Milani, L., Kinnaird, J.A., Naydenov, K.V., Saalmann, K.A., Kumar, M., 2015. Regional aeromagnetic and stratigraphic correlations of the Kalahari Copperbelt in Namibia and Botswana. Ore Geol. Rev. 71, 169–190.
Lombaard, A.F., Günzel, A., Innes, J., Krüger, T.L., 1986. The Tsumeb Lead–Copper–Zinc–Silver Deposit, South West Africa/Namibia. In: Anhaeusser, C.R., Maske, S. (Eds.), Mineral Deposits of Southern Africa II. Soc. S. Afr. Spec. Publ, Geol, pp. 1761–1787.
Maiden, K.J., Borg, G., 2011. The Kalahari Copperbelt in central Namibia: controls on copper mineralization. SEG Newsletter 87, 14–19.
Maiden, K.J., Hartmann, K., Steven, N.M., Armstrong, R.A., 2013. The Omitiomire deposit, Namibia: Late Tectonic copper emplacement in a Neoproterozoic (Pan-African) imbricate shear system. Extended Abstract, SGA Meeting, 12–15 Aug 2013. Sweden, Uppsala.
Meneghini, F., Kisters, A., Buick, I., Fagereng, A., 2014. Fingerprints of late Neoproterozoic ridge subduction in the Pan-African Damara Belt, Namibia. Geology 42, 903–906.
Miller, R.M.G., 1983. The Pan-African Damara Orogen of Namibia. In: Miller, R.,.M.G. (Ed.), Evolution of the Damara Orogen of South West Africa/NamibiaSpec. Publ. geol. Soc. S. Afr 11, 431–515.
Miller, R.M.G., 2008. The Geology of Namibia. Volume 2: Neoproterozoic to Lower Palaeozoic. Geological Survey of Namibia, Windhoek, Namibia, p. 320.
Passchier, C.W., Trouw, R.A.J., 2005. Microtectonics. Springer, Berlin, p. 366.
Porada, H., 1989. Pan-African rifting and orogenesis in southern and equatorial Africa and eastern Brazil. Precambrian Res. 44, 103–136.
Porada, H., Berhorst, V., 2000. Towards a new understanding of the Neoproterozoic–Early Palaeozoic Lufilian and northern Zambezi belts in Zambia and the democratic republic of Congo. J. Afr. Earth Sci. 30, 727–771.
Rainaud, C., Master, S., Armstrong, R.A., Robb, L.J., 2005. Geochronology and nature of the Palaeoproterozoic basement in the central African Copperbelt (Zambia and Democratic Republic of Congo), with regional implications. J. Afr. Earth Sci. 42, 1–31.
Sawyer, E.W., 1981. Damaran structural and metamorphic geology of an area south-east of Walvis bay. South West Africa/Namibia. Memoir of the Geological Survey of South Africa. 7.
Schneider, G.I.C., Seeger, K.G., 1992. Copper. The Mineral Resources of Namibia. Windhoek, Republic of Namibia, Ministry of Mines and Energy/Geological Survey 2.3–1 2.3–118.
Selley, D., Broughton, D., Scott, R., Hitzman, M., Bull, S.W., Large, R.R., McGoldrick, P.J., Croaker, M., Pollington, N., Barra, F., 2005. A new Look at the Geology of the Zambian Copperbelt. Economic Geology 100th Anniversary 965–1000.
Steven, N.M., Armstrong, R.A., Smalley, T.I., Moore, J.M., 2000. First geological description of a late Proterozoic (Kibaran) andesite-hosted chalcocite deposit at Omitiomire, Namibia. In: Cluer, J.K., Price, J.G., Struchsacker, E., Hardyman, R.F., Morris, C.L. (Eds.), Geology and Ore Deposits 2000: The Great Basin and Beyond. Geological Society of Nevada Symposium Proceedings, pp. 711–734.
Steven, N.M., Frimmel, H., Armstrong, R.A., 2001. A Pan-African (600–550 Ma) metamorphogenic chalcocite deposit formed from the redistribution of Kibaran (1115–1180 Ma) basite-hosted copper at Omitiomire, Namibia. In: Williams, P.J. (Ed.), 2001: A Hydrothermal Odyssey. Extended Conference Abstract, EGRU Meeting. Townsville, Australia 17–19 May, 2001.
Steven, N., Armstrong, R., 2003. A metamorphosed Proterozoic carbonaceous shale-hosted Co–Ni–Cu deposit at Kalumbila, Kabompo dome: the Copperbelt ore shale in northwestern Zambia. Econ. Geol. 98, 893–909.
Schwartz, M.O., Akanyang, P., Trippler, K., Ngwisanyi, T.H., 1995. The sediment-hosted Ngwako Pan copper deposit, Botswana. Econ. Geol. 90, 1118–1147.
Torrealday, H.I., Hitzman, M.W., Stein, H.J., Markley, R.J., Armstrong, R.A., Broughton, D., 2000. Re–Os and U–Pb dating of the vein-hosted mineralization at the Kansanshi copper deposit, Northern Zambia. Econ. Geol. vol. 95, 1165–1170.
Unrug, R., 1983. The Lufilian arc: a microplate in the Pan-African collision zone of the Congo and Kalahari cratons. Precambrian Res. 21, 181–196.
Wintsch, R.P., Christoffersen, R., Kronenberg, A.K., 1995. Fluid-rock reaction weakening of fault zones. J. Geophys. Res. 100, 13,021–13,032.

Chapter 3

Geometry of the orebody and sources of fluids and metals

This chapter presents the submitted research paper: "*Orebody geometry, fluid and metal sources of the Omitiomire copper deposit in the Ekuja Dome of the Damara Belt in Namibia"* by Shawn Kitt, Alexander Kisters, Torsten Vennemann and Nick Steven.

The manuscript was submitted to Mineralium Deposita on the 15th of September 2016 and accepted for publication on the 23 March 2017. The paper (1) describes the 3D geometry of ore bodies and shoots in the deposit, (2) combines structural, lithological and geochemical data to define the controls and internal architecture of high-grade shoots, (3) semi-quantitatively characterize element mobility in the mineralised shear zone through whole-rock geochemical data and mass balance calculations, (4) use stable isotopes to constrain the temperature conditions, fluid-rock ratios and potential sources of fluids and metals, (5) integrate deposit-scale data into the broader geological evolution of the Damara Belt and (6) correlate with similar styles of mineralisation in the Domes region of the Lufilian Arc in Zambia. The following aspects of the research was done independently by Shawn Kitt with supervision by Alex Kisters: (i) field work and sampling (ii) logging of ~15,000m of diamond drill core (iii) compilation and processing of ~100,000m of exploration drill hole data (iv) 3D modelling in Leapfrog Geo software (v) interpretation of results (vi) preparation of the manuscript. The stable isotope analyses was done by Torsten Vennemann and Helene Raud. Torsten Vennemann also assisted with the interpretation of the data and preparation of the manuscript. Alex Kisters contributed with editorial work towards the final draft.

Miner Deposita
DOI 10.1007/s00126-017-0731-y

ARTICLE

Orebody geometry, fluid and metal sources of the Omitiomire Cu deposit in the Ekuja Dome of the Damara Belt in Namibia

Shawn Kitt[1] · **Alexander Kisters**[1] · **Torsten Vennemann**[2] · **Nick Steven**[3]

Received: 15 September 2016 / Accepted: 23 March 2017

Abstract The Omitiomire Cu deposit (resource of 137 Mt at 0.54% Cu) in the Ekuja Dome of the Damara Belt in Namibia is hosted by an anastomosing, low-angle Pan-African (ca. 520 Ma) shear zone system developed around an older (ca. 1100–1060 Ma), late Mesoproterozoic intrusive breccia between a suite of mafic rocks (originally lava flows) and later tonalitic gneisses. High-grade ore shoots preferentially formed along contacts between tectonically interleaved biotite-epidote-quartz-chalcocite schists and felsic gneisses, and are directly related to an increase in the number and cumulative thickness of thin, contact-parallel mineralized shear zones. Alteration and mineralization are associated with elevated concentrations of K_2O, Cr, Rb, S, and Cu and a loss of Na_2O, CaO, and MgO. Oxygen isotope fractionation for quartz-biotite, quartz-feldspar, and quartz-amphibole mineral pairs support equilibrium temperatures of between 500 and 650 °C during the fluid/rock interaction. Mineral separates from amphibole-biotite gneisses and mineralized schists have similar ranges in $\delta^{18}O$ values of about 1.2 to 2 ‰ relative to VSMOW. Coexisting minerals are arranged in an order of increasing $\delta^{18}O$ values from biotite, to epidote, amphibole, and quartz, suggesting that the Omitiomire Shear Zone was a rock-dominated system. Similarly, H-isotope results for mineral separates from biotite-epidote schists and amphibole gneisses do not show any reversals for D/H fractionations, with δD values of between −48 and −82 ‰, typical of metamorphic-magmatic rocks. The homogeneous and low $\delta^{34}S$ values (−6.1 to −4.7 ‰ CDT) are compatible with a local redistribution of sulfur from magmatic rocks and interaction with sulfur derived from metamorphic fluids of metasedimentary origin. The relatively low fluid/rock ratios and elevated Cu values (>1500 ppm) from unaltered amphibolite point to a local redistribution of an earlier (late Mesoproterozoic) Keweenaw-type Cu mineralization into later Pan-African shear zones during the exhumation of the Ekuja Dome. The timing, polyphase evolution, and tectonic setting of the Omitiomire deposit show remarkable similarities with the large Cu deposits of the Domes Region in the adjoining Lufilian Arc of northern Zambia. This suggests the presence of a much larger, regionally significant Cu province extending from central Namibia, through northern Botswana, and into Zambia.

Keywords Damara Belt · Cu · Mesoproterozoic dome · Pan-African · Shear zone · Stable isotopes · Fluid/rock ratio · Lufilian Arc

Editorial handling: H. Frimmel

Electronic supplementary material The online version of this article (doi:10.1007/s00126-017-0731-y) contains supplementary material, which is available to authorized users.

✉ Shawn Kitt
shawnkitt@gmail.com

[1] Department of Earth Sciences, Stellenbosch University, Private Bag X1, Matieland, Stellenbosch 7602, South Africa

[2] Institute of Earth Surface Dynamics, University of Lausanne, Lausanne, Switzerland

[3] Rockwater Consulting, 10 Evergreen Lane, Constantia, Cape Town 7806, South Africa

Published online: 29 April 2017

Introduction

Central Africa is one of the major Cu provinces in the world. Traditionally, the Central African Copperbelt in the southern Democratic Republic of Congo (DRC) and northwestern Zambia has been known for its sediment-hosted, stratiform Cu deposits (e.g., Selley et al. 2005; Sillitoe et al. 2010;

Hitzman et al. 2012), with possible extensions into the Kalahari Copperbelt of Botswana and Namibia (Borg and Maiden 1989). For the most part, Cu mineralization is hosted by low-grade metamorphic, Neoproterozoic (ca. 880–760 Ma) metasedimentary rocks of the Lower Roan Group in Zambia and the overlying Mines Subgroup in the DRC (Selley et al. 2005; Cailteux et al. 2005; Hitzman et al. 2012). The more recent discoveries of large Cu, U, and Co deposits in the Domes Region in the Pan-African Lufilian Arc of northern Zambia represent a distinct style of Cu mineralization that does not conform to the typical Copperbelt-type mineralization. Instead, Cu mineralization is hosted by high-grade metamorphic, regional-scale domes made up of Meso- and Neoproterozoic basement gneisses surrounded by metasedimentary cover rocks that have a Pan-African tectonic and metamorphic overprint related to the late-stage evolution of convergent and collisional tectonics in the Lufilian Arc (John et al. 2004; Selley et al. 2005; Cailteux et al. 2005; Hitzman et al. 2012). Most studies highlight the high-grade metamorphic wall rock sequence and, in many cases, multiple stages of mineralization, but there is no clear consensus as to the style, controls, and absolute timing of mineralization (Benham et al. 1976; McGowan et al. 2003; Steven and Armstrong 2003; Selley et al. 2005; Bernau et al. 2013; Hitzman et al. 2012; Turlin et al. 2016).

The northeast-trending Damara Belt in Namibia is commonly interpreted to represent the southwestern continuation of the Lufilian Arc (Fig. 1). Both belts have accommodated the amalgamation of the Congo and Kalahari Cratons to form Gondwana in the latest Neoproterozoic and early Phanerozoic (Kampunzu and Cailteux 1999; Miller 1983). The Omitiomire Cu deposit is hosted by late Mesoproterozoic gneisses and schists that are structurally overlain by amphibolite-facies metasedimentary rocks of the Southern Zone (SZ) accretionary prism (Fig. 1 and electronic supplementary material (ESM) 1). The striking similarities between the Omitiomire deposit and the large Cu deposits in the Domes Region of Zambia suggest similar mineralization processes and controls and an extension of the Cu province from the Domes Region into Namibia (Kitt et al. 2016).

This paper describes the 3D geometry of ore bodies that constitute the Omitiomire deposit, modeled using an extensive drill hole data set. Copper grades and grade envelopes are combined with structural and lithological-geochemical data to describe the internal make up and controls of ore shoots within the deposit. Whole rock geochemical data and mass balance calculations are used to semi-quantitatively characterize element mobility within the mineralized shear zone system. Stable isotope mineral and whole rock data are used to (i) better constrain the temperature conditions of the mineralization and alteration, (ii) constrain fluid/rock ratios during fluid flow, and (iii) discuss the potential source of fluids and metals. Lastly, the deposit-scale data is integrated into the broader geological evolution of the Damara Belt in order to draw possible correlations with seemingly similar styles of mineralization in the Domes Region of the Lufilian Arc in Zambia.

Geological overview

The Pan-African Damara Belt formed by the high-angle convergence of the Congo and Kalahari Cratons during

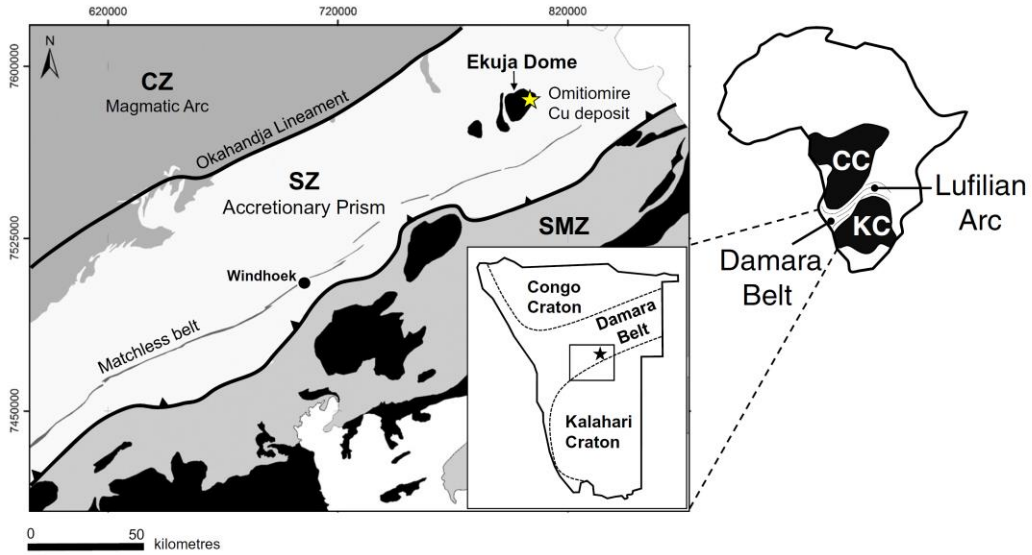

Fig. 1 Simplified geological map (after Miller 2008) showing the location of the Omitiomire Cu deposit relative to the Ekuja Dome and the Southern Zone (*SZ*) accretionary prism of the Damara Belt of Namibia. Also shown is the Central Zone (*CZ*), Southern Margin Zone (*SMZ*), and locations of the Damara Belt and Lufilian Arc relative to the Congo Craton (*CC*) and the Kalahari Craton (*KC*)

the late Neoproterozoic to early Phanerozoic between ca. 580 and 520 Ma (Coward 1981; Miller 1983, 2008; Gray et al. 2008). The Southern Zone (SZ) is the accretionary prism of the belt, developed as a south-verging fold-and-thrust belt that records the off-scraping and burial of the Khomas Sea and thick, trench-fill-type sediments of the Kuiseb Formation during northward subduction below the Congo Craton (Kukla and Stanistreet 1991; Meneghini et al. 2014). The Omitiomire deposit is situated in the Ekuja Dome, one of three gneiss domes at the base of the SZ prism (Fig. 1 and ESM 1). The gneiss domes are made up of late Mesoproterozoic (ca. 1100 Ma) tonalites and amphibolites (Steven et al. 2000) and are structurally overlain by the medium-P, medium-T amphibolite-facies metaturbiditic Kuiseb Formation, and imbricated slivers of serpentinite (Kasch 1986, 1987). Both the structural location and lithological assemblages point to a tectonic position of the gneiss domes close to, or within, the subduction channel, recording initial burial and subsequent expulsion of basement rocks during northward subduction of the Kalahari Craton (Kitt et al. 2016).

Geology of the Omitiomire deposit

Host rocks

The Omitiomire deposit is situated on the eastern flank of the Ekuja basement dome, close to the structural contact with the overlying Kuiseb Formation of the SZ prism (Fig. 1 and ESM 1). Most of the deposit area is covered by up to 10 m thick, transported Cenozoic (Kalahari) sand, silt, and calcrete. Except for sporadic outcrops in the ephemeral Nossob River and a small sampling pit in the southern part of the deposit, geological information is derived from drill hole data (Fig. 2). The Ekuja Dome is dominated by quartzo-feldspathic banded or augen gneisses of mainly tonalitic composition. The gneisses typically form large sheets and lenses that vary in thickness from a few centimeters up to tens of meters. The tonalitic magma intruded and brecciated a volumetrically subordinate mafic suite of amphibolite. Original intrusive contacts and the brecciation of the older amphibolitic sequence is preserved at lower strain intensities (Kitt et al. 2016) (ESM 2a). At higher strains, angular xenoliths appear progressively sheared out and transposed into the regional gneissic fabrics (S2), associated with the partial or near pervasive retrogression of the rocks (Kitt et al. 2016) (ESM 2b). The intrusive relationship between amphibolite and tonalite is confirmed by U-Pb zircon ages of 1115 ± 13 Ma for amphibolite and 1084 ± 7 and 1063 ± 9 Ma for quartzo-feldspathic gneisses (Steven et al. 2000).

Structure

Drill core logging and structural mapping of scattered outcrops in the area revealed at least two deformation phases (Kitt et al. 2016). The first phase (D1) in felsic gneisses is defined by the grain-shape preferred orientation of quartz-feldspar aggregates and biotite, and is only observed in the hinges of isoclinal, near recumbent F2 folds that refold the early S1 gneissosity. The second phase (D2) is associated with a regionally developed shallow dipping S2 gneissosity that is parallel to the dome margin and the contact between basement gneisses and overlying Damaran supracrustal rocks. S2 is a well-developed transposition fabric, formed through the progressive refolding of earlier intrusive contacts and the S1 gneissosity by tight to isoclinal F2 folds. This gneissic fabric forms the dominant structural element in the deposit (Steven et al. 2000; Kitt et al. 2016), as well as on a regional scale (Kasch 1987). F2 folds at Omitiomire show north-south trends and subhorizontal northerly or southerly plunges. Fold plunges are parallel to a prominent L2 stretching lineation, defined by rodding fabrics of quartz-feldspar aggregates in gneisses and the preferred alignment of hornblende, plagioclase, and biotite in mafic units along the shallow east-dipping S2 gneissic fabric (Kitt et al. 2016).

Mineralization

Copper mineralization is spatially associated with variably retrogressed mafic rocks that have formed through the progressive hydration of original amphibolite to amphibole-biotite gneiss and biotite-epidote schist (Steven et al. 2000; Maiden et al. 2013; Kitt et al. 2016). This retrogression is confined to an anastomosing system of mylonitic shear zones, henceforth referred to as the Omitiomire Shear Zone (OSZ). The OSZ is contained in the regional S2 fabric and centered around the lithologically heterogeneous intrusive breccia made up of original amphibolite and tonalite sheets (ESM 2). The Cu resource is largely made up of deeper seated sulfide ore. Shallower oxide-facies ore occurs up to a depth of ca. 40 m below surface and is made up of malachite and subordinate chrysocolla. Chalcocite is the main Cu ore mineral, accounting for more than 90% of sulfide minerals and is texturally intergrown with biotite and epidote. The highest Cu grades are associated with shear bands, veins, and pods that occur in biotite-epidote schists along the lithological contacts with felsic gneisses (Fig. 3a–f) (Kitt et al. 2016). The high-grade biotite-epidote-quartz shear bands are closely associated with either laminated or massive, ribbon-like, and pervasively recrystallized quartz veins or quartz vein relics. Quartz veins are invariably folded or boudinaged, typically forming dismembered boudins and lenses in the biotite-dominated mylonitic shear zones. Large (meter-size) mineralized quartz-biotite-epidote pods or lenses typically occur in the

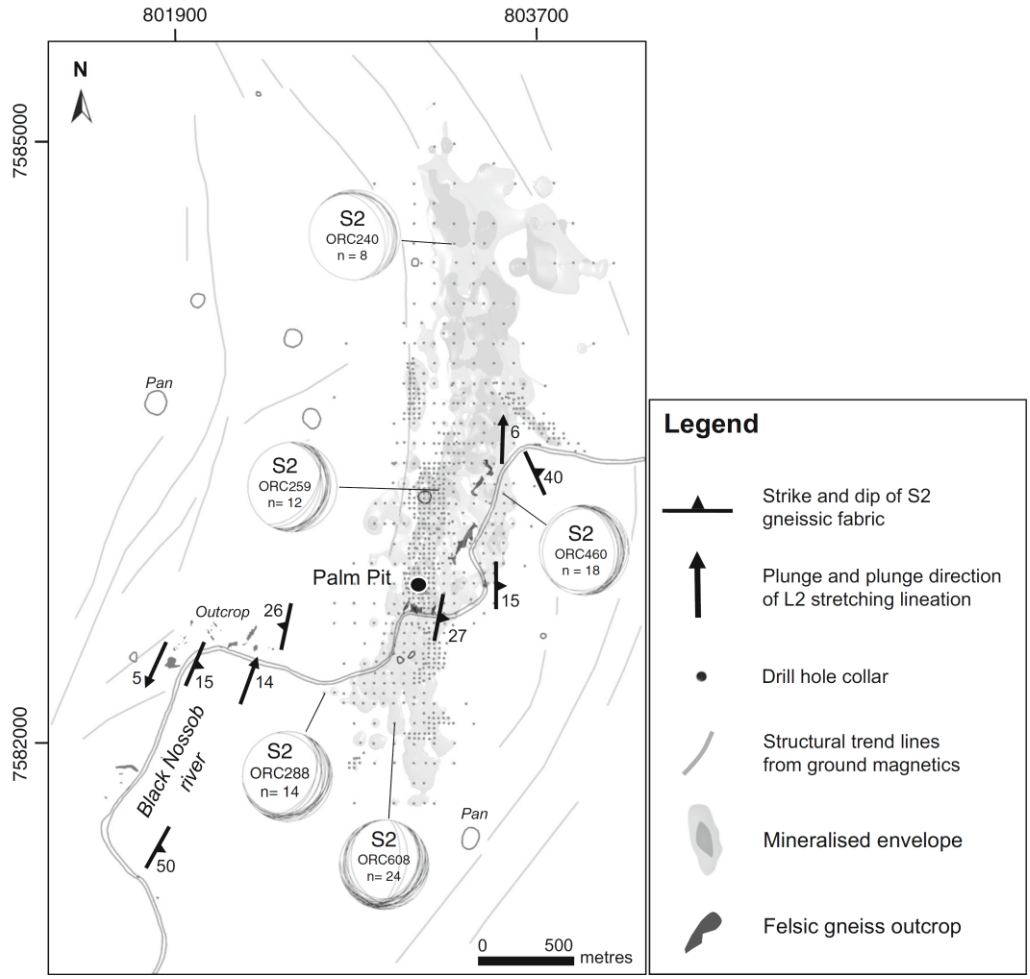

Fig. 2 Map of the Omitiomire Cu deposit, showing drill hole collars and the subsurface outlines of the orebody. Structural information was compiled from scattered outcrops along the ephemeral black Nossob River, panels along a bulk sample pit (Palm Pit), and data from downhole photography of drill holes (*ORC*). Equal area, lower hemisphere stereonets of structural orientation data of the dominant S2 fabric in selected holes are shown. Structural trend lines (*light gray*) are interpreted from ground magnetic data

low-strain domains at the contacts between deformed mafic and felsic lenses and are stretched in a north-south direction. Details of the structural controls and evolution of the Cu mineralization have been presented in Kitt et al. (2016).

3D implicit modeling

The visualization and description of the geometry of the subsurface geology and distribution of Cu mineralization relied on the 3D modeling of an extensive drill hole dataset, including geological, structural, and assay data from roughly 100 km of drilling (Figs. 2 and 4). The modeling was carried out using Leapfrog Geo 3D modeling software and an implicit modeling approach with drill hole data in a volume of 4 km in a north-south direction, 2 km from east to west, and up to 800 m below the surface (Fig. 4). Due to the structural and lithological complexity and relatively wide spacing of drill holes in some areas, a meaningful lithological model of the OSZ was only possible through the definition of wider and, in places, heterogeneous rock packages, without compromising the integrity of the data and losing necessary detail (Fig. 4a). For example, smaller, meter-wide sheets of felsic gneiss intercalated with mainly biotite-epidote and amphibole-biotite gneiss units were grouped together into the mafic-dominated unit. Similarly, meter-scale amphibolite and mafic schist bodies may appear as isolated and seemingly discontinuous units in otherwise felsic gneisses. These isolated and discontinuous amphibolite bodies probably formed rafts intruded and dismembered by tonalitic magma similar to the intrusive relationships developed

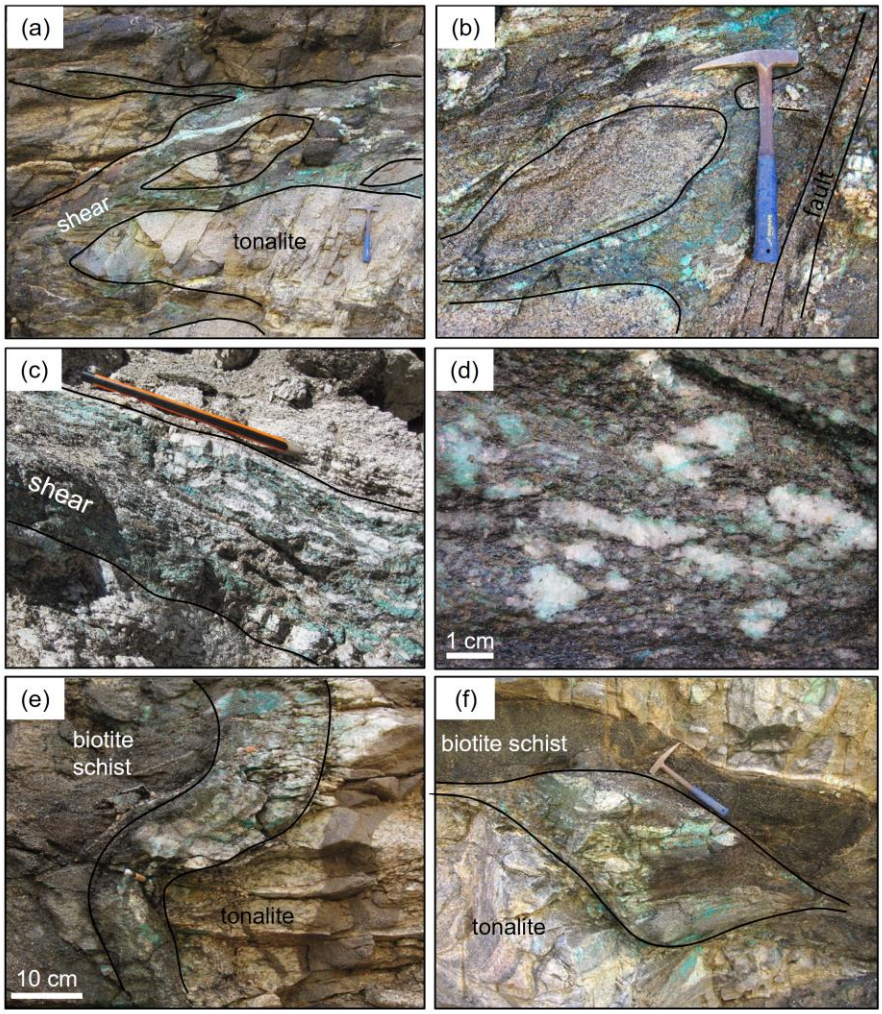

Fig. 3 Photographs of the main types of high-grade mineralization described in the Palm Pit at Omitiomire. **a** Mineralized biotite-epidote-quartz shears in biotite-epidote schist. Note rafts of tonalite enveloped by the shear zones. **b** Close-up of shears and tonalite rafts. **c** Mineralized quartz-biotite-epidote shear containing dismembered and boudinaged quartz veins and vein relics. **d** Close-up of shear zone showing patch-like stretched relics of milky quartz in a matrix of biotite, epidote, quartz, and malachite. **e** Steeply dipping folded, laminated quartz vein along the contact between biotite schist and tonalite. The vein selvedge is made up of biotite, epidote, and malachite. **f** Large quartz-biotite-epidote-malachite pod in a strain shadow at the contact between biotite schist and tonalite

in the southern sampling pit where amphibolite and tonalite formed an original intrusive breccia (Kitt et al. 2016). In the deposit-scale model, these small, isolated mafic units in the wall rocks were grouped together with the felsic gneisses (Fig. 4b).

For the assay model, some 80,139 Cu assays from 1 m sampling intervals from drill holes were processed and isotropic grade shells with cut-off grades of 0.1, 0.25, and 0.5 wt% Cu were created (Fig. 4c, d). A structural trend was created from structural data generated from downhole photography of drill holes and applied to the model. For descriptive purposes, the model was divided into northern, central, and southern domains.

3D model of the OSZ host rocks

The lithological model shows a central, gently undulating, shallowly east-dipping sequence dominated by biotite-epidote schists and amphibole-biotite gneisses (Figs. 4b and 5). This central unit is enveloped by mainly quartzo-feldspathic gneisses with only minor lenticular pods of biotite schist, amphibole gneiss, and/or interlayered banded mafic and felsic gneisses. Tight to isoclinal folds (F2) affected the interlayered gneisses and result in the large-scale transposition of structures and fabrics. Mylonitic fabrics are common, particularly in mafic schists and along lithological contacts between felsic gneisses and mafic schists. On a deposit scale, the 3D model indicates the presence of several tens of meters-thick lenses that pinch and swell and coalesce to form a large up to 100 m thick sequence of dominantly mafic gneisses and schists (Fig. 5). Individual mafic lenses are separated by sheet-like tonalitic gneisses and/or interlayered mafic-felsic gneisses and schists that vary in thickness from a few meters to several tens of meters. This central mafic unit is contained in the regional S2 fabric, evident from structural data generated from downhole photography and surface mapping (Figs. 2 and 5). It shows easterly dips, but with gentle undulations from moderately east dips (30°) in the northern domain, to shallowly east (15°) in the central domain, to

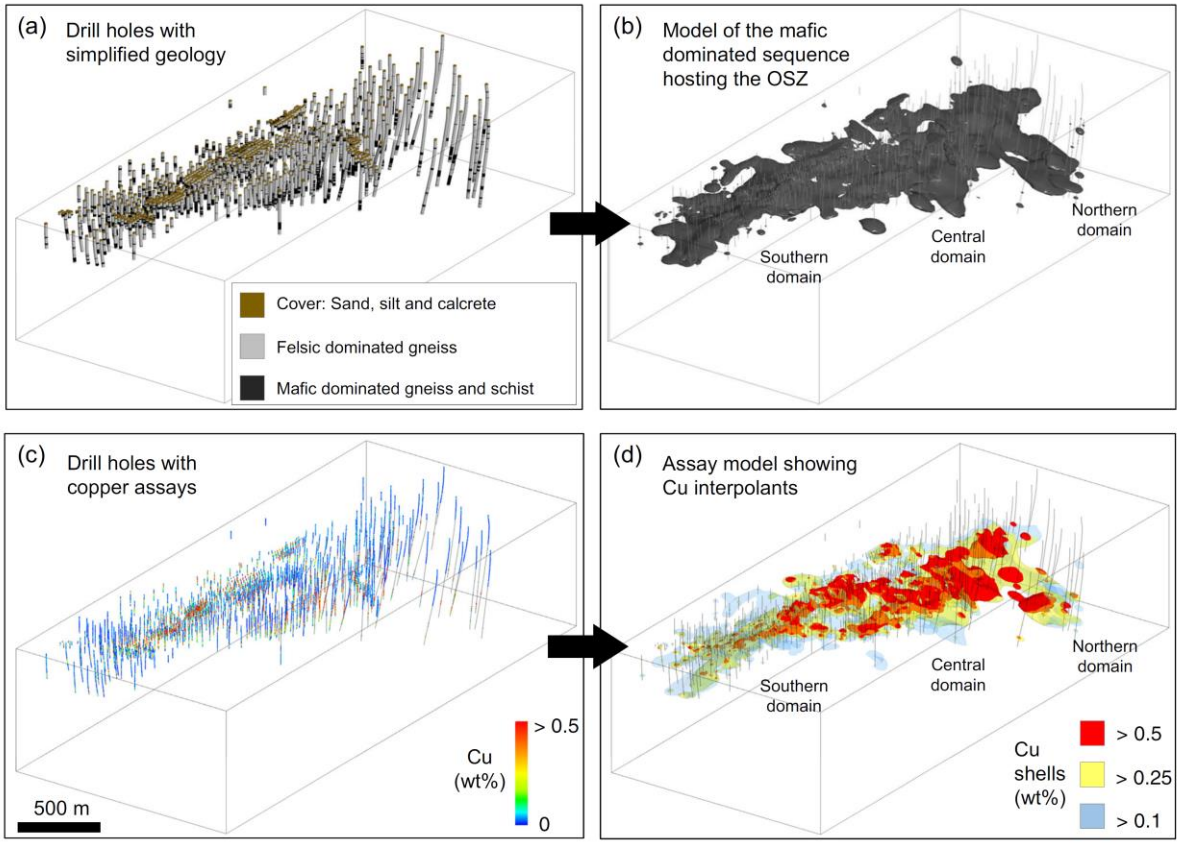

Fig. 4 Simplified workflow for the 3D implicit modeling of the Omitiomire deposit. **a** Geological drill hole logging data, simplified with the interval selection tool in Leapfrog Geo. **b** Lithological model (with structural trend applied) of the mafic gneiss and schist-dominated sequence that host the Omitiomire deposit. **c** Drill hole traces showing Cu assays at 1 m sampling intervals. **d** Assay model showing Cu > 0.5 wt%, Cu > 0.25 wt%, and Cu > 0.1 wt% interpolants with structural trend applied. The plunge and azimuth of the view direction is 25° and 325°

subhorizontal and shallowly (20°) westerly dips in the southern domain (Fig. 5). These variations describe an open arcuate geometry.

3D model of Cu assays

Potentially economic-grade (>0.25 wt% Cu) mineralization is confined to a gently undulating, overall tabular, arcuate zone that dips between 20° and 30° to the east. The overall deposit-scale geometry of the orebody resembles an asymmetric upward-curved lens with a long axis that strikes for more than 4 km in a north-south direction (Fig. 6a–c). The deepest part of the deposit occurs in the northern domain where the mineralization continues beyond 600 m below surface (Figs. 5 and 6b). Although largely covered by sand, silt, and calcrete, the orebody is at the surface in the western parts of the central domain (Fig. 6c). In the southern domain, the orebody is characterized by westerly and ESE dips and by a shallow plunge to the south (Fig. 6c). Both the down-dip and strike extent of the mineralization remain open. Current information suggests that there are no obvious late faults or major structural breaks that offset the mineralization.

Internal architecture and controls of high-grade ore shoots

The highest Cu grades generally occur in the upper parts of the main mineralized envelope along the hanging wall (HW) contact with the overlying felsic-dominated HW gneiss. The high-grade ore envelope is defined by >0.5 wt% Cu that forms a distinct lens-like shoot, composed of an up to 100 m thick central part based on current drill hole information (Fig. 6). The high-grade ore envelope also delineates zones of thickened high-grade mineralization that define two distinctly linear north-south trending ore shoots, here referred to as OS1 and OS2 (Fig. 6a–c). The gently undulating ore shoots are characterized by north-south to NNE strikes and shallow plunges to the north and south, parallel to the regional stretching lineation (L2). In cross section, both shoots have typical stacked

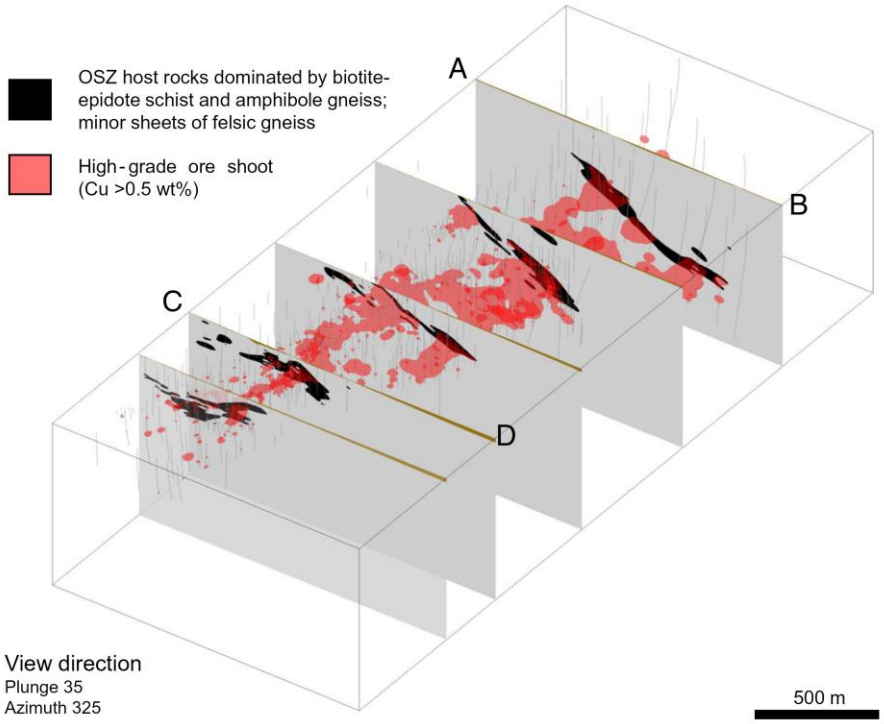

Fig. 5 Serial cross sections through the deposit showing the simplified lithological model and unsliced high-grade mineralized shell (Cu > 0.5 wt%). The locations of sections **A**, **B** and **C**, **D** presented in ESM 3 are shown

lens geometries and an associated thickening of the mafic-dominated host rock sequence (ESM 3). Copper mineralization correlates with intercepts of biotite-epidote schist, with the highest Cu grades closely associated with the contacts of larger mafic schist packages against quartzo-feldspathic gneisses or within intercalated schist-gneiss packages (ESM 3 and Fig. 7). This is the case not only for individual schist intersections but also for the ore lens as a whole. High-grade shoots are directly related to the occurrence of biotite-epidote-quartz shear bands and centimeter-scale quartz veins with mineralized selvedges in biotite-epidote schists (Fig. 7). Individual veins and shear bands are only 1–10 cm wide, but form part of a wider system of anastomosing mineralized shears where individual shears are tightly spaced. The shears and veins developed along the contacts of biotite-epidote schists against the felsic gneisses and high-grade ore shoots are directly related to an increase in the frequency of contact-parallel shears and veins (Fig. 7). This underlines the combined effects of the structural and lithological controls on Cu mineralization at Omitiomire (Kitt et al. 2016).

Hydrothermal alteration and mass balance

Petrography

The progressive replacement of original hornblende-plagioclase assemblages by hornblende-biotite and biotite-epidote assemblages in schists from within the OSZ suggests variable hydration and retrogression of original amphibolites during deformation and accompanying fluid flow (Steven et al. 2000; Kitt et al. 2016; Fig. 8).

Unaltered and unretrogressed amphibolites of the original wall rock sequence are dominated by hornblende and plagioclase that constitute up to 80 vol% of the rock. Quartz (<10 vol%), biotite (<5 vol%), titanite, rutile, ilmenite, and garnet occur in variable amounts, but rarely exceed more than a few percent. Compositional variations are indicated by different relative abundances of hornblende and plagioclase, distinguishing more melanocratic from relatively leucocratic varieties. Texturally, the amphibolites are granoblastic, massive to foliated or, more commonly, lineated, marked by the preferred alignment of aggregates of hornblende and plagioclase.

The hornblende-biotite gneisses are characterized by relics of hornblende that are progressively replaced and enveloped by S2-parallel aggregates of biotite that can constitute up to 30 vol% of the gneisses. Biotite is associated with small epidote porphyroblasts and minor amounts of disseminated chalcocite.

Biotite-epidote schists result from the near-complete replacement of original amphibolite and are made up of >50 vol% biotite, >15 vol% epidote, 10–20 vol% quartz and plagioclase, 5–10 vol% hornblende, 1–5 vol% chalcocite, and minor amounts of titanite, chlorite, apatite, and rutile. The biotite occurs as sheet-like aggregates that are wrapped around large porphyroblasts of epidote and relic hornblende/plagioclase, thus forming a strong anastomosing S2 fabric.

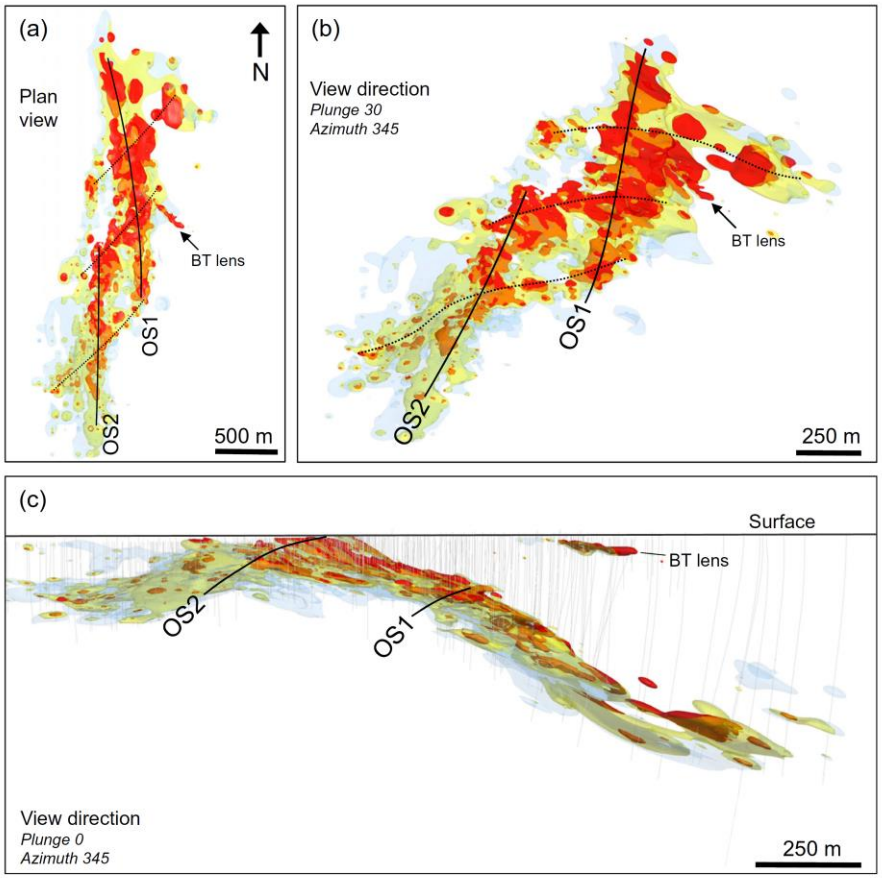

Fig. 6 Assay model of the deposit. High-grade (Cu > 0.5 wt%) shoots are in *red*, surrounded by lower grade Cu > 0.25 wt% in *yellow* and Cu > 0.1 wt% in *light blue*. **a** Plan view showing the north-south trend of high-grade shoots OS1 and OS2 and interpreted subordinate NE mineralized trends. **b** Oblique view to the NE, showing the high-grade shoots OS1 and OS2 and interpreted subordinate NE mineralized trends. **c** Unsliced cross section with view to the NE illustrating the upward convex lens shape of the orebody. The location of high-grade ore shoots OS1 and OS2 along the L2/S2 fabric and the disconnected BT lens in the hanging wall are shown

Mass balance

Chemical variations (e.g., enrichments and depletions) and volume change related to fluid/rock interaction during deformation and hydrothermal alteration can be quantitatively estimated by applying the isocon method (Grant 1986) to the bulk geochemistry of variably altered and unaltered samples. This approach is based on the theory of Gresens (1967) and has since been widely applied to studies of element mobility in shear zones (O'Hara 1988; Goddard and Evans 1995; Hippertt 1998; Streit and Cox 1998; Zulauf et al. 1999; Rolland et al. 2003; Barnes et al. 2004) and hydrothermal ore deposits (Gregory 2006; Fisher et al. 2013; Oliver et al. 2015).

Results

Element mobility

The whole rock XRF and ICP data of variably altered and mineralized drill core samples from the Omitiomire deposit were plotted against those of an unaltered sample collected some 7 km away from the deposit in order to compare the elemental gains and losses during alteration and mineralization (Fig. 9 and table in ESM 4). The altered samples include hornblende-plagioclase gneiss and biotite-epidote-chalcocite schist from high-grade shear zones in the deposit (Fig. 8). The element concentrations of the sample types were averaged and arbitrarily scaled for visualization purposes before plotting. Only elements deemed most important during the retrogression of amphibolite to biotite-epidote schist, as described above, are presented. Where possible, the isocon line has been chosen based on the linear correlation of as many elements as possible. Attempts were made to include immobile elements such as Al and Ti. However, some of the supposedly immobile elements were evidently slightly mobile during alteration and mineralization in some of the samples.

Figure 9a shows the average of analytical data from two weakly altered hornblende-plagioclase gneiss samples from the OSZ plotted against the average of two regional and unaltered amphibolite samples. Although none of the conventional

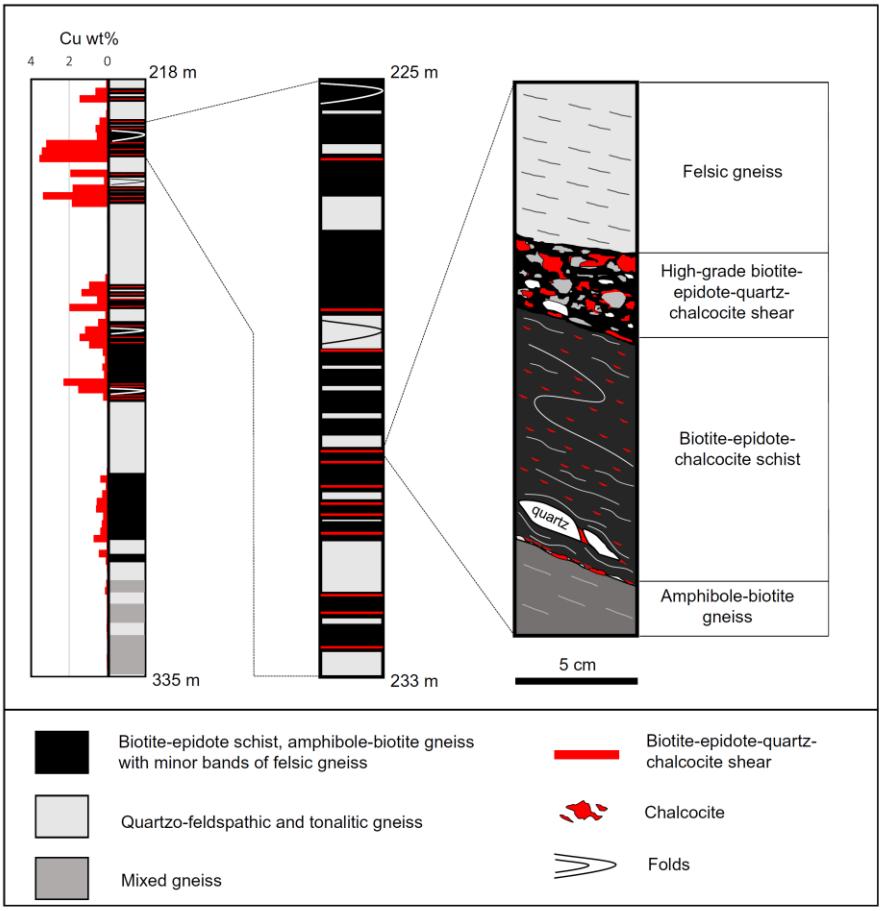

Fig. 7 Simplified geological log of drill core from a hole that intercepted the north-south trending high-grade shoot OS1 in the northern domain (sections A-B) of the Omitiomire deposit (Fig. 5 and ESM 3). The figure illustrates the association of high-grade Cu mineralization with the intercepts of centimeter-scale quartz-biotite-epidote-chalcocite shears and veins (in *red*) in units of biotite-epidote schist and amphibole gneiss (in *black*) close to the contacts with felsic gneisses. In the figure, OS1 is composed of an upper and lower lens of high-grade mineralization that is hosted by several closely spaced sheets of biotite-epidote schist and separated by a large 10 m thick lens of tonalitic gneiss. The upper lens is about 20 m thick and contained in 1–5 m thick sheets of biotite-epidote schist. The lower lens is about 22 m thick and hosted by sheets of biotite-epidote schist that vary in thickness from 1 to 12 m. In the upper lens, more than 12 high-grade biotite-epidote-quartz shears and veins were counted over a distance of 8 m, and up to 10 shears and veins over 22 m in the lower lens. On a deposit scale, high-grade shoots are directly related to the occurrence and cumulative thickness of the thin, mineralized shears and veins

immobile elements plot directly on a straight line, a best fit isocon can be fitted through Ti and Al. Elements such as Ce, Fe, and Zr also plot close to the isocon, which may suggest limited mobility. For this case, the isocon diagram indicates a depletion of CaO, MgO, and Zn and a slight enrichment in K_2O, Rb, Th, P_2O_5, Pb, and Cu.

Figure 9b plots the average analytical compositions from two mineralized biotite-epidote schists from high-grade shear zones in the OSZ against the average of the unaltered amphibolite samples. Although the diagram shows a much larger scatter of elements, an isocon was again selected based on a line of best fit through Al and Ti. The isocon diagram indicates a significant depletion of Na_2O, CaO, and to some extent MgO. In contrast, K_2O, Cu, Cr, Rb, S, and, to a lesser extent, Th, U, Pb, Ni, Fe, and Zn are markedly enriched in the schist relative to the country rocks.

Stable isotope compositions

Samples and analytical methods

Stable O- and H-isotope compositions of mineral separates from amphibole gneisses, biotite-epidote schists, and associated quartz veins in the deposit were used to constrain the likely fluid sources, fluid/rock ratios, and the conditions

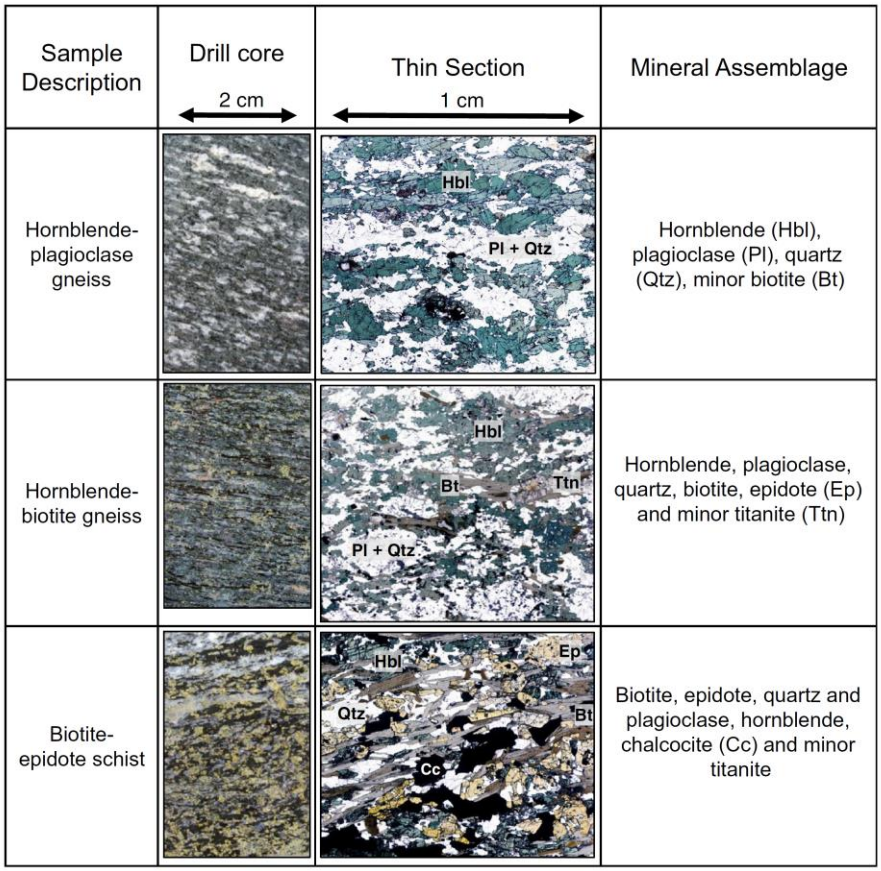

Fig. 8 Drill core photos and photomicrographs showing the main mineral assemblages associated with the progressive replacement of original hornblende-plagioclase assemblages by hornblende-biotite and biotite-epidote paragenesis in the Omitiomire Shear Zone

during deformation and Cu mineralization in the mineralized OSZ.

The oxygen isotope compositions (^{16}O, ^{18}O) were measured at the University of Lausanne, using a method similar to that first described by Sharp (1990) and in more detail in Vennemann et al. (2001). Between 0.5 and 2 mg of sample was loaded onto a small Pt-sample holder and pumped out to a vacuum of about 10^{-6} mbar. After pre-flourination of the sample chamber overnight, the samples were heated with a CO_2 laser in 50 mbar of pure F_2. Excess F_2 was separated from the O_2 produced by conversion to Cl_2 using KCl held at 150 °C. The extracted O_2 was collected on a molecular sieve (13X) and subsequently expanded into the inlet of a Thermo-Finnigan MAT 253 isotope ratio mass spectrometer. Oxygen isotope compositions are given in the standard δ-notation, expressed relative to VSMOW in per mill (‰). Replicate oxygen isotope analyses of the standard used (NBS-28 quartz; n = 12) has an average precision of ±0.1 ‰ for $\delta^{18}O$. The accuracy of $\delta^{18}O$ values is better than 0.2 ‰ compared to accepted $\delta^{18}O$ values for NBS-28 of 9.64 ‰.

Measurements of the hydrogen isotope compositions of minerals were made using high-temperature (1450 °C) reduction methods with He-carrier gas and a TC-EA linked to a Delta Plus XL mass spectrometer (Thermo-Finnigan) on 2 to 4 mg-sized samples according to a method adapted from Sharp et al. (2001) and described in more detail in Bauer and Vennemann (2014). The results are given in the standard δ-notation, expressed relative to VSMOW in per mill (‰). The precision of the in-house kaolinite and G1 biotite standards for hydrogen isotope analyses was better than 2 ‰ for the method used; all values were normalized using a value of −125 ‰ for the kaolinite standard and −65 ‰ for NBS-30.

The S-isotope compositions were measured in the Stable Isotope Laboratory of the University of Lausanne using a Carlo Erba (CE 1100) Elemental Analyzer linked to a ThermoFisher Delta V mass spectrometer. Samples were reacted at 1050 °C in a stream of He-carrier gas spiked with oxygen gas. The isotopic composition is expressed in the conventional δ-notation ($\delta^{34}S$) relative to V-CDT in parts per thousand (per mill). External reproducibility of standards and samples (all analyzed twice) is better than 0.15 ‰ and samples were calibrated against IAEA standards S1 and S3 (Ag_2S) and NBS-127 (ZnS) with accepted values of −0.3, −32.1, and 20.3 ‰, respectively.

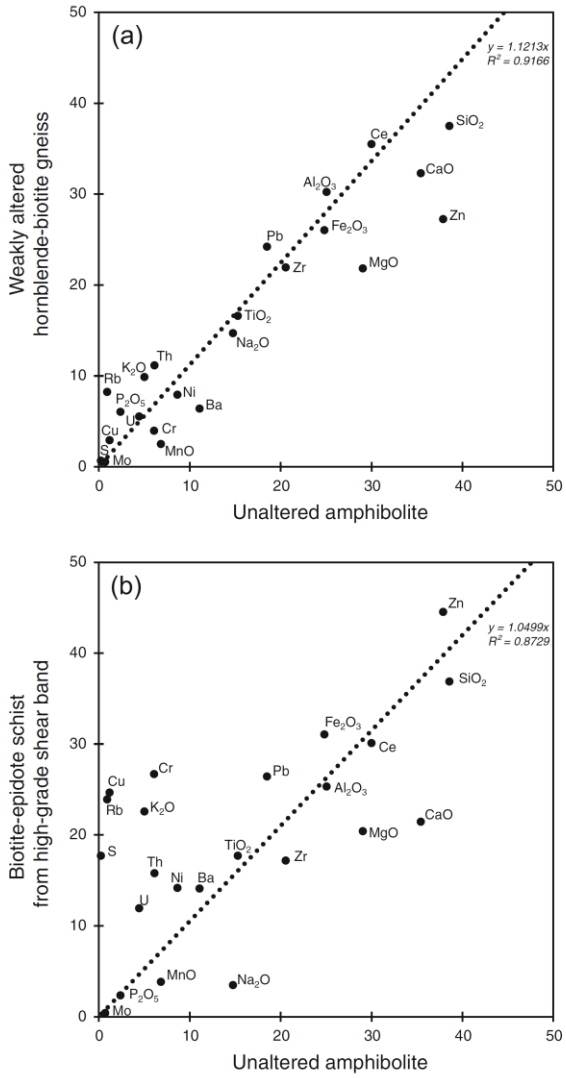

Fig. 9 Isocon diagrams of average element concentrations in unaltered amphibolite plotted against **a** weakly altered hornblende-biotite gneisses and **b** biotite-epidote schists from high-grade shear bands in the Omitiomire deposit. The isocon is defined by the linear correlation and relative immobility of TiO_2 and Al_2O_3. Elements that plot above the isocon were gained; elements below were depleted. The data was scaled for visualization purposes

Results

Oxygen isotope compositions

All stable isotope compositions are reported in a table in ESM 5. Quartz separates from quartz veins as well as separates from biotite-epidote-chalcocite schists have $\delta^{18}O$ values between 9.3 and 10.1 ‰. Similarly, the oxygen isotopic composition of quartz from amphibole-biotite gneisses and thin biotite-rich layers in banded felsic gneisses have values between 8.9 to 9.8 and 8.9 to 9.9 ‰, respectively. The $\delta^{18}O$ values of epidote and biotite from amphibole-biotite gneisses and biotite-epidote schists have a range between 5.2 and 6.4 and 3.2 and 5.0 ‰, respectively. Amphibole separates from partially retrogressed amphibole-biotite gneisses and schists have $\delta^{18}O$ values between 4.1 and 6.1 ‰. The mean value of $\delta^{18}O_{amp}$ in the gneisses is 5.8 ‰, somewhat higher than the mean of 4.6 ‰ of $\delta^{18}O_{amp}$ in the schists. The $\delta^{18}O$ values of feldspar from ore zone schists and gneisses are 9.8 and 7.5 ‰, respectively, while single chlorite and fuchsite separates have $\delta^{18}O$ values of 5.3 and 6.5 ‰. Hence, all minerals have similar ranges in their $\delta^{18}O$ values of about 1.2 to 2 ‰. This range is similar to the range in values measured for a sequence of whole rocks associated to the mineralization at Omitiomire (between 6 and 7.8 ‰). Furthermore, the coexisting minerals are arranged in an order of increasing $\delta^{18}O$ values from biotite, to epidote, amphibole, and quartz, as would be predicted from the theory of stable isotope fractionation between minerals (e.g., Hoefs 2009). Apparent temperatures of equilibration calculated for quartz-biotite and also quartz-amphibole O-isotope fractionations (based on fractionation factors after Bottinga and Javoy (1975) and/or theoretical fractionation factors based on Zheng (1995)) also have a small range of between 490 to 620 and 520 to 660 °C, respectively (ESM 5), values that are consistent with the regional grade of metamorphism (Kasch 1987).

Hydrogen isotope compositions

Hydrogen isotope compositions of hydrous minerals from the mineralized biotite-epidote schists and amphibole-biotite gneisses have a range of δD values between −48 and −82 ‰ (ESM 5). The δD values for biotite in all samples are between −58 and −82 ‰ and for amphibole between −66 and −79 ‰. Biotite-epidote schists (−58 to −70 ‰) have somewhat lower δD_{bt} values compared to the amphibole gneisses (−68 to −82 ‰) and felsic gneisses (−62 to −80 ‰), but the range in values does overlap to a large extent. Single fuchsite and chlorite separates have δD values of −48 and −60 ‰, respectively.

Sulfur isotope compositions

Only chalcocite separated from veins, whole rocks, and contact zones between different rock types was analyzed for its sulfur isotope composition (ESM 6). The values are remarkably homogeneous, irrespective of the location of the chalcocite (vein, pegmatite, whole rock matrix, contact zone), with an average of −5.4 ‰ (±0.45 ‰ at 1σ; n = 13).

Discussion

Fluid flow and development of the OSZ

The controls and petrographic characteristics of the Omitiomire Cu mineralization have recently been described by Kitt et al. (2016). In that study, it was established that Cu mineralization and fluid flow were structurally controlled and related to Pan-African, D2 deformation. The Pan-African timing of deformation is also indicated by U-Pb titanite ages of 520–485 Ma in the mineralized biotite-epidote schist (Steven et al. 2000; Maiden et al. 2013). Fluid flow was controlled by transient fracture permeability particularly along lithological contacts between original amphibolite and tonalite within and along the late Mesoproterozoic (ca. 1100–1060 Ma) intrusive breccia in gneisses of the Ekuja Dome. Initial veining and fluid flow were confined to the marginal zones of competent amphibolite xenoliths. The progressive retrogression of the rocks, notably of the mafic lithologies to biotite-dominated schists led to further strain localization, particularly along biotite-epidote schists that have formed along contacts between mafic xenoliths and quartzo-feldspathic gneisses (Kitt et al. 2016). This reaction softening accounts for the spatial relationship between mylonitic and highly transposed fabrics of the central OSZ system localized around the originally heterogeneous intrusive breccia (Kitt et al. 2016).

These detailed controls of fluid flow and mineralization find their manifestation in the deposit-scale controls of Cu mineralization and ore shoots. The detailed logging and sampling combined with the deposit-scale modeling indicates that potentially economic-grade Cu mineralization is not necessarily associated with thick intersections of relatively massive mafic rocks in the OSZ. Instead, the highest Cu grades are developed in intervals of closely interlayered mafic schist and felsic gneiss units and particularly along the upper contacts of schist units against gneisses. High Cu grades are commonly confined to narrow, contact-parallel shears along contacts between mafic units against surrounding gneisses (Fig. 7). The actual thickness of high-grade lenses or shoots is determined by the number and cumulative thickness of the thin, mineralized shear zones. This underlines the role of original wall rock heterogeneity for the structurally controlled fluid flow and mineralization. The distribution of wall rock heterogeneities and, thus, the occurrence of high-grade lenses and shoots are determined by the interaction and superimposition of the original geometry and extent of the late Mesoproterozoic intrusive breccia, and later Pan-African strains (D2), recorded by transposition folding, the duplication, and also attenuation of mafic units (Fig. 10). The strain localization into the central mafic schist unit is likely to have modified the original geometry of the intrusive breccia and original intrusive relationships. Notably, the ore shoots trend north-south, parallel to the regional stretch (L2) and are contained within the undulating high-strain S2 foliation (Fig. 6). This implies that the geometry and orientation of ore shoots or lenses in the OSZ and at higher finite strains are determined by D2 strains. The development of the OSZ as a regionally significant shear zone system able to channel regional-scale fluid flow probably hinged on the presence and distribution of closely spaced, albeit irregularly distributed mafic xenoliths in the central parts of the intrusive breccia. This may explain the lack of mineralization in isolated mafic xenoliths outside the central OSZ, mainly located in the hanging wall of the anastomosing shear zone and, thus, bypassed by the main fluid plumbing system. A localized mineralized lens (BT lens in Fig. 6c) in the HW of the main mineralization may represent the incipient case of shear zone formation. In this case, a cluster of mafic rocks resulted in strain localization and localized shearing, but without developing into a laterally more extensive shear zone system. This highlights the potentially very patchy geometry of the mineralization for the broader Ekuja Dome that reflects the combined effects of the original late Mesoproterozoic (about 1100 Ma) geometry of the intrusive breccia between amphibolite and tonalitic gneisses, overprinted and modified by later Pan-African strains that determined fluid flow in the shear zone system (Fig. 10).

Mass transfer during fluid flow

Petrographic studies and the chemical analysis of variably retrogressed samples from the OSZ provide a record of the chemical exchange that took place during deformation and fluid flow. The isocon method used here is not without problems since typically immobile elements have evidently been mobile, so that the mass balance diagrams may indicate trends of element mobility, but absolute values of element mobility have to be viewed with caution.

The mass balance diagrams document that the hydration of amphibolites to biotite-epidote schists in the OSZ is consistently associated with significant increases in Cu, Cr, Rb, S, and K_2O (Fig. 9). The increased K_2O and Rb contents during alteration and mineralization are reflected by the formation of biotite in biotite-epidote schists that host the mineralization (Fig. 8). Significant enrichments in Cr correlate with the Cu mineralization and Cr-epidote in the biotite-epidote alteration assemblage and, to a lesser extent, Cr-rich magnetite (Steven et al. 2000). The enrichment of the mineralized parts of the OSZ in Cr clearly points to the solubility of Cr in the mineralizing fluid. A potential source for Cr may be found in the alteration of originally ultramafic rocks to serpentinites that occur in abundance as structurally interleaved slivers at the top of the Ekuja Dome and with the structurally overlying Kuiseb Formation metaturbidites (ESM 1). The structurally imbricated serpentinite bodies underline the position of the

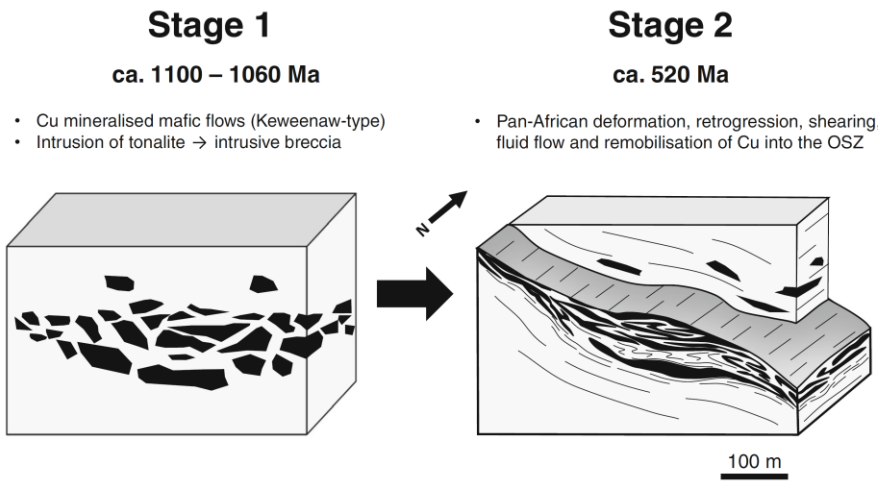

Fig. 10 Conceptual model illustrating the main stages for the development of the Omitiomire Cu deposit. *Stage 1* Late Mesoproterozoic (ca. 1100 Ma) basaltic rocks (originally lava flows) with Cu mineralization (Keweenaw-type) were intruded by voluminous tonalitic magma (ca. 1060 Ma) to form an intrusive breccia consisting of xenoliths of basalt in the tonalite. *Stage 2* Pan-African (ca. 520 Ma) deformation and hydration resulted in the retrogression of amphibolites to biotite-epidote schists, strain localization, fluid flow, and remobilization of Cu into mylonitic shear zones that formed in the schists. The highest grades are associated with quartz-biotite-epidote veins and shears in biotite-epidote schists close to the contacts with felsic gneisses. The highest density of veins and shears commonly developed along the hanging wall contact with the tonalitic gneisses

Ekuja Dome at the base of the SZ accretionary prism and close to, or within, the subduction channel of the Pan-African subduction zone. The depletion in CaO, Na_2O, and MgO most likely reflects the breakdown of plagioclase and hornblende from original amphibolite during alteration and retrogression to biotite-epidote schist (Fig. 8). The pervasive biotite alteration in mafic units is reflected in the increase in K_2O recorded throughout the mineralized parts of the OSZ. The immediately surrounding tonalitic gneisses or amphibolites of the Ekuja Dome are unlikely sources for the K_2O. However, the thick, quartz-biotite schist-dominated sequence of the Kuiseb Formation surrounding the Ekuja Dome seems a more likely source of K_2O and possibly water during retrogression and fluid flow under upper greenschist to mid-amphibolite conditions. This would again point to the external source of the fluids, derived from surrounding rocks of the accretionary prism and, indeed, a subduction channel.

Constraints on the conditions and origin of ore fluids

The retrogression of amphibolites in the OSZ points to post-peak metamorphic conditions of fluid flow. While syn-deformational (D2) biotite-epidote assemblages are dominant, late-stage chlorite replacing biotite occurs in minor amounts. This emphasizes the retrogression of initially upper and middle amphibolite-facies mineral assemblages to progressively lower amphibolite- and upper greenschist-facies assemblages in the OSZ and reflects deformation during the exhumation of the rocks (Kitt et al. 2016). This agrees with the crystal-plastic deformation and dynamic recrystallization of gneisses and mylonitization in the OSZ that points to temperature conditions of at least 450–500 °C (Passchier and Trouw 2005). The O-isotope fractionations, given not only the empirical calibration of Bottinga and Javoy (1975) but also the theoretical fractionations of Zheng (1995), provide temperatures for the quartz-biotite, quartz-feldspar, and quartz-amphibole pairs that are clearly compatible with upper greenschist- to middle amphibolite-facies conditions (temperatures of 500 to 650 °C) (ESM 5). The results show that the mineral pairs are in apparent equilibrium at these temperatures, but with quartz-biotite temperatures that are marginally lower than those for quartz-amphibole pairs. While quartz cannot be in equilibrium with both biotite and amphibole at different temperatures, the given temperatures may still approximate apparent formation temperatures as quartz is a dominant oxygen-bearing phase within the rocks. Moreover, the hydration fluid may well have been buffered by the rocks, and/or was relatively small in amount, hence close to equilibrium with the constituent minerals within the rocks. As such, no large changes in isotopic composition are to be expected as indicated by the absence of mineral-mineral reversals in terms of their order of ^{18}O enrichment, that is

$\delta^{18}O_{qtz} > \delta^{18}O_{plag} > \delta^{18}O_{ep} > \delta^{18}O_{amp} > \delta^{18}O_{bt}$. This underlines that there was not a pervasive throughput of large volumes of externally derived fluids in the OSZ. Instead, the rather low fluid/rock ratio points to the possible local redistribution of original Cu mineralization. In fact, Steven et al. (2000) suggested only local redistribution and concentration

of Cu mineralization from an initially late Mesoproterozoic (ca. 1100 Ma) Keweenaw-type mineralization, in which the originally basaltic flows and flow-top breccias were mineralized during later Pan-African tectonism and fluid flow. This notion of an original and subsequently remobilized Cu mineralization is supported by elevated Cu values of >1500 ppm in pristine and unretrogressed regional amphibolite from the farm Barreshagen. A primary introduction of Cu mineralization during original seafloor hydrothermal alteration of a mafic volcanic sequence can also not be excluded. In fact, the somewhat elevated $\delta^{18}O$ values of the mafic rocks (amphibolites), but good mineral-mineral equilibrium within these metamorphosed equivalents is typical of a closed-system metamorphism of seawater hydrothermally altered rocks (e.g., Putlitz et al. 2000).

The above is also compatible with the hydrogen isotope compositions of the minerals analyzed (biotite and amphibole), which also do not show any "reversals" in terms of their relative D enrichments and their range in values is typical of metamorphic-magmatic rocks. This is illustrated in the table in ESM 5, which indicates the range of calculated H- and O-isotopic compositions of waters in equilibrium with the minerals at the temperatures of equilibration (500 to 600 °C).

The homogeneous $\delta^{34}S$ values of the chalcocite in veins, pegmatites, whole rocks (retrogressed amphibolites), and in massive ore zones between different lithotypes (ESM 6) are also compatible with a local redistribution of sulfur during metamorphism. Comparisons with other studies on metamorphosed ore deposits, such as volcanic massive sulfide deposits or even Kuroko-style mineralization, indicates that the S-isotope compositions of precursor ore mineralization is often preserved in terms of average bulk values for the sulfides (e.g., Ohmoto 1986; Large 1992). However, in contrast to typical metamorphosed volcanic massive sulfide (VMS) deposits that generally have a range in $\delta^{34}S$ values of between 0 and 10 ‰, the range in $\delta^{34}S$ values measured for Omitiomire is rather low at −4.7 to −6.1 ‰, averaging −5.4 ‰. For both the VMS deposits as well as Kuroko-style deposits, the range in $\delta^{34}S$ values is argued to be related to a complex interaction of magmatic sulfur-bearing solutions with seawater sulfate, but where the seawater is the minor constituent (e.g., Ohmoto et al. 1983; Ohmoto 1986; Large 1992). Given the large range of seawater sulfate $\delta^{34}S$ values over geologic time, the actual range in $\delta^{34}S$ values for different VMS deposits is also quite large and correlates with that of the seawater sulfate for the period of mineralization (Large 1992). In fact, some VMS deposits have $\delta^{34}S$ values that extend down to an average of −5 ‰ (e.g., Mt. Chalmers in Large 1992). In other cases, homogeneous $\delta^{34}S$ values with negative values, such as measured for Omitiomire, have been noted for magmatic intrusive rocks, notably the Bushveld Igneous Complex (Liebenberg 1970), the Keweenawan Cu deposits (e.g., Donoghue et al. 2014), but also in the case of the oxide zone ores in Kuroko deposits (Ohmoto 1986). In all such cases, an interaction with sediments and sedimentary sulfur sources, often of biogenic or diagenetic origin, are considered as explanations for the range extending towards negative $\delta^{34}S$ values. Such interactions are clearly possible for the case of Omitiomire, where the relationship of chalcocite mineralization with epidote-biotite mineralization and the parallel enrichment in K hint at metamorphic fluids that may have been derived from the regionally metamorphosed sedimentary rocks of the Kuiseb Formation and have interacted with a pre-existing sulfide mineralization of likely magmatic origin.

Regional correlations

Basement gneiss complexes in the SZ of the Damara Belt show remarkable similarities with Palaeo- to late Mesoproterozoic basement complexes in the Domes Region of the Lufilian Arc of Zambia, both in terms of their geochronology and tectonostratigraphic position, as well as the structural and metamorphic evolution (Unrug 1983; Kampunzu and Cailteux 1999; Porada and Berhorst 2000; Rainaud et al. 2005; Lehmann et al. 2015). With the discovery of major new Cu deposits in recent years, the Domes Region has become an important Cu district in Zambia, accounting for up to 10% of Cu resources in the Central African Copperbelt (Sillitoe et al. 2015). Unlike the world-class low metamorphic grade sedimentary-hosted stratiform deposits that characterize the Central African Copperbelt, Cu mineralization in the Domes Region is associated with high-grade, amphibolite-facies, basement inliers (Benham et al. 1976; Cosi et al. 1992 Bernau et al. 2013). Most recently, several studies on Cu mineralization in the Mwombezhi Dome, Western Zambian Copperbelt, have focused on the geology and geochemistry (Bernau et al. 2013), geochronology (Sillitoe et al. 2015; Turlin et al. 2016), and petrography and microstructure (Turlin et al. 2016). These studies emphasize that the Cu mineralization occurred through the remobilization of an older (Palaeo- to late Mesoproterozoic) precursor mineralization episode that was focused into high-grade metamorphic, Pan-African (530–510 Ma) shear zones in and along granite-gneiss hosted basement sequences. Both the timing and the constrictional-type shear zones associated with Cu mineralization in the Mwombezhi Dome are remarkably similar to the high-strain zones described from the OSZ in the Ekuja Dome (Bernau et al. 2013; Kitt et al. 2016). These similarities and the likely continuation of tectonostratigraphic zones from the Damara Belt through northern Botswana to the Lufilian Arc suggest a close correlation between the development of the Omitiomire deposit and the Cu deposits in the Domes Region of

Zambia, pointing to a much larger regional extent of this Cu province (Kitt et al. 2016).

Conclusions

Cu mineralization of the Omitiomire deposit in the Southern Zone of the Pan-African Damara Belt is the result of a multi-stage evolution involving two main mineralizing events, one in the late Mesoproterozic and one during the Pan-African. Early-stage mineralization is related to the emplacement of Cu-mineralized basaltic flows at ca. 1100 Ma. These basaltic flows were probably similar to Keweenaw-type basalts. Brecciation and dismemberment of the basaltic rocks occurred as a result of the later (ca. 1060 Ma) intrusion of mainly tonalitic melt into the previously formed basalt (stage 1 in Fig. 10). The subsequent Pan-African tectonism and subduction of the Kalahari Craton (580–520 Ma) led to the initial burial of the rocks and amphibolite-facies metamorphism of the original basalts and intrusive tonalites, but earlier intrusive contacts and the breccia-like textures between amphibolite and gneiss are still discernible in low-strain domains of the Ekuja Dome. The late-stage exhumation of the dome was associated with the expulsion of the Ekuja Dome at the base of the Southern Zone prism during northward-directed subduction. Exhumation was localized along discrete shear zones. Associated fluid flow, retrogression to middle amphibolite- to upper greenschist-facies (ca. 650–500 °C) conditions and reaction softening of original amphibolites to biotite-epidote schists led to further strain localization centered around the heterogeneous amphibolite-gneiss breccia, eventually forming the Omitiomire Shear Zone system (stage 2 in Fig. 10). Despite this, fluid/rock ratios remained low, but deformation and fluid flow led to the local redistribution of Cu into the retrograde shear zones, particularly along lithological contacts. The progressive transposition, duplication, and stacking of Pan-African structures in the shear zone system resulted in the development of linear ore shoots parallel to the pervasive north-south Pan-African stretch. There are striking similarities in the timing and polyphase evolution of the mineralization, as well as structural controls and ore body geometries at Omitiomire compared to Cu deposits in the Domes Region of the Lufilian Arc. This may suggest the existence of a much larger contiguous Cu province, with important implications for exploration.

Acknowledgements We are grateful to International Base Metals Limited (IBML) and Craton Mining and Exploration (Pty) Ltd. for supporting this project. Hélène Raud is acknowledged for the work done during the sampling and the many tedious hours spent separating the minerals analyzed in the stable isotope laboratory, as is the assistance of Benita Putlitz for her help in guiding Hélène through the laboratory tasks. We acknowledge the technical staff at the ICP-MS and XRF analytical facilities (CAF) in Stellenbosch. Leapfrog Africa and ARANZ Geo (Pty) Ltd. is thanked for generously providing training and an academic license for the Leapfrog Geo 3D modeling software. We thank Karl Hartmann, Ken Maiden, Hartwig Frimmel, and Editor-in-chief Bernd Lehmann for providing constructive reviews that significantly improved the manuscript. This project relied on geological logging data from an extensive drill hole database and we acknowledge the work of the many geologists and sampling crews who worked at Omitiomire over the years, including the detailed logging done by Ken Hart.

References

Barnes JD, Selverstone J, Sharp ZD (2004) Interactions between serpentinite devolatilization, metasomatism and strike-slip strain localization during deep-crustal shearing in the Eastern Alps. J Metamorph Geol 22:283–300

Bauer K, Vennemann TW (2014) Analytical methods for the measurement of hydrogen isotope composition and water content in clay minerals by TC/EA. Chem Geol 363:229–240

Benham DG, Greig DD, Vink BW (1976) Copper occurrences of Mwombezhi Dome area, northwestern Zambia. Econ Geol 71: 433–442

Bernau R, Roberts S, Richards M, Nisbet B, Boyce AJ, Nowecki J (2013) The geology and geochemistry of the Lumwana Cu (±Co ± U) deposits, NW Zambia. Mineral Deposita 48:137–153

Borg G, Maiden KJ (1989) The middle Proterozoic Kalahari copper belt of Namibia and Botswana. In: Boyle RW, Brown AC, Jefferson CW, Jowett EC, Kirkham RV (eds) Sediment-hosted stratiform copper deposits, Geol Assoc Can Spec Paper, vol 36, pp 525–540

Bottinga Y, Javoy M (1975) Oxygen isotope partitioning among minerals in igneous and metamorphic rocks. Rev Geophys 13:401–418

Cailteux JLH, Kampunzu AB, Lerouge C, Kaputo AK, Milesi JP (2005) Genesis of sediment-hosted stratiform copper–cobalt deposits, central African Copperbelt. J Afr Earth Sci 42:134–158

Cosi M, de Bonis A, Gosso G, Hunziker J, Martinotti G, Moratto S, Robert JP, Ruhlman F (1992) Late Proterozoic thrust tectonics, high-pressure metamorphism and uranium mineralization in the domes area, Lufilian Arc, northwestern Zambia. Precamb Res 58: 215–240

Coward MP (1981) The junction between Pan-African mobile belts in Namibia: its structural history. Tectonophysics 76:59–73

Donoghue KL, Ripley EM, Li C (2014) Sulfur isotope and mineralogical studies of Ni-Cu sulfide mineralization in the bovine igneous complex intrusion, Baraga Basin, northern Michigan. Econ Geol 109: 325–341

Fisher LA, Cleverley JS, Pownceby M, MacRae C (2013) 3D representation of geochemical data, the corresponding alteration and associated REE mobility at the ranger uranium deposit, Northern Territory, Australia. Mineral Deposita 48:947–966

Goddard JV, Evans JP (1995) Chemical changes and fluid–rock interaction in faults of crystalline thrust sheets, northwestern Wyoming, USA. J Struct Geol 17:533–547

Grant JA (1986) The isocon diagram—a simple solution to Gresen's equation for metasomatic alteration. Econ Geol 81:1976–1982

Gray DR, Foster DA, Meert JG, Goscombe BD, Armstrong R, Trouw RAJ, Passchier CW (2008) A Damaran perspective on the assembly of southwestern Gondwana. Geol Soc London Spec Publ 294:257–278

Gregory MJ (2006) Copper mobility in the Eastern Creek Volcanics, Mount Isa, Australia: evidence from laser ablation ICP-MS of iron-titanium oxides. Mineral Deposita 41:691–711

Gresens RL (1967) Composition–volume relationships of metasomatism. Chem Geol 2:47–55

Hippertt JF (1998) Breakdown of feldspar, volume gain and lateral mass transfer during mylonitization of granitoid in a low metamorphic grade shear zone. J Struct Geol 20:175–193

Hitzman MW, Broughton D, Selley D, Woodhead J, Wood D, Bull S (2012) The Central African Copperbelt: diverse stratigraphic, structural, and temporal settings in the world's largest sedimentary copper district. Soc Econ Geol Spec Publ 16:487–514

Hoefs J (2009) Stable isotope geochemistry. Springer, Berlin

John T, Schenk V, Mezger K, Tembo F (2004) Timing and PT evolution of whiteschist metamorphism in the Lufilian Arc-Zambezi Belt orogen (Zambia): implications for the assembly of Gondwana. J Geol 112:71–90

Kampunzu AB, Cailteux J (1999) Tectonic evolution of the Lufilian Arc (Central Africa Copper belt) during Neoproterozoic Pan African orogenesis. Gondwana Res 2:401–421

Kasch KW (1986) Tectonic subdivision, lithostratigraphy and structural geology of the upper black Nossob River area. Comm Geol Soc Namibia 2:117–129

Kasch KW (1987) Metamorphism of pelites in the upper black Nossob River area of the Damara Orogen. Comm Geol Soc Namibia 3:63–82

Kitt S, Kisters A, Steven N, Maiden K, Hartmann K (2016) Shear-zone hosted copper mineralisation of the Omitiomire deposit—structural controls of fluid flow and mineralisation during subduction accretion in the Pan-African Damara Belt of Namibia. Ore Geol Rev 75: 1–15

Kukla PA, Stanistreet IG (1991) The record of the Damaran Khomas Hochland accretionary prism in central Namibia: refutation of the 'ensialic' origin of a Late Proterozoic orogenic belt. Geology 19: 473–476

Large RR (1992) Australian volcanic-hosted massive sulfide deposits: features, styles, and genetic model. Econ Geol 87:471–510

Lehmann J, Master S, Rankin W, Milani L, Kinnaird JA, Naydenov KV, Saalmann KA, Kumar M (2015) Regional aeromagnetic and stratigraphic correlations of the Kalahari Copperbelt in Namibia and Botswana. Ore Geol Rev 71:169–190

Liebenberg L (1970) The sulphides in the layered sequences of the Bushveld complex. Geol Soc South Africa Spec Publ 1:108–207

Maiden KJ, Hartmann K, Steven NM, Armstrong RA, (2013) The Omitiomire deposit, Namibia: Late Tectonic copper emplacement in a Neoproterozoic (Pan-African) imbricate shear system. Ext Abstr, SGA Meeting, 12–15 Aug 2013. Sweden, Uppsala.

McGowan RR, Roberts S, Foster RP, Boyce AJ, Coller D (2003) Origin of the copper-cobalt deposits of the Zambian Copperbelt; an epigenetic view from Nchanga. Geology 31:497–500

Meneghini F, Kisters A, Buick I, Fagereng A (2014) Fingerprints of late Neoproterozoic ridge subduction in the Pan-African Damara Belt, Namibia. Geology 42:903–906

Miller RMG (1983) The Pan-African Damara Orogen of Namibia. In: evolution of the Damara Orogen of south west Africa/Namibia. Geol Soc South Africa Spec Publ 11:431–515

Miller RMG (2008) The geology of Namibia. Geological Society of Namibia, Windhoek

O'Hara K (1988) Fluid flow and volume loss during mylonitization: an origin for phyllonite in an overthrust setting, North Carolina, USA. Tectonophysics 156:21–36

Ohmoto H (1986) Stable isotope geochemistry of ore deposits. In: stable isotopes in high temperature geologic processes. Min Soc America Rev Min 16:491–559

Ohmoto H, Mizukami M, Drummond SE, Eldridge CS, Pisutha-Arnond V, Lenagh TC (1983) Chemical processes of Kuroko Formation. Econ Geol Monograph 5:570–604

Oliver NHS, Thomson B, Freitas-Silva FH, Holcombe RJ, Rusk B, Almeida BS, Faure K, Davidson GR, Esper EL, Guimarães PJ, Dardenne MA (2015) Local and regional mass transfer during thrusting, veining, and boudinage in the genesis of the giant shale-hosted Paracatu gold deposit, Minas Gerais, Brazil. Econ Geol 110: 1803–1834

Passchier CW, Trouw RAJ (2005) Microtectonics. Springer, Berlin

Porada H, Berhorst V (2000) Towards a new understanding of the Neoproterozoic-Early Paleozoic Lufilian and northern Zambezi belts in Zambia and the Democratic Republic of Congo. J Afr Earth Sci 30:727–771

Putlitz B, Matthews A, Valley JW (2000) Oxygen and hydrogen isotope study of high pressure metagabbros and metabasalts (Cyclades, Greece): implications for the subduction of oceanic crust. Contrib Mineral Petrol 138:114–126

Rainaud C, Master S, Armstrong RA, Phillips D, Robb LJ (2005) Monazite U–Pb dating and 40Ar–39Ar thermochronology of metamorphic events in the central African Copperbelt during the Pan-African Lufilian orogeny. J Afr Earth Sci 42:183–199

Rolland Y, Cox S, Boullier AM, Pennacchioni G, Mancktelow N (2003) Rare earth and trace element mobility in mid-crustal shear zones: insights from the Mont Blanc massif (Western Alps). Earth Planet Sci Lett 214:203–219

Selley D, Broughton D, Scott R, Hitzman M, Bull SW, Large RR, McGoldrick PJ, Croaker M, Pollington N, Barra F, (2005) A new Look at the Geology of the Zambian Copperbelt. Econ Geol 100th Anniversary Vol: 965–1000.

Sharp ZD (1990) A laser-based microanalytical method for the in-situ determination of oxygen isotope ratios of silicates and oxides. Geochim Cosmochim Acta 54:1353–1357

Sharp ZD, Atudorei V, Durakiewicz T (2001) A rapid method for determination of hydrogen and oxygen isotope ratios from water and hydrous minerals. Chem Geol 178:197–210

Sillitoe RH, Perello J, Garcia A (2010) Sulfide-bearing veinlets throughout the stratiform mineralization of the central African Copperbelt: temporal and genetic implications. Econ Geol 105:1361–1368

Sillitoe RH, Perelló J, Creaser RA, Wilton J, Dawborn T (2015) Two ages of copper mineralization in the Mwombezhi Dome, northwestern Zambia: metallogenic implications for the central African Copperbelt. Econ Geol 110:1917–1923

Steven N, Armstrong R (2003) A metamorphosed Proterozoic carbonaceous shale-hosted Co-Ni-Cu deposit at Kalumbila, Kabompo Dome: the Copperbelt ore shale in northwestern Zambia. Econ Geol 98:893–909

Steven NM, Armstrong RA, Smalley TI, Moore JM (2000) First geological description of a late Proterozoic (Kibaran) andesite-hosted chalcocite deposit at Omitiomire, Namibia. In: geology and ore deposits: the Great Basin and beyond. Geol Soc of Nevada Symp Proc:711–734

Streit JE, Cox SF (1998) Fluid infiltration and volume-change during mid-crustal mylonitization of Proterozoic granite, King Island, Tasmania. J Metamorph Geol 16:197–212

Turlin F, Eglinger A, Vanderhaeghe O, André-Mayer A, Poujol M, Mercadier J, Bartlett R (2016) Synmetamorphic Cu remobilization during the Pan-African orogeny: microstructural, petrological and geochronological data on the kyanite-mica schists hosting the Cu (−U) Lumwana deposit in the western Zambian Copperbelt of the Lufilian Belt. Ore Geol Rev 75:52–75

Unrug R (1983) The Lufilian Arc: a microplate in the Pan-African collision zone of the Congo and the Kalahari Cratons. Precamb Res 21: 181–196

Vennemann TW, Morlok A, von Engelhardt WE, Kyser TK (2001) Stable isotope composition of impact glasses from the Nördlinger Ries impact crater, Germany. Geochim Cosmochim Acta 65:1325–1336

Zheng YF (1995) Oxygen isotope fractionation in magnetites: structural effect and oxygen inheritance. Chem Geol 121:309–316

Zulauf G, Palm S, Petschick R, Spies O (1999) Element mobility and volumetric strain in brittle and brittle–viscous shear zones of the superdeep well KTB (Germany). Chem Geol 156:135–149

Chapter 4

Structural, geochronological and P-T constraints on subduction-accretion processes in the Deep Level Southern Zone (DLSZ) of the Damara Belt in Namibia

This chapter presents a research paper submitted to Precambrian Research titled: "*Structural, geochronological and P-T constraints on subduction-accretion processes in a Pan-African accretionary wedge – the Deep Level Southern Zone of the Damara Belt in Namibia*" by Shawn Kitt, Alex Kisters, Ian Buick and Jan Kramers.

The manuscript was submitted to Precambrian Research on the 5th July 2017. The paper combines (1) regional structural and lithological data with (2) new $^{40}Ar/^{39}Ar$ and xenotime U-Pb LA-ICP-MS ages from the Ekuja-Otjihangwe domes and (3) new forward thermobarometric modeling (pseudosections) to (4) partially reconstruct the P-T-t paths for different tectonostratigraphic units in the DLSZ and (5) discuss the internal dynamics and complexities of subduction-accretion processes in the accretionary prism of the Damara Belt. The following aspects of the research was done independently by Shawn Kitt with supervision by Alex Kisters: (i) field work and sampling, (ii) interpretation of results and the (iii) preparation of the manuscript. Alex Kisters also contributed with editorial work towards the final draft. The pseudosections was done in THERIAK-DOMINO by Ian Buick who also assisted with the (iv) petrography and mineral chemistry, (v) identification of xenotime (vi) interpretation of results and (vii) preparation of the manuscript. The $^{40}Ar/^{39}Ar$ analysis and data reduction was done by Jan Kramers who also assisted with (viii) interpretation of results and the (ix) preparation of the manuscript. The LA-ICP-MS xenotime U-Pb dating and data reduction was done by Dirk Frei.

PRECAMBRIAN RESEARCH, **Submitted, manuscript ref:** PRECAM_2017_285

Structural, geochronological and P-T constraints on subduction-accretion processes in a Pan-African accretionary wedge – the Deep Level Southern Zone of the Damara Belt in Namibia.

Shawn Kitt [a*], Alexander Kisters [a], Ian Buick [a], Jan Kramers [b]

[a]*Department of Earth Science, Stellenbosch University, Stellenbosch, South Africa*
[b]*Department of Geology, University of Johannesburg, Johannesburg, South Africa*

*Corresponding author: shawnkitt@gmail.com

Abstract

The Southern Zone (SZ) accretionary prism of the Damara Belt in Namibia records the burial, offscraping and accretion of marine and original trench sediments during the Pan-African (~580-500 Ma) convergence of the Congo and Kalahari Cratons. Although the structure and metamorphic conditions of the prism sediments have been documented, the processes that lead to the imbrication of 100 km^2 slivers of Mesoproterozoic basement gneisses with the overlying prism metasediments are poorly understood. This study combines structural data with PT estimates and in-situ LA-ICP-MS U-Pb xenotime and Ar-Ar age determinations, to give insight into the dynamics of subduction and exhumation in the deeply eroded, tectonically interleaved Deep Level Southern Zone (DLSZ). Peak metamorphic assemblages in garnet-bearing amphibole gneisses from the Ekuja basement dome record PT conditions of 8.5-9.15 kbar and 635-655°C, suggesting burial to ca. 35 km. Garnet zoning patterns and breakdown textures show that peak metamorphism was followed by a clockwise retrograde P-T-t evolution. Exhumation of the Ekuja Dome is supported by structural observations and the retrogression of amphibole-plagioclase assemblages to biotite and epidote in the Omitiomire Shear Zone (OSZ). $^{40}Ar/^{39}Ar$ dating of biotite from the OSZ constrain the timing of exhumation of the Ekuja Dome to between 526.4 ± 3.5 and 521.9 ± 3.6 Ma. Peak metamorphic assemblages in garnet-kyanite schist from the overlying prism metasediments at Hochberg record PT conditions of 7-9.25 kbar and 640-675 °C, suggesting burial to 27-35 km. U-Pb dating of xenotime constrain the timing of peak metamorphism in the overlying metasediments to ca. 515 Ma, ca. 10 Ma after the onset of exhumation of the Ekuja Dome. This indicates that the Ekuja Dome was already exhumed while the overlying Hochberg metasedimentary unit was still undergoing burial, and reflects the dynamics of burial and exhumation along intraprism thrusts at the interface between the downgoing plate and the overlying prism sediments in accretionary complexes. The similarities in tectonometamorphic events between the Damara Belt and the Lufilian Arc points to a contiguous convergent margin along the leading edge of the Congo Craton that was active to at least ca. 515 Ma.

Key words: Damara Belt; accretionary prism; exhumation; pseudosection modelling; LA-ICP-MS U-Pb xenotime; Ar-Ar geochronology

1. Introduction

Accretionary prisms form an integral part of most subduction zones, recording the offscraping and accretion of material from the downgoing plate to the base of the overriding plate (Karig, 1983; Cloos and Shreve, 1988; Moore, 1989; von Huene and Scholl, 1991). Lateral growth and thickening of the prism occur through a combination of frontal accretion of material at the toe and underplating to the base of the prism, mainly via arc-ward dipping thrust systems (Platt, 1986; Cloos and Shreve, 1988). Parts of the accreted material may eventually be subducted, but most will be offscraped along or close to the leading edge of the overriding plate. In the latter case, continued subduction and sediment accretion leads to the uplift and eventual exhumation of previously buried sediments at the backstop of the prism, where the off-scraped sediments are forced upwards (Platt, 1986, 1993). The complex internal dynamics of accretionary wedges are mainly documented from active or recent subduction zones (Glodny et al., 2005; Agard et al., 2009; Angiboust et al., 2013, 2016; Plunder et al., 2015) and much of our understanding of the mechanisms, flow trajectories and rates of material transfer comes from analogue and numerical models of accretionary systems (Cloos, 1982; Gutscher et al., 1998; Yamada et al., 2006; Graveleau et al., 2012). The dynamics of ancient, Paleozoic and older accretionary prisms, in contrast, are less well documented, either as a consequence of the poorer preservation of the rocks or later events that have obscured original structures and P-T trajectories.

The Southern Zone (SZ) of the Pan-African (580-500 Ma) Damara belt in central Namibia represents the deeply eroded accretionary prism of the orogen that formed during the northward convergence of the Kalahari Craton towards the Congo Craton (Fig. 1; Miller, 1983, 2008). The prism is made up of a thick (>10,000 m), southeast-verging succession of imbricated amphibolite-facies metaturbidites, collectively referred to as the Khomas Complex (Miller, 2008). Despite its antiquity, the Southern Zone prism preserves original convergence-related structures remarkably well, probably as a result of the only soft collision between the Kalahari and Congo cratons and the lack of later rifting events during Gondwana break-up that have affected most other Pan-African belts in southern Africa (Meneghini et al., 2014). Previous studies have identified a broad zonation of metamorphic grades parallel to the NE extent of the SZ (Fig. 1b; Kasch, 1983). Medium- to high-P, medium-T conditions of 8-10 kbar and 520-600°C prevail in the southern parts of the SZ and record the tectonic burial of the rocks during south- and southeast-vergent thrusting and imbrication (e.g., Sawyer, 1981; Kasch, 1983; Cross et al., 2015). In the north, rocks of the SZ border against the Central Zone magmatic arc of the belt. Here, SZ rocks record lower P and similar to higher T conditions (P ca. 4-6 kbar, T ca. 600-720°C) and a late-stage isothermal decompression of between 1-3 kbar (Kasch, 1987; Clemens et al., 2017a; see comprehensive summary in Miller 2008).

The reasons for the late-stage isothermal decompression path of SZ rocks are controversially discussed and tentatively related to the intrusion of the large, late-tectonic composite ca. 530-510 Ma Donkerhuk batholith (Clemens et al., 2017b) in the southwestern parts of the SZ, where most metamorphic studies were undertaken. To date, the works by Kasch (1986, 1987) are the only studies that document the tectonostratigraphic inventory and metamorphic evolution of the less well exposed eastern parts of the prism, away from the Donkerhuk batholith. This part of the accretionary prism is also referred to as the Deep-Level Southern Zone (DLSZ). It records the imbrication of older, Namaqua-age (ca. 1100 – 1000 Ma) gneisses, probably derived from the down-going Kalahari Craton with serpentinite slivers and the Kuiseb Formation metasediments of the overlying prism.

Kitt et al. (2016) suggested the juxtaposition of rocks and the mélange-like lithological assemblage to be the result of the southward expulsion of previously subducted rocks close to the subduction zone channel of the Pan-African convergent system. However, there are to date no P-T or geochronological data that would allow for a more detailed characterisation of these dynamics in the SZ accretionary prism. In this study, we present new structural, P-T and geochronological (U-Pb and Ar-Ar ages) data from the Mesoproterozoic Ekuja gneiss dome and the structurally overlying Kuiseb Formation metasediments. The paper intends to document the processes that led to the juxtaposition of the different tectonostratigraphic units at, or close to, the base of the SZ prism and to characterise aspects of the complex kinematic evolution within this ancient accretionary complex.

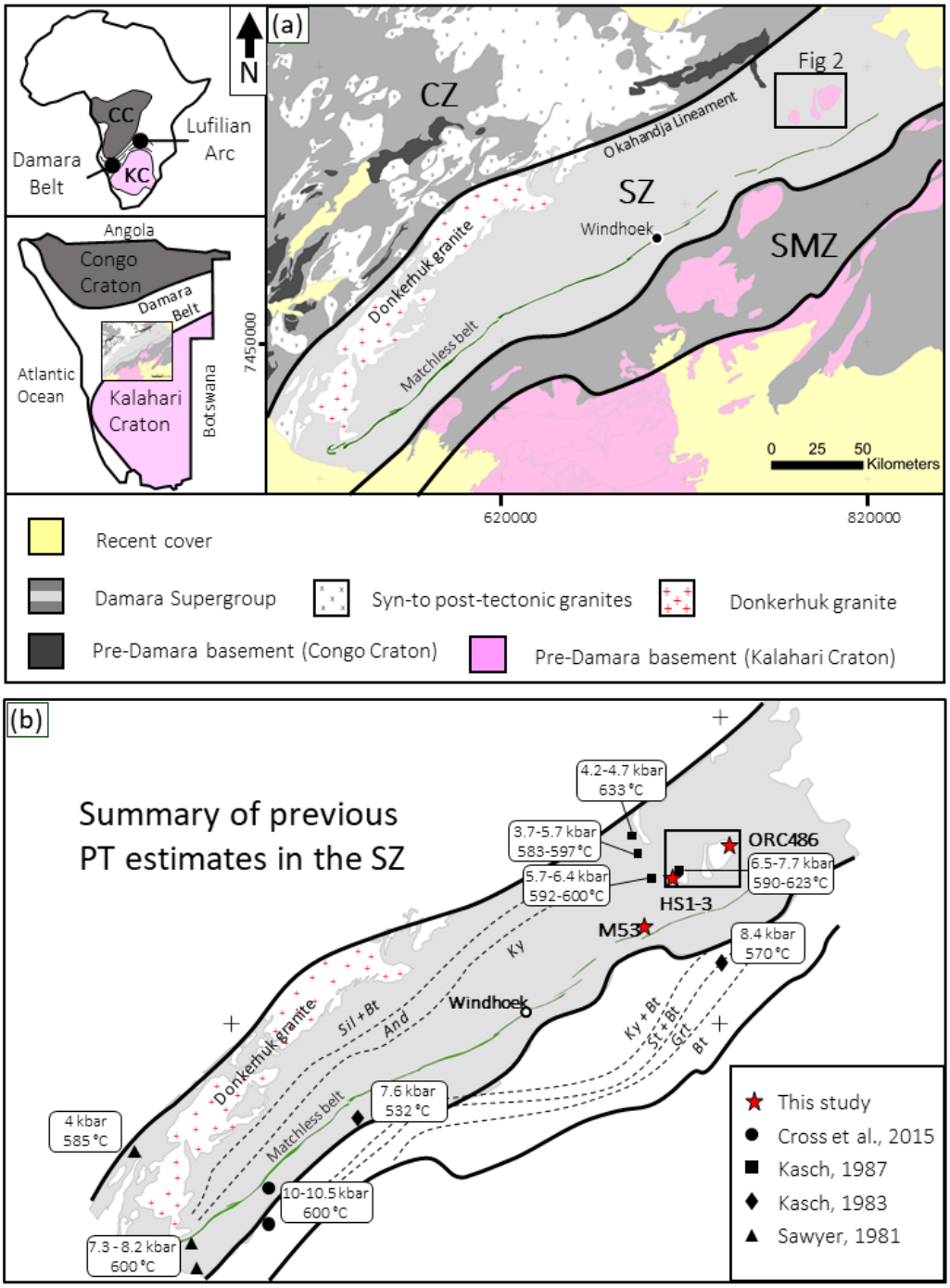

Fig. 1. (a) Simplified geological map (after Miller, 2008) of the southern part of the Damara Belt, showing the Central Zone (CZ), Southern Zone (SZ) and the Southern Margin Zone (SMZ). The location of the study area (Fig 2) is indicated. The insets shows the location of the Pan-African Damara Belt and Lufilian Arc relative to the Kalahari and Congo cratons and the position of Figure 1a in relation to the cratons. (b) Summary map of previous PT estimates in the Southern Zone. The location of samples collected during this study is shown. The mineral isograds after Kasch (1983).

2. Regional Geology

2.1. Geological framework of the Damara belt

The Damara Belt extends from the Atlantic coast of Namibia in a NE direction through central Namibia and northern Botswana into the Lufilian Arc of Zambia and the Democratic Republic of Congo (DRC) (Fig. 1; Miller, 1983; Kampunzu and Cailteux, 1999). It forms part of a series of Neoproterozoic to Early Paleozoic orogenic belts in southern Africa that records the Pan-African amalgamation of the Archean-Mesoproterozoic Congo and Kalahari cratons to form Gondwana (Coward, 1981; Miller, 1983; Gray et al., 2008). The orogen evolved through successive phases of intracontinental rifting, spreading and ocean basin formation between ca. 800-600 Ma followed by the reversal of plate motion, subduction and eventual collision (Miller, 1983). Convergence began at ca. 590 Ma and resulted in the northward, mainly high-angle subduction of the Khomas Ocean below the Congo Craton (Miller, 2008; Lehmann et al., 2016). The Southern Zone (SZ) together with the Southern Margin Zone (SMZ) constitute the deeply eroded accretionary prism of the orogen (Miller, 1983; Kukla and Stanistreet, 1991). The Southern Zone contains a thick sequence of imbricated metaturbidites, collectively referred to as the Kuiseb Formation, and intrusive as well as structurally interleaved MORB-type mafic metavolcanic and gabbroic rocks of the Matchless Amphibolite Belt (Miller, 1983; 2008; Meneghini et al., 2014). South- to southeast vergent folding and thrusting, and amphibolite-facies metamorphism record the accretion of the sediments through offscraping, underplating and burial during northward-directed subduction of the Khomas Ocean and partial underthrusting of the Kalahari Craton below the overriding Congo Craton (Kukla and Stanistreet, 1991; Miller, 2008). Granitic plutonism between ca. 575 and 470 Ma is widely recorded in the high-T, low-P Central Zone (CZ), situated on the leading edge of the Congo plate to the north of the SZ prism (Miller, 1983, 2008, Longridge et al., 2011, 2017, Kisters et al., 2012). The late-tectonic composite 530-510 Ma Donkerhuk batholith is intrusive into Kuiseb Formation rocks of the SZ and underlies much of the southwestern parts of the accretionary prism (Fig. 1; Sawyer, 1981; Miller, 1983; 2008; Clemens et al., 2017a, b). The northern boundary of the SZ against the CZ is the Okahandja Lineament, which is regarded as the backstop of the prism (Miller, 1983; Kukla and Stanistreet, 1991). The metamorphic grade increases from south to north, showing a near-isothermal drop in pressure from ~7 kbar and ~550-600°C in the south to ~3.7-5.7 kbar and ~585-620°C in the north (Fig. 1b; Sawyer, 1981; Kasch, 1983, 1987; Miller, 2008). Donkerhuk batholith magmas were emplaced into the northern part of the SZ at ~4.5 kbar and anatectic metapelitic rocks along the southern margin of the batholith record peak metamorphic P-T conditions of ~3.7-4.6 kbar and ~660-710 ˚C (Clemens et al., 2017a). A recent study by Cross et al., (2015) on metapelites and metabasites from the Kuiseb and Ghaub river areas in the western SZ demonstrated a two stage prograde evolution involving tectonic burial followed by near-isobaric heating from 540-560°C to peak PT conditions of ~10.5 kbar and 600°C. This two-stage thermal evolution is related to ridge subduction below the prism, as first proposed by Meneghini et al. (2014).

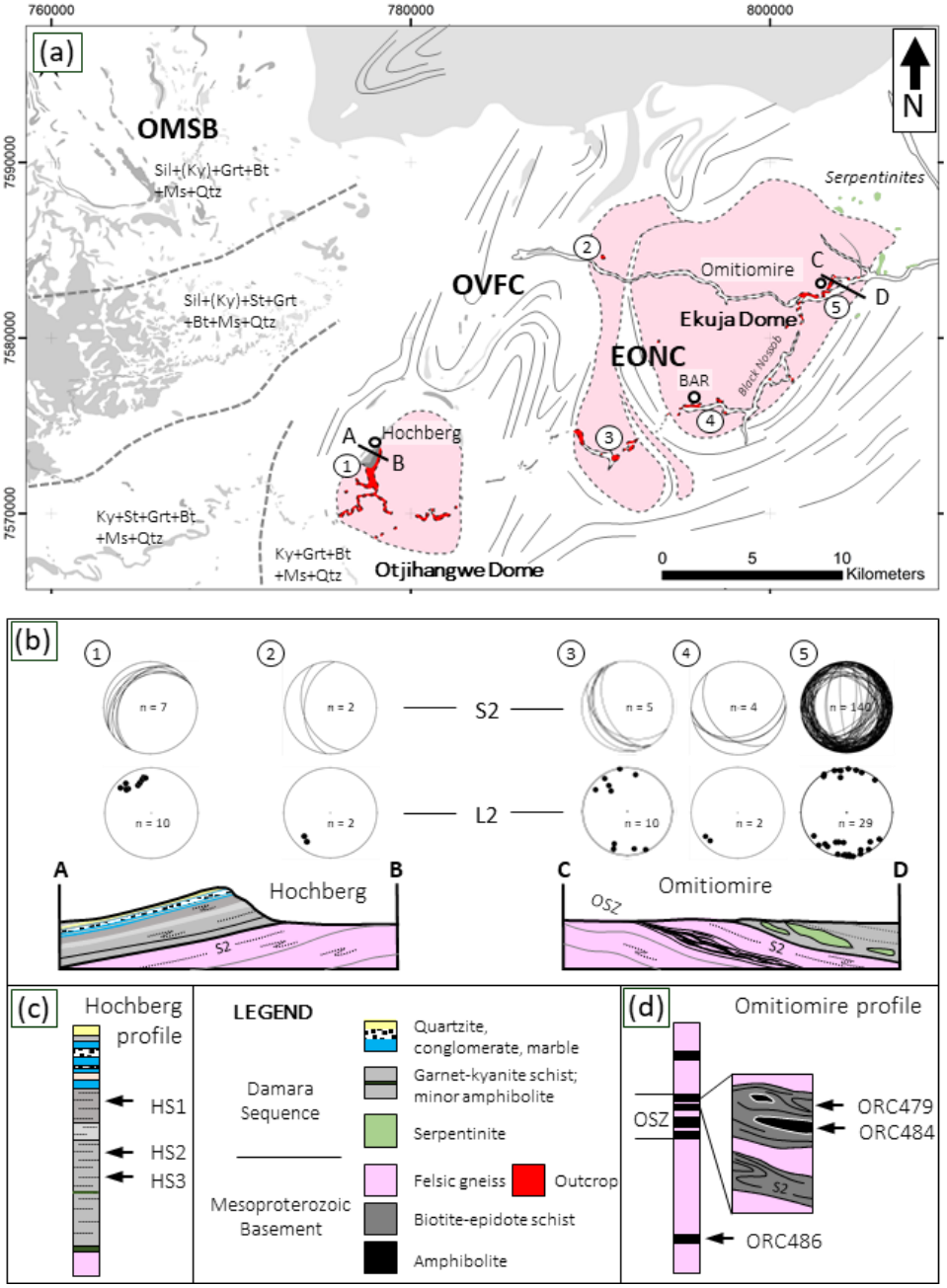

Fig. 2. (a) Simplified geological and structural form line map of the study area in the DLSZ, modified from Kasch, 1986, 1987 and the 2117D Ekuja Sheet from the Geological survey of Namibia 1:100,000 map series. The main tectonostratigraphic units and sampling sampling localities are shown. OMSB - Onyati Mountain Schist Belt; OVFC - Onjona Vrolikheid Fold Complex; EONC - Ekuja-Otjihangwe Nappe Complex. (b) Simplified cross sections A-B (Hochberg) and C-D (Omitiomire) as shown in Figure 2a. The relative location of the Omitiomire Shear Zone (OSZ) is indicated. Stereonets are lower hemisphere, equal area and show the orientations of S2 foliations and L2 lineations as mapped in the localities shown on the map. Simplified stratigraphic columns of (c) the lower Damara Sequence as exposed at Hochberg on the western side of the Otjihangwe Dome (after Kasch, 1986) and (d) basement gneisses and schist of the Ekuja Dome as intersected at Omitiomire. The relative position of the samples collected during this study is indicated.

Regional tectonic studies in the Damara Belt generally agree on a polyphase structural evolution of the orogen (Coward, 1981; Sawyer, 1981; Miller 1983, 2008; Kasch, 1983, 1986; Kisters et al. 2004, 2012; Longridge et al., 2011, 2017; Lehmann et al., 2016; Passchier et al., 2016; Kruger and Kisters, 2016; Goscombe et al., 2017). In the Central and Southern zones, up to three main deformation phases (D1-D3) have been described by Miller (1983, 2008) and others in recent years (Kasch, 1986; Kisters et al., 2012; Longridge, 2011, 2017; Kitt et al., 2016), and can be outlined as follows:

D1 is the earliest phase and record deformation during the initial convergence between the Kalahari and Congo Cratons. It is characterised by low-angle fabrics such as a scarcely recognisable bedding-parallel foliation and rare intrafolial folds. The second phase, D2 is the most pervasive deformation and developed regional scale tight to isoclinal, South-SE verging recumbent (F2) folds, thrusts and nappe structures. It is the dominant fabric preserved in the accreted prism metasediments of the SZ and associated with a penetrative, SE-verging S2 cleavage, high strain shear zones and a L2 stretching lineation. In the SZ, the L2 lineation plunge to the NW, roughly perpendicular to the NE plunge in the CZ. D3 deformation has been linked to collision between the Kalahari and Congo Cratons during the later stages of the Damara orogeny. It is characterised by kilometre-scale, northeast-trending, doubly-plunging F3 domal structures that define the regional scale tectonic architecture in most of the CZ.

2.2. Deep Level Southern Zone

The easternmost part of the SZ is also referred to as the Deep Level Southern Zone (DLSZ) (Miller, 2008). It exposes deeper stratigraphic levels, in which rocks of the Kuiseb Formation of the SZ prism are in contact and structurally interleaved with supracrustal rocks, but also older, Namaqua-age basement gneisses, that show a closer affinity to the SMZ situated on the under-thrust Kalahari Craton to the south (Kasch, 1986, 1987; Miller, 2008). The gneisses form kilometer-scale dome structures surrounded by Kuiseb Formation metasediments and likely contribute to the disturbed and irregular magnetic signature of aeromagnetic surveys (Miller, 2008). A regional study by Kasch (1986, 1987) in the DLSZ around the Ekuja and Otjihangwe gneiss domes identified three structurally overlying tectonostratigraphic units with distinct lithologies, structures and metamorphic histories (Fig. 2a).

The cores of the gneiss domes are referred to as the Ekuja-Otjihangwe Nappe Complex (EONC) (Kasch, 1986; 1987). This basal unit is composed of partially migmatised, banded and augen gneisses of mainly tonalitic composition interleaved with minor amphibolites and biotite-epidote schists. Late- to post-Damaran pegmatites are intrusive into this sequence. The pre-Damaran age of the gneiss domes is confirmed by U-Pb zircon ages of 1084 ± 7 and 1063 ± 9 Ma for quartzo-feldspathic gneisses and 1115 ± 13 Ma for the amphibolites (Steven et. al., 2000). The ages are interpreted to represent magmatic crystallisation ages, and are in agreement with actual intrusive relationships that show younger tonalites intruding and brecciating older amphibolites (Kitt et. al, 2016). The gneisses are characterised by isoclinal, intrafolial folds, a shallow outward-dipping S2 gneissosity and a unidirectional, northerly trending stretching lineation (L2) (Kitt et al., 2016). Along the eastern margins of the Ekuja Dome, several tens-of-meter sized bodies of serpentinite and talc-carbonate schists form tectonic slivers along the basement-cover interface (Kasch, 1986). The Onyati Mountains Schist Belt (OMSB) forms the structurally highest unit

and part of the SZ prism (sensu stricto). The OMSB comprises Kuiseb Formation pelitic and psammitic schists that are intercalated with amphibolites and calc-silicate felses. The Kuiseb Formation in the OMSB shows polyphase, mainly south-verging, tight-to-isoclinal folds and associated thrusts with top-to-the-south kinematics. Fold hinges and mineral stretching lineations plunge shallowly to the W and NW. The basement complexes of the EONC are separated from the metaturbidites of the OMSB by the Onjona-Vrolikheid Fold Complex (OVFC). This complex is made up of quartzites, meta-conglomerates, marbles and amphibolites more characteristic of the lower Damara Supergroup. Structurally, the OVFC forms a transitional zone between the EONC basement domes and the OMSB fold-and-thrust belt. It records the progressive rotation and refolding of the roughly east-west trending structural elements from the overlying OMSB to the N-S structural trends of the EONC basement domes (Kasch, 1986).

Kasch (1987) used phase equilibria and conventional geothermobarometry to constrain PT conditions of the Kuiseb Formation metapelites that overlie the Ekuja and Otjihangwe domes in the DLSZ. Based on kyanite-sillimanite and staurolite isograds, Kasch (1987) delineated four metamorphic zones that show a general increase in temperature and decrease in pressure from south to north (Fig. 2a). West of the EONC, estimated peak metamorphic conditions in the OMSB vary from ~6kb/~600°C in the south to ~4kb/~630°C in the north (Fig. 1b). Garnet-kyanite-bearing metapelites that directly overlie basement gneisses in the EONC record similar temperatures of between 590°C and 623°C, but higher pressures ranging from 6.5 kbar up to 7.7 kbar (Kasch, 1987). Metamorphic reaction textures and garnet zoning profiles show that the metapelites experienced late-stage isothermal decompression and, in the case of the garnet-kyanite schists overlying the EONC, decompression post-dated an episode of isobaric heating. Importantly, based on reaction textures, Kasch (1987) noted the early metamorphic history of the EONC to be different from that of the overlying OMSB, but did not provide any structural or P-T data from the basement complex.

3. Local Geology

For the purpose of this study, and in order to characterise the processes that led to the juxtaposition of the older gneiss domes against the prism metasediments, we have mapped and sampled the Mesoproterozoic basement gneisses and schists from the Ekuja and Otjihangwe domes (EONC) and the overlying Damara metasediments from the OVFC (Fig. 1b and Fig. 2). The localities and descriptions of samples are listed in the Table A1 in the supplementary material.

3.1. Mesoproterozoic basement

Much of the area is covered by Kalahari sands, but sparse outcrops along the ephemeral Black Nossob river expose mainly sheet-like, shallowly dipping quartzo-feldspathic felsic gneisses (Fig. 2a).

Two deformation phases, D1 and D2, are recognized in the gneisses (Kitt et al., 2016). D1 forms an early gneissosity, defined by the grain-shape preferred orientation of biotite and quartz-feldspar aggregates, and is only rarely observed in the hinges of younger F2 folds (Kitt et al., 2016). D2 is the main deformation phase observed in the EONC and is correlated with the D3 phase in the EONC and the OVFC as described by Kasch (1986). It forms an S2 gneissosity along which earlier lithological contacts or D1 fabrics are transposed by cm- to m-scale and probably larger isoclinal, intrafolial F2 folds (Fig. 3). F2 folds plunge

shallowly to the north, parallel to a prominent northerly trending, shallow, doubly plunging rodding lineation (L2) contained in S2 (Fig. 2b and Fig. 3a; Kitt et al., 2016). Amphibolite, hornblende-biotite gneiss and biotite-epidote schist form up to 100 m thick intercalations within the mainly sheet-like tonalitic gneisses of the EONC, as intersected by diamond drill core on the farm Omitiomire in the eastern parts of the Ekuja Dome (Steven et al., 2000; Kitt et al., 2016). The Omitiomire Shear Zone (OSZ) is a heterogeneous zone composed of anastomosing shears centered along mylonitic biotite-epidote schists that wrap around lenses of tonalitic gneisses and amphibolites (Fig. 2b, d and Fig. 3c; Kitt et al., 2016). Deformation and fluid flow was heterogeneous on all scales, as is evidenced by relics of amphibole even on a micro scale. Kinematic indicators (S-C fabrics) in shallow dipping, mylonitic high-strain zones show top-to-the-south sense of movement parallel to a prominent shallow plunging stretching lineation (Fig. 3e; Kitt et al., 2016).

3.2. Lower Damara Sequence and Basement cover contacts

The contact between gneisses of the EONC and the overlying OFVC and OMSB is best exposed along a prominent hill on the western side of the Otjihangwe basement dome (Fig. 2a and Fig. 4a). The Hochberg hill forms one of the few topographic highs in the region. It exposes a vertical section through shallowly dipping banded and tightly folded, transposed (S2) basement gneisses structurally overlain by a heterogeneous, supracrustal sequence made up of garnet-kyanite-bearing biotite schists, marbles, metaconglomerates and a coarsely recrystallised fuchsite-bearing quartzites assigned to the lower Damara Supergroup (Fig. 2b, c and Fig. 4; Kasch, 1986). Similar to the underlying gneisses, the overlying schist package preserves evidence of two deformation phases. An earlier S1 foliation is only observed in the hinges of isoclinal, recumbent folds (F2) that refold and transpose the earlier S1 foliation into the pervasive and regionally developed S2 foliation. The S2 foliation is associated with the NNW-trending and very prominent L2 stretching lineation, and is defined by the preferred alignment of all mineral aggregates and, most prominently, the rodding of quartzites and pebbles in conglomerates towards the top of the exposed sequence (Fig. 4d).

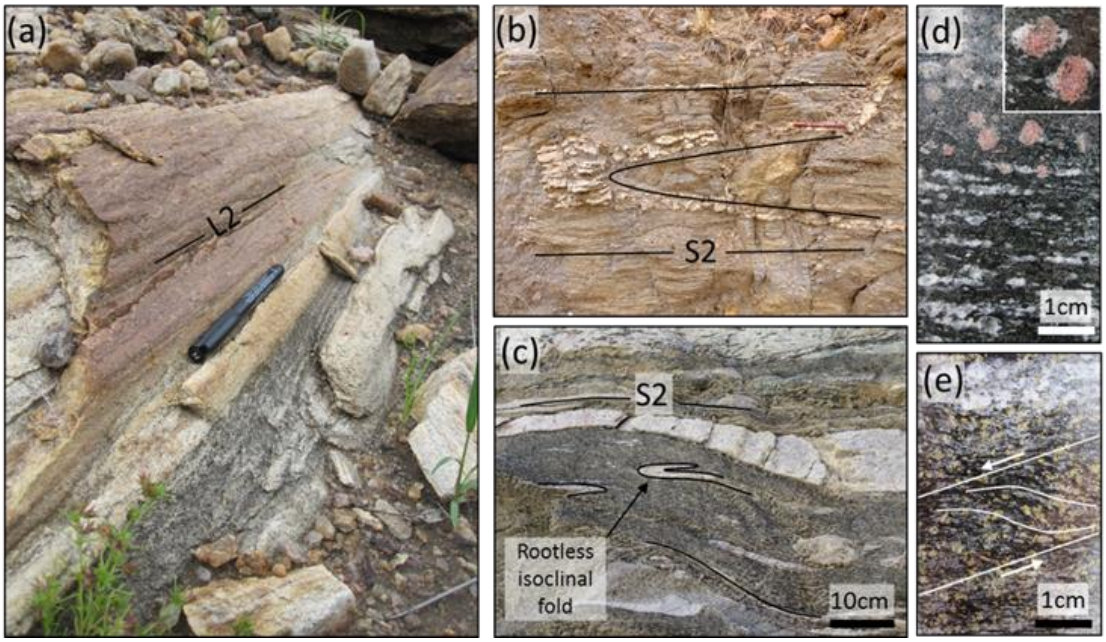

Fig. 3. Photographs showing the dominant structural elements and textural relationships preserved in the basement gneisses from the Ekuja Dome and in the Omitiomire Shear Zone (OSZ). (a) L2 rodding lineation in felsic gneiss from the Ekuja Dome. (b) Rare F1 fold in felsic gneiss at Omitiomire. (c) Transposed biotite schists with remnants of felsic gneisses, including rootless isoclinal fold in the OSZ. (d) Garnets in an amphibolite gneiss from Omitiomire showing typical decompression textures. (e) S-C fabric (top to the south) in mylonitic biotite-epidote schists from the OSZ.

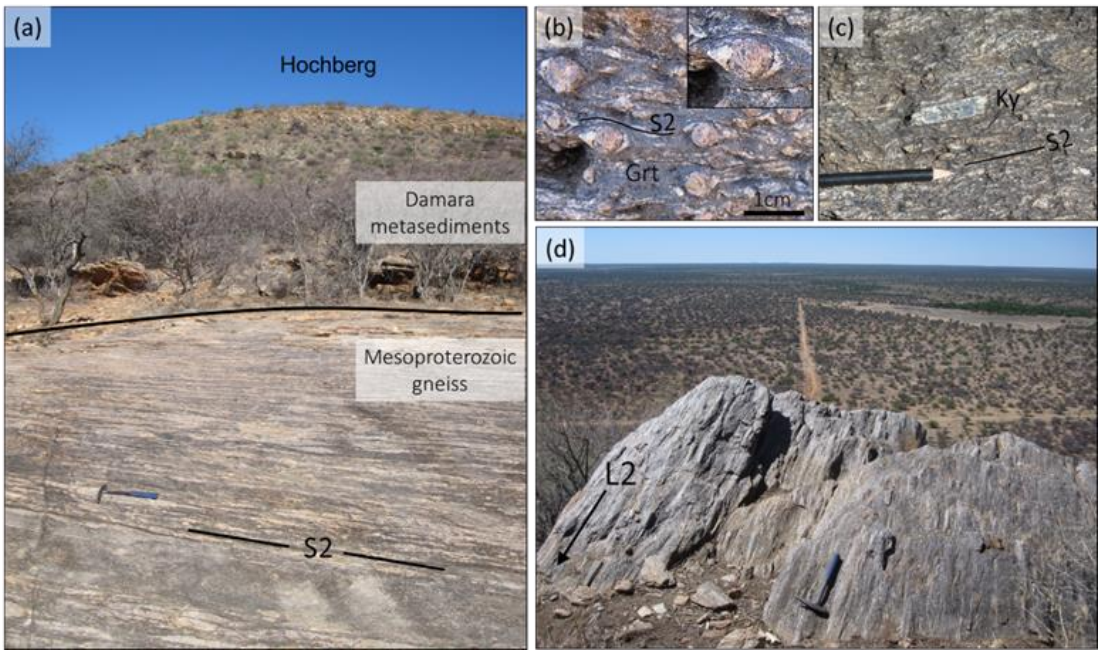

Fig. 4. Photographs showing outcrops of the lower Damara Sequence metasediments and the underlying basement gneisses exposed at Hochberg. (a) Photo of Hochberg hill (looking west) showing the contact between the basement gneisses and the overlying metasediments. (b) Garnet-kyanite schist (sample HS1) with S2 foliation wrapping around garnet porphyroblast. Plagioclase in strain shadows replacing garnet is characteristic for the schist and indicate decompression. (c) Large S2 parallel kyanite in a garnet-kyanite schist (samples HS2 and HS3). (d) NNE trending L2 rodding lineation defined by stretched clasts in a conglomerate layer at the top of Hochberg.

4. Analytical techniques

Five samples were selected for thermobarometric work based on their whole rock and mineral chemistry (Table A1 in supplementary material). Samples HS1, HS2 and HS3 are garnet-kyanite-bearing metapelites from the lower Damara Supergoup collected on the Hochberg hill within 20-80 m of the basement-cover contact (Fig. 1b and Fig. 2c). Sample M53 was collected in the Orumbungo river some 30 km southwest of Hochberg and is a garnet-kyanite metapelite from higher up in the Kuiseb Formation (Fig. 1b). Sample ORC486 is from basement gneiss of the EONC taken from a drill core sample of garnet-hornblende gneiss in the footwall of the OSZ (Kitt et al., 2016), some 25 km to the east of Hochberg (Fig. 2a and Fig. 2d). The samples were prepared and analysed at the Central Analytical Facilities (CAF) at the University of Stellenbosch. The samples were crushed using a jaw crusher and pulverized by a tungsten swing mill. The whole rock compositions were determined by X-ray fluorescence spectrometry (XRF). Carbon-coated polished thin sections were used to analyse the mineral compositions of selected samples. Mineral major element compositions were determined on a Zeiss EVO MA15VP Scanning Electron Microscope and quantified by EDS (energy dispersive spectroscopy), using an Oxford Instruments 133 keV detector and Oxford INCA software. The analyses were carried out using a 20 kV acceleration voltage, a 20 nA beam current and a working distance of 8.5 mm. Counting times were 10 seconds for live-time and 4 seconds process time. The compositions were quantified using internal Astimex Scientific mineral standards.

In order to constrain the timing of metamorphism, U-Pb ages were obtained from metamorphic xenotime, a rare-earth element rich phosphate found in the garnet-kyanite schists on the Hochberg hill. The xenotime grains were located in polished thin sections using optical microscopy and a Zeiss EVO MA15VP Scanning Electron Microscope at the University of Stellenbosch. Back-scattered electron (BSE) images were made of the largest grains, and later used for the description of the internal zoning and textural relationships. In-situ U-Pb isotopic analysis was undertaken at the Central Analytical Facility (CAF) at the University of Stellenbosch by laser ablation-single collector-magnetic sector field-inductively coupled plasma-mass spectrometry (LA-SF-ICP-MS) using a Thermo Finnigan Element2 mass spectrometer coupled to a Resonetics Resolution S155 excimer laser ablation system, including a Laurin Technic dual volume sample cell (see methodology in Table A2 in supplementary material). The LA-ICP-MS U-Pb isotope data were collected in situ on xenotime grains in the polished thin sections at an ablation spot size of 8 µm, using a standard-unknown bracketing approach. Because of the scarcity of xenotime standards in SIMS/LA-ICP-MS laboratories we employed a non-matrix matched approach using the monazite reference material USGS 44069 (425 Ma, Aleinikoff et al., 2006) as the primary calibration material, and the xenotime reference material Z6413 (997 Ma; Fletcher et al., 2004) as a secondary (quality control) standard. Data reduction, employed an in house Excel spreadsheet based on the method of Frei and Gerdes (2009), and ages were calculated using the Isoplot add-in for Excel (Ludwig, 2003). Using the non-matrix matched dating approach, xenotime Z6413 yielded a concordia age of 998 ± 4 Ma (2σ; MSWD of concordance and equivalence (MSWD(C+E)) = 0.91);

in excellent agreement with the published TIMS ^{207}Pb-^{206}Pb age of 997 ± 1 Ma (Fletcher et al., 2004). This suggests that, for the low fluences (~2.8 J/cm^2) used in this study, the matrix effect associated with using monazite as the primary calibrant was negligible, and hence the xenotime ages obtained from samples in this study and presented below are robust. U-Pb isotope ratios and calculated spot dates from xenotime from the three metapelites, and from the secondary control standard, are given in Table A3 in the supplementary material. The uncertainties on individual isotope ratios and spot dates are quoted at 2σ.

5. Petrography & mineral chemistry

The whole-rock compositions and a summary of mineral assemblages and textural relationships of the metapelites and metabasites are given in Table 1 and Table 2. A summary of the composition of the main minerals in the samples are presented in Table 3 and the representative mineral analyses are given in Table 4 and Table 5.

Table 1: Whole-rock compositions (in wt %) used for the pseudosections.

Sample description	Grt-Ky schist	Grt-Ky schist	Grt-Ky schist	Grt-Ky schist	Amphibolite
Type	Damara metapelites	Damara metapelites	Damara metapelites	Damara metapelites	Ekuja Basement
Location	Hochberg	Hochberg	Hochberg		Omitiomire
Sample name	HS1	HS2	HS3	M53	ORC486
Oxides wt%					
SiO_2	56.02	66.84	53.00	57.63	51.94
TiO_2	0.91	0.78	1.06	1.10	0.81
Al_2O_3	17.70	14.94	20.59	18.75	15.54
Cr_2O_3	0.02	0.02	0.02	0.02	0.03
Fe_2O_3	8.27	8.00	10.59	8.26	11.78
MnO	0.10	0.10	0.08	0.11	0.14
MgO	4.90	3.12	3.95	4.01	6.72
CaO	3.09	1.07	1.65	1.31	7.75
Na_2O	2.46	1.34	1.76	1.97	3.61
K_2O	3.67	2.50	4.83	5.07	0.47
P_2O_5	0.23	0.13	0.23	0.19	0.03
L.O.I.	1.69	1.16	2.31	1.82	0.97
Total	99.06	100.00	100.07	100.24	99.79

Table 2: Summary of the mineral assemblages in the samples investigated for PT estimates.

Sample	Grt	Ky	Qtz	Pl	Ms	Bt	Hbl	Ep	Chl	Rt	Ilm	Hem	Mag	Xtm	Ttn
HS1	*p **	*p */*	*p # ʘ*	*p # ʘ*	*p # f*	*p # f ʘ*		*# r*	*# r*	*p # ʘ*	*ʘ*				
HS2	*p **	*p */*	*p # ʘ*	*p # ʘ*	*p # f*	*p # f ʘ*		*# r*	*# r*	*# ʘ*		*p # ʘ*		*#*	
HS3	*p **	*p */*	*p # ʘ*	*p # ʘ*	*p # f*	*p # f ʘ*		*# r*	*# r*			*p # ʘ*		*# ʘ*	
M53	*p **	*p */*	*p # ʘ*	*p #*	*p # f*	*p # f ʘ*		*# r*	*# r*		*p # ʘ*				
ORC486	*p **		*p # ʘ*	*p # ʘ /*		*# r*	*p # ʘ*		*# r*		*p # ʘ*		*ʘ*		*# r*
*# = occur in matrix; * = occur as a porphyroblast; p = peak mineral*															
f = define a foliation; l = define a lineation															
ʘ = occur as an inclusion in garnet; r = retrograde mineral															

Table 3: Summary of the composition of main minerals found in the samples for PT estimates.

Sample	Grt				Pl			Ms	Bt	Hbl
	XAlm	*XGrs*	*XPrp*	*XSps*		*XAn*	*XAb*	*XMg*	*XMg*	*XMg*
HS1	0.59-0.67	0.19-0.30	0.06-0.15	0.09-0.1	matrix	38-44	56-63	0.54-0.59	0.57-0.61	
					Garnet inclusion	27-38	62-73		0.58-0.67	
HS2	0.44-0.52	0.10-0.16	0.1-0.18	0.19-0.31	matrix	26-29	71-74	0.31-0.35	0.65 - 0.71	
HS3	0.48-0.55	0.07-0.15	0.1-0.17	0.15-0.31	matrix	27-37	63-75	0.34-0.39	0.66	
M53	0.59-0.70	0.11-0.21	0.07-0.12	0.06-0.16	matrix	14-21	79-86	0.31-0.51	0.54-0.55	
ORC486	0.61-0.67	0.16-0.28	0.1-0.14	0.02-0.03	matrix	23-29	72-77			0.40-0.48
					Garnet inclusion	20-31	69-80			0.33-0.39

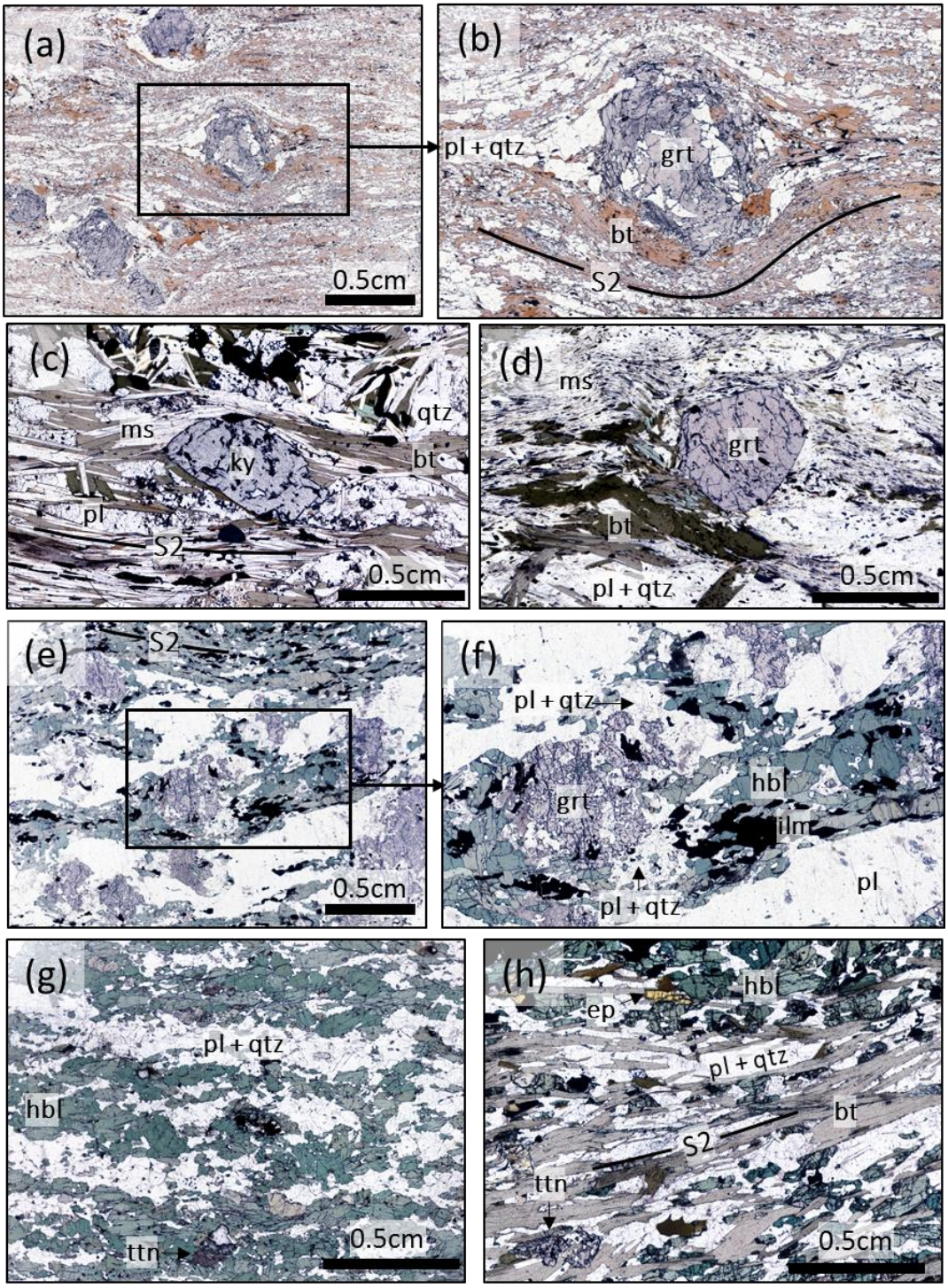

Fig. 5. Photomicrographs. (a) Sample HS1, a fine grained garnet-kyanite schist showing garnet porphyroblasts enveloped by S2-parallel peak assemblages of biotite, plagioclase and quartz. (b) Close up of garnet porphyroblast showing replacement by plagioclase and quartz in the strain shadow (c) Sample HS2, a coarse grained garnet-kyanite schist showing kyanite porphyroblasts and peak assemblage muscovite, biotite, plagioclase and quartz. (d) Sample M53, a coarse grained garnet-kyanite schist showing a garnet porphyroblast and peak assemblage of muscovite, biotite, plagioclase and quartz. (e) Sample ORC486, a garnet-amphibole gneiss from the Omitiomire Shear Zone. (f) Close up of corroded garnet porphyroblasts showing replacement by plagioclase and quartz. Photomicrographs of (g) sample BAR, an amphibole-plagioclase gneiss from Barreshagen in the Ekuja Dome and (h) sample ORC479, a biotite-epidote-amphibole schist from the Omitomire Shear Zone.

5.1. Damara metapelites

Garnet-kyanite-bearing schist samples (HS1-HS3) from the Hochberg hill section are fine- to medium-grained and composed of biotite, muscovite, garnet, kyanite, quartz, plagioclase and some late epidote and chlorite (Fig. 5a-c and Table 2). Accessory minerals occur in variable amounts and include rutile, hematite, apatite, zircon, xenotime, and minor ilmenite.

Sample HS1 is a fine-grained biotite schist with porphyroblasts of kyanite and garnet in a matrix made up of biotite, quartz, plagioclase and minor muscovite (Fig. 4b and Fig. 5). Biotite and muscovite occur as elongated foliation-parallel aggregates to form an anastomosing S2 foliation that wraps around large (2-5mm) garnet porphyroblasts. Flattened, recrystallised quartz aggregates form ribbons between alternating biotite layers. Rutile and apatite are the main accessory phases in the matrix. Kyanite occurs as small (1-5 mm) crystals that are aligned parallel to, but also overgrow the main S2 fabric. Coarser, randomly orientated biotite and large inequigranular quartz and plagioclase grains occur along the margins and in the strain shadows of garnet grains. The garnet porphyroblasts are commonly poikilitic with inclusions of quartz, plagioclase, biotite, apatite, calcite, and texturally intergrown rutile and ilmenite. Rutile is the stable Ti-bearing accessory phase in the rock matrix. Some garnets have sigmoidal inclusion trails suggesting their synkinematic rotation. Garnet exhibits different stages of retrogression, from subhedral, zoned garnets with somewhat serrated boundaries, to highly irregular subhedral crystals that are intensely corroded, to pseudomorphed garnet that has almost completely been replaced by plagioclase, quartz and biotite. The composition (mol%) of zoned garnet porphyroblasts are $Alm_{59-67}Grs_{19-30}Prp_{6-15}Sps_{1-9}$, with an increase in almandine and pyrope and a decrease in grossular and spessartine components from core to rim (Fig. 6a). Retrogressed garnets show narrow resorption rims that are characterised by an increase in spessartine and a decrease in pyrope and almandine. The composition of plagioclase (oligoclase-andesine) varies from $Ab_{62-73}An_{27-38}$ in the matrix to Ab_{56-63} An_{37-44} in garnet, and $Ab_{61-64}An_{36-39}$ in the strain shadows of garnets. The X_{Mg} values (= Mg/(Mg + Fe)) of biotite varies from 0.57-0.61 in the matrix to 0.58-0.67 in garnet, and 0.52-0.58 in garnet strain shadows.

Samples HS2 and HS3 are medium- to coarse-grained garnet-kyanite-bearing schists (Fig. 4c and Fig. 5c). The mineral assemblages are dominated by muscovite, biotite, plagioclase, quartz and chlorite (late) and porphyroblasts of kyanite and garnet. Accessory minerals in the matrix include hematite, rutile, apatite, zircon and xenotime. The hematite and rutile are commonly texturally intergrown. Muscovite and biotite occur as large (>5 mm) elongated grains that form foliation-parallel aggregates to define the anastomosing S2 foliation in the schist. Large (>5 mm) recrystallized quartz and plagioclase grains are elongated parallel to the foliation. Kyanite occurs as large (5-40 mm) porphyroblasts that may overprint, but also define the S2 fabric. Garnet porphyroblasts are small (~5 mm), equidimensional, subhedral and enveloped, but also overprint the main S2 foliation. Inclusion trails of hematite, quartz, plagioclase and biotite are commonly observed in both garnet and kyanite. Garnet porpyroblasts in HS2 and HS3 have similar compositions (mol%) of $Alm_{44-52}Sps_{19-31}Prp_{10-18}Grs_{10-16}$ and $Alm_{48-55}Sps_{15-31}Prp_{10-17}Grs_{7-15}$ and show a gradual increase in almandine and pyrope, accompanied by a decrease in spessartine and

grossular components, from core to rim. The outer rims of garnet show resorption and are characterised by a sharp increase in spessartine and a decrease in almandine and pyrope components.

Plagioclase in HS2 and HS3 are either oligoclase or andesine ($Ab_{63-75}An_{26-37}$). The X_{Mg} values of biotite are similar for both samples and vary between 0.65 - 0.71.

Sample M53 is a garnet-kyanite schist with a matrix composed of muscovite, biotite, quartz and plagioclase (Fig. 5d). Accessory minerals include ilmenite, apatite and late chlorite and epidote. These phases occur in the matrix as well as inclusions in garnet. Muscovite occurs as fine, sheath-like aggregates that define an anastomosing foliation and crenulation cleavage in the rock. Biotite occurs as large, foliation-parallel grains that are texturally intergrown with muscovite, or as large, randomly oriented porphyroblasts that cut the main fabric. Plagioclase and quartz are intergrown with biotite and muscovite. Kyanite and garnet occur as large porphyroblasts that either overgrow the foliation, or are enveloped by the main S2 fabric. Garnet is almandine rich ($Alm_{59-70}Grs_{11-21}Sps_{6-16}Prp_{7-12}$) and contains inclusion trails of ilmenite, quartz, apatite and biotite. The almandine component shows a gradual increase from core to rim, whereas grossular and spessartine contents decrease rimwards (Fig. 6b). Plagioclase is oligoclase and has a composition of Ab_{79-86} An_{14-21}. The X_{Mg} value of biotite is 0.55 irrespective of textural position.

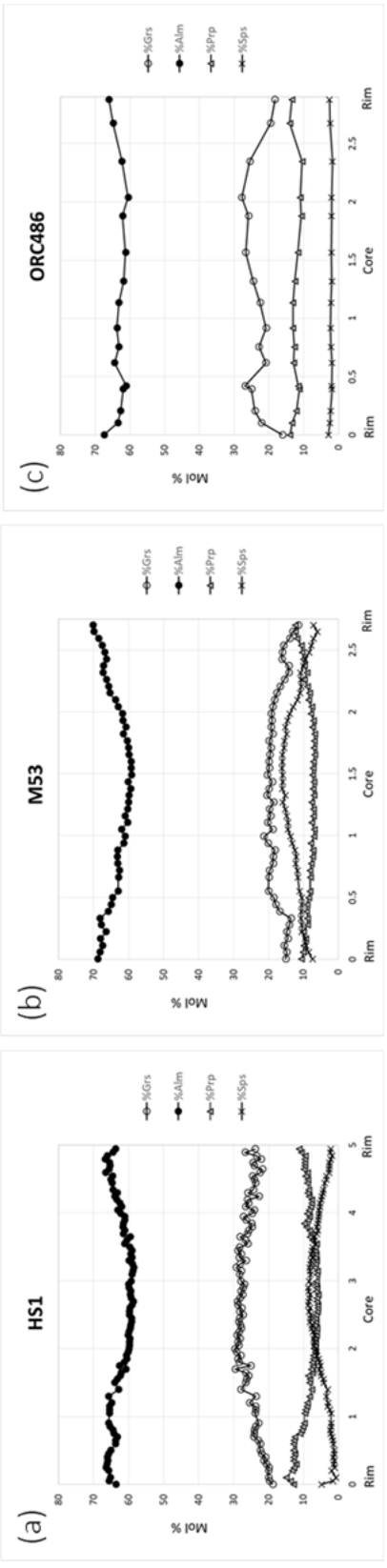

Fig 6. Garnet zoning profiles of X_{Grs}, X_{Alm}, X_{Prp} and X_{Sps} in garnet-kyanite schist from (a) the lower Damara Sequence at Hochberg (HS1), (b) upper Damara sequence (M53) and (c) basement gneiss from the Omitiomire Shear Zone.

Table 4. Representative mineral chemistry of metapelites from the Damara Sequence.

Mineral	Bt	Bt	Bt	Bt	Bt	Bt	MS	Ms	Ms	Ms
Sample	HS1	HS1	HS1	HS2	HS3	M53D	HS1	HS2	HS3	M53D
Location	grt inclusion	grt strain shadow	matrix	matrix	matrix	matrix	matrix	matrix	matrix	matrix
SiO_2	38.52	38.49	38.59	39.43	38.68	38.30	46.06	47.40	47.22	48.81
TiO_2	2.36	1.80	2.21	0.93	1.22	1.42	0.58	0.38	0.46	0.56
Al_2O_3	19.74	19.83	19.03	19.55	18.87	18.78	34.79	29.25	33.49	34.93
FeO	16.28	12.52	15.09	13.19	13.54	17.92	1.89	3.74	3.54	2.73
MgO	11.69	14.22	12.98	14.99	14.98	12.38	1.39	0.92	1.08	0.87
MnO	0.00	0.00	0.00	0.25	0.26	0.00	0.00	0.00	0.00	0.00
CaO	0.00	0.24	0.00	0.00	0.00	0.00	0.00	0.00	0.00	0.00
Na_2O	0.19	0.17	0.26	0.47	0.35	0.00	1.00	1.38	1.17	1.00
K_2O	8.98	9.00	9.28	8.97	8.97	8.93	9.60	9.32	9.40	9.14
Oxygens	22	22	22	22	22	22	22	22	22	22
Total	97.74	96.28	97.43	97.77	96.88	97.73	95.31	92.38	96.36	98.04
Formula										
Si	5.56	5.55	5.57	5.61	5.58	5.58	6.13	6.56	6.26	6.30
Ti	0.26	0.20	0.24	0.10	0.13	0.15	0.06	0.04	0.05	0.05
Al	3.36	3.37	3.24	3.28	3.21	3.22	5.46	4.77	5.23	5.31
Fe	1.97	1.51	1.83	1.57	1.63	2.18	0.21	0.43	0.39	0.30
Mg	2.52	3.06	2.80	3.18	3.22	2.69	0.28	0.19	0.21	0.17
Mn	0.00	0.00	0.00	0.03	0.03	0.00	0.00	0.00	0.00	0.00
Ca	0.00	0.04	0.00	0.00	0.00	0.00	0.00	0.00	0.00	0.00
Na	0.05	0.05	0.07	0.13	0.10	0.00	0.26	0.37	0.30	0.25
K	1.65	1.66	1.71	1.63	1.65	1.66	1.63	1.65	1.59	1.50
XMg	0.56	0.67	0.61	0.67	0.66	0.55	0.57	0.31	0.35	0.36

Mineral	Pl	Pl	Pl	Pl	Pl	Pl	Pl
Sample	HS1	HS1	HS1	HS2	HS3	HS3	M53D
Location	grt inclusion	grt strain shadow	matrix	matrix	pl core	pl rim	matrix
SiO_2	59.32	59.73	60.37	63.57	60.72	60.20	66.08
TiO_2	0.00	0.00	0.00	0.00	0.00	0.00	0.00
Al_2O_3	23.87	24.08	24.28	22.05	23.31	23.79	22.74
FeO	0.44	0.00	0.00	0.00	0.00	0.00	0.00
MgO	0.00	0.00	0.00	0.00	0.00	0.00	0.00
MnO	0.00	0.00	0.00	0.00	0.00	0.00	0.00
CaO	8.37	8.52	8.51	5.87	7.78	8.08	3.11
Na_2O	7.63	7.29	7.59	9.02	7.95	7.91	9.37
K_2O	0.00	0.00	0.00	0.00	0.00	0.00	0.00
Oxygens	8	8	8	8	8	8	8
Total	99.64	99.62	100.76	100.52	99.76	99.98	101.30
Formula							
Si	2.67	2.68	2.68	2.81	2.72	2.69	2.86
Ti	0.00	0.00	0.00	0.00	0.00	0.00	0.00
Al	1.27	1.27	1.27	1.15	1.23	1.25	1.16
Fe	0.02	0.00	0.00	0.00	0.00	0.00	0.00
Mg	0.00	0.00	0.00	0.00	0.00	0.00	0.00
Mn	0.00	0.00	0.00	0.00	0.00	0.00	0.00
Ca	0.40	0.41	0.40	0.28	0.37	0.39	0.14
Na	0.67	0.63	0.65	0.77	0.69	0.69	0.79
K	0.00	0.00	0.00	0.00	0.00	0.00	0.00
XAn	37.74	39.24	38.26	26.44	35.09	36.08	15.49
XAb	62.26	60.76	61.74	73.56	64.91	63.92	84.51

Mineral	Grt	Grt	Grt	Grt	Grt	Grt	Grt	Grt
Sample	HS1	HS1	HS2	HS2	HS3	HS3	M53	M53
Location	rim	core	rim	core	rim	core	rim	core
SiO_2	37.46	37.60	37.27	36.99	37.18	37.86	36.80	37.24
TiO_2	0.00	0.00	0.00	0.00	0.00	0.00	0.00	0.13
Al_2O_3	20.73	20.65	21.02	20.68	20.66	20.45	20.44	20.68
FeO	29.84	27.94	22.66	21.51	22.36	24.82	31.85	29.12
MgO	3.05	1.50	3.89	2.65	3.12	2.79	2.96	1.79
MnO	0.57	3.85	11.98	13.37	13.69	9.60	3.68	5.74
CaO	7.12	9.25	3.07	4.60	2.76	4.63	3.47	6.04
Na_2O	0.00	0.00	0.00	0.18	0.00	0.00	0.00	0.00
K_2O								
Oxygens	12	12	12	12	12	12	12	12
Total	98.77	100.80	99.88	99.98	99.78	100.15	99.19	100.73
Formula								
Si	3.01	2.99	2.98	2.96	2.99	3.03	2.98	2.98
Ti	0.00	0.00	0.00	0.00	0.00	0.00	0.00	0.01
Al	1.96	1.93	1.98	1.95	1.96	1.93	1.95	1.95
Fe	2.00	1.85	1.51	1.44	1.51	1.66	2.16	1.95
Mg	0.37	0.18	0.46	0.32	0.37	0.33	0.36	0.21
Mn	0.04	0.26	0.81	0.91	0.93	0.65	0.25	0.39
Ca	0.61	0.79	0.26	0.39	0.24	0.40	0.30	0.52
Na	0.00	0.00	0.00	0.03	0.00	0.00	0.00	0.00
K	0.00	0.00	0.00	0.00	0.00	0.00	0.00	0.00
XMg	0.15	0.09	0.24	0.20	0.21	0.17	0.15	0.10
%Grs	20.62	28.80	9.45	15.60	8.43	13.25	10.97	18.72
%Alm	66.20	59.04	48.41	44.38	48.33	54.44	69.46	62.51
%Prp	12.14	5.93	15.55	10.87	12.52	10.97	11.99	7.15
%Andr	0.01	0.44	0.26	1.17	0.17	0.01	0.38	0.33
%Sps	1.30	8.68	27.22	31.18	31.19	21.49	8.46	13.02

Table 5. Representative mineral chemistry of garnet-amphibole gneiss from the OSZ in the Ekuja Dome.

Mineral	amph	amph	pl	pl	pl	grt	grt
Sample	ORC486	ORC486	ORC486	ORC486	ORC486	ORC486	ORC486
Location	matrix	matrix	matrix	in grt	rim around grt	rim	core
SiO_2	41.88	42.28	63.84	61.19	62.54	37.19	37.36
TiO_2	0.71	0.78	0.00	0.00	0.00	0.00	0.00
Al_2O_3	14.46	14.49	21.38	22.45	21.80	21.44	21.58
MnO	0.00	0.00	0.00	0.00	0.00	1.28	0.84
MgO	8.81	8.89	0.00	0.00	0.00	3.49	3.16
CaO	10.38	10.43	5.15	6.80	6.03	5.42	8.25
FeO	17.87	17.88	0.00	0.00	0.00	30.53	28.18
Na_2O	2.19	2.13	9.56	8.49	9.10	0.00	0.00
Oxygens	23	23	8	8	8	12	12
Total	96.30	96.86	99.94	98.92	99.47	99.36	99.37
Si	6.35	6.36	2.83	2.76	2.80	2.97	2.97
Ti	0.08	0.09	0.00	0.00	0.00	0.00	0.00
Al	2.58	2.57	1.12	1.19	1.15	2.02	2.02
Mn	0.00	0.00	0.00	0.00	0.00	0.09	0.06
Mg	1.99	2.00	0.00	0.00	0.00	0.42	0.37
Ca	1.69	1.68	0.25	0.33	0.29	0.46	0.70
Fe	2.27	2.25	0.00	0.00	0.00	2.04	1.88
Na	0.64	0.62	0.82	0.74	0.79	0.00	0.00
Total	15.60	15.57	5.02	5.02	5.02	8.00	8.01
XMg	0.47	0.47				0.17	0.17
An			22.95	30.70	26.80		
Ab			77.05	69.30	73.20		
%Grs						16.16	24.53
%Alm						67.48	61.84
%Prp						14.00	12.59
%And						0.06	0.07
%Sps						2.91	1.91

5.2. Mesoproterozoic rocks

Metamorphosed mafic rocks from the Mesoproterozoic basement gneisses of the Ekuja Dome comprise amphibolite, hornblende-biotite gneiss and biotite-epidote schist (Fig. 3d, e). The hornblende-biotite gneisses and biotite schists represent variably retrogressed and possibly metasomatised equivalents of original amphibolites that were retrogressed and hydrated along the Omitiomire shear zone (Fig. 5e-h; Steven et al., 2000; Kitt et al., 2016).

Amphibolite gneiss (ORC486) contains amphibole (hornblende tschermakite), garnet, plagioclase (oligoclase-andesine, An_{25} to An_{35}), quartz and accessory minerals, ilmenite, Cr-magnetite, zircon, apatite and late biotite, titanite and chlorite (Fig. 5e-g). The gneissic fabric (S2) is defined by the preferred orientation of flattened grains of amphibole, plagioclase and quartz. Large (~5 mm) anhedral, poikiloblastic garnet occurs with inclusions of Cr-magnetite, ilmenite, plagioclase, quartz and hornblende (Fig. 3d and Fig. 5e, f). The garnet porphyroblasts are highly corroded due to the intense resorption by plagioclase. Garnet has a composition $Alm_{61-67}Grs_{16-28}Prp_{10-14}Sps_{2-3}$ that shows small increases in almandine and a decrease in grossular from core to rim (Fig. 6c). The composition of plagioclase (mainly oligoclase) ranges from $Ab_{72-77}An_{23-29}$ in the matrix to $Ab_{69-80}An_{20-31}$ in garnet to $Ab_{73-78}An_{22-27}$ along the rim of garnet. Hornblende in the matrix has an X_{Mg} of 0.40-0.47, whereas the X_{Mg} of hornblende included in garnet varies between 0.33 and 0.39.

6. P-T condition modelling

The petrographic observations, whole-rock geochemistry and mineral chemistry allows for the estimation of the metamorphic conditions during the evolution of the metapelites and metabasites. The peak mineral assemblages in the Damara metapelites (samples HS1-3, M53) consist primarily of biotite + muscovite + garnet + kyanite + quartz and plagioclase, indicative of broadly amphibolite-facies metamorphic conditions. Similar conditions are indicated by the amphibole + plagioclase + garnet + quartz assemblage in amphibolite (sample ORC486) from the Ekuja basement.

The metamorphic conditions and PT evolution of the metapelites and metabasites were constrained by calculating pseudosections using the THERIAK-DOMINO modelling software (De-Capitani and Petrakakis, 2010) and an updated 2003 version of the internally consistent thermodynamic dataset of Holland and Powell (1998), and mineral activity-composition (a-x) relationships based on the Thermocalc 5.5 dataset, as coded by Doug Tinkham (Laurentia University, Canada). For the metapelites modelling was done within the $MnO-Na_2O-CaO-K_2O-FeO-MgO-Al_2O_3-SiO_2-H_2O-TiO_2$ (MnNCKFMASHT) system for HS1 and M53, and the $MnO-Na_2O-CaO-K_2O-FeO-MgO-Al_2O3-SiO_2-H_2O-TiO_2-O_2$ (MnNCKFMASHTO) system for samples HS2 and HS3. The smaller chemical system used for HS1 and M53, compared with HS2 and HS3, is justified by the lack of an Fe^{3+}-bearing accessory phase as part of the peak-metamorphic assemblage in this sample. In the case of HS2 and HS3, the minimum Fe^{3+} content of the rock required to stabilise the peak-metamorphic mineral assemblage was estimated by an isobaric T-XFe^{3+} section calculated at 7 kbar, prior to calculation of the P-T pseudosection.

For the amphibolite sample ORC486, the Na_2O-CaO-FeO-MgO-Al_2O_3-SiO_2-H_2O-TiO_2 (NCFMASHT) system was used for pseudosection calculations. K_2O was omitted because of the low biotite content in the rock and because the amphibole a-x models currently available in Theriak-Domino do not take into account substitutions involving K_2O in amphiboles, which would affect their stability. ORC486 contains minor Cr-rich magnetite as an accessory phase and titanite. Preliminary calculations in the system NCFMASHTO system found no mutual stability for a peak metamorphic assemblage containing magnetite and we suspect that magnetite in ORC486 has been stabilised by high Cr contents. Due to the lack of a-x models for silicate and oxide minerals that incorporate Cr-end-members we have undertaken calculations in the Fe^{3+}- and Cr-free system. The activity-composition models used with the dataset of Holland and Powell (1998) are: plagioclase (C1 field; Holland and Powell, 2003), chlorite (Mahar et al., 1997, as modified by Tinkham et al., 2001), staurolite (Holland and Powell, 1998), cordierite (Holland and Powell, 1998), garnet and biotite (White et al., 2005), muscovite (Coggon and Holland, 2002; with their pyrophillite and margarite members excluded), ilmenite-hematite (White et al., 2000), clinopyroxene (Green et al., 2007), and hornblende (Diener et al., 2007, updated by Diener and Powell, 2012). Quartz, rutile, titanite, and Al_2SiO_5 polymorphs were assumed to be pure end-member phases while H_2O was assumed to be saturated in all assemblages. The bulk rock compositions used are presented in Table 1 and calculated pseudosections presented in Figure 7 and Figure 8. None of the samples in this study show evidence for partial melting.

For samples M53 and HS1, P-T conditions for the beginning of garnet growth, and thus a point on the prograde P-T-t path, were estimated by contouring the relevant pseudosection with garnet core compositional isopleths (Vance & Holland, 1993). No attempt was made to do this for samples HS2 and HS3 because: (1) HS1-3 were sampled close together in the field, and hence likely experienced the same P-T-t path. Prograde garnet growth strongly fractionates elements such as Mn and Fe at low temperatures. As a result, the effective bulk composition may change and deviate substantially from the whole-rock composition during late stages of the garnet growth (Marmo et al., 2002). The effect of prograde garnet growth and associated element fractionation on the effective bulk composition increases with increasing garnet abundance. In this study, no attempt was made to remove the components sequestered into the cores of garnet growing in the metapelites because of the low garnet modal abundance in these rocks. Garnet in metabasite ORC486 is compositionally weakly zoned to unzoned, except where it was partially resorbed to form hornblende-plagioclase intergrowths.

6.1. Results

6.1.1. Garnet-kyanite-mica schist from the OVFC (HS1-HS3)

The pseudosections calculated for garnet-kyanite schist samples HS1-HS3 from the lower Damara Sequence metasediments at Hochberg are shown in Fig. 7a-c. The samples were collected from similar structural levels and have therefore likely experienced similar P-T conditions. The pseudosection calculated for the bulk composition of HS1 contains an inferred peak-metamorphic assemblage of garnet + kyanite + biotite + plagioclase + muscovite + rutile + quartz that is constrained in a relatively small field between 6.75 and 7.50 kbar and 625-665 °C (Fig. 7a). The peak-metamorphic assemblage is bounded by the loss of

kyanite at higher pressures and the loss of muscovite at lower pressures. Kyanite-free, garnet-staurolite ± sillimanite fields occur at lower temperature and rutile becomes stable above 6 kbar. Garnet-bearing assemblages appear above 5.5kb at lower temperatures and at ~4 kbar above 570 °C. The calculated isopleths of garnet core compositions for spessartine, almandine and grossular end-members intersect in a Pl-Grt-Bt-Chl-Ms-Rt field and models the first growth of garnet at 7.4 kbar and 560 °C. The inferred P-T-t segment is consistent with a prograde P-T vector of near-isobaric heating at ~ 7 kbar. At ~560 ˚C the garnet core isopleth intersection is ~1.5 kbar above the garnet-in line, suggesting that either the garnet-in reaction has been overstepped or, more likely, that the thin section has not exposed the true garnet core composition in this rock. The partial to almost complete replacement of garnet by unoriented biotite and plagioclase (Fig. 5a, b) suggests that the sample underwent post-peak metamorphic decompression.

Sample HS2 contains the peak-metamorphic assemblage garnet + kyanite + biotite + muscovite + hematite + plagioclase + quartz. In the calculated pseudosection (Fig. 7b) this assemblage occurs over a relatively large stability field between 7.1 and ~10 kbar and 625-670 °C. Kyanite is lost at lower temperatures and pressures, where staurolite or sillimanite become stable. At higher pressures and slightly lower temperatures, paragonite and epidote are stable. Garnet is generally stable at pressures above 6-7 kbar and temperatures higher than 540 °C. Sample HS3 contains the same peak-metamorphic assemblage as HS3, which is stable in a large field between 6.5 and 9.3 kbar and 640-675 °C (Fig. 7c). At lower pressures and temperatures, sillimanite or staurolite are introduced at the expense of kyanite. Garnet occurs at pressures above 6 kbar for temperatures higher than 550 °C. Because the three HS samples originate from the same field locality it is likely that they experienced the same peak P-T conditions, as defined by the mutual overlap in inferred peak metamorphic phase fields in Fig. 7c (i.e. inferred peak P-T conditions of 7-9.25 kbar and 640-670 °C).

6.1.2. Garnet-kyanite-mica schist from the OMSB (M53)

The pseudosection calculated for sample M53 is presented in Fig. 7d. The inferred peak assemblage of garnet + kyanite + muscovite + biotite + plagioclase + ilmenite defines a small field between 6.25 and 6.75 kbar and 630-650 °C. It is bounded by large kyanite-free fields at both higher and lower pressures, and temperatures below 630 °C. At lower pressures and temperatures, kyanite is replaced by staurolite or sillimanite. Garnet is introduced at pressures between 4 and 5 kbar and at temperatures higher than 560 °C. At lower temperatures, garnet only occurs above 6 kbar. Calculated isopleths of garnet core composition for spessartine, almandine and grossular intersect in a large field of Pl-Grt-Bt-Chl-Ms-Ilm, and models the first growth of garnet at ~6.75 kbar and 555 °C. The isopleth intersection point is not as far displaced from the garnet-in line as for HS1, suggesting that most likely the thin section from M53 was cut closer to true garnet cores than in HS1. As with the case of HS1, the garnet core isopleth intersection suggests a prograde P-T-t segment that involves near-isobaric heating.

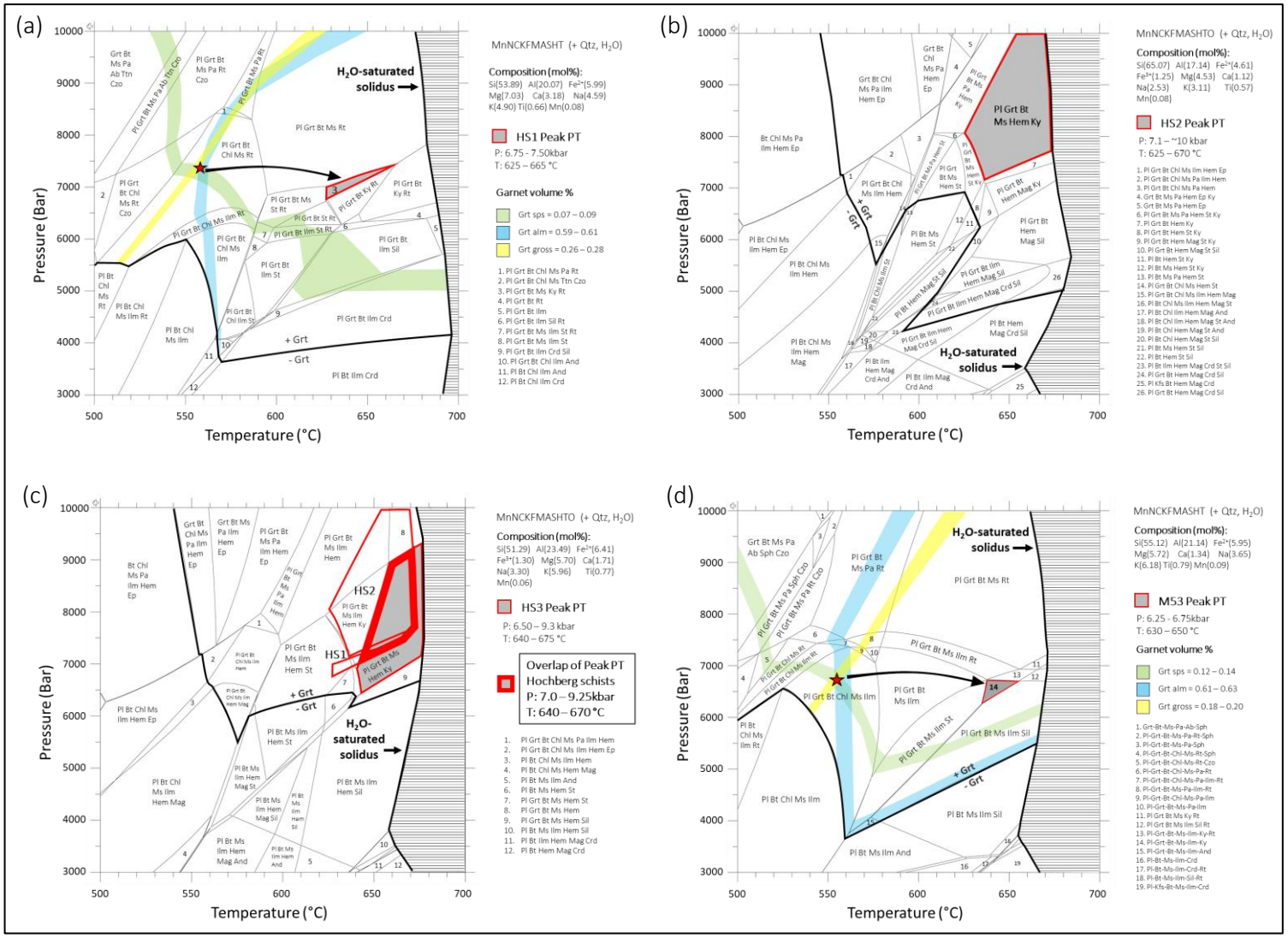

Fig. 7. Pseudosections for Damara metapelites. (a-c) Garnet-kyanite schist samples (HS1-HS3) from Hochberg and (d) a garnet-kyanite schist sample (M53) taken from the Kuiseb schist.

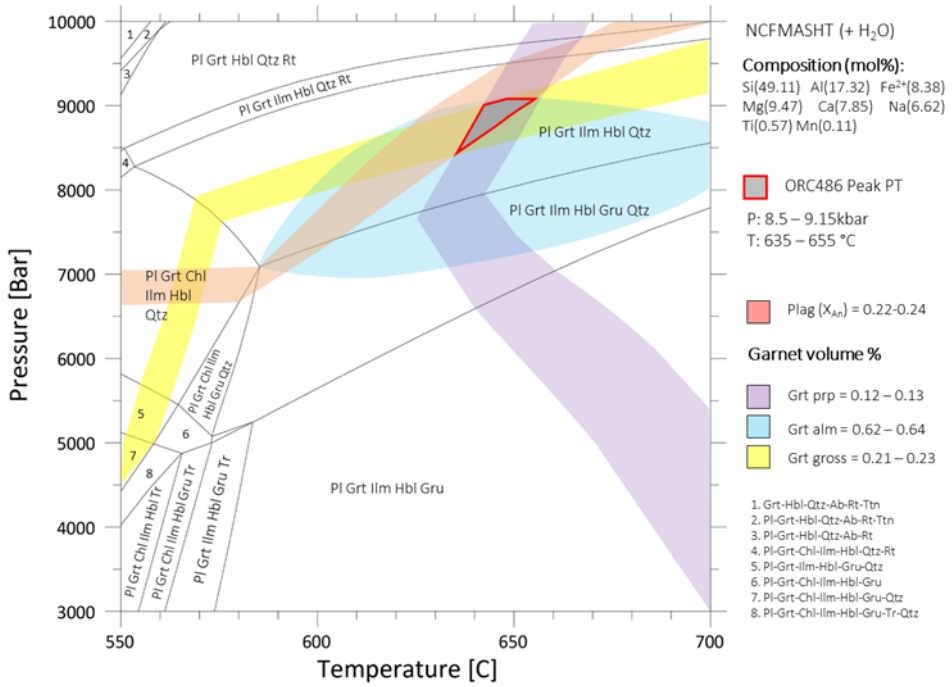

Fig 8. Pseudosection for garnet-amphibole gneiss in the Ekuja basement dome.

6.1.3. Amphibolite from Ekuja basement from the EONC (ORC486)

The pseudosection for amphibolite sample ORC486 from the Ekuja basement is presented in Fig. 8. The inferred peak-metamorphic assemblage is comprised of garnet, hornblende, plagioclase, ilmenite and quartz. This assemblage is stable in a large field between 7 kbar and 9.75 kbar and temperatures of 555-700 °C. Hornblende is stable over the whole P-T range, but also occurs with grunerite (P < 8 kbar and T > 560 °C) and tremolite (P < 5.5 kbar and T < 580 °C). At higher pressures rutile is introduced, while ilmenite is stable for most of the pseudosection at pressures below ~9 kbar. Chlorite is introduced below 8 kbar and 580 °C, while titanite occurs at pressures above 9.5 kbar and temperatures below 560 °C. Garnet is stable in all fields. Garnet porphyroblasts from metabasite ORC486 are partially replaced by intergrowths of hornblende and plagioclase that post-date penetrative deformation and that are interpreted to reflect a component of post-peak metamorphic decompression. Compared to garnet porphyroblasts from the structurally overlying kyanite schists these garnets do not show evidence for prograde growth zoning. Instead, the garnet porphyroblasts from ORC486 are characterised from core to near-rim (i.e. within ~500 µm of the rim) positions by flat compositional profiles for spessartine content, relatively uniform (2-4 mol% variation) in almandine and pyrope contents, and irregular variation of up to ~8 mol% in grossular content. In contrast the outermost portions of the garnet are characterised by rimwards decreases in grossular, and increases in almandine and, to a much lesser extent, pyrope and spessartine content. We interpret the compositional profiles in the garnets from ORC486 to reflect two processes: (i) incomplete homogenisation of prograde growth zoning at elevated temperatures;

and (ii) modification of garnet rim compositions by retrograde garnet-consuming net transfer reactions. Incomplete homogenisation of growth zoning by volume diffusion is consistent with the observation that grossular exhibits the largest concentration range in the garnet interiors; the diffusivity of Ca in garnets is well known to be significantly lower than that of the other divalent cations in garnet (e.g. Vielzeuf et al., 2007). The decreasing grossular contents in the near-rim region of the porphyroblasts are consistent with the growth of texturally late plagioclase and hornblende that replace the garnet. Because of the effects of incomplete homogenisation and subsequent modification of the near-rim garnet compositions by post-peak garnet consumption we have used the compositions of garnet with the lowest grossular contents ($Alm_{62-64}Prp_{12-13}Grs_{21-23}Sps_2$) immediately inboard of the these near-rim zones, combined with the composition of matrix plagioclase (X_{An} = 22-24) to contour the P-T pseudosection in order to best estimate peak P-T conditions in the metabasite. The intersection of the calculated almandine, pyrope and grossular isopleths from the garnet core, together with the X_{An} of matrix plagioclase, constrains the peak PT conditions between 8.5 and 9.15 kbar and 635-655 °C.

7. Geochronology

7.1. Xenotime U-Pb LA-ICP-MS geochronology

The textural relationships and internal zoning of xenotime grains in garnet-kyanite schists from Hochberg are presented in the BSE images in Fig. 9. The xenotime grains occur as euhedral to subhedral grains in the matrix of the schist or associated with garnet porphyroblasts. In sample HS2, three xenotime grains (HS2A to HS2C) are texturally intergrown with biotite and muscovite in the matrix (Fig. 9a-c). The unzoned to weakly zoned grains vary between 60 µm and 100 µm in diameter, which allowed for the in situ analyses of 19 spots (Fig. 9d-f). Analytical data are characterised by high U concentrations (1345-4255ppm) and Th/U ratios that range between 0.14 and 0.3 (Table A3 in supplementary material). In the Concordia diagram, the overall data array for HS2 yielded an upper intercept of 513.5 ± 6.1 Ma and a lower intercept age of -143 ± 300 Ma (MSWD = 0.33) (Fig. 10a). The lower intercept suggests minor recent Pb loss. A subset (n = 15) of the analyses are concordant and gave a concordia age of 514.7 ± 2.4 Ma (2σ; MSWD (C+E) = 1.16).

Xenotime grains in sample HS3 are found in three textural positions (Fig. 9g, j): (i) intergrown with muscovite in the matrix (HS3A and HS3B), (ii) next to hematite as an inclusion trail in garnet (HS3C) and (iii) associated with coarse muscovite and biotite that replace garnet along the garnet rim (HS3D). The four xenotime grains (HS3A to HS3D) vary in size between 50 µm and 200 µm and allowed for 27 in situ spot analyses (Fig. 9g-l). The analytical data are characterised by very high U concentrations that vary between 1398 ppm and 8337 ppm and Th/U ratios between 0.12 and 0.34 (Table A3 in supplementary material). The xenotime inclusion in garnet (HS3C) has the highest U contents whereas the xenotime along the garnet rim (HS3D) has the lowest concentration of U. Regardless of textural position, all of the in situ analyses plot on the same discordia line segment on the Concordia diagram, yielding an upper intercept of 512.9 ± 4.2 Ma and a lower intercept of -274 ± 290 Ma, with the latter again suggesting minor recent Pb loss (Fig. 10b). A concordant cluster of 21 analyses yielded a concordia age of 517.1 ± 2 Ma (2σ; MSWD (C+E) = 0.88).

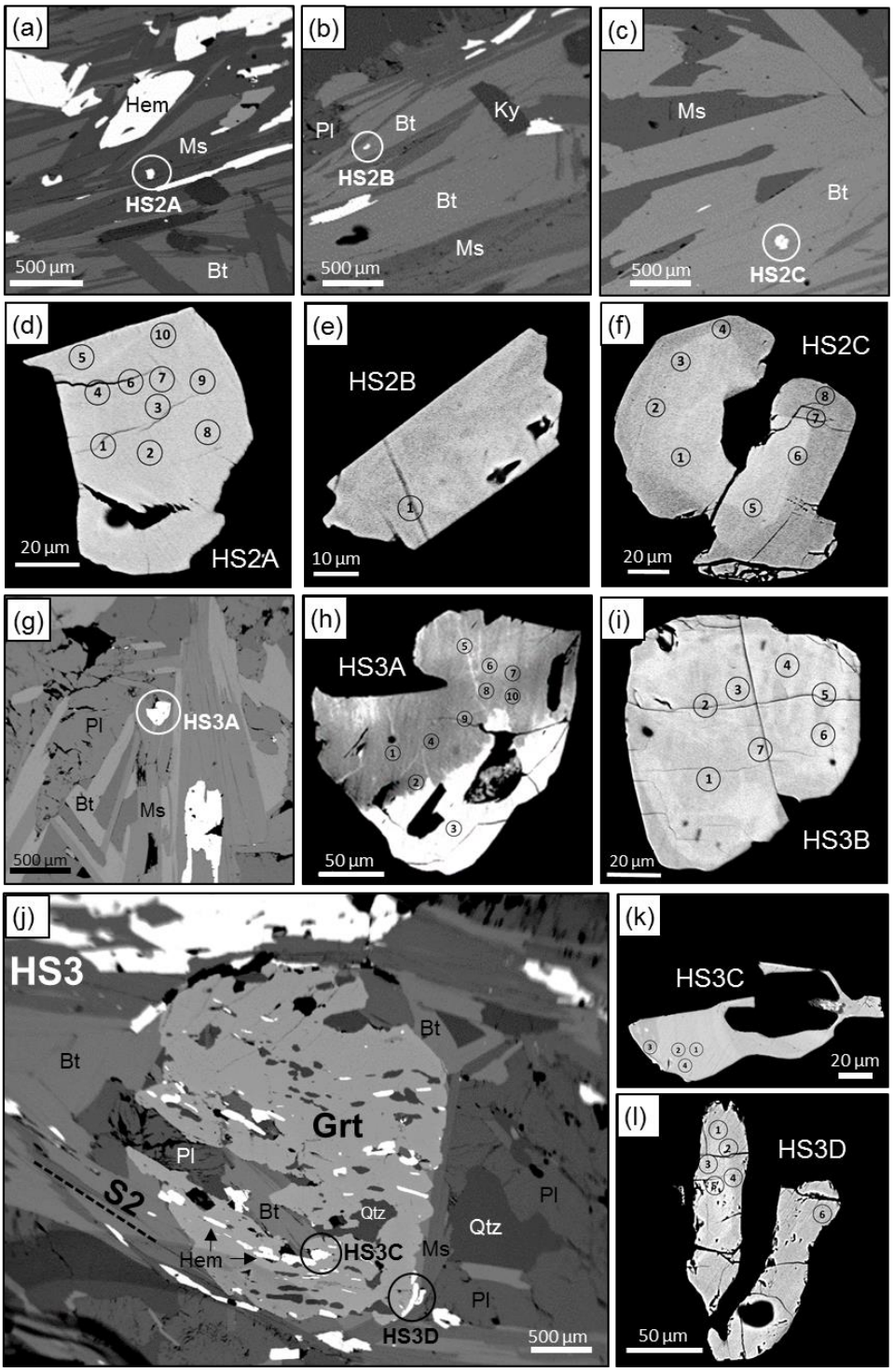

Fig. 9. Back scattered electron (BSE) images of xenotime grains in polished thin sections of garnet-kyanite schist from Hochberg showing textural relationships, internal zoning and U-Pb dating spots. (a-c) Sample HS2 showing xenotime grains texturally intergrown with muscovite and biotite in the matrix of the schist. (d-f) Close up of xenotime grains in HS2. (g) Sample HS3 showing xenotime intergrown with muscovite in the matrix of the schist. (h-i) Close up of xenotime grains (j) Sample HS3 showing the association of xenotime with garnet. HS3C is a S2 parallel xenotime inclusions in garnet and HS3D xenotime in (late) biotite that formed from the breakdown of garnet. (k-l) Close up of xenotime grains.

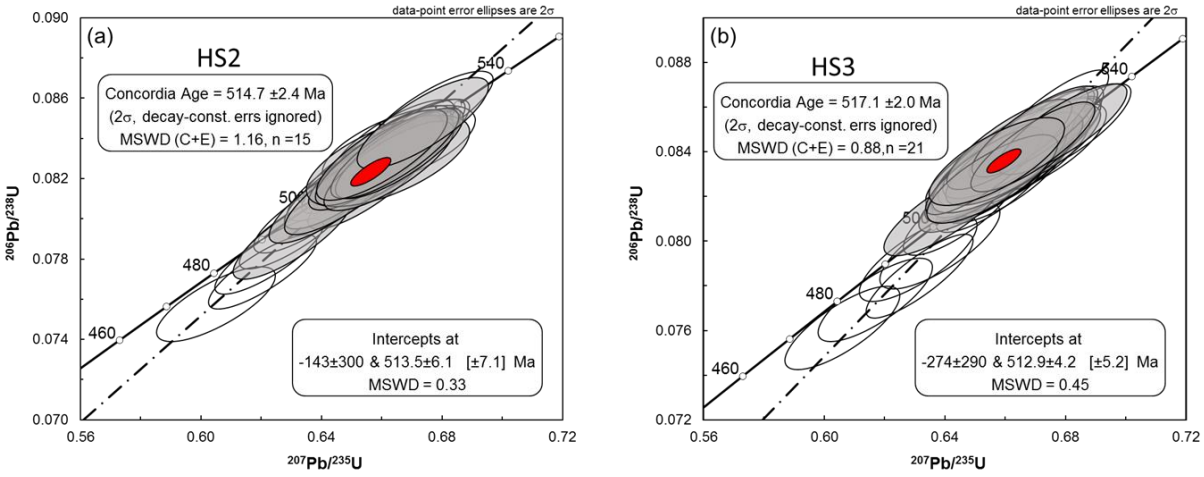

Fig. 10. U-Pb concordia diagrams obtained through in-situ U-Pb LA-SF-ICP-MS isotopic analysis of xenotime in garnet-kyanite schist from the lower Damara Sequence at Hochberg. MSWD (C + E) is the mean square of weighted deviations for the aggregated concordance and equivalence.

7.2. Ar-Ar geochronology

In order to constrain the timing of shearing and exhumation, biotite and amphibole were separated from samples of amphibole-biotite gneiss (ORC484) and biotite-epidote schist (ORC479a) with relic amphibole-biotite gneiss layers (ORC479b) that make up the Omitiomire Shear Zone (Fig. 2d and Fig. 5h). In addition, amphibole was separated from an unaltered amphibolite sample (BAR) that was collected on the farm Barreshagen some kilometres away (Fig. 2a and Fig. 5g). It is largely composed of hornblende and plagioclase that define a gneissic fabric with variable amounts of minor quartz, biotite and accessory minerals that include titanite. Sample ORC484 has a similar composition to ORC486, but includes some retrograde biotite. Hornblende, plagioclase and quartz define a gneissic S2 fabric that envelope large garnet prophyroblasts that appear highly corroded due to intense resorption by plagioclase and quartz.

Sample ORC479a contains biotite, epidote, quartz, plagioclase and hornblende (Fig. 3e and Fig. 5h). Accessory minerals include titanite, chlorite, apatite, rutile and chalcocite. Sheet-like aggregates of biotite define the anastomosing S2 fabric that wraps around large porphyroblasts of epidote and relic hornblende or plagioclase. Large (up to 10 mm) anhedral epidote porphyroblasts are strongly poikilitic and contain inclusions of hornblende, plagioclase, quartz, titanite, rutile, ilmenite and chalcocite. Epidote overgrows the main biotite-dominated fabric, but is also enveloped by biotite, suggesting that its growth was broadly syntectonic. Smaller grains of epidote and titanite show a preferred alignment parallel to the main schistosity.

$^{40}Ar/^{39}Ar$ dating was carried out in the noble gas laboratory of the SPECTRUM analytical facility at the University of Johannesburg, as described by Makhubela et al. (2017) following earlier work of Phillips et al., (1998, 1999). Irradiation was done in the SAFARI1 nuclear reactor at Pelindaba, Pretoria, operated by NTP®, a subsidiary of the Nuclear Energy Corporation of South Africa (NECSA). With the reactor running at 20 MW, the samples were irradiated for 20 hours (Phillips et al., 1999; Barton et al., 2003). Stepwise heating (mostly 12-16 steps) was done by a defocused beam from a SPECTRON® continuous Nd-YAG 1064 nm laser, capable of producing up to 9W in Too mode. The argon isotopes were measured in seven cycles using a Johnston electron multiplier detector operated in analogue mode. The total ^{40}K decay constant value used is (5.554 ± 0.014) × 10-10 yr-1 (Kossert and Günther, 2004; Renne et al., 2010). Fluence monitors placed at the bottom and top of the stack were: Hb3GR amphibole (1080.4 ± 1.1 Ma, Renne et al., 2010), McClure Mountain amphibole (MMhb, 523.1 ± 1 Ma, Renne et al., 1998), and Fish Canyon sanidine (FCs, 28.201 ± 0.046 Ma, Kuiper et al., 2008). Measurements, run regressions, corrections and age calculations were done using software developed in-house, which includes full error propagation (including uncertainties of the decay constant and J-values) by Monte Carlo simulations. The full analytical data set and further details are given in Table A4 in the supplementary material.

7.2.1. Results

A summary of the $^{40}Ar/^{39}Ar$ dating results of biotite and amphibole from mafic gneisses and schists of the EONC of the Ekuja basement dome is presented in Fig. 11. The results show a range of plateau and near-plateau ages from 560 to 515 Ma. The oldest ages are associated with amphibole separates from an unaltered amphibolite sample (BAR). The pooled gas ages (>95% of ^{39}Ar released) of the duplicates are identical and well within the 95% confidence limits, which lends confidence in the result although some disturbance is seen in the age spectra (Fig. 11a, b). Significantly younger ages were returned for the OSZ samples. Amphibole separate for sample ORC484, a partially retrogressed amphibolite (now hornblende-biotite gneiss) from the OSZ, show an undisturbed plateau age of 529.5 ± 7.5 Ma (Fig. 11c). Duplicate analyses of biotite from the biotite-epidote (± hornblende) schist sample ORC479-1a yield plateau ages of 526.4 and 521.9 Ma, with 95% confidence error limits (± 3.5 and ± 3.6 Ma) Ma overlapping between 523 and 525.5 Ma (Fig. 11e, f). The plateau age for biotite from ORC479-1b (523.7 ± 3.9 Ma) falls in this range (Fig. 11h). Amphibole separates from sample ORC479-1a yield a near-plateau age of 527.5 ± 5.8 Ma (duplicated by a one-step age, see Table A4 in supplementary material), which also overlaps within error limits with the three biotite ages (Fig. 11d). However, amphibole from ORC479-1b yields a plateau age of 515.2 ± 6.2 Ma, significantly (outside 95% confidence limits) younger than the other separates (Fig. 11c).

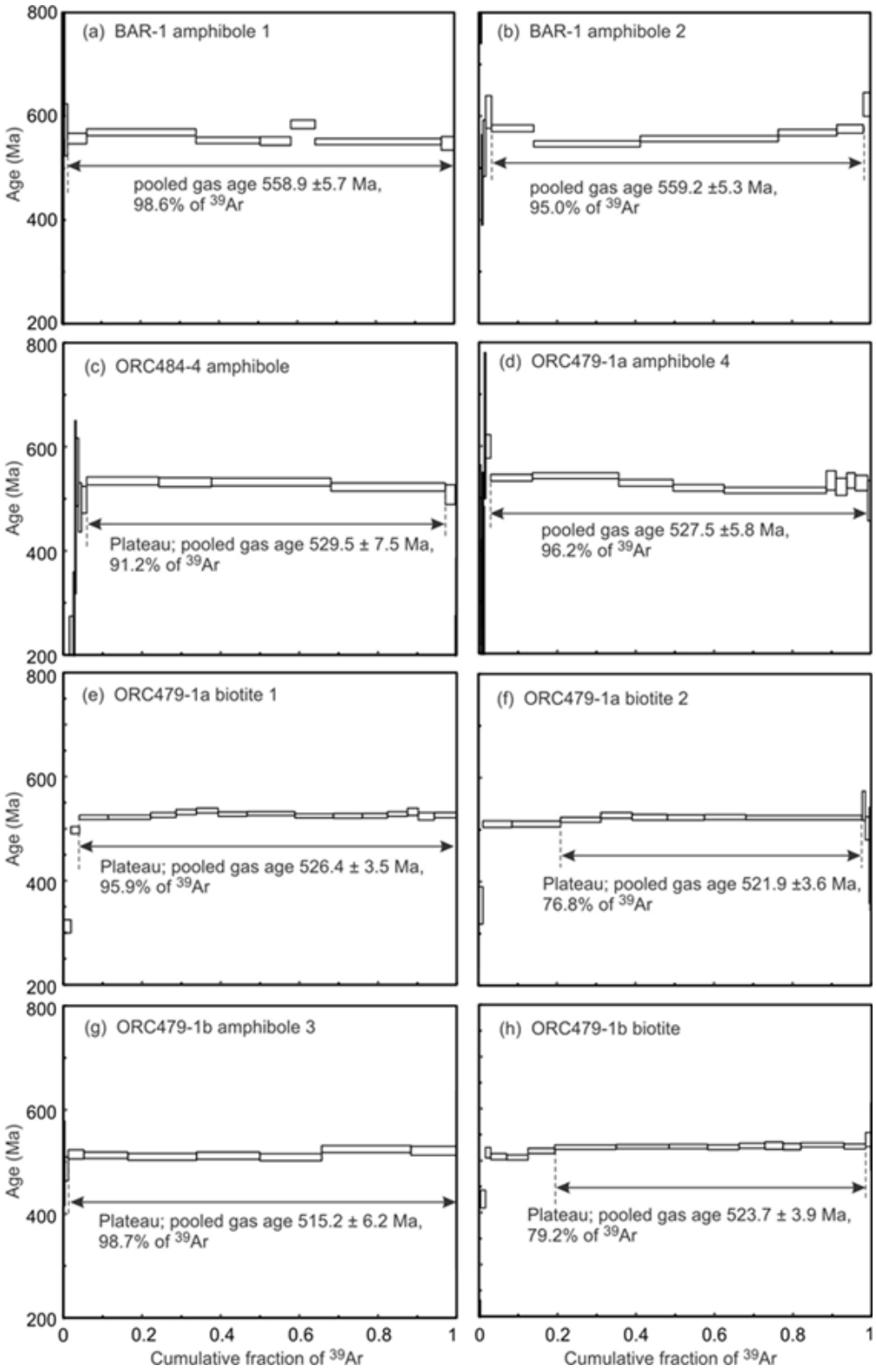

Fig. 11. $^{40}Ar/^{39}Ar$ step heating release spectrum diagrams showing calculated for (a,b) amphibole in amphibole gneiss from Barreshagen, (c) amphibole in amphibole gneiss from the Omitiomire Shear Zone, (d,g) amphibole in biotite-epidote schists from the Omitiomire Shear Zone and (e,f,h) biotite in biotite-epidote schist from the Omitiomire Shear Zone. Box heights indicate 95% confidence limits as listed. One-step result for ORC479-1a amphibole 3 (not shown, see Table A4 in the supplementary material) is identical to ORC479-1a amphibole 3 (d).

8. Discussion

8.1. Interpretation of P-T-t data

The P-T and geochronological data do not allow for a complete reconstruction of P-T-t paths of the various lithological units of the DLSZ. However, the estimated peak-metamorphic P-T conditions and the timing of peak metamorphism, together with the subsequent retrogression of rocks provide information on at least segments of the respective P-T loops. Our study presents the first P-T estimates from basement rocks in the DLSZ. One of the key observations of this study is that basement gneisses and the structurally overlying metasediments describe different P-T-t paths that allude to more complex dynamics of burial and exhumation than hitherto described for the SZ prism. These aspects will be discussed in the following section.

Amphibolite gneisses from basement rocks in the Ekuja Dome yield peak-metamorphic P-T conditions of 8.5-9.15 kbar and 635-655°C (Fig. 8). This suggests the burial of the rocks to depths of 35 km, assuming a crustal density of 2.7 g/cm^3. Garnet zoning patterns (Fig. 6c) and breakdown textures (Fig. 3d and Fig. 5e, f) point to the subsequent decompression of the rocks, as is evidenced by the retrogression of amphibole-plagioclase assemblages in the OSZ to biotite and epidote (Fig. 5g, h). Top-to-the-south shear sense indicators in retrograde shear zones such as the OSZ and the prominent north-south trending rodding lineation (L2) are parallel to the regionally developed stretching lineation in basement gneisses of the Ekuja Dome and directly overlying schists at Hochberg (Fig. 2b, Fig. 3a, e and Fig. 4d), but normal to the E-trending folds and fabrics of the structurally overlying Kuiseb Formation prism sediments (e.g. Kasch, 1986; Kitt et. al., 2016). The latter relate to the imbrication of Kuiseb metasediments during northward subduction. The N-S trending constrictional fabrics and associated kinematics record, in turn, the exhumation, return flow and southward expulsion of the Ekuja basement gneisses and their immediate cover in the structurally deeper parts of the prism (Kitt et al., 2016). $^{40}Ar/^{39}Ar$ dating of S2 parallel biotite and amphibole from mylonitic retrograde shear zones (OSZ) at Omitiomire in the Ekuja Dome (EONC) yields ages between ca. 530 Ma and 515 Ma, while an unaltered sample (BAR) some ~10 km kilometres away yield an age of ca. 559 Ma (Fig. 2a and Fig. 11). This age range also overlaps with U-Pb dating of titanite in biotite-epidote schist from the OSZ which returned ages of 520-485 Ma (Maiden et al., 2013).

The interpretation of $^{40}Ar/^{39}Ar$ age data from high-grade metamorphic rocks is not without problems and apparent ages can be considered to represent either cooling or crystallization ages (Villa, 1998; Di Vincenzo et al., 2004). Biotite-epidote assemblages, the pervasively recrystallized mineral textures and oxygen isotope thermometry on mineral pairs from the mylonitic shear zones point to temperatures of > 500°C and as high as 600°C during deformation and retrogression in the mylonitic shear zones (Kitt et al., 2017). These temperatures are significantly higher than the 300°C commonly assumed to be the "closure temperatures" for biotite, although closure temperatures strongly depend on the grain size of minerals, cooling rate and diffusion parameters (Dodson, 1973). Notably, biotite ages fall in the same range as amphibole ages (Fig. 11). In fact, the youngest (plateau) age of 515 Ma was obtained from an amphibole. Given the much higher thermal retentivity of amphibole than biotite for Ar systematics (Villa, 1998), this observation rules out a slow cooling interpretation. Villa (1998) pointed out

that temperature has a limited effect on isotopic exchange compared to the effects of fluids and deformation. Although the concept of cooling ages is still widely accepted, several studies in recent years have shown that micas retained isotopic signatures even when exposed to PT conditions well above their closing temperatures (Villa, 1998; Maurel et al., 2003; Rodriquez et al., 2003; Di Vincenzo et al., 2004; Di Vincenzo et al., 2007). Similarly, Hermansson et al., (2008) demonstrated the structural control of age distribution in several generations of $^{40}Ar/^{39}Ar$ hornblende ages, with the oldest ages restricted to tectonic lenses and the youngest ages associated with enveloping high-strain shear zones.

Based on the above considerations we interpret the $^{40}Ar/^{39}Ar$ biotite ages as dating the crystallization of biotite in the OSZ during the open-system replacement of the amphibole-plagioclase assemblages in amphibolite gneisses by biotite and epidote. This constrains the timing of retrogression in the OSZ and exhumation of the Ekuja Dome to between 526.4 ± 3.5 Ma and 521.9 ± 3.6 Ma. Although amphibole in an unaltered sample (BAR) has retained older $^{40}Ar/^{39}Ar$ ages of 558.9 ± 5.7 Ma and 559.2 ± 5.3 Ma, the disturbance of the spectra (Fig. 11a, b) probably results from metamorphism post-dating that age, as shown by the other samples. Notably, the ~559 Ma age from the Ekuja Dome corresponds with a reported timing of collision between Kalahari and Congo cratons around 555-550 Ma (Gray et al., 2006; Goscombe et al., 2017). Furthermore, the slightly older $^{40}Ar/^{39}Ar$ ages from the Ekuja Dome suggests that the $^{40}Ar/^{39}Ar$ ages do not record cooling ages but rather crystallization ages and therefore the relative timing of deformation and exhumation of the Ekuja Dome.

Maximum pressure estimates of 7-9.25 kbar for the directly overlying metasediments at Hochberg (HS1-HS3) indicate their burial to depths of 27-35 km (Fig. 7a-c). Garnet-kyanite schist (sample M53) from the Kuiseb Formation, some 30 km to the southwest, record somewhat similar temperature estimates but at lower peak pressures of 6.25-6.75 kbar, which translate to a burial depth of only 25 km (Fig. 7d). The peak temperature estimates in the metapelites are similar to those in the underlying basement gneisses but are characterised by an isobaric heating event from ~560 °C to peak temperatures of ~ 650 °C (Fig. 7a, d). A similar isobaric heating of the prism rocks by 60-80°C was recorded by Cross et al. (2015) in the far western parts of the SZ, which these authors related to the subduction of the ridge during closure of the Khomas Sea (Meneghini et al., 2014). Like the basement rocks, garnet zoning patterns and reaction textures in the Hochberg schists indicate that peak metamorphic conditions were followed by decompression (Fig. 4b, Fig. 5b and Fig. 6).

U-Pb dating of xenotime in the Hochberg schists returned almost identical ages with overlapping margins of error between 517 and 515 Ma (Fig. 10). Although U-Pb dating of xenotime is less established than monazite, a high U (and Th) content and low concentration of common Pb, makes it ideal for U-Pb dating (Cherniak, 2006). A slow diffusivity of Pb in xenotime (Cherniak, 2006), means that the ages obtained are not cooling ages, but crystallization ages. Like monazite, the growth of xenotime has been linked to both prograde and retrograde reactions because the concentration of phosphorus and REE (e.g. yttrium) in these phases can be coupled or are in near equilibrium, with silicate phases (such as garnet) during metamorphism (Spear and Pyle, 2002; Pyle and Spear, 2000; Pyle et al., 2001; Mahan, 2006; Di

Vincenzo, 2007; Kim, 2009). This implies that detailed textural and petrographic studies and the correlation of accessory and major phases along a PT path, can give temporal information on the P-T evolution of a rock (Pyle and Spear, 1999; Pyle et al., 2001; Foster, 2000, 2002; Spear and Pyle, 2002). Xenotime in garnet-kyanite schist from Hochberg is found in three textural positions namely, (i) as inclusions in S2 parallel biotite and muscovite in the matrix of the schists, (ii) as S2 parallel inclusion trails in garnet, and (iii) as inclusions in late biotite and muscovite along the rim of garnet (Fig. 9). The S2-parallel orientation of xenotime inclusions in garnet and the association of xenotime with peak assemblages (biotite and muscovite) in the matrix indicate formation as a prograde phase, whereas xenotime along garnet rims where likely overgrown by biotite and muscovite during retrograde metamorphism.

8.2. Implications for subduction-accretion processes in the DLSZ

Even when considering the error margins, the geochronological data suggest that the Ekuja basement gneisses, exhumed from ca. 35 km, were already on their exhumation path at ca. 525 Ma, when the overlying schists were still undergoing burial at ca. 517 Ma. This also suggests that final juxtaposition of basement gneisses and schists to their present-day configuration only occurred after 515 Ma. Previous studies have recognised the lithologically and structurally heterogeneous makeup of the DLSZ compared to the rest of the SZ accretionary prism (Miller, 1983; Kasch, 1986, 1987). This complexity relates to the detachment, underplating and exhumation of 100 km^2 size slivers from different crustal levels to their present positions at or close to the base of the prism as it is widely recorded from the subduction channel at the interface between the down-going plate and the overlying accretionary complexes (e.g., Glodny et al., 2005; Angiboust et al., 2013). The envisaged evolution for the DLSZ of the Damara belt is schematically sketched as a four stage evolutionary path in Figure 12.

Crustal convergence and closure of the Khomas Sea from ca. 590 Ma onwards led to the offscraping and burial of marine and trench sediments represented by the thick imbricated pile of the Kuiseb Formation that underlies much of the SZ prism. During the advanced stages of convergence, the leading edge of the Kalahari Craton entered the subduction zone and results in the burial of the continental crust to depths of 32-35 km (Fig. 12, stage 1). The timing of the burial is unknown, but $^{40}Ar/^{39}Ar$ biotite ages from the retrograde OSZ suggests a minimum age of >526 Ma. This is supported by $^{40}Ar/^{39}Ar$ amphibole ages from the OSZ that are >528 Ma. The preservation of these older (prograde) ages in the amphibolites suggest that they were likely shielded from resetting during the later stages of retrogression and fluid infiltration in the OSZ. Kitt et al. (2016) documented the strongly focused fluid flow and strain partitioning along the retrograde OSZ. The retrograde biotite-epidote assemblages in the OSZ mark the retrogression and onset of exhumation of the Ekuja Dome. This would correspond to the detachment of the gneisses from the down-going slab and stacking of basement slices through underthrusting, underplating to form antiformal nappe structures (Fig. 12, stage 2; Glodny et al., 2005; Agard et al., 2009; Angiboust et al., 2013). The timing of the exhumation of the basement gneisses is constrained to between 526.4 ± 3.5 Ma and 521.9 ± 3.6 Ma by $^{40}Ar/^{39}Ar$ ages for retrograde biotite from mylonitic shear zones in the OSZ.

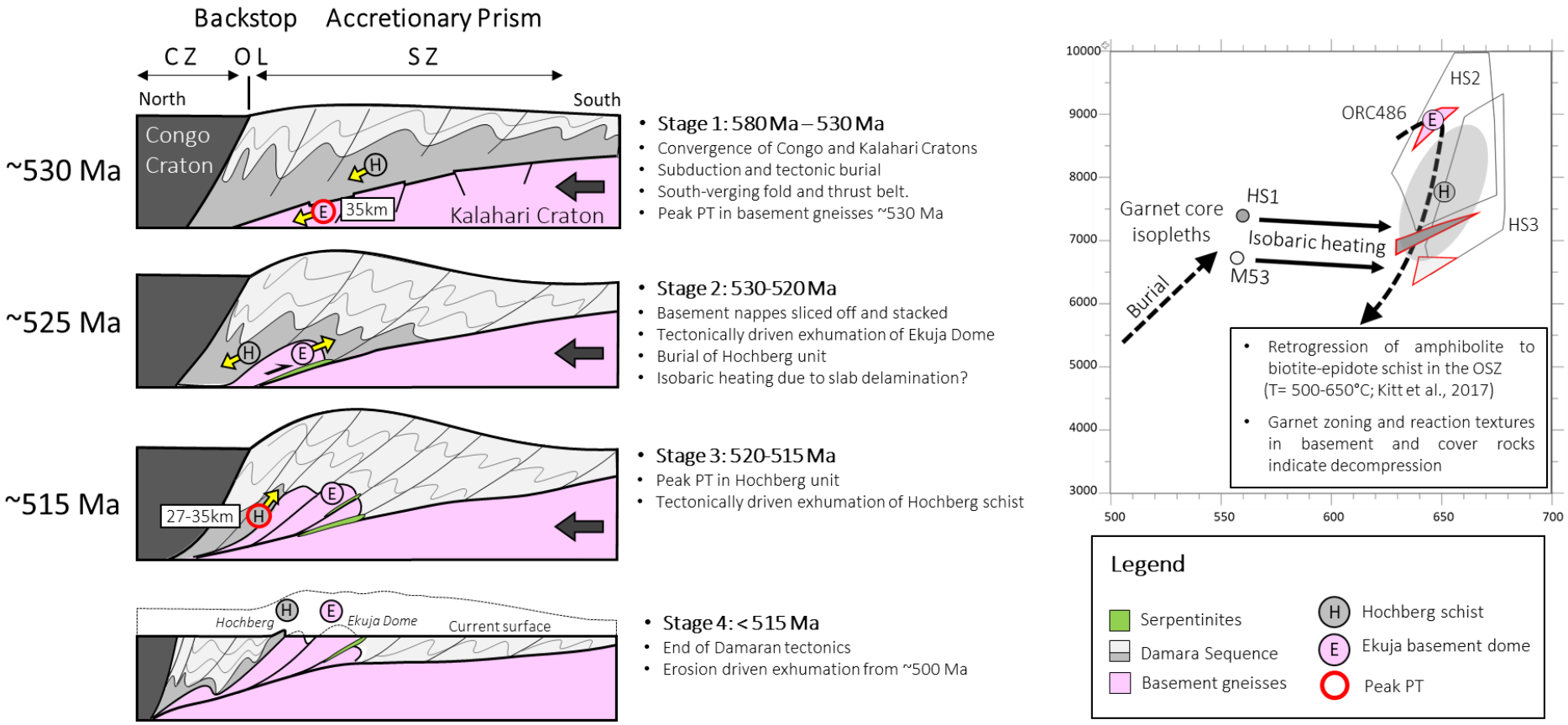

Fig. 12. Conceptual model for the P-T-t evolution of the Southern Zone accretionary prism showing different stages of burial, accretion, underplating and exhumatio n of slices of basement gneiss and metasedimentary cover rock. P-T estimates for amphibolites (ORC486) from the Ekuja basement dome indicate burial to ~35 km. The timing of peak metamorphism is unknown. Burial was followed by exhumation of the basement gneisses ca. 525 Ma. The timing of exhumation is constrained by Ar-Ar ages for retrograde biotite from the mylonitic OSZ. P-T estimates (shaded ellipse) for the overlying Hochberg schist indicate burial to 27-35 km. The timing of peak metamorphism is constrained by xenotime U-Pb ages at ca. 515 Ma. Garnet zoning and reaction textures in metapelites from Hochberg indicate decompression following peak metamorphism.

Whereas the overlying south-verging and east-west trending fold-and-thrust belt records the off-scraping of metasediments from the subducting slab, expulsion and exhumation of rocks during northward subduction at the base of the prism results in a prominent N-S trending L-S fabric in basement gneisses and directly overlying metasediments (Kitt et al., 2016). This is associated with the exhumation of buried rocks close to the subduction zone channel (Fig. 12, stage 2) and is comparable to studies in other subduction zones (Glodny et al., 2005; Angiboust et al., 2013). Imbricated and tectonized slivers of serpentinites and serpentinite massifs are likely to have lubricated the exhumation of the gneisses along the subduction channel (Guillot et al., 2000). Importantly, the peak metamorphic conditions and burial of metapelites to 27-35 km in the Hochberg schists is recorded at only ca. 515 Ma and some 5-10 Ma after the onset of exhumation of the Ekuja Dome (Fig. 12, stage 3). In other words, P-T-t paths for the respective packages indicate exhumation of basement gneisses while the overlying Hochberg schists were undergoing burial. Final juxtaposition of the two can only have occurred at ca. 515 Ma, indicating the thrusting of the structurally overlying schists on top of basement gneisses during exhumation of the Hochberg unit. The near absence of ca. 515 Ma Ar-Ar ages from the OSZ also suggests that deformation in the basement gneisses had ceased by that time and that strain had moved into the overlying schist.

8.3. Implications for the Southern Zone accretionary prism

Tectonic underplating and stacking of nappes at the base of the prism will invariably lead to the uplift and exhumation of overlying prism metasediments. This effect is particularly pronounced closer the backstop of the prism, where initially buried rocks that are not subducted are forced upwards (e.g., Platt, 1986; Glodny et al., 2005; Angeboust et al., 2013). This return flow of rocks could explain the broader P-T distribution in the SZ from south to north and the commonly documented late-stage isothermal decompression along much of its strike (Fig. 1b; Kasch, 1983, Miller, 2008). Previous studies have correlated these regional variations in P-T with the intrusion of the Donkerhuk batholith along the northwestern boundary of the SZ prism (Sawyer, 1981; Kasch, 1983; Miller, 1983, 2008; Jung and Mezger, 2001). However, the absence of Donkerhuk or related granites in the DLSZ suggest that a return flow of rocks along the Okahandja Lineament Zone as the backstop of the prism may provide an alternative explanation for the systematic P-T variations, highlighting the fact that these are regional processes with much broader significance. While previous works tried to constrain the timing of peak metamorphism in the SZ (e.g. M1 at ca. 550 Ma and M2 at ca. 535 Ma - Miller, 1983, 2008; ca. 545 Ma - Meneghini et al., 2014), our results illustrate the complexity of burial and exhumation of rocks in the prism with no distinct regional metamorphic peak. Different tectonic packages reached peak conditions at different times, depending on when and how they were buried (e.g., frontal versus basal accretion) and how and if they were exhumed. These processes probably operated for more than 30 Ma (Meneghini et al., 2014) and reflect the dynamics of burial and return flow in the

prism over a prolonged period of time, very much comparable with scenarios described for recent prisms and documented in analogue models (Glodny et al., 2005; Agard et al., 2009; Angiboust et al., 2013; Plunder et al., 2015). It also suggest that convergence was ongoing to at least 515 Ma, as is similarly recorded from the CZ (Jung and Mezger, 2003; Longridge et al., 2011, 2017; Kisters et al., 2012; Goscombe et al., 2017). The ages also overlap within error with monazite concordia ages of 519 ± 3 Ma and 514 ± 3 Ma for deformed granite sheets in the Donkerhuk (Clemens et al., 2017b) and with new U-Pb ages from monazite that constrain the timing of peak metamorphism in the SZ and SMZ between ~530-517 Ma (Goscombe et al., 2017, Goscombe et al., in press).

The timing of tectonic processes described here for the DLSZ coincides with the emplacement of the bulk of the large Donkerhuk batholith in the Southern Zone prism between 530-515 Ma (Blaxland et al. 1979; Jung and Mezger, 2003; Miller, 2008; Clemens et al., 2017a). Magmas of the Donkerhuk batholith were emplaced at depths of ca. 16-18 km (ca. 4.5 kbar; Clemens et al., 2017a) from partial melting of rocks at depths of ca. 22-24 km (ca. 6 kbar). In other words, these crustal levels of partial melting are comparable to levels currently exposed in the DLSZ along strike of the Donkerhuk batholith. The geochemistry and isotope geochemistry of the magmas is not indicative of partial melting of rocks with compositions of the Kuiseb Formation, but instead point to isotopically older rocks not exposed at the emplacement level of the batholith (Clemens et al., 2017a, b). However, rocks in the DLSZ are not restitic in composition, and evidence of in-situ partial melting is only very sporadic, so that the source of the Donkerhuk magmas remains enigmatic.

8.4. Regional correlations

The Damara Belt can be directly correlated with the Lufilian Arc and Zambezi Belt of Zambia through the along-strike continuation of tectonostratigraphic units from geophysical data (Fig. 1; Unrug, 1983; Coward et al., 1984; Kampunzu and Cailteux, 1999; Gray et al., 2008; Lehmann et al., 2015). In the Domes Region of the Lufilian Arc, Palaeo -to Mesoproterozoic basement domes show remarkable similarities in geochronology, structure, metamorphism and mineralisation to basement domes in DLSZ of the Damara Belt (Rainaud et al., 2005; Bernau et al., 2013; Eglinger et al., 2016; Kitt et al., 2016; Turlin et al., 2016). Like the DLSZ, the basement rocks are composed of various gneisses and garnet-bearing amphibolites that are structurally imbricated with the overlying Neoproterozoic metasediments. Basement-cover contacts are characterised by the occurrence of kyanite-bearing schists or whiteschists that host flat-lying shear zones with a strong N-S trending, shallow plunging stretching lineation and a top-to-the-north sense of shear (Bernau et al., 2013). Recent P-T-t studies in the Domes Region of the Lufilian Arc give estimated peak metamorphic conditions of ~13 kbar and ~750°C at ca. 530 Ma (John et al., 2004) and ~9-11 kbar and ~640-660 °C at ca. 530 Ma (Eglinger et al., 2016). Similar conditions have been reported for dome structures toward the SE e.g., 7.5-9.3 kbar and 620-700 °C for the Matala Dome (Neydenov et al., 2015) and 7.9-8.6 kbar and 590-717 °C dated at ca. 524 ± 16 Ma for the Chewore Inliers in the Zambezi Belt (Goscombe et al., 1998). Peak P-T conditions in the Luilian Arc were followed by syn-tectonic exhumation and isothermal decompression at pressures of 6 - 8 kbar between 530 and 500 Ma (Eglinger et al., 2016). This is supported by $^{40}Ar/^{39}Ar$

ages between 529.3 ± 5.6 and 526.3 ± 6.2 Ma from retrograde schist in the Matala Dome that are interpreted to constrain the timing of exhumation (Neydenov et al., 2015). These similarities between the Domes Region of the Lufilian Arc and the Southern Zone of the Damara Belt has important implications for the exploration of Cu deposits along strike from the well know Central African Copperbelt in Zambia and in the DRC (Kitt et al., 2016; Sillitoe, 2017).

9. Conclusions

New PT estimates combined with structural, petrographic and geochronological data allow for a partial reconstruction of P-T-t paths for different tectonostratigraphic units in the DLSZ, and demonstrates for the first time the internal dynamics and complexities of subduction-accretion processes in the accretionary prism of the Damara Belt. Peak metamorphic conditions of 8.5-9.15 kbar and 635-665°C and $^{40}Ar/^{39}Ar$ biotite ages from the retrograde Omitiomire Shear Zone indicate that basement gneisses from the Ekuja Dome were exhumed from ~35 km at ca. 525 Ma while the overlying Hochberg schists were still undergoing burial to 27-35 km. Final juxtaposition of the two units occurred only after 515 Ma, shortly after peak metamorphism in the Hochberg schists. This complexity arises from the detachment, underplating, stacking and exhumation of nappes at the base of the prism and may also explain the broader P-T distribution and late-stage isothermal decompression in the Southern Zone. This correlates well with similar P-T-t conditions, albeit at slightly higher pressures, described for the Domes Region in the Lufilian Arc and allows for a direct comparison with the Damara belt.

10. Acknowledgments

This project was supported by International Base Metals Limited (IBML) and Craton Mining and Exploration (Pty) Ltd. In particular, we thank Karl Hartmann and Ken Maiden for their support and valuable geological insight during the course of this study. Dirk Frei is acknowledged for the U-Pb xenotime geochron analysis and data reduction. Madelaine Frazenburg and the technical staff at the XRF and SEM analytical facilities in Stellenbosch are thanked for their kind assistance. ISB acknowledges funding from the NRF (South Africa) through the "Incentives for Rated Researchers" Programme. Andrew Cross (Geoscience Australia) provided a small aliqout of xenotime U-Pb reference material Z6413. Ute Schreiber from the Geological Survey of Namibia is thanked for generous assistance with geological maps and data. Frik Badenhorst is acknowledged for the good company and discussions around the camp fire. This paper greatly benefitted from constructive reviews by Åke Fagereng and an anonymous reviewer.

11.References

Agard, P., Yamato, P., Jolivet, L., Burov, E., 2009. Exhumation of oceanic blueschists and eclogites in subduction zones: timing and mechanisms. Earth-Science Reviews 92, 53–79.

Aleinikoff JN, Schenck WS, Srogi LA, Fanning CM, Kamo SL & Bosbyshell H (2006) Deciphering igneous and metamorphic events in high-grade rocks of the Wilmington Complex, Delaware: Morphology, cathodoluminescence and backscattered electron zoning, and SHRIMP U-Pb geochronology of zircon and monazite. GSA Bulletin 118: 39-64.

Angiboust, S., Agard, P., De Hoog, J.C.M., Plunder, A., 2013. Insights on deep, accretionary subduction processes from the Sistan ophiolitic "mélange" (Eastern Iran). Lithos 156-159, 139-158.

Angiboust, S., Agard, P., Glodny, J., Omrani, J. & Oncken, O. 2016. Zagros blueschists: Episodic underplating and long-lived cooling of a subduction zone. Earth and Planetary Science Letters. 443, 48-58.

Barton, J.M. Jr, Barnett, W.P., Barton, E.S., Barnett, M., Doorgapershas, A., Twiggs, C., Klemd, R., Matin, J., Mellonig, L. and Zenglein, R., 2003. The geology of the area surrounding the Venetia kimberlite pipes, Limpopo Belt, South Africa: a complex interplay of nappe tectonics and granitoid magmatism. South African Journal of Geology, 106, 109-128.

Bernau R, Roberts S, Richards M, Nisbet B, Boyce AJ, Nowecki J (2013) The geology and geochemistry of the Lumwana Cu (±Co ± U) deposits, NW Zambia. Mineral Deposita 48,137- 153.

Blaxland, A., Gohn, E., Haack, U. & Hoffer, E. 1979. Rb/Sr ages of late-tectonic granites in the Damara Orogen, Southwest Africa/Namibia. Neues Jahrbuch für Mineralogie, Monatshefte, 11, 498–508.

Cherniak, D.J., 2006. Pb and rare earth element diffusion in xenotime. Lithos 88, 1–14.

Cloos, M., 1982. Flow melanges — numerical modeling and geologic constraints on their origin in the Franciscan subduction complex, California. Geological Society of America Bulletin 93, 330–345.

Cloos, M. & Shreve, R. L., 1988. Subduction channel model of prism accretion, mélange formation, sediment subduction, and subduction erosion at convergent plate margins: 1. Background and description. Pure Appl. Geophys. 128, 455–500.

Clemens, J.D., Buick, I.S., Kisters, A.F.M, 2017a. The Donkerhuk batholith, Namibia: A giant S-type granite emplaced in the mid crust, in a core-arc setting. Journal of the Geological Society 174, 157-169.

Clemens, J.D., Buick, I.S., Kisters, A.F.M., Frei, D., 2017b. Petrogenesis of the granitic Donkerhuk batholith in the Damara Belt of Namibia: protracted, syntectonic, short-range, crustal magma transfer. Contrib Mineral Petrol 172:50.

Coggon, R. & Holland, T.J.B., 2002. Mixing properties of phengitic micas and revised garnet phengite thermobarometers. Journal of Metamorphic Geology, 20, 683–696.

Coward M.P., 1981. The junction between Pan-African mobile belts in Namibia: its structural history. Tectonophysics 76:59–73

Cross, C.B., Diener, J.F.A., Fagereng, A., 2015. Metamorphic imprint of accretion and ridge subduction in the Pan-African Damara Belt, Namibia. Journal of Metamorphic Geology 33, 633-648.

de Capitani, C. & Petrakakis, K. 2010. The computation of equilibrium assemblage diagrams with Theriak/Domino software. American Mineralogist, 95, 1006–1016.

Diener, J.F.A., Powell, R., White, R.W. & Holland, T.J.B., 2007. A new thermodynamic model for clino- and orthoamphiboles in the system Na2O–CaO–FeO–MgO–Al2O3–SiO2–H2O–O. Journal of Metamorphic Geology, 25, 631–656.

Diener, J.F.A. & Powell, R., 2012. Revised activity–composition relations for clinopyroxene and amphibole. Journal of Metamorphic Geology, 30, 131–142.

Di Vincenzo, G., Carosi, R., Palmeri, R., 2004. The relationship between tectono–metamorphic evolution and argon isotope records in white mica: constraints from in situ ^{40}Ar–^{39}Ar laser analysis of the Variscan basement of Sardinia (Italy). Journal of Petrology, 45, 1013–1043.

Di Vincenzo, G., Carosi, R., Palmeri, R., Tiepolo, M., 2007. A comparative U–Th–Pb (zircon–monazite) and ^{40}Ar–^{39}Ar (muscovite–biotite) study of shear zones in northern Victoria Land (Antarctica): implications for geochronology and localized reworking of the Ross Orogen. Journal of Metamorphic Geology 25, 605-630.

Dodson, M. H., 1973. Closure temperature in cooling geochronological and petrological systems. Contributions to Mineralogy and Petrology 40, 259-274.

Eglinger, A., Vanderhaeghe, O., André-Mayer, A.-S., Goncalves, P., Zeh, A., Durand, C., Deloule, E., 2016. Tectono-metamorphic evolution of the internal zone of the Pan-African Lufilian orogenic belt (Zambia): Implications for crustal reworking and orogenic uranium mineralizations. Lithos 240–243, 167–188.

Frei D and Gerdes A (2009) Precise and accurate in situ U–Pb dating of zircon with high sample throughput by automated LA-SF-ICPMS. Chemical Geology 261: 261–270.

Fletcher, I.R., McNaughton, N.J., Aleinikoff, J.A., Rasmussen, B., Kamo, S.L., 2004. Improved calibration procedures and new standards for U–Pb and Th–Pb dating of Phanerozoic xenotime by ion microprobe. Chem. Geol. 209, 295–314.

Foster, G., Kinny, P., Prince, C., Vance, D., Harris, N., 2000. The significance of monazite U–Th Pb age data in metamorphic assemblages; a combined study of monazite and garnet chronometry. Earth Planet. Sci. Lett. 181, 327– 340.

Foster, G., Gibson, H.D., Parrish, R., Horstwood, M., Fraser, J., Tindle, A., 2002. Textural, chemical and isotopic insights into the nature and behaviour of metamorphic monazite. Chemical Geology 191, 183–207.

Glodny, J., Lohrmann, J., Echtler, H., Grafe, K., Seifert W., Collao, S., Figueroa O., 2005. Internal dynamics of a paleoaccretionary wedge: insights from combined isotope tectonochronology and sandbox modelling of the South-Central Chilean forearc. Earth Planet. Sci. Lett. 231, 23-29.

Goscombe B.D., Armstrong R. and Barton J.M., 1998. Tectonometamorphic evolution of the Chewore Inliers: Partial re-equilibration of high-grade basement during the Pan-African Orogeny. Journal of Petrology 39, 1347-1384.

Goscombe, B., Foster, D.A., Gray, D., Wade, B., Marsellos, A., Titus, J., (2017). Deformation correlations, stress field switches and evolution of an orogenic intersection: the Pan-African Kaoko-Damara orogenic junction, Namibia. Geoscience Frontiers.

Goscombe, B., Foster, D.A., Gray, D., Wade, B., (in press). Metamorphic response and crustal architecture in a classic collisional orogen: The Damara Belt, Namibia, Gondwana Research (in press).

Gray, D.R., Foster, D.A., Goscombe, B., Passchier, C.W., Trouw, R.A.J., 2006. 40Ar/39Ar thermochronology of the Pan-African Damara Orogen, Namibia, with implications for tectonothermal and geodynamic evolution. Precambrian Research 150, 49-72.

Gray D.R., Foster D.A., Meert J.G., Goscombe B.D., Armstrong R, Trouw R.A.J., Passchier C.W., 2008. A Damaran Perspective on the Assembly of Southwestern Gondwana. Geol Soc London Spec Publ 294, 257-278.

Green, E.C.R., Holland, T.J.B. & Powell, R., 2007. An order–disorder model for omphacitic pyroxenes in the system jadeite–diopside–hedenbergite–acmite, with applications to eclogitic rocks. American Mineralogist, 92, 1181–1189.

Guillot, S., Hattori, K., de Sigoyer, J., 2000. Mantle wedge serpentinization and exhumation of HP rocks: insights from Eastern Ladakh. Geology 28, 199–202.

Gutscher, M.A., Kukowski, N., Malavieille, J., Lallemand, S., 1998. Material transfer in accretionary wedges from analysis of a systematic series of analog experiments. Journal of Structural Geology 20, 407–416.

Holland, T.J.B. & Powell, R. 1998. An internally consistent thermodynamic data set for phases of petrological interest. Journal of Metamorphic Geology, 16, 309–344.

Holland, T.J.B. & Powell, R. 2003. Activity–composition relations for phases in petrological calculations: an asymmetric multicomponent formulation. Contributions to Mineralogy and Petrology, 145, 492–501.

John, T., Schenk, V., Mezger, K., Tembo, F., 2004a. Timing and PT evolution of whiteschist metamorphism in the Lufilian Arc-Zambezi Belt orogen (Zambia): implications for the assembly of Gondwana. Journal of Geology 112, 71–90.

Jung, S. and Mezger, K. 2001. Geochronology in migmatites—a Sm–Nd, U–Pb and Rb–Sr study from the Proterozoic Damara Belt (Namibia)—implications for polyphase development of migmatites in high-grade terranes. Journal of Metamorphic Geology, 19, 77–97.

Jung, S. and Mezger, K., 2003. Petrology of basement-dominated terranes: I. Regional metamorphic P–T–t path from U–Pb monazite and Sm–Nd garnet geochronology (Central Damara orogen, Namibia). Chemical Geology 198, 223–247.

Kampunzu A.B., and Cailteux J., 1999. Tectonic evolution of the Lufilian arc (Central Africa Copper belt) during Neoproterozoic Pan African orogenesis. Gondwana Res. 2, 401–421.

Karig D.E., 1983. Accreted terranes in the northern part of the Philippine Archipelago. Tectonics, 2, 211-236.

Kasch, K.W., 1983. Continental collision, suture progradation and thermal relaxation: a plate model for the Damara orogen in central Namibia. In: R.McG. Miller (Editor), Evolution of the Damara Orogen of South West Africa/Namibia. Geol. Soc. of S. Afr. Spec. Publ. 11: 423-429.

Kasch K.W., 1986. Tectonic subdivision, lithostratigraphy and structural geology of the Upper Black Nossob river area. Comm Geol Soc Namibia 2, 117–129.

Kasch K.W., 1987. Metamorphism of pelites in the Upper Black Nossob river area of the Damara Orogen. Comm Geol Soc Namibia 3, 63–82.

Kisters, A.F.M., Jordaan, L.S. and Neumaier, K., 2004. Thrust-related dome structures in the Karibib district and the origin of orthogonal fabric domains in the south Central Zone of the Pan-African Damara belt, Namibia. Precambrian Research, 133, 283-303.

Kisters, A.F.M., Vietze, M.E., Buick, I., 2012. Deformation and age of the Stinkbank Pluton and implications for the correlation of tectonometamorphic episodes in the Pan-African Damara belt. South African Journal of Geology 115, 309-326.

Kitt S, Kisters A, Steven N, Maiden K, Hartmann K, 2016. Shear-zone hosted copper mineralisation of the Omitiomire deposit — Structural controls of fluid flow and mineralisation during subduction accretion in the Pan-African Damara Belt of Namibia. Ore Geol Rev. 75, 1-15.

Kitt S, Kisters A, Vennemann T, Steven N, 2017. Orebody geometry, fluid and metal sources of the Omitiomire Cu deposit in the Ekuja Dome of the Damara Belt in Namibia. Mineralium Deposita (in press).

Kossert, K. and Günther, E., 2004. LSC measurements of the half-life of ^{40}K. Applied Radiation and Isotopes, 60, 459-464.

Kruger T. and Kisters A.F.M., 2016. Magma accumulation and segregation during regional-scale folding: The Holland's dome granite injection complex, Damara belt, Namibia. Journal of Structural Geology 89, 1-8.

Kuiper, K.F., A. Deino, A., Hilgen, F.J., Krijgsman, W., P., Renne, P.R. and Wijbrans, J.R., 2008. Synchronizing Rock Clocks of Earth History. Science, 320, 500-504

Kukla P.A., and Stanistreet I.G., 1991. The record of the Damaran Khomas Hochland accretionary prism in Central Namibia: refutation of the 'ensialic' origin of a Late Proterozoic orogenic belt. Geology 19, 473-476.

Lee, J-Y., Marti, K., Severinghaus, J.P., Kawamura, K., Yoo, H-S., Lee, J-B., Kim, J-S, 2006. A redetermination of the isotopic abundances of atmospheric Ar. Geochimica et Cosmochimica Acta, 70, 4507–4512.

Lehmann J, Master S, RankinW, Milani L, Kinnaird JA, Naydenov KV, Saalmann KA, Kumar M (2015) Regional aeromagnetic and stratigraphic correlations of the Kalahari Copperbelt in Namibia and Botswana. Ore Geol Rev 71, 169–190.

Lehmann, J., K. Saalmann, K. V. Naydenov, L. Milani, G. A. Belyanin, H. Zwingmann, G. Charlesworth, and J. A. Kinnaird (2016), Structural and geochronological constraints on the Pan-African tectonic evolution of the northern Damara Belt, Namibia, Tectonics, 35, 103–135

Longridge, L., Gibson, R.L., Kinnaird, J.A. and Armstrong, R.A., 2011. Constraining the timing of deformation in the southwestern Central Zone of the Damara Belt, Namibia. Geological Society of London Special Publications 357, 107-135.

Longridge, L., Gibson, R.L., Kinnaird, J.A. and Armstrong, R.A. 2017. New constraints on the age and conditions of LPHT metamorphism in the southwestern Central Zone of the Damara Belt, Namibia and implications for tectonic setting. Lithos 278-281, 361-382.

Ludwig, K.R., 2003. User's Manual for Isoplot 3.00, A Geochronological Toolkit for Microsoft Excel. Berkeley Geochronology Center, 70 pp

Mahar, E. M., Baker, J. M., Powell, R., Holland, T. J. B. & Howell, N. (1997). The effect of Mn on mineral stability in metapelites. Journal of Metamorphic Geology 15, 223–238.

Maiden KJ, Hartmann K, Steven NM, Armstrong RA, (2013) The Omitiomire deposit, Namibia: Late Tectonic copper emplacement in a Neoproterozoic (Pan-African) imbricate shear system. Ext Abstr, SGA Meeting, 12–15 Aug 2013. Sweden, Uppsala.

Makhubela, T.V., Kramers, J.D., Belyanin, G.A., Dirks, P.H.G.M. and Roberts, E.M., 2017. Proterozoic $^{40}Ar/^{39}Ar$ ages from cave deposits of the Malapa, Sterkfontein and Dinaledi fossil sites, Cradle of Humankind, South Africa. South African Journal of Geology, in Press.

Marmo, B. A., Clarke, G. L. & Powell, R., 2002. Fractionation of bulk composition due to porphyroblast growth: effects on eclogite facies mineral equilibria, Pam Peninsula, New Caledonia. Journal of Metamorphic Geology, 20, 151–165.

Maurel, O., Monie´, P., Respaut, J. P., Leyreloup, A. F., Maluski, H., 2003. Pre-metamorphic $^{40}Ar/^{39}Ar$ and U–Pb ages in HP metagranitoids from the Hercynian belt (France). Chemical Geology, 193, 195–214.

Meneghini F, Kisters A, Buick I, Fagereng A, 2014. Fingerprints of late Neoproterozoic ridge subduction in the Pan-African Damara Belt, Namibia. Geology 42, 903–906.

Miller R.M., 1983. The Pan-African Damara Orogen of Namibia. In: Evolution of the Damara Orogen of SouthWest Africa/Namibia. Geol Soc South Africa Spec Publ 11, 431–515.

Miller, R.M., 2008. The Geology of Namibia. Volume 2: Neoproterozoic to Lower Palaeozoic. Geological Survey of Namibia, Windhoek, Namibia.

Moore, J.C., 1989. Tectonics and hydrogeology of accretionary prisms: role of the decollement zone. Journal of Structural Geology 11, 95-106.

Naydenov, K.V., Lehmann, J., Saalmann, K., Milani, L., Poterai, J., Kinnaird, J. A., Charlesworth, G., Kramers, J.D. (2015). The geology of the Matala Dome: an important piece of the Pan-African puzzle in Central Zambia. Int J Earth Sci (Geol Rundsch) 105.

Passchier, C.W., Trouw, R. and Schmitt, R.S., 2016. How to make a transverse triple junction – New evidence for the assemblage of Gondwana along the Kaoko-Damara belts, Namibia. Geology 44, 843-846.

Phillips, D., Machin, K. J., Kiviets, G. B., Fourie, L. F., Roberts, M. A., Skinner, E. M. W., 1998. A petrographic and $^{40}Ar/^{39}Ar$ geochronological study of the Voorspoed Kimberlite, South Africa; implications for the origin of Group II kimberlite magmatism. South African Journal of Geology, 101, 299-306.

Phillips, D., Kiviets, G.B., Barton, E.S., Smith, C.B., Viljoen, K.S. and Fourie, L.F., 1999. $^{40}Ar/^{39}Ar$ dating of kimberlites and related rocks: problems and solution. Proc. of 7th Intl. Kimberlite Conf., Cape Town, 677-687.

Platt, J.P., 1986. Dynamics of orogenic wedges and the uplift of high-pressure metamorphic rocks. Geological Society of America Bulletin 97, 1037–1053.

Platt, J.P., 1993. Exhumation of high-pressure rocks — a review of concepts and processes. Terra Nova 5, 119–133.

Plunder, A., Agard, P., Chopin, C., Pourteau, A., Okay, A.I., 2015. Accretion, underplating and exhumation along a subduction interface: from subduction initiation to continental subduction (Tav ¸sanlızone, W. Turkey). Lithos 226, 233–254.

Pyle, J. M. & Spear, F. S., 1999. Yttrium zoning in garnet: coupling of major and accessory phases during metamorphic reactions. Geological Materials Research, 1, 1–49.

Pyle, J. M., Spear, F. S., Rudnick, R. L. & McDonough, W. F., 2001. Monazite–xenotime–garnet equilibrium in metapelites and a new monazite–garnet thermometer. Journal of Petrology, 42, 2083–2107.

Rainaud C, Master S, Armstrong RA, Phillips D, Robb LJ (2005) Monazite U–Pb dating and ^{40}Ar–^{39}Ar thermochronology of metamorphic events in the central African Copperbelt during the Pan-African Lufilian orogeny. J Afr Earth Sci 42, 183–199.

Renne, P. R., Swisher C. C., Deino A. L., Karner D. B., Owens T. and DePaolo D. J., (1998) Intercalibration of standards, absolute ages and uncertainties in $^{40}Ar/^{39}Ar$ dating. Chemical Geology (Isotope Geoscience Section), 145, 117–152.

Renne, P.R., Mundil, R., Balco, G., Min, K., Ludwig, K.R., 2010. Joint determination of ^{40}K decay constants and $^{40}Ar^*/^{40}K$ for the Fish Canyon sanidine standard, and improved accuracy for $^{40}Ar/^{39}Ar$ geochronology. Geochimica et Cosmochimica Acta 74, 5349–5367.

Renne, P.R., Norman, E.B., 2001. Determination of the half-life of 37Ar by mass spectrometry. Physical Review C 63 (047302), 3 pp.

Rodrıguez, J., Cosca, M. A., Gil Ibarguchi, J. I. & Dallmeyer, R.D., 2003. Strain partitioning and preservation of $^{40}Ar/^{39}Ar$ ages during Variscan exhumation of a subducted crust (Malpica-Tui complex, NW Spain). Lithos, 70, 111–139.

Sawyer, E.W., 1981. Damaran structural and metamorphic geology of an area southeast of Walvis Bay, South West Africa/Namibia. Geol. Surv. South West Africa Memoir 7, 94 pp.

Sillitoe, R.H., Perello, J., Creaser, R., Wilton, J., Wilson, A.J., Dawborn, T. (in press). Age of the Zambian Copperbelt. Mineralium Deposita (in press).

Spear, F. S. & Pyle, J. M., 2002. Apatite, monazite, and xenotime in metamorphic rocks. Reviews in Mineralogy & Geochemistry, 48, 293–331.

Steven N.M., Armstrong R.A., Smalley T.I., Moore J.M., 2000. First geological description of a late Proterozoic (Kibaran) andesite-hosted chalcocite deposit at Omitiomire, Namibia. In: Geology and Ore Deposits: The Great Basin and Beyond. Geol Soc of Nevada Symp Proc. 711–734.

Stoenner, R.W., Schaeffer, O.A., Katcoff, S., 1965. Half-lives of argon-37, argon-39, and argon-42. Science 148, 1325–1328.

Tinkham, D. K., Zuluaga, C. A. & Stowell, H. H. (2001). Metapelitic phase equilibria modelling in MnNCKFMASH: the effect of variable Al2O3 and MgO/(MgO + FeO) on mineral stability. Geological Materials Research 3, 1–42.

Turlin F, Eglinger A, Vanderhaeghe O, André-Mayer AS, Poujol M, Mercadier J, Ryan B (2016) Synmetamorphic Cu remobilization during the Pan-African orogeny: microstructural, petrological and geochronological data on the kyanite-micaschists hosting the Cu(-U) Lumwana deposit in the Western Zambian Copperbelt of the Lufilian belt. Ore Geol Rev 75, 52–75.

Unrug R (1983) The Lufilian Arc: a microplate in the Pan-African collision zone of the Congo and the Kalahari Cratons. Precamb Res 21, 181–196

Vance, D., Holland, T., 1993. A detailed isotopic and petrological study of a single garnet from the Gassetts Schist, Vermont. Contributions to Mineralogy and Petrology 114, 101–118.

Vielzeuf, D., Baronnet, A., Perchuk, Laporte, D., Baker, M.B., 2007. Calcium diffusivity in alumino-silicate garnets: an experimental and TEM study. Contributions to Mineralogy and Petrology, 154, 153-170.

Villa, I. M., 1998. Isotopic closure. Terra Nova, 10, 42–47.

von Huene, R., and Scholl, D.W., 1991, Observations at convergent margins concerning sediment subduction, subduction erosion, and the growth of continental crust: Reviews of Geophysics, v. 29, 279–316.

Warren C.J., Hanke F., Kelley S.P., 2012. When can muscovite $^{40}Ar/^{39}Ar$ dating constrain the timing of metamorphic exhumation? Chemical Geology 291, 79-86.

White, R.W., Powell, R., Holland, T.J.B. & Worley, B.A. 2000. The effect of TiO2 and Fe2O3 on metapelitic assemblages at greenschist and amphibolite facies conditions: mineral equilibria calculations in the system K2O–FeO–MgO–Al2O3–SiO2–H2O–TiO2–Fe2O3. Journal of Metamorphic Geology, 18, 497–511.

White, R.W., Pomroy, N.E. & Powell, R. 2005. An in-situ metatexite–diatexite transition in upper amphibolite facies rocks from Broken Hill, Australia. Journal of Metamorphic Geology, 23, 579–602.

Yamada, Y., Baba, K., Matsuoka, T. 2006. Analogue and numerical modelling of accretionary prisms with a decollement in sediments. In: Buiter, S.J.H., Schreurs, G. (Eds.), Analogue and Numerical Modelling of Crustal-Scale Processes. Geological Society, London, pp. 169–183. Special Publications, London.

Graveleau, F., Malavieille, J., Dominguez, S. 2012. Experimental modelling of orogenic wedges: A review. Tectonophysics 538-540, 1-66.

Chapter 5

Conclusion

5.1.Synopsis

This thesis progresses from a detailed deposit-scale investigation that highlights the geometry, controls and source of fluid flow and Cu mineralisation in the Omitiomire deposit (Chapters 2 and 3), to a regional-scale study of the conditions and processes that resulted in the exhumation of the Ekuja Dome and development of the mineralised Omitiomire Shear Zone (OSZ) (Chapter 4). The key outcomes from this study are (1) the recognition that the Omitiomire Cu deposit represents a new type of polyphase Cu mineralisation that seems to defy the current classification scheme of Cu mineralisation, (2) the association of Cu mineralisation with the evolution of the OSZ during the exhumation of the Ekuja dome and (3) the correlation, based on similar geodynamic settings, metamorphic grade and timing of mineralisation with deposits in the Domes Region of the Lufilian Arc of Zambia.

5.2.Characteristics of the deposit

The results from this multi-scale study of the Omitiomire Cu deposit highlight distinct features that can be used to explore for similar types of deposits elsewhere in the Damara Belt and beyond. Based on host rocks, metamorphic grade, controls and timing of mineralisation, the the Omitiomire deposit is separated from the classic deposit types described in the current classification scheme of Cu mineralisation. In the following section, the main characteristics of the deposit are summarised (Fig 5.1):

Cu mineralisation is hosted by the shallowly-dipping, anastomosing Pan-African (ca. 520 Ma) shear zone system of the OSZ contained in late-Mesoproterozoic basement gneisses of the Ekuja Dome. The retrograde, mylonitic shear zones are centred along a lithologically heterogeneous amphibolite-gneiss sequence, interpreted as an original intrusive breccia between a suite of older (1100 Ma) mafic rocks (originally lava flows) and later (1060 Ma) tonalitic intrusions. The shear zones are confined to biotite-epidote schist that formed through the progressive hydration and retrogression of the amphibolites and acted as pathways for fluid flow and Cu mineralisation during deformation. Chalcocite is the main Cu ore mineral and occur disseminated and intergrown with biotite and epidote along the retrograde shear fabric in the schists. The highest Cu grades are associated with biotite-epidote-quartz-chalcocite shears, veins and pods in biotite-epidote schist along the contact of tectonically interleaved schists and felsic gneisses. The geometry of the orebody is defined by the spatial coincidence of the original intrusive amphibolite–tonalite breccia and associated inherent heterogeneity, and the heterogeneous high-strain OSZ. On the deposit-scale, the ore body is made up of several mineralised lenses that collectively form a gently undulating, east dipping body with an overall tabular, arcuate geometry that is parallel to the regional S2 gneissosity of the Ekuja Dome. High-grade ore shoots are linked to zones of thickened high-grade mineralisation and related to an increase in the number and cumulative thickness of contact-parallel mineralised shear zones and veins in the upper parts of the orebody. The N-S trending shoots plunge shallowly to the north and south, parallel to the characteristic L2 stretching lineation in the Ekuja Dome. This indicates the structural-lithological control of mineralisation and the importance of competency contrast on all scales.

5.3. Multi-stage evolution: Origin and timing of mineralisation

While the origin of the fluids and metals remains ambiguous, this study proposes the overprinting and remobilisation by epigenetic fluid flow of originally syngenetic Cu mineralisation hosted by original basaltic flows. The syngenetic mineralisation is associated with the Mesoprotereozoic (ca. 1100 Ma) emplacement of Cu-mineralised basaltic flows that were subsequently brecciated by the intrusion of tonalites ca. 1060. This mineralisation may be similar to the Cu mineralisation found in Keweenaw-type basalts, as supported by (1) elevated Cu values in unaltered amphibolites in the basement gneisses and (2) stable isotope results that point to a low fluid/rock ratio and a local redistribution of sulfur from magmatic rocks.

The epigenetic mineralisation is associated with the remobilisation of the syngenetic Cu mineralisation during the Pan-African (ca. 580-500 Ma) subduction of the Kalahari Craton. Initial burial and amphibolite-facies metamorphism was followed by detachment, imbrication and exhumation of the Ekuja basement gneiss dome and resulted in the retrogression from amphibolite to upper greenschist-facies conditions (Fig. 5.1). The OSZ developed from the progressive localisation of strain and fluid flow along the heterogenous amphibolite-gneiss breccia due to reaction softening from the breakdown of amphibolite to biotite-epidote schist. Deformation and fluid flow resulted in the redistribution of the original syngenetic Cu mineralisation along the OSZ. The timing of the epigenetic Cu mineralisation is associated with the formation of biotite and epidote in the OSZ and is constrained by $^{40}Ar/^{39}Ar$ biotite ages between 526.4 ± 3.5 and 521.9 ± 3.6 Ma. This also dates the timing of exhumation of the Ekuja basement dome in the Deep Level Southern Zone accretionary prism of the Damara Belt.

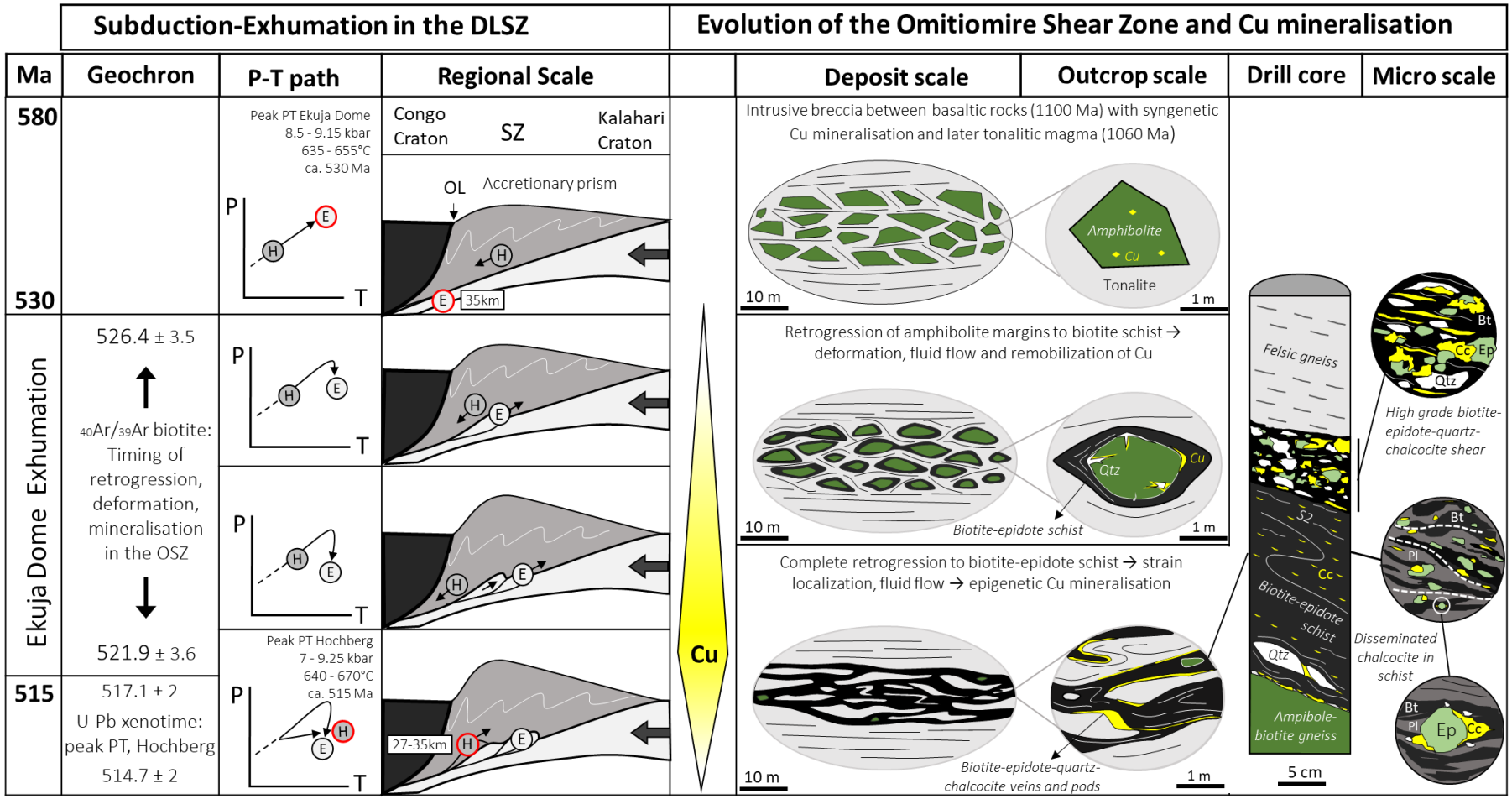

Fig. 5.1 Multi-scale summary diagram to illustrate the polyphase evolution of the Omitiomire Cu deposit. The deposit formed from the overprinting and remobilisation by epigenetic fluid flow of originally syngenetic Cu mineralisation. Deformation, fluid flow and Cu mineralisation in the Omitiomire Shear Zone occurred during the Pan-African exhumation (ca. 530 Ma – 515 Ma) of basement gneisses from the Ekuja Dome in the Southern Zone accretionary prism of the Damara Belt. E: Ekuja Dome; H: Hochberg metasediments; OL: Okahandja Lineament; SZ Southern Zone.

5.4. Correlation with Domes Region, Lufilian Arc

The timing, polyphase evolution, and tectonic setting of the Omitiomire deposit show remarkable similarities with the basement-associated Cu deposits in the Domes Region of the Lufilian Arc in northwest Zambia. In recent years, due to major new discoveries, the Domes Region have become an important Cu district, accounting for up to 10% of Cu resources in the Central African Copperbelt (Sillitoe et al., 2015). Some of the largest deposits, like Lumwana, Kansanshi and Sentinel are hosted by high-grade, amphibolite-facies rocks that wrap around or occur within the basement gneiss domes (Steven et al., 2003; Hitzmann et al., 2012; Bernau et al., 2013; Sillitoe et al., 2015). The predominantly strata-bound mineralisation is structurally controlled and, in the case of Lumwana, associated with constrictional-type strains in shear zones (Bernau et al., 2013). Cu mineralisation occurs either as disseminated sulfides or as quartz-carbonate-sulfide veins (Sillitoe et al., 2015). The origin of fluids and metals are contentious, but recent studies have pointed to the pre-Katangan basement (Van Wilderode et al., 2015; Sillitoe et al., 2015). This is supported by Mesoproterozoic (1084-1059 Ma) Re-Os molybdenite ages associated with Cu mineralisation in the Mwombezhi Dome (Sillitoe et al., 2015). It is also suggest two metallogenic events in the Domes Region with the timing of epigenetic Cu mineralisation dated between 540-490 Ma (Sillitoe et al., 2017). This age-range coincides with the burial (D1: > 530 Ma) and exhumation (D2: 530-500 Ma) of basement gneiss rocks and overlying metasediments during convergence of the Congo and Kalahari cratons in the Pan-African Lufilian orogenic belt (Eglinger et al., 2015) and links the tectonic processes and Cu mineralisation in the Lufilian Arc with the Damara Belt of Namibia.

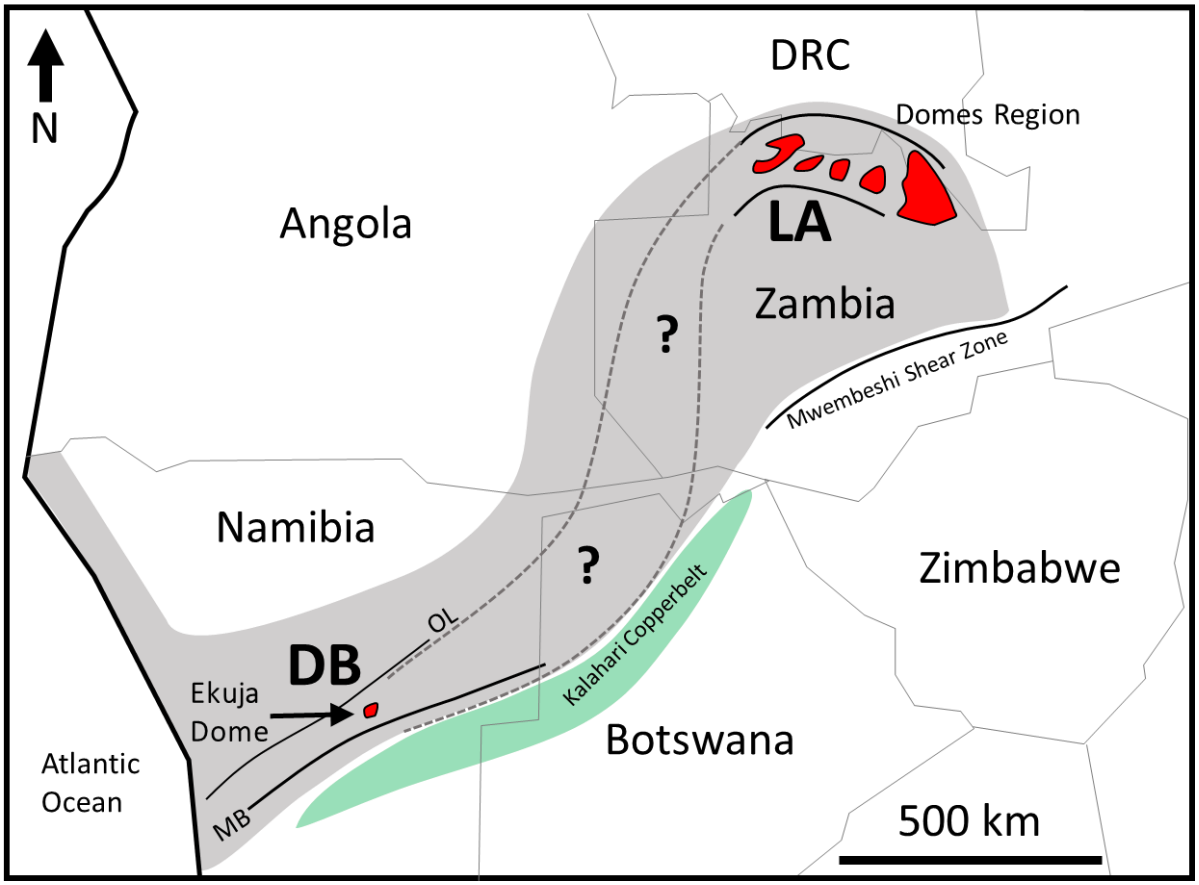

Fig. 5.2. Simplified map (modified from Borg and Maiden, 1989; Key et al., 2001; Singletary et al., 2003; Sillitoe et al., 2010, 2017 and Lehmann et al., 2015) showing the possible geographical extent of prospective Cu mineralisation associated with exhumed basement domes (in red), starting in the DLSZ of the Damara Belt, through NE Namibia and NW Botswana, to SW Zambia and the Domes Region in the Lufilian Arc of NW Zambia. DB: Damara Belt; LA: Lufilian Arc; MB: Matchless Belt; OL: Okahandja Lineament.

5.5. Concluding remarks

The near identical correlations between the Omitiomire Cu deposit and similar basement associated Cu deposits in the Domes Region suggests the existence of a contiguous metalliferous province between the Southern Zone of the Damara Belt and the Domes Region of Lufilian Arc in Zambia that was active to at least ~515 Ma (Fig 5.2). This presents exciting exploration opportunities for similar types of Cu deposits between the two belts.

Exploration between NE Namibia and SW Zambia is complicated by the extensive cover of thick Kalahari sands. Regional airborne geophysics is an essential tool and a detailed GIS-based academic study of the sub-surface geology is critical. Ultimately, exploration success is dependent on an innovative and holistic targeting process. Critical, is the identification of the key elements that constitutes the deposit type e.g. (1) tectonic setting along a Pan-African convergent margin, (2) association with exhumed basement gneiss domes, (3) upper-amphibolite to upper-greenschist facies metamorphic conditions, (4) proximity to a Cu rich protolith (syngenetic mineralisation) (5) epigenetic Cu mineralisation associated with Pan-African constrictional-type shear zones and quartz veining and (6) a structural-lithological control of mineralisation (e.g. low strain domains, lithological contacts). In this regard, this study clearly shows the advantages of using a multiscale and multidisciplinary approach.

5.6. References

Bernau R, Roberts S, Richards M, Nisbet B, Boyce AJ, Nowecki J (2013) The geology and geochemistry of the Lumwana Cu (±Co ± U) deposits, NW Zambia. Mineral Deposita 48:137–153.

Borg G, Maiden KJ (1989) The middle Proterozoic Kalahari copper belt of Namibia and Botswana. In: Boyle RW, Brown AC, Jefferson CW, Jowett EC, Kirkham RV (eds) Sediment-hosted stratiform copper deposits, Geol Assoc Can Spec Paper, vol 36, pp 525–540.

Eglinger, A., Vanderhaeghe, O., André-Mayer, A.-S., Goncalves, P., Zeh, A., Durand, C., Deloule, E., 2016. Tectono-metamorphic evolution of the internal zone of the Pan-African Lufilian orogenic belt (Zambia): Implications for crustal reworking and orogenic uranium mineralisations. Lithos 240–243, 167–188.

Hitzman MW, Broughton D, Selley D, Woodhead J, Wood D, Bull S (2012) The Central African Copperbelt: diverse stratigraphic, structural, and temporal settings in theworld's largest sedimentary copper district. Soc Econ Geol Spec Publ 16:487–514.

Lehmann J, Master S, RankinW, Milani L, Kinnaird JA, Naydenov KV, Saalmann KA, Kumar M (2015) Regional aeromagnetic and stratigraphic correlations of the Kalahari Copperbelt in Namibia and Botswana. Ore Geol Rev 71:169–190

Sillitoe RH, Perello J, Garcia A (2010) Sulfide-bearing veinlets throughout the stratiform mineralisation of the central African Copperbelt: temporal and genetic implications. Econ Geol 105:1361–1368.

Sillitoe RH, Perelló J, Creaser RA, Wilton J, Dawborn T (2015) Two ages of copper mineralisation in the Mwombezhi Dome, northwestern Zambia: metallogenic implications for the central African Copperbelt. Econ Geol 110:1917–1923.

Sillitoe, R.H., Perello, J., Creaser, R., Wilton, J., Wilson, A.J., Dawborn, T. (in press). Age of the Zambian Copperbelt. Mineralium Deposita (in press).

Singletary, S.J., Hanson, R.E., Martin, M.W., Crowley, J.L., Bowring, S.A., Key, R.M., Ramokate, L.V., Direng, B.B., Krol, M.A., 2003. Geochronology of basement rocks in the Kalahari Desert, Botswana, and implications for regional Proterozoic tectonics. Precambrian Research 121, 47 -71.

Steven, N., Armstrong, R., 2003. A metamorphosed Proterozoic carbonaceous shale hosted Co–Ni–Cu deposit at Kalumbila, Kabompo dome: the Copperbelt ore shale in northwestern Zambia. Econ. Geol. 98, 893–909.

Appendices

Appendix A:

Abstract presented at Roy Miller Symposium, Windhoek, Namibia, 18 Aug 2014

The Omitiomire deposit, Namibia: Late tectonic copper emplacement in a Damaran imbricate shear system

Shawn Kitt, Department of Earth and Environmental Sciences, Stellenbosch University, South Africa
Ken Maiden, International Base Metals, 47 Neridah Street, Chatswood, NSW 2057, Australia
Karl Hartmann, Craton Mining and Exploration, PO Box 81136, Olympia, Windhoek, Namibia
Nick Steven, Rockwater Consulting Namibia, PO Box 27344, Windhoek, Namibia
Alex Kisters, Department of Earth and Environmental Sciences, Stellenbosch University, South Africa

The Omitiomire copper deposit (> 1 million tonnes contained copper metal) is developed in an imbricate shear plane system on the eastern margin of the Namaqua-age Ekuja basement dome in the Deep Southern Zone of the Damara Belt. Dome rocks comprise predominantly felsic gneiss (meta-dacite and tonalite intrusions) and subordinate amphibolite and mafic schists (probably mafic volcanics). SHRIMP U-Pb studies on zircon and titanite cores provide ages of ~1115 Ma for amphibolite, ~1084 Ma for felsic gneiss and ~1063 Ma for foliated tonalite. REE chemistry (high La/Yb) and a recent stable isotope study of the gneisses suggests a collisional arc (Andean-type) setting for the volcanism. The precursors to the gneisses are of similar age to the Oorlogsende ignimbrite (Nauzerus Group) and the Kgwebe volcanics in NW Botswana. These ~1100 Ma rocks were metamorphosed to amphibolite grade (7-8 kbar, 600°C) during the Damaran orogeny (zircon rims have SHRIMP U-Pb ages of ~550 Ma; titanites have U-Pb ages of 525 and 485 Ma).

Stacked ore lenses define a copper-bearing system which varies from 10 m to >100 m in thickness. The lenses dip at a moderate angle to the east. The ore system plunges shallowly to both the NNE and SSW. Evaluation drilling (>70,000 m) has shown a deposit which extends for 4,000 m and remains 'open' both down-dip and down-plunge. Highest copper grades occur in a retrograde Damaran mineral assemblage dominated by biotite and Cr-epidote that is focused along an imbricate system of narrow shear zones (a heterogenous high strain zone). Recent detailed surface mapping, relogging of 13,000 m of drill core and the examination of an

extensive down-the-hole photographic database provide the basis for a structural reassessment of the controls on ore localisation. Although the copper-mineralising event was late in the tectonic cycle, observations from core clearly show folded chalcocite, as well as chalcocite along foliation planes and in strain shadows of competent minerals. The close relationship between copper grades and the retrograde mylonitic fabrics, quartz veining and structural sites such as lithological contacts, dilational jogs and/or strain shadows strongly suggest fluid flow and/or remobilisation of copper mineralisation during dome exhumation. Northerly trending, sub-horizontal, high-grade ore shoots contained in the mineralised zone are parallel to the regional rodding lineation in the mylonites bounding the dome. In totality, shear sense indicators on the east side of the Ekuja Dome show dominant top to the NE or east sense of movement.

Copper mineralisation occurs primarily as hypogene chalcocite hosted by mafic schist and amphibolite. Inter-banded felsic gneisses are barren. There is a spatial association between copper and biotite, Cr-epidote, sphene, fuchsite, chlorite and Cr- and Ti-magnetite. The copper ore mineralogy is chalcocite/digenite (~90%), subordinate bornite (~8%) and trace chalcopyrite. Petrographic studies suggest an evolution of ore fluids: early chalcopyrite-bornite, a main phase of chalcocite and a minor, final phase of hematite precipitation. There are neither iron sulphides, nor any Zambian-style mineral zonation across the deposit, though bornite concentrations are higher at depth. Chalcocite inclusions within late- to post-tectonic epidote demonstrate that the sulphide is not supergene in origin. Chalcocite persists to a depth of >400 m below surface and is locally replaced by hypogene hematite. Chalcocite has a sulphur isotope composition in the range of $\delta^{34}S$ -4.2 to -7.8‰. Fluid inclusions in quartz and epidote show two-phase aqueous inclusions that are highly saline. We interpret that retrograde, oxidised and saline metamorphic fluids, channelled along shear zones, reacted with sheared metabasite. Changes in Eh-pH conditions were the likely copper precipitation mechanism. Original, Namaqua-age intrusive relationships between felsic rocks and amphibolites (especially the brecciation at intrusion contacts) and later, Pan-African strains developed during the exhumation of the basement dome are considered crucial for the development of the copper mineralisation and highlight the polyphase evolution of the seemingly unique Omitiomire deposit.

Appendix B: Electronic Supplementary Material for Chapter 3

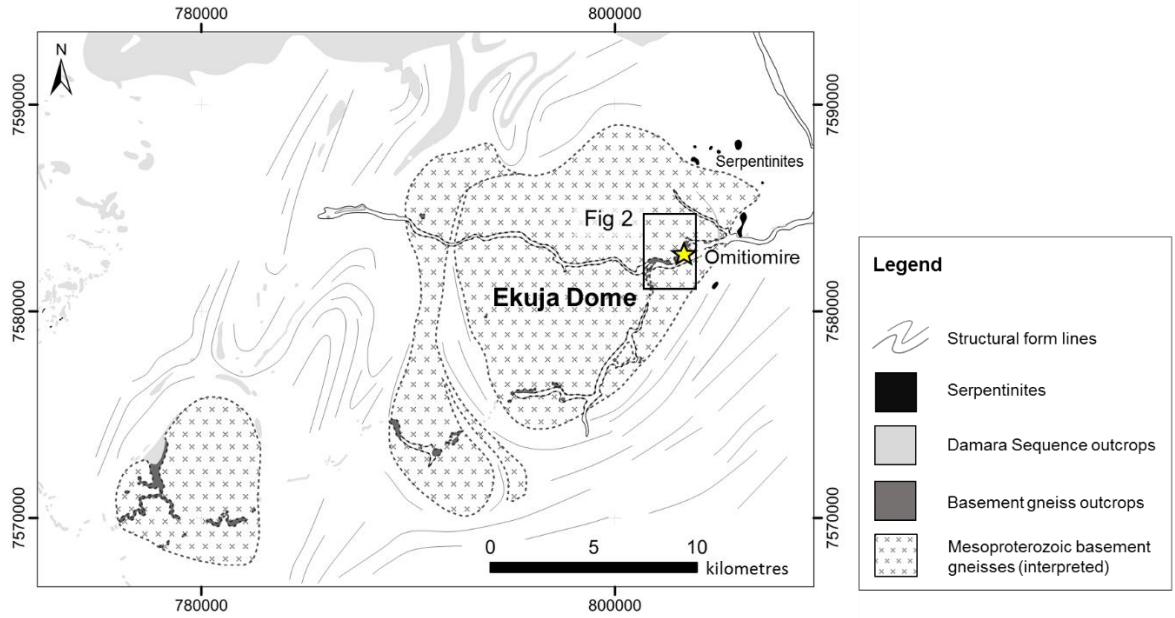

ESM 1. Simplified geological and structural form line map showing the Ekuja Dome and adjoining gneiss complexes in the Southern Zone (modified from Kasch, 1986). The area is poorly exposed and geological investigations relied on interpretations from satellite imagery and observations from isolated outcrops (dark grey) along the Black Nossob river. The location of the Omitiomire Cu deposit is indicated by the star. The box indicates the location of Fig. 2.

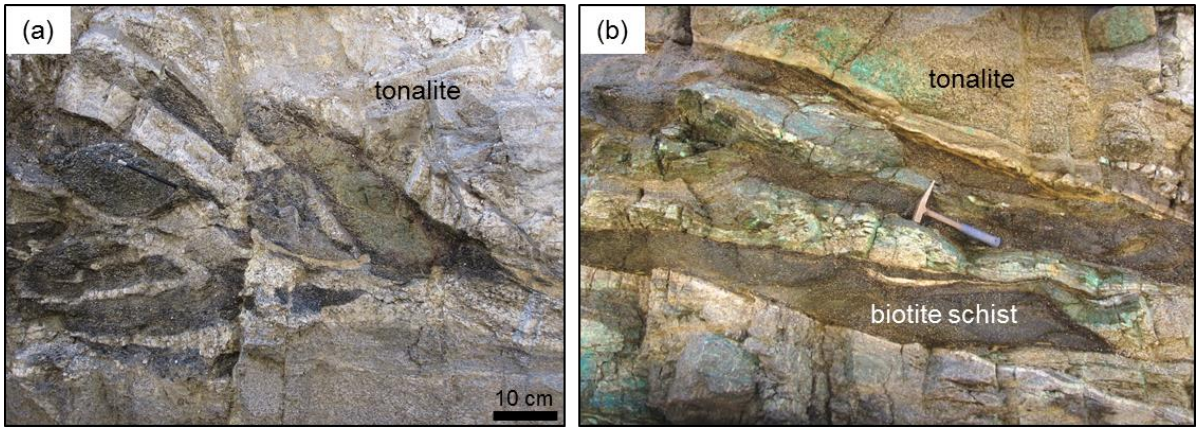

ESM 2. Photographs of panels in the Palm pit showing (a) xenoliths of amphibolite (partially retrogressed to biotite schist) intruded by tonalitic magma and (b) sheet-like, transposed biotite-epidote schist surrounded by large sheets of tonalite, but still retaining original intrusive contacts.

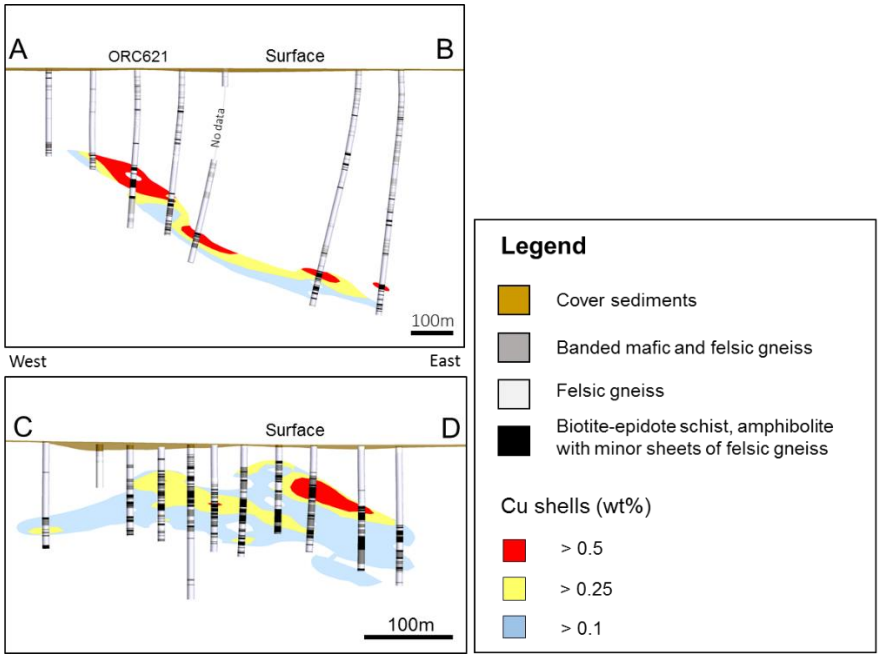

ESM 3. Cross-sections through the Omitiomire deposit showing simplified geological logging data from drill holes and Cu interpolants from assay data. The locations of the cross-sections are shown in Figure 5. (a) Section A-B is through the northern domain and intercepted OS1 in drill hole ORC621. (b) Section C-D is through the southern domain and intercepted OS2.

ESM 4. Table of whole-rock geochemistry of unaltered amphibolite and variably retrogressed mafic gneiss and schist samples from the Omitiomire deposit.

Sample type	Unaltered amphibolite	Unaltered amphibolite	Weakly altered amphibolite	Weakly altered amphibolite	Biotite-epidote-chalcocite schist	Biotite-epidote-chalcocite schist	Scaling factor
Sample ID	BAR	BAR1xx	OMI10	OMI14	OMI2	OMI13	
wt.%							
Al_2O_3	12.61	12.45	14.95	15.28	12.35	12.96	0.5
CaO	8.91	8.81	7.85	8.3	5.75	4.97	0.25
Fe_2O_3	7.50	7.39	8	7.61	8.74	9.89	0.3
K_2O	0.76	0.75	1.84	1.12	3.54	3.23	0.15
MgO	7.33	7.20	5.53	5.38	5.01	5.19	0.25
MnO	0.21	0.20	0.08	0.07	0.11	0.12	0.03
Na_2O	2.97	2.94	2.59	3.29	0	1.39	0.2
P_2O_5	0.24	0.24	0.58	0.63	0.24	0.23	0.1
SiO_2	58.11	57.63	56.06	56.43	55.21	55.38	1.5
TiO_2	0.77	0.76	0.81	0.85	0.83	0.94	0.05
ppm							
S	0.0	0.0	0.1	0.0	2.4	0.5	0.08
Cr	609.3	607.4	422.5	370.0	3301.5	2037.1	100
Ni	261.8	257.3	245.1	230.2	464.2	385.8	30
Cu	1535.1	1339.1	3529.3	3469.3	38356.8	20789.8	1200
Zn	149.2	153.9	117.5	100.4	176.4	179.8	4
Rb	6.6	6.5	72.3	43.1	182.9	151.8	7
Zr	138.1	150.0	181.0	126.2	98.5	141.9	7
Mo	0.8	0.7	0.5	0.5	0.4	0.4	1
Ba	536.2	572.3	342.5	296.2	671.8	738.6	50
Ce	45.2	44.8	48.7	57.8	43.5	46.8	1.5
Pb	7.2	7.6	10.0	9.3	12.1	9.1	0.4
Th	3.0	3.1	4.5	6.6	8.1	7.7	0.5
U	1.6	1.5	1.9	2.0	5.8	2.5	0.35
ρ	2.97		2.96		3		

ESM 5. Isotopic composition (δ^{18}OVSMOW and δDVSMOW) of mineral separates from drill core of the Omitiomire deposit.

Mineral separates (Omitiomire)	Description	d18O VSMOW (permil)	dD VSMOW (permil)
ORC-329-39.80 Qtz	orezone, peg; contact with felsic gneiss peg, Bt, Ep schist and Cc	9.7	
ORC-329-39.80 Ep		5.2	
ORC-329-39.80 Am		4.9	-67
ORC-329-39.80 Bio		4.2	-68
ORC-329-48.55 Qtz	thin orezone in the deformed tonalite	10.1	
ORC-329-48.55 Fsp		8.1	
ORC-329-48.55 Ep		5.6	
ORC-329-48.55 Bio		4.5	-79
ORC 329-58.7 Qtz	orezone; contact between felsic gneiss, Ep, Bt, Am, Cc	9.4	
ORC 329-58.7 Bio		4.1	-69
ORC 329-58.7 Am			-67
ORC-329-80.00 Qtz	orezone, vein; qtz vein, and Bt, Ep, Chl? schist, orezone, Mag	9.3	
ORC-329-80.00 Ep		5.5	
ORC-329-80.00 Bio		4.6	-82
ORC-329-81.90 Qtz	orezone; fine-grained felsic gneiss with abundant Ep and zone rich in Bt	8.9	
ORC-329-81.90 Ep		5.4	
ORC-329-81.90 Bio		4.4	-72
ORC 329-101.25 Qtz	orezone, vein; Bt-Ep schist with qtz veins	9.6	
ORC 329-101.25 Bio		4.0	-77
ORC-485-217.2 Qtz	wall rock; banded gneiss, Bt, Ep, plag, intermediate qtz between felsic and mafic gneiss	9.4	
ORC-485-217.2 Fsp		7.5	
ORC-485-217.2 Bio		3.5	-78
ORC 485-225.8 Qtz	vein; qtz veins, Bt-rich zone, banded gneiss	8.9	
ORC 485-225.8 Bio		3.8	-74
ORC-485-293.63 Am	glimmerite, qtz, Chlorite(?), Bt, mottled gneiss		-64
ORC-485-293.63 Bio			-65
ORC-485-293.63 Chl		5.3	
ORC-485-317.05 Qtz	A; Am, Bt-alteration, Spn, may be unmineralised	9.8	
ORC-485-317.05 Am		5.7	-68
ORC-485-317.05 Bio		4.4	-58
ORC 485-347.5 Qtz	wall rock; mafic gneiss, Bt, Ep, maybe some Cu	9.4	
ORC 485-347.5 Bio		3.6	-68
ORC-485-425.25 Qtz		9.6	
ORC-485-446 Qtz	peg, orezone; pegmatitic vein in a mafic orezone, Bt, Ep, Cc	9.8	
ORC-485-446 Ep		5.7	
ORC-485-446 Bio		4.7	-74
ORC-485-452.25 Qtz	vein, orezone; orezone in contact with felsic gneiss, qtz vein	9.1	
ORC-485-452.25 Ep		6.4	
ORC-485-452.25 Am		5.9	-66
ORC-485-452.25 Bio		5.0	-64
ORC-485-471.2 Qtz	orezone, vein; Bt-Ep orezone, qtz vein truncating felsic gneiss	10.0	
ORC-485-471.2 Ep		5.7	

ORC-485-471.2 Bio		5.0	-75
ORC-496-166 Qtz	wall rock, peg; tonalite, Bt-rich zones, pegmatitic veins, Bt grains of Fsp	9.9	
ORC-496-166 Ep		5.7	
ORC-496-166 Bio		4.8	-80
ORC 496-173.65 Qtz	vein; small veins of veins of Bt, Ep	9.3	
ORC 496-173.65 Bio		4.1	-62
ORC-496-188.6 Fuchs	orezone; Ep-Bt schist, Cc, fuchsite	6.5	-48
ORC-496-188.6 Bio		3.9	-71
ORC 496-193.7 Qtz	orezone, vein; mafic gneiss, Bt, Ep, Cc, qtz veins	9.3	
ORC 496-193.7 Bio		3.2	-68
ORC 496-193.7 Am			-66
ORC-496-209 Qtz	orezone; Am, fine-grained, Bt, Spn, Ep, Cc disseminated	8.5	
ORC-496-209 Qtz		9.5	
ORC-496-209 Bio		4.6	
ORC-496-209A Am		6.1	
ORC-496-213.8 Qtz	orezone; Ep, Bt, Cc	9.5	
ORC-496-213.8 Ep		5.7	
ORC-496-213.8 Am		4.7	-79
ORC-496-213.8 Bio		4.3	-75
ORC-496-223.2 Qtz	orezone, vein; Bt, Cc, fuchsite, Ep, qtz veins	9.8	
ORC-496-223.2 Ep		5.2	
ORC-496-223.2 Bio		4.3	
ORC-496-223.2 Bio		4.1	
ORC-496-234.6 Qtz	orezone; contact between spotted mafic gneisses, and Am, Bt-Ep, qtz, Cc	9.8	
ORC-496-234.6 Ep		5.7	
ORC-496-234.6 Am		5.4	-79
ORC-496-234.6 Bio		4.4	-70
ORC-496-234.6 Chl			-60
ORC-496-247.3 Qtz(+Fsp)	vein, orezone, peg; qtz vein in ore zone Bt-Ep-Cc schist	9.6	
ORC-496-247.3 Fsp		9.8	
ORC-496-247.3 Ep		5.4	
ORC-496-247.3 Bio		4.3	-71

ESM 6. Table of sulfur isotope compositions of chalcocite separates from veins, whole rocks and contact zones from drill cores of the Omitiomire deposit.

Sample	Type	$\delta^{34}S$ (per mil, VCDT)
ORC 329 -101.25	Cc in qtz vein of Bt-Ep schist	-5.8
ORC 485 -443.7	Cc with qtz-Mag in contact mafic schist - felsic gneiss	-5.3
ORC 485 -446	Cc in qtz vein in amphibolite-Bt-Ep schist	-5.9
ORC 485 -452.25	qtz vein with Cc in contact with felsic gneiss - schist	-5.1
ORC 485 -462.8	Cc with Ep, Bt in amphibolite lens within felsic gneiss	-5.4
ORC 496 -173.65	Cc vein with qtz, Bt, Ep	-4.7
ORC 496 -178.8	Cc, Bt, Ep, as lenses in tonalite	-5.3
ORC 496 -188.6	ore zone Ep-Bt schist with Cc and fuchsite	-6.1
ORC 496 -189.2	Bt-Ep schist with Cc, qtz veins as ore zone	-5.5
ORC 496 -193.7	mafic gneiss, Bt, Ep, Cc, qtz veins	-5.2
ORC 496 -213.8	Ep, Bt, Cc ore zone schist	-4.8
ORC 496 -223.2	Bt, Cc, fuchs, Ep, qtz veins in ore zone schist	-6.1
ORC 496 -234.6	spotted mafic gneiss and amphibolite contact with, Bt-Ep, qtz, Cc as ore zone	-5.5

Appendix C: Electronic Supplementary Material for Chapter 4

Table 1A. Sample locations, field descriptions and methodology.

Sample	Locality	Co-ordinates*		Descriptions	Analytic method		
		X	Y				
M53	Along M53 road (Farm Orumbungo)	764987	7545175	Garnet-kyanite micaschist	Mineral Equilibria modelling		
HS1	Hochberg	777741	7572798	Garnet-kyanite micaschist	Mineral Equilibria modelling		
HS2	Hochberg	777751	7572759	Garnet-kyanite micaschist	Mineral Equilibria modelling	Xenotime U-Pb geochronology	
HS3	Hochberg	777762	7572761	Garnet-kyanite micaschist	Mineral Equilibria modelling	Xenotime U-Pb geochronology	
ORC486	Omitiomire	804101	7584371	Hornblende-plagioclase-garnet gneiss	Mineral Equilibria modelling		
ORC484	Omitiomire	804000	7584372	Hornblende-plagioclase-garnet gneiss			Ar-Ar geochronology
ORC479	Omitiomire	803790	7583971	Biotite-epidote schist			Ar-Ar geochronology
BAR	Barreshagen	796584	7576439	Hornblende-plagioclase gneiss			Ar-Ar geochronology
*WGS84 UTM zone 33S							

Table 2A. LA-SF-ICP-MS U-Th-Pb dating methodology CAF, Stellenbosch University.

Laboratory & Sample Preparation	
Laboratory name	Central Analytical Facility, Stellenbosch University
Sample type / mineral	Thin section / Xenotime
Sample preparation	Conventional thin section preparation
Imaging	Zeiss EVO MA15VP Scanning Electron Microscope
Laser ablation system	
Make, Model & type	Resonetics Resolution S155, ArF Excimer Coherent CompexPro 110
Ablation cell & volume	Laurin Technology S155 double Helix large volume cell
Laser wavelength	193 nm
Pulse width	20 ns
Fluence	2.8 J/cm^{-2} (measured with external energy meter above sample funnel)
Repetition rate	5.5 Hz
Spot size	8 µm
Sampling mode / pattern	20 µm single spot analyses
Cell carrier gas	100% He, Ar and N_2 make-up gases combined using injectors into double Helix sampling funnel
Pre-ablation laser warm-up (background collection)	3 cleaning shots followed by 20 seconds background collection
Ablation duration	20 seconds
Wash-out delay	15 seconds
Cell carrier gas flows	330 ml/min He
ICP-MS Instrument	
Make, Model & type	Thermo Finnigan Element2 single collector HR-SF-ICP-MS
Sample introduction	Via Nylon 10 tubing
RF power	1350 W
Make-up gas flow	910 ml/min Ar & 0.03 ml/min N_2
Detection system	Single collector secondary electron multiplier
Masses measured	202, 204, 206, 207, 208, 232, 233, 235, 238
Integration time per peak	4 ms
Total integration time per reading	1 sec *(represents the time resolution of the data)*

Sensitvity	30000 cps/ppm Pb
Dead time	6 ns
Data Processing	
Gas blank	20 second on-peak
Calibration strategy	Non-matrix matched dating. Monazite USGS 44069 used as primary reference material, Xenotime Z6413 used as secondary reference material (Quality Control).
Reference Material info	USGS 44069 (425 Ma; Aleinikoff et al., 2006); xenotime Z6413 (997 Ma; Fletcher et al., 2004)
Data processing package used / Correction for LIEF	In-house spreadsheet data processing using intercept method for LIEF correction
Mass discrimination	Standard-sample bracketing with $^{207}Pb/^{206}Pb$ and $^{206}Pb/^{238}U$ normalized to reference material USGS 44069
Common-Pb correction, composition and uncertainty	204-method, Stacey & Kramers (1975) composition at the projected age of the mineral, 5% uncertainty assigned
Uncertainty level & propagation	Ages are quoted at 2σ absolute, propagation is by quadratic addition. Reproducibility and age uncertainty of reference material and common-Pb composition uncertainty are propagated.
Quality control / Validation	Xenotime Z6413: Concordia age = 998 ± 4 Ma (2σ, MSWD = 0.91)
Other information	For detailed method description see Frei & Gerdes (2009)

Table 3A. Analytical results of U-Pb LA-SF-ICPMS dating of xenotime.

							RATIOS								AGES [Ma]							Conc.
Sample	Analysis	U [ppm][a]	Pb [ppm][a]	Th [ppm][a]	Th/U[a]		$^{207}Pb/^{235}U$[b]	2 s[d]	$^{206}Pb/^{238}U$[b]	2 s[d]	rho[c]	$^{207}Pb/^{206}Pb$[e]	2 s[d]		$^{207}Pb/^{235}U$	2 s	$^{206}Pb/^{238}U$	2 s	$^{207}Pb/^{206}Pb$	2 s	%
HS2	HS2A-1	4255	351	1047	0.25		0.659	0.015	0.0826	0.0016	0.83	0.0579	0.0015		514	12	511	10	525	56	97
HS2	HS2A-2	2771	222	502	0.18		0.635	0.015	0.0803	0.0016	0.82	0.0574	0.0016		499	12	498	9	507	59	98
HS2	HS2A-3	2164	181	386	0.18		0.666	0.016	0.0836	0.0016	0.83	0.0578	0.0015		519	12	517	10	523	57	99
HS2	HS2A-4	3813	315	1157	0.30		0.652	0.015	0.0825	0.0016	0.83	0.0573	0.0015		509	12	511	10	501	58	102
HS2	HS2A-5	4020	311	914	0.23		0.620	0.015	0.0774	0.0015	0.82	0.0581	0.0016		490	12	481	9	534	59	90
HS2	HS2A-6	2484	207	653	0.26		0.664	0.015	0.0834	0.0016	0.83	0.0578	0.0015		517	12	516	10	520	56	99
HS2	HS2A-7	2553	209	488	0.19		0.647	0.015	0.0819	0.0016	0.82	0.0573	0.0016		507	12	508	10	503	60	101
HS2	HS2A-8	2669	220	481	0.18		0.652	0.015	0.0823	0.0016	0.83	0.0574	0.0015		510	12	510	10	508	57	100
HS2	HS2A-9	2864	239	506	0.18		0.660	0.016	0.0834	0.0016	0.81	0.0574	0.0016		514	12	517	10	504	61	102
HS2	HS2A-10	3765	294	1021	0.27		0.622	0.015	0.0782	0.0015	0.82	0.0577	0.0015		491	12	485	9	520	59	93
HS2	HS2B- 1	3908	310	769	0.20		0.630	0.015	0.0794	0.0015	0.83	0.0576	0.0015		496	12	493	9	513	55	96
HS2	HS2C-1	1358	114	187	0.14		0.665	0.021	0.0836	0.0017	0.64	0.0577	0.0028		518	16	518	10	517	105	100
HS2	HS2C-2	1345	113	197	0.15		0.663	0.017	0.0839	0.0017	0.79	0.0573	0.0018		517	13	519	10	504	67	103
HS2	HS2C-3	1534	131	225	0.15		0.676	0.017	0.0853	0.0017	0.80	0.0575	0.0017		524	13	528	10	509	64	104
HS2	HS2C-4	2063	173	315	0.15		0.663	0.016	0.0837	0.0016	0.80	0.0574	0.0017		516	13	518	10	508	63	102
HS2	HS2C-5	1613	135	235	0.15		0.665	0.016	0.0834	0.0016	0.79	0.0579	0.0017		518	13	517	10	524	66	99
HS2	HS2C-6	1971	166	326	0.17		0.669	0.016	0.0840	0.0016	0.80	0.0578	0.0017		520	13	520	10	520	64	100
HS2	HS2C-7	2215	186	371	0.17		0.667	0.016	0.0840	0.0016	0.80	0.0576	0.0017		519	13	520	10	515	63	101
HS2	HS2C-8	3090	234	520	0.17		0.605	0.016	0.0758	0.0015	0.76	0.0579	0.0020		480	13	471	9	524	75	90
HS3	HS3A-1	3347	279	654	0.20		0.658	0.016	0.0835	0.0016	0.81	0.0571	0.0016		513	12	517	10	496	61	104
HS3	HS3A-2	2813	237	488	0.17		0.672	0.016	0.0844	0.0016	0.81	0.0577	0.0016		522	12	523	10	518	61	101
HS3	HS3A-3	2783	229	528	0.19		0.655	0.016	0.0824	0.0016	0.81	0.0577	0.0016		512	12	510	9	519	61	98
HS3	HS3A-4	2980	248	694	0.23		0.660	0.016	0.0831	0.0016	0.80	0.0576	0.0016		515	12	514	10	515	62	100
HS3	HS3A-5	3265	271	945	0.29		0.658	0.016	0.0829	0.0016	0.81	0.0576	0.0016		513	12	513	9	513	61	100
HS3	HS3A-6	4958	415	839	0.17		0.660	0.015	0.0836	0.0016	0.82	0.0572	0.0015		515	12	518	10	500	59	104
HS3	HS3A-7	5964	502	989	0.17		0.672	0.017	0.0842	0.0016	0.76	0.0579	0.0019		522	13	521	10	526	72	99
HS3	HS3A-8	2470	206	393	0.16		0.661	0.017	0.0833	0.0016	0.76	0.0575	0.0019		515	13	516	10	512	73	101
HS3	HS3A-9	5184	422	892	0.17		0.645	0.015	0.0813	0.0016	0.81	0.0575	0.0016		505	12	504	9	510	61	99
HS3	HS3A-10	4020	336	650	0.16		0.663	0.016	0.0836	0.0016	0.78	0.0575	0.0018		516	13	518	10	510	68	101
HS3	HS3B-1	2046	158	511	0.25		0.616	0.015	0.0774	0.0015	0.78	0.0578	0.0018		488	12	481	9	520	68	92
HS3	HS3B-2	2412	191	470	0.20		0.631	0.016	0.0793	0.0016	0.78	0.0577	0.0018		496	13	492	9	518	69	95
HS3	HS3B-3	3417	260	737	0.22		0.605	0.016	0.0762	0.0015	0.78	0.0577	0.0019		481	12	473	9	516	71	92
HS3	HS3B-4	4688	374	927	0.20		0.638	0.016	0.0798	0.0016	0.78	0.0580	0.0019		501	13	495	9	528	70	94
HS3	HS3B-5	2654	221	651	0.25		0.661	0.017	0.0833	0.0016	0.76	0.0576	0.0019		516	13	516	10	513	74	101
HS3	HS3B-6	4081	343	1373	0.34		0.665	0.017	0.0840	0.0017	0.78	0.0574	0.0018		517	13	520	10	506	69	103
HS3	HS3B-7	2346	196	466	0.20		0.666	0.017	0.0837	0.0017	0.78	0.0577	0.0019		518	14	518	10	519	72	100
HS3	HS3C-1	5279	452	657	0.12		0.675	0.015	0.0857	0.0016	0.84	0.0571	0.0014		524	12	530	10	496	54	107
HS3	HS3C-2	7587	644	1202	0.16		0.670	0.015	0.0848	0.0016	0.86	0.0573	0.0013		521	12	525	10	504	51	104
HS3	HS3C-3	4002	314	1343	0.34		0.631	0.014	0.0785	0.0015	0.85	0.0583	0.0014		497	11	487	9	542	54	90
HS3	HS3C-4	8337	693	1302	0.16		0.657	0.015	0.0832	0.0016	0.85	0.0573	0.0014		513	12	515	10	501	53	103
HS3	HS3D-1	1852	156	275	0.15		0.665	0.016	0.0844	0.0016	0.82	0.0571	0.0016		517	12	522	10	496	60	105
HS3	HS3D-2	2086	177	346	0.17		0.673	0.016	0.0849	0.0017	0.82	0.0574	0.0015		522	12	526	10	508	58	104
HS3	HS3D-3	1491	127	217	0.15		0.681	0.016	0.0850	0.0017	0.81	0.0581	0.0016		527	13	526	10	533	61	99
HS3	HS3D-4	1398	116	204	0.15		0.659	0.017	0.0828	0.0016	0.78	0.0577	0.0018		514	13	513	10	519	69	99
HS3	HS3D-5	2908	246	433	0.15		0.672	0.016	0.0845	0.0016	0.83	0.0577	0.0015		522	12	523	10	517	58	101
HS3	HS3D-6	1985	166	305	0.15		0.661	0.017	0.0836	0.0016	0.75	0.0573	0.0020		515	13	518	10	503	75	103
Z6413	A_05	5807	979	1590	0.27		1.688	0.040	0.16866	0.00320	0.81	0.0726	0.0020		1004	24	1005	18	1002	56	100
Z6413	A_06	3486	584	902	0.26		1.655	0.039	0.16741	0.00318	0.81	0.0717	0.0020		992	23	998	18	978	55	102
Z6413	A_13	10108	1691	2629	0.26		1.664	0.039	0.16729	0.00320	0.81	0.0722	0.0020		995	24	997	18	990	56	101
Z6413	A_14	11263	1909	2844	0.25		1.685	0.040	0.16947	0.00324	0.80	0.0721	0.0021		1003	24	1009	18	989	58	102
Z6413	A_23	8995	1506	2189	0.24		1.653	0.041	0.16739	0.00324	0.77	0.0716	0.0023		991	25	998	18	976	64	102
Z6413	A_24	7778	1306	1912	0.25		1.670	0.041	0.16786	0.00326	0.80	0.0721	0.0021		997	24	1000	18	990	59	101
Z6413	A_33	6016	1028	1466	0.24		1.700	0.039	0.17095	0.00328	0.83	0.0721	0.0019		1008	23	1017	18	990	52	103
Z6413	A_34	6208	1049	1561	0.25		1.681	0.038	0.16889	0.00324	0.85	0.0722	0.0017		1001	23	1006	18	992	48	101
Z6413	A_47	6579	1101	1571	0.24		1.664	0.040	0.16728	0.00322	0.79	0.0721	0.0021		995	24	997	18	990	59	101
Z6413	A_48	5250	883	1225	0.23		1.669	0.040	0.16812	0.00324	0.81	0.0720	0.0020		997	24	1002	18	986	56	102
Z6413	A_59	3842	653	969	0.25		1.685	0.039	0.16988	0.00326	0.84	0.0719	0.0018		1003	23	1012	18	984	50	103
Z6413	A_60	5905	992	1542	0.26		1.656	0.037	0.16798	0.00322	0.86	0.0715	0.0016		992	22	1001	18	971	47	103
Z6413	A_73	3302	546	864	0.26		1.640	0.039	0.16530	0.00320	0.80	0.0720	0.0021		986	24	986	18	985	58	100
Z6413	A_74	3404	568	812	0.24		1.667	0.040	0.16676	0.00322	0.81	0.0725	0.0020		996	24	994	18	999	56	99
Z6413	A_86	5029	838	1411	0.28		1.672	0.041	0.16671	0.00324	0.79	0.0727	0.0022		998	24	994	18	1006	60	99
Z6413	A_87	3207	540	848	0.26		1.693	0.040	0.16826	0.00328	0.82	0.0730	0.0020		1006	24	1003	18	1013	55	99

[a] U and Pb concentrations and Th/U ratios are calculated relative to reference monazite USGS 44069

[b] Corrected for background and within-run Pb/U fractionation and normalised to reference monazite USGS 44069 (ID-TIMS values/measured value); $^{207}Pb/^{235}U$ calculated using $(^{207}Pb/^{206}Pb)/(^{238}U/^{206}Pb * 1/137.88)$

[c] Rho is the error correlation defined as the quotient of the propagated errors of the $^{206}Pb/^{238}U$ and the $^{207}/^{235}U$ ratio

[d] Quadratic addition of within-run errors (2 SD) and daily reproducibility of reference monazite USGS 44069

[e] Corrected for mass-bias by normalising to USGS reference monazite (~0.6 per atomic mass unit) and common Pb using the model Pb composition of Stacey & Kramers (1975)

Table 4A: Argon isotope data from individual heating steps.

Sample: BAR1 amphibole 1				Irradiation position 9 (Z = 7.2 mm)					J-value: 0.008304 ± 0.000021				57.6 days after irradiation						
		Corrected for fractionation, ^{39}Ar, ^{36}Ar(Ca) and ^{40}Ar(K) ----------								Radiogenic -----								
Step #	µmol ^{40}Ar	^{40}Ar/^{39}Ar	± 1SE	^{40}Ar/^{36}Ar	± 1SE	^{37}Ar/^{39}Ar	± 1SE	^{38}Ar/^{39}Ar	± 1SE	^{40}Ar*/^{39}Ar	± 1SE	%^{39}Ar	Age Ma	± 95%	Incl.	Ca/K	± 2SE	Cl/K	±2SE
1	4.31E-09	485.49	23.57	1.89E+03	4.2E+02	8.06E-01	2.1E-01	1.36E-01	5.9E-02	408.67	29.34	0.10	2671.2	194.1	0	1.61	0.42	0.0173	0.0076
2	1.03E-09	77.54	3.01	7.08E+02	2.1E+02	7.62E-01	1.5E-01	4.27E-02	3.4E-02	44.85	8.54	0.15	571.4	183.3	0	1.52	0.31	0.0054	0.0044
3	1.06E-09	68.20	3.23	4.79E+02	9.2E+01	1.24E+00	1.3E-01	5.08E-02	2.6E-02	25.73	8.27	0.18	349.5	205.9	0	2.49	0.29	0.0065	0.0034
4	1.79E-09	80.10	2.25	1.11E+03	3.0E+02	1.49E+00	1.1E-01	4.72E-02	2.6E-02	58.52	5.98	0.25	714.8	115.1	0	2.97	0.27	0.0060	0.0034
5	2.86E-09	46.05	0.65	1.38E+04	1.7E+05	4.45E+00	1.0E-01	7.10E-02	1.2E-02	45.06	2.30	0.71	573.6	50.2	0	8.90	0.50	0.0090	0.0017
6	1.87E-08	43.72	0.22	7.27E+04	1.9E+06	5.30E+00	4.1E-02	8.42E-02	3.0E-03	43.54	0.40	4.85	557.0	10.1	1	10.59	0.55	0.0107	0.0009
7	1.10E-07	44.80	0.14	8.55E+04	1.0E+05	5.15E+00	1.9E-02	7.58E-02	8.3E-04	44.65	0.24	27.86	569.1	6.6	1	10.29	0.53	0.0096	0.0008
8	6.30E-08	43.67	0.12	2.93E+04	1.4E+04	5.24E+00	2.0E-02	7.91E-02	1.3E-03	43.22	0.24	16.38	553.5	6.1	1	10.48	0.54	0.0101	0.0008
9	3.05E-08	44.19	0.21	1.20E+04	2.8E+03	5.86E+00	4.5E-02	9.19E-02	1.6E-03	43.09	0.35	7.85	552.0	8.2	1	11.71	0.61	0.0117	0.0009
10	2.53E-08	46.47	0.21	3.24E+04	2.3E+04	5.11E+00	3.3E-02	9.04E-02	1.9E-03	46.04	0.32	6.17	584.3	8.2	1	10.21	0.53	0.0115	0.0009
11	1.22E-07	43.03	0.11	3.91E+05	2.3E+06	5.09E+00	1.8E-02	8.15E-02	1.0E-03	43.00	0.22	32.19	551.0	5.9	1	10.17	0.52	0.0104	0.0008
12	1.27E-08	43.60	0.25	1.44E+04	8.5E+04	4.64E+00	4.2E-02	2.72E-01	4.6E-03	42.70	0.56	3.31	547.7	13.1	1	9.28	0.48	0.0346	0.0028
								pooled gas data for included steps:				**98.61**	**558.89**	**5.68**		**10.37**	**0.53**	**0.0111**	**0.0009**

Sample: BAR1 amphibole 2				Irradiation position 9 (Z = 7.2 mm)					J-value: 0.008304 ± 0.000021				49.8 days after irradiation						
		Corrected for fractionation, ^{39}Ar, ^{36}Ar(Ca) and ^{40}Ar(K) ----------								Radiogenic -----								
Step #	µmol ^{40}Ar	^{40}Ar/^{39}Ar	± 1SE	^{40}Ar/^{36}Ar	± 1SE	^{37}Ar/^{39}Ar	± 1SE	^{38}Ar/^{39}Ar	± 1SE	^{40}Ar*/^{39}Ar	± 1SE	%^{39}Ar	Age Ma	± 95%	Incl.	Ca/K	± 2SE	Cl/K	±2SE
1	3.34E-08	1358.51	36.54	1.90E+03	7.1E+01	2.51E+00	1.3E-01	7.19E-01	4.1E-02	1145.53	39.59	0.18	4245.9	119.6	0	5.01	0.51	0.0914	0.0114
2	5.97E-09	173.39	3.73	3.08E+03	3.2E+03	8.08E-01	5.3E-02	5.24E-02	3.2E-02	156.59	6.94	0.26	1503.5	87.9	0	1.61	0.18	0.0067	0.0041
3	2.51E-09	67.09	2.25	-2.37E+03	1.7E+04	1.63E+00	3.0E-01	6.96E-02	6.9E-02	75.54	7.48	0.28	878.8	138.7	0	3.26	0.66	0.0088	0.0088
4	1.92E-09	45.45	1.11	1.50E+03	6.1E+03	1.03E+00	6.4E-02	2.41E-02	2.9E-02	36.42	3.79	0.32	476.9	87.2	0	2.06	0.22	0.0031	0.0037
5	4.61E-09	48.65	0.73	2.13E+03	1.5E+03	3.16E+00	7.1E-02	6.88E-02	6.5E-03	41.84	2.32	0.71	538.2	54.4	0	6.32	0.57	0.0087	0.0013
6	9.37E-09	47.51	0.38	-1.94E+04	8.2E+04	5.21E+00	6.4E-02	8.33E-02	4.7E-03	48.24	1.41	1.47	608.1	31.5	0	10.41	0.92	0.0106	0.0013
7	6.65E-08	45.80	0.13	2.81E+04	1.3E+04	5.26E+00	2.3E-02	8.38E-02	1.5E-03	45.32	0.27	10.85	576.5	6.5	1	10.52	0.93	0.0107	0.0012
8	1.56E-07	42.80	0.09	5.99E+04	5.3E+04	5.10E+00	1.5E-02	7.99E-02	8.0E-04	42.59	0.21	27.19	546.5	5.9	1	10.19	0.90	0.0102	0.0011
9	2.06E-07	43.74	0.10	5.30E+04	3.8E+04	4.89E+00	1.2E-02	7.77E-02	7.5E-04	43.49	0.21	35.21	556.5	5.6	1	9.78	0.86	0.0099	0.0011
10	8.97E-08	44.74	0.11	7.31E+04	8.3E+04	5.41E+00	1.9E-02	8.23E-02	1.1E-03	44.56	0.24	14.97	568.2	6.2	1	10.82	0.95	0.0105	0.0012
11	4.12E-08	45.57	0.18	3.94E+04	4.2E+04	5.23E+00	2.7E-02	8.08E-02	1.9E-03	45.22	0.33	6.75	575.5	8.2	1	10.46	0.92	0.0103	0.0012
12	1.26E-08	51.74	0.44	7.30E+03	4.5E+03	1.01E+01	1.2E-01	1.69E-01	5.2E-03	49.62	1.04	1.82	622.8	22.8	0	20.15	1.79	0.0214	0.0025
								pooled gas data for included steps:				**94.97**	**559.16**	**5.31**		**10.19**	**0.90**	**0.0102**	**0.0011**

Sample: ORC479-1a amphibole 4				Irradiation position 10 (Z = 8 mm)					J-value: 0.008306 ± 0.000021				50.7 days after irradiation						
		Corrected for fractionation, ^{39}Ar, ^{36}Ar(Ca) and ^{40}Ar(K) ----------								Radiogenic -----								
Step #	µmol ^{40}Ar	^{40}Ar/^{39}Ar	± 1SE	^{40}Ar/^{36}Ar	± 1SE	^{37}Ar/^{39}Ar	± 1SE	^{38}Ar/^{39}Ar	± 1SE	^{40}Ar*/^{39}Ar	± 1SE	%^{39}Ar	Age Ma	± 95%	Incl.	Ca/K	± 2SE	Cl/K	±2SE
1	2.39E-08	312.57	4.22	3.29E+02	5.2E+00	1.17E+00	4.0E-02	1.70E-01	8.8E-03	29.12	7.46	0.57	390.9	172.7	0	2.35	0.28	0.0216	0.0031
2	4.05E-09	87.93	2.23	3.91E+02	2.7E+01	1.02E+00	5.4E-02	1.12E-01	2.0E-02	20.77	5.54	0.34	287.3	133.1	0	2.04	0.26	0.0142	0.0032
3	1.72E-09	52.64	1.11	6.90E+02	2.4E+02	4.20E-01	1.1E-01	6.64E-02	2.2E-02	29.88	6.17	0.24	400.0	149.6	0	0.84	0.24	0.0084	0.0030
4	1.46E-09	48.22	1.37	5.90E+02	1.7E+02	3.77E-01	7.1E-02	7.24E-02	2.1E-02	23.83	6.22	0.22	326.0	157.8	0	0.75	0.17	0.0092	0.0030
5	2.26E-09	46.37	1.09	-2.87E+03	2.9E+04	3.00E+00	1.5E-01	2.51E-01	4.1E-02	51.20	6.76	0.36	639.5	141.0	0	6.00	0.75	0.0319	0.0068
6	8.00E-09	46.75	0.41	-2.09E+04	2.3E+05	4.90E+00	6.8E-02	3.99E-01	8.8E-03	47.42	0.99	1.27	599.3	22.7	0	9.79	1.12	0.0507	0.0070
7	6.08E-08	42.22	0.11	3.90E+04	2.5E+04	5.19E+00	2.0E-02	3.83E-01	2.6E-03	41.89	0.23	10.66	538.9	6.4	1	10.38	1.18	0.0487	0.0066
8	1.26E-07	42.29	0.09	3.32E+05	1.7E+06	5.25E+00	1.5E-02	3.97E-01	1.7E-03	42.26	0.21	22.02	542.9	5.6	1	10.50	1.19	0.0505	0.0069
9	7.75E-08	41.42	0.12	3.00E+04	1.5E+04	5.13E+00	1.9E-02	3.90E-01	2.4E-03	41.01	0.24	13.86	529.0	6.5	1	10.26	1.16	0.0495	0.0068
10	7.31E-08	41.58	0.12	8.69E+03	1.3E+03	5.10E+00	2.1E-02	3.82E-01	3.2E-03	40.15	0.24	13.01	519.4	6.3	1	10.19	1.15	0.0486	0.0066
11	1.41E-07	40.01	0.08	4.12E+04	3.0E+04	5.30E+00	1.6E-02	3.90E-01	1.5E-03	39.72	0.21	26.11	514.6	5.7	1	10.60	1.20	0.0496	0.0067
12	1.32E-08	40.66	0.28	-1.58E+04	3.7E+04	6.65E+00	6.0E-02	4.83E-01	7.4E-03	41.43	0.81	2.40	533.7	18.5	1	13.30	1.51	0.0614	0.0084
13	1.54E-08	40.96	0.23	1.92E+04	2.4E+05	5.31E+00	4.5E-02	3.80E-01	5.9E-03	40.33	0.71	2.79	521.4	16.4	1	10.61	1.20	0.0483	0.0066
14	1.19E-08	40.65	0.18	-1.58E+04	3.7E+05	5.04E+00	3.8E-02	3.74E-01	8.4E-03	41.42	0.68	2.17	533.6	14.6	1	10.08	1.14	0.0475	0.0066
15	1.78E-08	41.35	0.21	3.35E+04	1.8E+06	5.07E+00	3.8E-02	4.10E-01	4.5E-03	40.98	0.62	3.19	528.7	14.7	1	10.13	1.15	0.0521	0.0071
16	4.55E-09	42.70	0.52	2.70E+03	2.0E+03	5.26E+00	9.9E-02	5.09E-01	1.6E-02	37.98	1.71	0.79	494.8	39.0	0	10.52	1.21	0.0647	0.0090
								pooled gas data for included steps:				**96.21**	**527.48**	**5.77**		**10.49**	**1.19**	**0.0498**	**0.0068**

Sample: ORC479-1a amphibole 3				Irradiation position 10 (Z = 8 mm)					J-value: 0.008306 ± 0.000021				92.8 days after irradiation						
		Corrected for fractionation, ^{39}Ar, ^{36}Ar(Ca) and ^{40}Ar(K) ----------								Radiogenic -----								
Step #	µmol ^{40}Ar	^{40}Ar/^{39}Ar	± 1SE	^{40}Ar/^{36}Ar	± 1SE	^{37}Ar/^{39}Ar	± 1SE	^{38}Ar/^{39}Ar	± 1SE	^{40}Ar*/^{39}Ar	± 1SE	%^{39}Ar	Age Ma	± 95%	Incl.	Ca/K	± 2SE	Cl/K	±2SE
6	3.62E-07	41.47	0.04	2.97E+04	1.2E+04	5.04E+00	9.1E-03	4.04E-01	1.3E-03	**41.05**	**0.19**	**98.52**	**529.4**	**5.4**	**1**	**10.07**	**0.52**	**0.0513**	**0.0040**
7	3.59E-09	41.47	0.54	3.78E+03	3.4E+04	5.17E+00	9.0E-02	4.08E-01	1.1E-02	38.20	1.80	0.98	497.3	39.9	0	10.34	0.56	0.0519	0.0043
												Results of step 6 used (steps 1-5 are blanks)							

Sample: ORC479-1a biotite 1				Irradiation position 10 (Z = 8 mm)					J-value: 0.008306 ± 0.000021				93.6 days after irradiation						
		Corrected for fractionation, ^{39}Ar, ^{36}Ar(Ca) and ^{40}Ar(K) ----------							Radiogenic -----										
Step #	µmol ^{40}Ar	$^{40}Ar/^{39}Ar$	± 1SE	$^{40}Ar/^{36}Ar$	± 1SE	$^{37}Ar/^{39}Ar$	± 1SE	$^{38}Ar/^{39}Ar$	± 1SE	$^{40}Ar^*/^{39}Ar$	± 1SE	%^{39}Ar	Age Ma	± 95%	Incl.	Ca/K	± 2SE	Cl/K	±2SE
1	2.99E-08	48.21	0.16	5.65E+02	9.8E+00	9.76E-02	8.2E-03	5.69E-02	1.0E-03	22.74	0.50	1.89	312.3	12.7	0	0.1952	0.0415	0.0072	0.0016
2	2.83E-08	39.57	0.14	8.50E+03	1.7E+03	8.24E-03	3.8E-03	4.83E-02	1.0E-03	38.18	0.28	2.18	497.1	6.9	0	0.0165	0.0082	0.0061	0.0014
3	9.78E-08	40.84	0.06	2.65E+04	6.0E+03	6.42E-03	1.9E-03	4.66E-02	5.5E-04	40.38	0.12	7.29	521.9	4.2	1	0.0128	0.0046	0.0059	0.0013
4	1.45E-07	40.61	0.06	5.35E+04	1.7E+04	0.00E+00	0.0E+00	4.62E-02	4.2E-04	40.38	0.08	10.84	522.0	4.1	1	0.0000	0.0000	0.0059	0.0013
5	8.64E-08	40.89	0.08	9.21E+04	1.6E+06	4.40E-03	1.6E-03	4.65E-02	7.6E-04	40.76	0.13	6.43	526.2	4.6	1	0.0088	0.0037	0.0059	0.0013
6	7.09E-08	41.63	0.10	3.33E+04	2.3E+04	6.40E-03	2.7E-03	4.82E-02	6.9E-04	41.26	0.16	5.18	531.8	5.0	1	0.0128	0.0060	0.0061	0.0014
7	7.53E-08	41.65	0.06	1.10E+05	5.5E+06	2.82E-03	1.9E-03	4.67E-02	5.2E-04	41.54	0.13	5.50	534.9	4.5	1	0.0056	0.0040	0.0059	0.0013
8	1.00E-07	41.13	0.08	5.63E+04	5.7E+04	1.48E-02	2.0E-03	4.82E-02	6.2E-04	40.91	0.11	7.40	527.9	4.2	1	0.0297	0.0070	0.0061	0.0014
9	1.65E-07	41.27	0.06	4.57E+04	7.8E+03	2.60E-02	1.6E-03	4.75E-02	5.3E-04	41.00	0.07	12.16	528.9	3.8	1	0.0520	0.0107	0.0060	0.0013
10	1.32E-07	41.03	0.07	3.08E+04	4.2E+03	2.85E-02	2.1E-03	4.73E-02	5.6E-04	40.63	0.09	9.77	524.7	3.8	1	0.0569	0.0119	0.0060	0.0013
11	9.85E-08	40.84	0.08	5.71E+04	2.0E+05	1.77E-02	2.2E-03	4.68E-02	6.1E-04	40.63	0.11	7.34	524.8	4.4	1	0.0353	0.0082	0.0059	0.0013
12	8.63E-08	40.89	0.07	5.11E+04	9.7E+04	4.05E-02	2.2E-03	4.78E-02	7.3E-04	40.65	0.13	6.42	525.0	4.4	1	0.0811	0.0165	0.0061	0.0014
13	6.84E-08	41.07	0.08	8.45E+04	6.7E+06	4.54E-02	3.4E-03	4.85E-02	8.1E-04	40.93	0.15	5.07	528.1	4.4	1	0.0907	0.0190	0.0062	0.0014
14	3.71E-08	41.21	0.11	-1.29E+05	7.4E+05	4.19E-02	5.1E-03	4.84E-02	1.2E-03	41.31	0.26	2.74	532.3	6.9	1	0.0838	0.0193	0.0062	0.0014
15	5.54E-08	41.36	0.20	1.49E+04	4.5E+03	2.74E-02	2.8E-03	4.76E-02	7.3E-04	40.54	0.27	4.07	523.7	7.1	1	0.0549	0.0121	0.0060	0.0013
16	7.75E-08	41.21	0.09	2.64E+04	7.8E+03	3.43E-02	2.4E-03	4.85E-02	4.1E-04	40.74	0.15	5.72	526.0	4.9	1	0.0687	0.0143	0.0062	0.0014
								pooled gas data for included steps:				95.94	526.38	3.54		0.0440	0.0087	0.0060	0.0013

Sample: ORC479-1a biotite 2				Irradiation position 10 (Z = 8 mm)					J-value: 0.008305 ± 0.000021				56.7 days after irradiation						
		Corrected for fractionation, ^{39}Ar, ^{36}Ar(Ca) and ^{40}Ar(K) ----------							Radiogenic -----										
Step #	µmol ^{40}Ar	$^{40}Ar/^{39}Ar$	± 1SE	$^{40}Ar/^{36}Ar$	± 1SE	$^{37}Ar/^{39}Ar$	± 1SE	$^{38}Ar/^{39}Ar$	± 1SE	$^{40}Ar^*/^{39}Ar$	± 1SE	%^{39}Ar	Age Ma	± 95%	Incl.	Ca/K	± 2SE	Cl/K	±2SE
1	3.82E-10	29.72	2.01	-9.31E+02	1.9E+05	8.38E-01	2.0E-01	0.00E+00	0.0E+00	39.24	12.01	0.10	509.1	260.0	0	1.6754	0.4146	0.0000	0.0000
2	3.76E-09	29.62	0.35	2.54E+03	8.1E+04	4.81E-01	4.3E-02	3.11E-02	8.6E-03	26.14	1.51	1.02	354.6	37.6	0	0.9622	0.0988	0.0040	0.0011
3	3.62E-08	39.23	0.15	-7.02E+04	1.7E+07	7.43E-02	3.0E-03	4.27E-02	1.1E-03	39.39	0.23	7.41	510.8	6.1	0	0.1485	0.0097	0.0054	0.0004
4	6.11E-08	39.54	0.14	1.02E+05	7.0E+05	3.77E-02	2.9E-03	4.54E-02	1.0E-03	39.42	0.19	12.40	511.2	5.5	0	0.0754	0.0070	0.0058	0.0005
5	5.10E-08	40.03	0.12	-1.19E+05	1.1E+06	2.75E-02	2.2E-03	4.34E-02	9.8E-04	40.13	0.17	10.24	519.1	5.0	1	0.0549	0.0053	0.0055	0.0005
6	4.02E-08	40.49	0.14	-3.01E+04	2.8E+05	3.23E-02	3.6E-03	4.72E-02	1.3E-03	40.89	0.22	7.98	527.7	5.9	1	0.0645	0.0079	0.0060	0.0005
7	4.51E-08	40.30	0.16	-4.37E+04	2.1E+05	4.36E-02	1.6E-03	4.27E-02	1.4E-03	40.57	0.20	8.97	524.1	5.3	1	0.0871	0.0056	0.0054	0.0005
8	4.72E-08	40.32	0.13	-5.73E+04	1.3E+05	3.24E-02	1.9E-03	4.39E-02	8.1E-04	40.53	0.16	9.40	523.7	5.0	1	0.0647	0.0051	0.0056	0.0005
9	5.35E-08	40.55	0.10	-2.66E+05	1.2E+07	4.13E-02	1.5E-03	4.60E-02	1.0E-03	40.60	0.14	10.60	524.4	4.4	1	0.0827	0.0052	0.0058	0.0005
10	1.49E-07	40.44	0.09	-1.49E+05	4.7E+07	3.32E-02	9.1E-04	4.46E-02	7.1E-04	40.52	0.10	29.64	523.5	4.2	1	0.0663	0.0039	0.0057	0.0005
11	3.99E-09	41.57	0.49	-1.27E+04	9.1E+06	4.91E-02	1.9E-02	5.02E-02	7.7E-03	42.55	1.26	0.77	546.2	26.2	0	0.0983	0.0376	0.0064	0.0011
12	4.94E-09	39.53	0.39	1.40E+04	1.3E+06	3.29E-02	1.7E-02	2.60E-02	3.2E-03	38.68	1.02	1.00	502.8	22.6	0	0.0657	0.0349	0.0033	0.0005
13	1.08E-09	38.82	1.10	2.49E+03	3.7E+04	1.39E-02	6.1E-02	8.84E-02	1.4E-02	34.16	3.90	0.22	450.8	92.0	0	0.0279	0.1214	0.0112	0.0019
14	1.14E-09	37.27	0.41	2.15E+03	5.3E+03	0.00E+00	0.0E+00	1.16E-01	1.4E-02	32.10	3.58	0.24	426.5	82.4	0	0.0000	0.0000	0.0148	0.0022
								pooled gas data for included steps:				76.82	521.90	3.61		0.0691	0.0038	0.0057	0.0004

Sample: ORC479-1b amphibole 3				Irradiation position 11 (Z = 8.8 mm)					J-value: 0.008305 ± 0.000021				51.8 days after irradiation						
		Corrected for fractionation, ^{39}Ar, ^{36}Ar(Ca) and ^{40}Ar(K) ----------							Radiogenic -----										
Step #	µmol ^{40}Ar	$^{40}Ar/^{39}Ar$	± 1SE	$^{40}Ar/^{36}Ar$	± 1SE	$^{37}Ar/^{39}Ar$	± 1SE	$^{38}Ar/^{39}Ar$	± 1SE	$^{40}Ar^*/^{39}Ar$	± 1SE	%^{39}Ar	Age Ma	± 95%	Incl.	Ca/K	± 2SE	Cl/K	±2SE
1	1.20E-09	170.11	79.11	4.67E+02	3.2E+03	0.00E+00	0.0E+00	1.28E+00	6.8E-01	61.37	199.04	0.05	743.4	3468.6	0	0.00	0.00	0.1625	0.0925
2	1.36E-09	137.47	8.63	5.62E+02	1.0E+02	2.99E+00	3.1E-01	5.07E-01	8.2E-02	64.42	15.30	0.07	773.4	304.8	0	5.98	1.18	0.0645	0.0162
3	2.00E-09	52.78	1.15	1.08E+03	3.1E+02	4.97E+00	1.8E-01	2.74E-01	1.9E-02	38.18	3.49	0.26	497.1	81.6	0	9.93	1.70	0.0349	0.0071
4	5.32E-09	43.14	0.56	2.19E+03	3.2E+02	5.41E+00	8.6E-02	3.09E-01	1.1E-02	37.25	1.01	0.83	486.5	23.1	0	10.81	1.82	0.0392	0.0077
5	2.37E-08	40.07	0.17	3.30E+04	3.1E+04	5.94E+00	3.4E-02	3.15E-01	3.8E-03	39.71	0.34	3.98	514.4	8.7	1	11.88	1.99	0.0400	0.0077
6	6.61E-08	39.80	0.11	4.79E+04	4.6E+04	6.09E+00	2.5E-02	3.17E-01	2.6E-03	39.55	0.25	11.19	512.6	6.2	1	12.17	2.04	0.0403	0.0078
7	1.03E-07	39.63	0.10	3.44E+04	2.2E+04	6.01E+00	2.0E-02	3.06E-01	1.8E-03	39.29	0.23	17.47	509.7	6.6	1	12.02	2.02	0.0389	0.0075
8	9.47E-08	39.66	0.09	7.04E+04	9.3E+04	5.96E+00	2.2E-02	3.11E-01	1.8E-03	39.49	0.25	16.09	511.9	6.8	1	11.91	2.00	0.0396	0.0076
9	9.23E-08	39.50	0.12	4.25E+04	3.5E+04	6.00E+00	2.1E-02	3.20E-01	2.1E-03	39.22	0.26	15.74	508.9	6.8	1	12.00	2.01	0.0407	0.0078
10	1.38E-07	40.82	0.11	6.00E+04	6.5E+04	6.14E+00	1.9E-02	3.31E-01	1.4E-03	40.61	0.25	22.69	524.6	6.6	1	12.27	2.06	0.0421	0.0081
11	6.92E-08	40.55	0.10	5.32E+04	8.3E+04	9.65E+00	3.1E-02	4.05E-01	2.1E-03	40.32	0.36	11.50	521.3	8.5	1	19.29	3.23	0.0515	0.0099
12	6.45E-10	33.38	0.92	-4.84E+03	1.7E+04	8.10E+00	3.1E-01	1.26E+00	5.1E-02	35.44	7.20	0.13	465.6	170.1	0	16.19	2.78	0.1606	0.0316
								pooled gas data for included steps:				98.67	515.23	6.20		12.91	2.16	0.0417	0.0080

Sample: ORC479-1b biotite 2				Irradiation position 11 (Z = 8.8 mm)					J-value: 0.008305 ± 0.000021				53.7 days after irradiation						
		Corrected for fractionation, ^{39}Ar, ^{36}Ar(Ca) and ^{40}Ar(K) ----------							Radiogenic -----										
Step #	µmol ^{40}Ar	$^{40}Ar/^{39}Ar$	± 1SE	$^{40}Ar/^{36}Ar$	± 1SE	$^{37}Ar/^{39}Ar$	± 1SE	$^{38}Ar/^{39}Ar$	± 1SE	$^{40}Ar^*/^{39}Ar$	± 1SE	%^{39}Ar	Age Ma	± 95%	Incl.	Ca/K	± 2SE	Cl/K	±2SE
1	1.39E-09	16.14	0.17	2.08E+03	1.2E+04	6.20E-02	2.2E-02	7.05E-02	8.5E-03	13.82	1.38	0.42	196.2	35.5	0	0.1239	0.0490	0.0090	0.0022
2	8.82E-09	34.31	0.27	4.53E+03	1.8E+03	3.18E-02	4.5E-03	5.00E-02	2.4E-03	32.05	0.69	1.25	425.9	17.1	0	0.0636	0.0147	0.0064	0.0014
3	1.07E-08	39.44	0.23	-3.36E+04	2.5E+05	0.00E+00	0.0E+00	4.88E-02	3.1E-03	39.79	0.44	1.32	515.3	10.0	0	0.0000	0.0000	0.0062	0.0013
4	3.29E-08	39.10	0.15	-6.51E+05	3.9E+06	4.36E-03	2.6E-03	4.69E-02	1.0E-03	39.11	0.20	4.09	507.7	5.8	0	0.0087	0.0054	0.0060	0.0012
5	4.37E-08	39.05	0.11	1.52E+05	3.0E+06	6.28E-03	1.7E-03	4.63E-02	1.1E-03	38.98	0.16	5.43	506.1	4.9	0	0.0126	0.0041	0.0059	0.0012
6	5.57E-08	39.93	0.13	-7.49E+04	2.8E+05	5.12E-03	1.7E-03	4.73E-02	1.2E-03	40.09	0.17	6.77	518.7	5.0	0	0.0102	0.0039	0.0060	0.0013
7	1.33E-07	41.15	0.08	2.93E+04	3.0E+03	3.92E-03	7.0E-04	4.76E-02	5.8E-04	40.73	0.10	15.69	525.8	4.2	1	0.0078	0.0020	0.0061	0.0013
8	1.13E-07	40.69	0.08	-8.34E+04	2.0E+04	1.58E-03	7.2E-04	4.59E-02	5.7E-04	40.83	0.09	13.47	527.0	3.9	1	0.0032	0.0016	0.0058	0.0012
9	8.17E-08	40.53	0.10	-3.71E+04	8.4E+03	2.25E-03	9.6E-04	4.64E-02	5.6E-04	40.85	0.12	9.79	527.2	4.2	1	0.0045	0.0021	0.0059	0.0012
10	6.73E-08	40.65	0.14	-1.65E+05	2.0E+06	4.69E-03	8.8E-04	4.57E-02	6.9E-04	40.72	0.14	8.05	525.7	4.6	1	0.0094	0.0025	0.0058	0.0012
11	5.47E-08	40.85	0.13	-9.21E+04	2.9E+05	5.31E-03	1.5E-03	4.66E-02	9.3E-04	40.98	0.15	6.51	528.6	4.7	1	0.0106	0.0036	0.0059	0.0012
12	3.97E-08	41.24	0.21	4.82E+04	3.2E+05	6.79E-03	1.7E-03	4.63E-02	1.2E-03	40.98	0.26	4.68	528.7	7.0	1	0.0136	0.0042	0.0059	0.0012
13	3.80E-08	40.91	0.15	1.42E+05	1.3E+06	3.56E-03	1.7E-03	4.68E-02	1.2E-03	40.82	0.20	4.51	526.9	5.9	1	0.0071	0.0036	0.0059	0.0012
14	9.28E-08	41.07	0.09	-2.52E+05	3.4E+06	6.84E-03	8.3E-04	4.77E-02	8.5E-04	41.12	0.11	10.97	530.2	4.0	1	0.0137	0.0030	0.0061	0.0013
15	4.64E-08	40.76	0.11	-1.48E+05	5.7E+06	1.52E-02	2.2E-03	4.56E-02	1.2E-03	40.84	0.16	5.52	527.1	4.8	1	0.0305	0.0071	0.0058	0.0012
16	1.13E-08	41.51	0.38	-2.36E+04	4.6E+05	6.59E-03	4.6E-03	5.02E-02	3.3E-03	42.04	0.56	1.32	540.4	13.4	0	0.0132	0.0095	0.0064	0.0014
17	1.69E-09	41.54	0.76	-1.22E+04	2.1E+05	0.00E+00	0.0E+00	8.35E-02	1.3E-02	42.56	2.95	0.20	546.2	64.4	0	0.0000	0.0000	0.0106	0.0027
								pooled gas data for included steps:				79.20	523.73	3.94		0.0097	0.0019	0.0059	0.0012

Sample: ORC484-4 amphibole 1				Irradiation position 12 (Z = 8.8 mm)					J-value: 0.008305 ± 0.000021					52.6 days after irradiation						
		Corrected for fractionation, ^{39}Ar, $^{36}Ar(Ca)$ and $^{40}Ar(K)$ ----------									Radiogenic -----									
Step #	µmol ^{40}Ar	$^{40}Ar/^{39}Ar$	± 1SE	$^{40}Ar/^{36}Ar$	± 1SE	$^{37}Ar/^{39}Ar$	± 1SE	$^{38}Ar/^{39}Ar$	± 1SE	$^{40}Ar^*/^{39}Ar$	± 1SE	$\%^{39}Ar$	Age Ma	± 95%	Incl.	Ca/K	± 2SE	Cl/K	±2SE
1	2.33E-09	19.23	0.15	4.85E+02	4.5E+01	4.70E-01	1.6E-02	9.42E-02	3.6E-03	7.39	1.15	1.56	107.5	31.2	0	0.94	0.20	0.0120	0.0029
2	2.67E-09	36.95	0.62	5.14E+02	4.9E+01	5.02E-01	3.6E-02	2.09E-01	1.4E-02	15.50	2.19	0.93	218.5	55.8	0	1.00	0.22	0.0265	0.0065
3	3.08E-09	95.52	2.32	3.59E+02	1.6E+01	1.18E+00	5.6E-02	4.27E-01	2.4E-02	16.05	4.78	0.42	225.8	133.7	0	2.36	0.50	0.0542	0.0131
4	1.46E-09	64.68	1.61	6.98E+02	2.2E+02	1.86E+00	1.2E-01	7.83E-01	3.6E-02	37.02	7.19	0.29	483.8	166.7	0	3.71	0.81	0.0995	0.0239
5	2.66E-09	54.19	0.83	1.45E+03	4.5E+02	2.66E+00	7.1E-02	9.12E-01	2.9E-02	43.05	2.89	0.63	551.6	65.3	0	5.32	1.12	0.1160	0.0276
6	2.40E-09	40.84	0.56	3.17E+03	2.8E+04	2.75E+00	8.7E-02	8.34E-01	2.5E-02	37.00	2.12	0.76	483.6	47.2	0	5.50	1.16	0.1060	0.0252
7	4.86E-09	48.32	0.44	1.44E+03	1.6E+02	5.22E+00	8.4E-02	1.48E+00	2.1E-02	38.27	1.18	1.30	498.1	25.8	0	10.44	2.18	0.1886	0.0445
8	6.01E-08	42.20	0.12	1.75E+04	7.5E+03	7.85E+00	3.1E-02	2.16E+00	9.9E-03	41.48	0.32	18.37	534.2	7.7	1	15.70	3.27	0.2744	0.0647
9	4.37E-08	42.01	0.19	1.69E+04	6.4E+03	7.21E+00	4.0E-02	2.00E+00	1.2E-02	41.27	0.35	13.40	531.9	8.9	1	14.42	3.00	0.2536	0.0598
10	9.81E-08	41.57	0.12	4.90E+04	5.4E+04	7.32E+00	2.9E-02	1.98E+00	8.2E-03	41.32	0.30	30.42	532.4	7.5	1	14.64	3.05	0.2520	0.0594
11	9.17E-08	40.67	0.11	5.18E+04	6.1E+04	8.04E+00	2.4E-02	2.13E+00	7.1E-03	40.43	0.30	29.06	522.5	7.8	1	16.08	3.35	0.2712	0.0640
12	7.92E-09	40.44	0.31	9.38E+03	2.2E+04	9.29E+00	9.0E-02	2.44E+00	2.6E-02	39.15	0.83	2.52	508.0	18.9	0	18.56	3.87	0.3105	0.0733
13	4.78E-10	44.33	2.17	2.64E+02	6.4E+01	7.91E+00	4.8E-01	2.07E+00	1.5E-01	-5.82	11.85	0.14	-89.4	365.1	0	15.81	3.43	0.2634	0.0650
14	6.76E-10	41.69	1.95	4.12E+02	1.3E+02	7.71E+00	3.6E-01	2.96E+00	1.3E-01	11.47	8.29	0.21	164.2	221.4	0	15.41	3.29	0.3768	0.0905
								pooled gas data for included steps:				91.24	529.54	7.49		15.28	3.18	0.2629	0.0620

Temperatures range from c. 600 C for step 1 to fusion (c. 1300 C) at the last 2 to 3 steps								
Heating time: 5 Min. for each step.								
Exponential fractionation factor: -0.321								
All values regressed to time of gas inlet into mass spectrometer.								
Blank measurements carried out after 3 or 4 step measurements using exactly same protocol.								
Typical ^{40}Ar blank level at gas-in time: 1E-10 µMol								
Measured signals were blank corrected, using blank time functions, before regression.								
Ca/K factor: 1.999 ± 0.103								
Cl/K factor: 0.127 ± 0.010		Both from measurements on McClure Mountains hornblende						
Constants used:								
Atmospheric argon ratios:								
$(^{40}Ar/^{36}Ar)_A$		298.56 ± 0.31		Lee et al., 2006				
$(^{38}Ar/^{36}Ar)_A$		0.1885 ± 0.0003		Lee et al., 2006				
Interfering isotope production ratios:								
$(^{39}Ar/^{37}Ar)_{Ca}$		(8.6 ± 0.1)E-4		Own calibrations of position B2W in Safari1 reactor				
$(^{36}Ar/^{37}Ar)_{Ca}$		(2.8 ± 1.1)E-4		Own calibrations of position B2W in Safari1 reactor				
$(^{40}Ar/^{39}Ar)_K$		0.0426 ± 0.0041		Own calibrations of position B2W in Safari1 reactor				
Decay constants:								
^{40}K total		(5.541 ± 0.014)E-10 a^{-1}		Kossert and Günther 2004				
^{39}Ar		0.00258 ± 0.00003 a^{-1}		Stoenner et al. (1965)				
^{37}Ar		0.01975 ± 0.0005 day^{-1}		Renne and Norman (2001)				